A theoretical study of creep deformation mechanisms of Type 316H stainless steel at elevated temperatures

Jianan Hu

Supervisor: Prof. Alan Cocks

St Anne's College

Solid Mechanics and Materials Engineering

Department of Engineering Science

University of Oxford

A thesis submitted for the degree of

Doctor of Philosophy

Hilary 2015

Abstract

The currently operating Generation II Advanced Gas-Cooled Reactors (AGR) in the nuclear power stations in the UK, mainly built in the 1960s and 1970s, are approaching their designed life. Besides the development of the new generation of reactors, the government is also seeking to extend the life of some AGRs. Creep and failure properties of Type 316H austenitic stainless steels used in some components of AGR at elevated temperature are under investigation in EDF Energy Ltd. However, the current empirical creep models used and examined in EDF Energy have deficiency and demonstrate poor agreement with the experimental data in the operational complex thermal/mechanical conditions. The overall objective of the present research is to improve our general understanding of the creep behaviour of Type 316H stainless steels under various conditions by undertaking theoretical studies and developing a physically based multiscale state variable model taking into account the evolution of different microstructural elements and a range of different internal mechanisms in order to make realistic life prediction.

A detailed review shows that different microstructural elements are responsible for the internal deformation mechanisms for engineering alloys such as 316H stainless steels. These include the strengthening effects, associated with forest dislocation junctions, solute atoms and precipitates, and softening effects, associated with recovery of dislocation structure and coarsening of precipitates. All the mechanisms involve interactions between dislocations and different types of obstacles. Thus change in the microstructural state will lead to the change in materials' internal state and influence the mechanical/creep property.

Based on these understandings, a multiscale self-consistent model for a polycrystalline material is established, consisting of continuum, crystal plasticity framework and dislocation

link length model that allows the detailed dislocation distribution structure and its evolution during deformation to be incorporated. The model captures the interaction between individual slip planes (self- and latent hardening) and between individual grains and the surrounding matrix (plastic mismatch, leading to the residual stress). The state variables associated with all the microstructure elements are identified as the mean spacing between each type of obstacles. The evolution of these state variables are described in a number of physical processes, including the dislocation multiplication and climb-controlled network coarsening and the phase transformation (nucleation, growth and coarsening of different phases). The enhancements to the deformation kinetics at elevated temperature are also presented.

Further, several simulations are carried out to validate the established model and further evaluate and interpret various available data measured for 316H stainless steels. Specimens are divided into two groups, respectively ex-service plus laboratory aged (EXLA) with a considerable population of precipitates and solution treated (ST) where precipitates are not present. For the EXLA specimens, the model is used to evaluate the microscopic lattice response, either parallel or perpendicular to the loading direction, subjected to uniaxial tensile and/or compressive loading at ambient temperature, and macroscopic Bauschinger effect, taking into account the effect of pre-loading and pre-crept history. For the ST specimens, the model is used to evaluate the phase transformation in the specimen head volume subjected to pure thermal ageing, and multiple secondary stages observed during uniaxial tensile creep in the specimen gauge volume at various temperatures and stresses. The results and analysis in this thesis improve the fundamental understanding of the relationship between the evolution of microstructure and the creep behaviour of the material. They are also beneficial to the assessment of materials' internal state and further investigation of deformation mechanism for a broader range of temperature and stress. These results were reported (or to be reported) in several publications in peer-reviewed journals and conference proceedings.

Acknowledgement

At the outset, I would like to express my profound appreciation and gratitude to my supervisor Prof. Alan Cocks, for his direction and support throughout my DPhil. His constant enthusiasm, dedication and carefulness deeply impressed and inspired me. It was his constant trust and steady encouragements in my most difficult times that have been essential to my success through the last 4 years. It is a great privilege to have worked with him. His personalities and professional research skills are a great fortune that will benefit me in my future career.

The episode of acknowledgement would not be complete without the mention of my family. I wish to thank my parents for their love and patience both mentally and financially during the past 4 years. Also, I would like to present my special sincere thanks to my wife Tan Sui, who has offered me tireless and loving support and many useful advices in the thesis writing and editing. The encouragement from my daughter Shengxin Hu was invaluable as well. Any words are weak here to express my gratitude to my family. I wish I can dedicate this thesis to them, and thank them with all my heart for their love, care and patience.

I am grateful to my collaborators, Prof. David Smith and Prof. Peter Flewitt (University of Bristol, U.K.), Dr. Bo Chen (University of Manchester, U.K.) and Graham Green (University of Loughborough) for their kind assistance. It was an unforgettable experience to work with them. I must also thank my sponsor, EDF Energy, for supplying the material and supporting the research. ISIS facility is also acknowledged for the provision of neutron beamtime at ENGIN-X beamline at the Rutherford Appleton Laboratory.

My sincere thanks to Prof. John Huber, Prof. Alexander Korsunsky and Prof. Fionn Dunne whom I have had opportunities to have a number of fruitful discussions with. Many have

provided helpful hints throughout the project. I would also like to thank my friends and also colleagues in Solid Mechanics and Materials Engineering group of Department of Engineering Science, in particular Ding Shin Huang, Dr. David Gonzalez, Dr. Mehmet Kartal, Dr. Tuncay Yalcinkaya, Mengyin Xie, Bo Lan and Zailing Zhu. Thanks them for valuable advice on my research. Thanks to all other members in the group for the warm friendship.

Gratefully acknowledge to St Anne's College and Department of Engineering Science at University of Oxford, for offering me the technical support.

Contents

Nomenclature

T	Absolute temperature, or the orientation matrix for individual grains
G	Shear modulus
b	Length of the Burgers vector
ϕ_c	Breakaway angle between obstacles
τ_d, τ_p, τ_s	Internal resistance associated with forest dislocation junctions, precipitates (Orowan strength) and solute atoms
α_d, α_s	Obstacle strength of forest dislocation junctions and solute atoms
τ_{LC}, τ_{GC}	Threshold stress for local climb (LC) and general climb (GC) over particles
τ_{cr}	Overall internal resistance or critical resolved shear strength (CRSS)
L_d, L_p, L_s	Mean spacing between forest dislocation junctions, precipitates and solute atoms on individual slip planes
N_d, N_A	Number density of forest dislocation junctions and precipitates on individual slip planes
N_p	Number density of precipitates per unit volume
N_l	Number of secondary dislocation loops
λ	Dislocation link length
$\lambda_{th}, \bar{\lambda}$	Threshold (average) link length
$\phi(\lambda)$	Two-dimensional dislocation distribution function
ρ	Total dislocation density
f_v, f_A	Volume (area) fraction of precipitates
r_p	Mean size (radius) of precipitates

τ_m^r, τ_p^r	Type III internal stress in the matrix and precipitates
$\dot{\gamma}_0$	Reference shear strain rate
σ^a, ε^a	Stress-strain field in individual grains
L^a, C^a	Stiffness and compliance matrix of an anisotropic grain
L^i, C^i	Stiffness and compliance matrix of the isotropic polycrystal
$\varepsilon^{ta}, \varepsilon^{t*}$	Misfit strain (mismatch) in the real inhomogeneous inclusion and equivalent homogeneous inclusion
S^i	Eshelby shape tensor
X^a	Type II internal stress in individual grains
ΔF_0	Total activation energy required to overcome obstacles without aid from external stress
F_{sol}	Thermal solute drag factor
a_c	Area of dislocation core
$\bar{c}, c_p$	Solute concentration in the matrix and precipitates
c_{eq}	Equilibrium solute concentration in the matrix
k, R	Boltzmann's constant and gas constant
D, D_c	Bulk and dislocation core diffusivity
V_m, v_m	Molar volume (molecular volume) of a given phase
r_c	Critical radius for stable nuclei

List of Tables

List of Figures

Publication resulting from this thesis

Journal Publication:

1. **JN Hu**, ACF Cocks. A multi-scale self-consistent model describing the lattice deformation in polycrystalline austenitic stainless steels. Int. J. Solids. Struct. Under review, 2015.
2. **JN Hu**, ACF Cocks. On the evaluation of Bauschinger effect in a polycrystalline austenitic stainless steel—The role of precipitates and the misfit stress. In preparation, 2015.
3. **JN Hu**, ACF Cocks. Effect of creep and recovery on the evolution of internal resistance and internal stress in a polycrystalline austenitic stainless steel. In preparation, 2015.
4. **JN Hu**, ACF Cocks. Evaluation of the microstructure evolution and its influence on creep properties of austenitic stainless steels. In preparation, 2015.
5. B Chen, **JN Hu**, PEJ Flewitt, DJ Smith, ACF Cocks, SY Zhang. Quantifying internal stress and internal resistance associated with thermal ageing and creep in a polycrystalline material. Acta Mater. 2014(67): 207-219.
6. B Chen, **JN Hu**, YQ Wang, SY Zhang, SV Petegem, ACF Cocks, DJ Smith, PEJ Flewitt. Role of the misfit stress between grains on the Bauschinger effect for a polycrystalline material. Acta Mater. 2014(85): 229-242.
7. B Chen, **JN Hu**, YQ Wang, S Kabra, ACF Cocks, DJ Smith, PEJ Flewitt. Internal strains between grains during creep deformation of an austenitic stainless steel. J Mater Sci. 2015(50): 5809-5816.

8. B Chen, **JN Hu**, PEJ Flewitt, ACF Cocks, RA Ainsworth, DJ Smith, DW Dean, F Scenini. Effect of thermal ageing on creep and oxidation behaviour of Type 316H stainless steel. Materials at High Temperature. 2015(0): 1-15.

Conference Contribution:

1. **JN Hu**, B Chen, DJ Smith, ACF Cocks. A self-consistent model in the local residual stress evaluation of 316H stainless steel. ICF13 (13th International Conference on Fracture) Proceedings, Beijing, 2013.
2. **JN Hu,** B Chen, DJ Smith, PEJ Flewitt, ACF Cocks. Self-consistent modelling and the evaluation of lattice deformation in a polycrystalline austenitic stainless steels. Materials Today: Proceedings, 2015(2): S424-S433.
3. B Chen, **JN Hu**, SY Zhang, DJ Smith, PEJ Flewitt. Effects of thermal ageing on the lattice strains in a single phase polycrystalline material measured by neutron diffraction. ESIA12 (12th International Conference on Engineering Structural Integrity Assessment) Proceedings, Manchester, 2013.
4. **JN Hu**, ACF Cocks. Correlation between microstructure evolution and creep properties of polycrystalline austenitic stainless steels. SMiRT (Structural Mechanics in Reactor Technology), Manchester, 2015.

Chapter 1

Introduction

1.1. Motivation and practical problem

A nuclear power plant is a thermal power station with one or more nuclear reactors as the heat source (Figure 1.1a), where the heat is used to generate steam in driving a steam turbine connected to a generator in order to convert kinetic energy supplied by the turbine into electrical energy. The UK, once the world leader in the development of nuclear technology, has developed Generation I technology systems of Magnox reactors in the 1950s and Generation II gas-cooled systems in the 1960s and 70s including the current operating reactors mainly of Advanced Gas-Cooled Reactors (AGR) (Figure 1.1b).

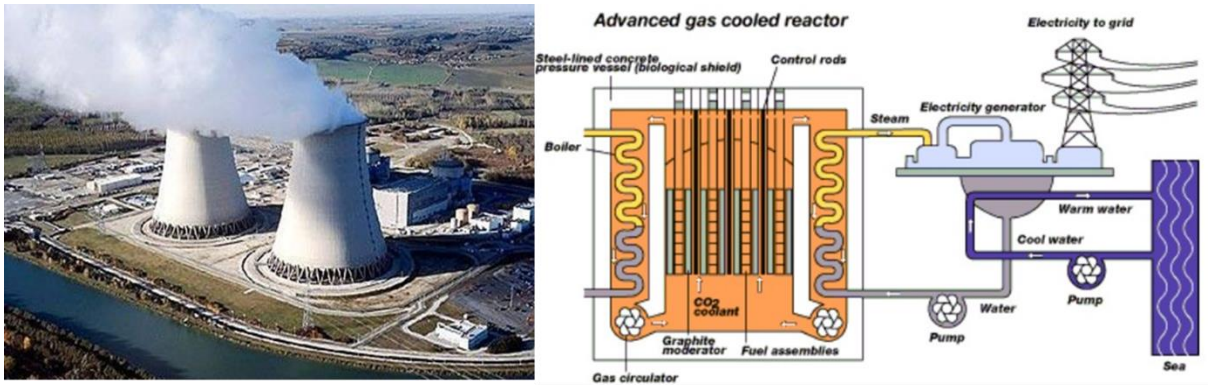

(a) (b)

Fig. 1.1 (a) A nuclear power plant station; (b) The Advanced Gas-Cooled Reactors (AGR) in the Generation II gas-cooled systems [1]

At present, the AGR reactors of Generation II systems are approaching their designed life. Besides the development of new Generation III systems of mainly Pressurised Water

Reactors (PWR) with advanced safety systems, the government and the operating company EDF Energy / British Energy Ltd are also seeking to extend the life of AGR due to economical purposes. The operation mode of the AGR often generates complex thermal/mechanical loading conditions either globally or locally within the components. One of the life limiting issues of the components at elevated temperatures is the creep deformation (a time-dependent inelastic deformation under long-term exposure of stresses and elevated temperatures) and failure caused by excessive inelastic strain. Unexpected failure of the components could cause closure of the whole nuclear power plant.

At the current time, EDF Energy has reduced the operating temperature of some of its AGRs in order to extend the life of the reactors. At the same time, creep and failure properties of the austenitic engineering alloy Type 316H stainless steels, used extensively in structural AGR components are under investigation in EDF Energy / British Energy Ltd [2]. Tests are being carried out on components at different temperatures and/or stresses to provide a more detailed understanding of the creep response. Simple models provided by the R66 AGR Materials Data Handbook have been used by EDF Energy to interpret and fit the experimental data. However, the models are empirical and have been derived from uniaxial constant load data, and fits are generally across a range of different batches, with different compositions within the wide bands allowed by the specification for 316H, and different pre-loading histories, which can give rise to different creep properties and large error bars for the fitted equations. The model prediction demonstrates poor agreement in some complex cyclic stress or temperature conditions, producing significant differences to experimentally observed behaviour or plant experience. Moreover, due to the huge cost and time-consuming characteristic of long-term creep tests, structural integrity assessments require that the available short timescale experimental data are used for the constitutive models to fit and further to predict long timescale behaviour. Therefore, a comprehensive understanding of

creep deformation and failure mechanisms of Type 316H stainless steels is essential. Simple and applicable constitutive models mechanistically motivated with foundations in physics that could successfully deal with different thermal/mechanical loading and material conditions are required for realistic life prediction.

1.2. Aims and scope of the current research

The overall aim of the present research is to improve our general understanding of the creep behaviour of Type 316H stainless steels by undertaking theoretical studies that link events and processes at the microscale (the scale of dislocations and precipitates within individual grains) with behaviour at the macroscale. The detailed objectives are

- To review the creep deformation mechanisms, including strengthening and softening effects by different constituents in the material and find the most appropriate state variables to describe the material internal state and determine how the state variables influence the material's creep behaviour.
- To establish a simple theoretical and physically based constitutive framework to illustrate the detailed kinetics and evolution of the material state variables across a range of practically important stresses and temperatures.
- To validate the model and assess its ability and applicability by evaluating available data for 316H stainless steel provided by EDF Energy and collaborators and then to predict long-term creep response of the material.

In this research, deformation is the focus rather than failure. Emphasis is put on the creep deformation driven by dislocation motion rather than pure atom diffusion. EDF has provided the typical temperature and stress range of the component in service, which is approximately 470^{o}C-550^{o}C at stresses 100-300MPa or 650^{o}C at stresses 10~100MPa. However, since the life prediction requires long-term data, which is not available at the current stage, some short-

term tests on specimens even beyond the operating temperature (up to 750^{o}C) are also being carried out and considered as accelerated simulations of the evolution of the material internal state (typically microstructure) for long-term exposure at relatively low temperatures. Care needs to be taken in the interpretation of data in such accelerated tests, since there are a range of kinetic processes which can change as the temperature is changed. In another word, the mechanisms at higher temperatures may not be completely representative of those at lower temperatures, i.e. different mechanisms may operate.

1.3. Thesis structure

Chapter 2 starts with general background information on creep deformation and mechanisms, with the focus on creep resulting from dislocation motion; the range of dominance of each mechanism is represented on suitable deformation-mechanism maps. Then the current empirical models used by EDF Energy and the critical problems or deficiencies are briefly described. This is followed by a detailed literature review on the basis of strengthening and softening mechanisms associated with different microstructural elements, typically forest dislocations, solid solution elements and precipitates. The influence of these microstructural elements on dislocation motion at elevated temperatures is also presented. Following on from this discussion, the mechanistic concepts of internal resistance and internal stress are introduced. Finally, a detailed account is given of several representative analytical models of creep deformation that have been proposed in literature.

Chapter 3 establishes the detailed athermal physical plasticity model for a single crystal, based on the original dislocation link length framework proposed by Lagneborg and his co-workers [3, 4]. Specific emphasis is put on the detailed evolution of the dislocation structure on each individual slip plane consisting of a random distribution of dislocation links. Hardening on each slip plane is characterised by the increase of the number of dislocation

links during plastic deformation. The remaining part focuses on the additional contribution of precipitation and solid solution on the athermal strengthening of each slip plane, where the distributions of the two elements are also random, but fixed, at ambient temperature.

Chapter 4 extends Chapters 3 by establishing a crystal based plasticity framework embedded in a multi-scale self-consistent model for a polycrystalline material. Plastic strain of each individual grain or crystal is determined by collecting the plastic responses on all the elementary slip systems. The self-consistent model is employed to simulate the behaviour of the polycrystalline aggregate from the collection of responses of all individual grains. The self-consistent scheme captures the interaction between slip planes and between individual grains and the surrounding matrix.

Chapter 5 presents an application of the athermal multi-scale self-consistent model established in Chapters 3 and 4 on the evaluation of micro-scale *in situ* lattice deformation of different subsets of grains and the macro-scale Bauschinger effect of a F.C.C. Type 316H polycrystalline austenitic stainless steel subjected to uniaxial loading at ambient temperatures. Relevant experimental data is shown, measured by the advanced non-destructive neutron diffraction technique, and is compared with the model predictions. The detailed mechanism of athermal deformation of the material is illustrated.

Chapter 6 enhances the athermal model established in Chapters 3 and 4 by incorporating mechanisms active at elevated temperatures. The change of kinetics of dislocation motion is modelled at the first place, which includes thermally activated dislocation glide, dislocation climb-controlled bypassing over precipitates and thermal solute drag process. Particular effort is then put mainly on modelling the evolution of different microstructural elements at elevated temperatures and the associated influence on further dislocation motion. Such evolution includes recovery of dislocation structure, nucleation, growth and coarsening of precipitates (phase transformation) and depletion of solute elements as a result of the

precipitation process. All these evolution processes lead to a variation in the strengthening and softening effect of the material at elevated temperatures. All these enhancements together with the athermal plasticity model established in Chapters 3 and 4 make a comprehensive material model that is able to simulate the detailed creep deformation at elevated temperatures.

Chapter 7 focuses on some applications of the comprehensive model, with enhancements incorporated in Chapter 6, on the evaluation of high temperature behaviour of Type 316H austenitic stainless steels. Three applications are presented respectively, including: influence of creep deformation on the macroscopic Bauschinger effect; phase transformation during pure thermal ageing; and simulation of the complex phenomenon of multiple secondary stages observed in some creep rate vs. time curves at different stresses and/or temperatures. The model predictions are compared with relevant experimental data obtained elsewhere. Mechanisms of creep deformation at various conditions are identified and illustrated.

Chapter 8 summarizes the conclusions obtained from the research so far, and presents an outlook of the direction for future work.

Chapter 2

Scientific background and literature review

2.1. Brief overview on creep deformation

Creep deformation is a time and temperature-dependent inelastic strain accumulation under long-time exposure at constant load or stress for both single and polycrystalline solids. Unlike conventional plastic deformation, creep can occur even when the load or stress is below the yield strength. The total strain ε^{tot} is the sum of the elastic strain ε^{e} and inelastic strain ε^{ine} [5].

$$\varepsilon^{tot} = \varepsilon^{e} + \varepsilon^{ine} \tag{2.1}$$

The elastic component conforms to Hooke's Law, $\varepsilon^{e} = \sigma / E$ (E: Young's modulus) in uniaxial loading, or more generally, $\varepsilon_{ij}^{\ e} = F_{ijkl}\sigma_{kl}$ (F_{ijkl}: fourth order compliance tensor) under either uniaxial or multiaxial loading. The inelastic component during creep deformation may consist of time-independent and time-dependent plastic strain, with the latter usually called creep strain [6]. Since creep is also a form of plastic deformation, in this research we do not distinguish between creep strain and plastic strain. The general relationship between the strain rate and the stress can be given by

$$\dot{\varepsilon}_{ij} = \frac{3}{2}\dot{\varepsilon}_{ef}\frac{s_{ij}}{\sigma_{ef}} \tag{2.2}$$

for an isotropic material, where $\dot{\varepsilon}_{ef}$ is the effective strain rate as a function of the effective stress σ_{ef}, and s_{ij} is the deviatoric components of stress ($s_{ij} = \sigma_{ij} - \sigma_{kk}\delta_{ij}/3$). The accumulated effective strain is then given by the integration

$$\varepsilon_{ef} = \int_0^t \dot{\varepsilon}_{ef} dt \tag{2.3}$$

At any instant, the strain rate and the corresponding yield strength, which is defined as the critical stress needed to produce further plastic flow, depend on the material state, exposure time and temperature [7].

2.1.1. Stages of creep and state variable

2.1.1.1. Standard creep curve

Under a constant load and temperature, a typical creep curve may consist of three stages [8]: I) Primary or transient stage; II) Steady state, stationary or secondary stage; III) Tertiary stage. An idealized creep curve from the standard creep test is shown in Figure 2.1, where Figure 2.1(a) plots the creep strain vs time curves while Figure 2.1(b) plots the equivalent creep strain rate vs time curves. The primary stage is the early stage of creep when the creep rate gradually decreases with time. The secondary almost linear stage is reached afterwards, during which the creep rate remains constant. This is followed by the tertiary stage with accelerating strain rate resulting from mechanical (i.e. external or internal necking) or microstructural instability and leading to failure.

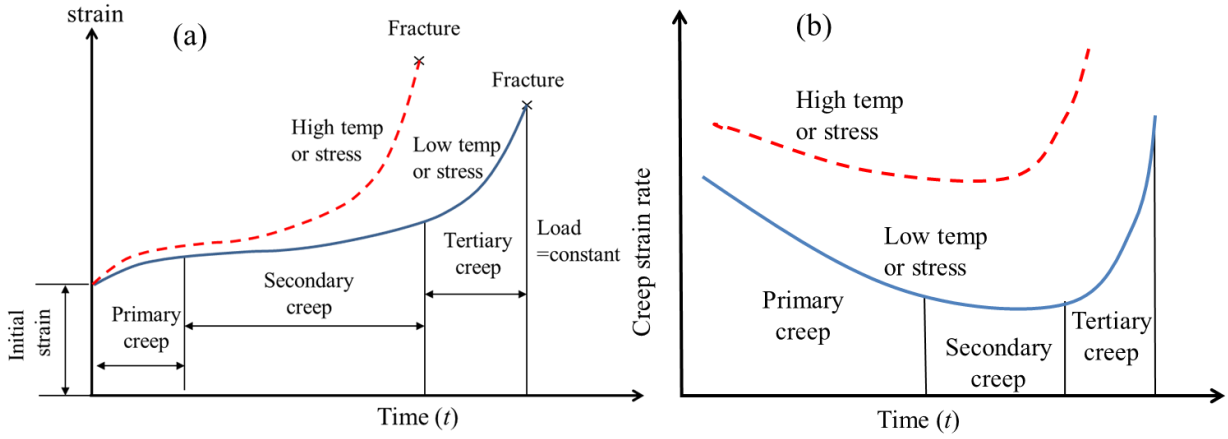

Fig. 2.1. Standard creep curves during constant loading and temperature conditions: (a) creep strain vs time; (b) creep strain rate vs time. The initial strain in (a) represents the pre-strain history. Red dashed lines refer to the curves at higher temperatures or stresses.

Figure 2.1 also illustrates that different temperatures or stresses may result in different creep strain rates in different stages thus different creep curves, where higher creep strain rates are always understood to be associated with higher temperatures or stresses.

2.1.1.2 State variable

Different mechanisms may operate during different creep stages. The effective way to identify and capture the dominant mechanism is to use state variables, which can be represented as a point in the state space, and the change in the system's state can be visualized as tracing a path over time in state space. This path is called the state trajectory [9]. The plastic deformation can be described using state variables that determine the mechanical state of the material, together with their rate equations as their evolution [10]. The inelastic response can be determined by integrating along the state trajectory of the material.

2.1.2. Mechanisms of creep deformation

There are three different basic mechanisms that may contribute to creep deformation at different stages, namely diffusional flow, dislocation glide/climb motion and grain boundary sliding [11]. The first two may dominate in the primary and stationary stage, while the last one may dominate in the tertiary stage.

2.1.2.1. Stationary stage creep

Investigation of stationary stage creep has drawn more attention than the other two stages due to its stable characteristics. The model is simple since the state variables in this stage are understood to be unchanged. In the steady state, the material state is a function of the applied

stress and temperature and thus the creep strain rate can be expressed as independent of the state variables. The general form of the rate equation is then:

$$\dot{\varepsilon}_{ij}^{\ ss} = f(\sigma_{ij}, T) \tag{2.4}$$

where $\dot{\varepsilon}_{ij}^{\ ss}$ is the multiaxial strain rate in the stationary stage and T is the absolute temperature. In practice, this stage can often dominate the creep behaviour, i.e. the period of which is usually much greater than those for primary or tertiary stage creep. Frost and Ashby [11] have drawn various deformation-mechanism maps for different materials in the stationary stage, where a typical map for 316 stainless steels is shown in Figure 2.2.

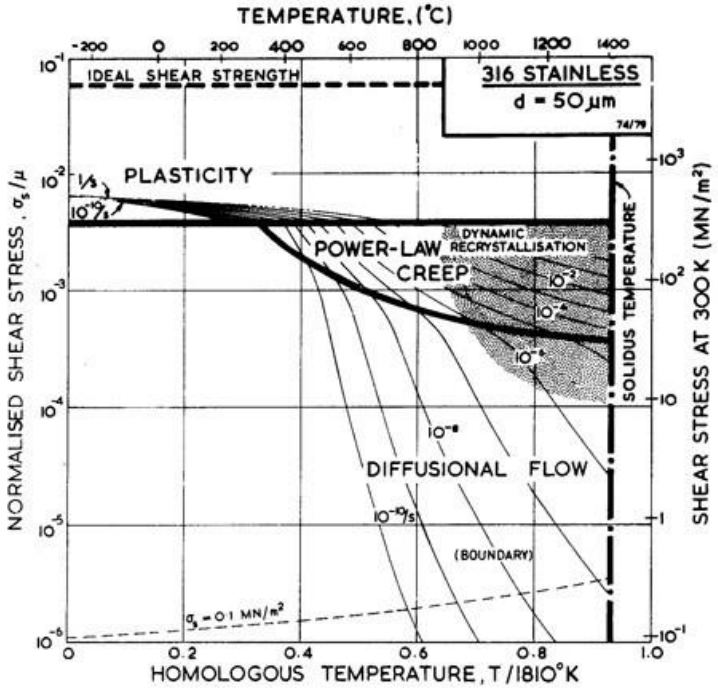

Fig. 2.2. Deformation-mechanism map for Type 316 stainless steels of grain size 50μm in the stationary stage [11]

All the data below the time-independent plasticity line in Figure 2.2 are derived from short-term creep tests at constant uniaxial loads. In general, two mechanisms can be observed clearly in the map, respectively diffusional flow (associated with low stresses) and power-law creep (associated with higher stresses than diffusional flow). The map distinguishes the

dominant region of each mechanism, but the boundary of each mechanism can be different with different grain sizes.

a) Diffusion-controlled creep

At low stresses (<$10^{-4}G$, G: shear modulus), diffusion-controlled creep dominates, which occurs by transport of material via diffusion of atoms within a grain or along grain boundaries. The plastic strain rate is linearly proportional to the stress and demonstrates an Arrhenius relationship [11]

$$\dot{\varepsilon}^{ss} = A\sigma \exp\left(-\frac{Q}{RT}\right) \quad \text{(uniaxial)} \tag{2.5a}$$

$$\dot{\varepsilon}_{ij}^{\ ss} = A\sigma_{ef} \exp\left(-\frac{Q}{RT}\right)\frac{3s_{ij}}{2\sigma_{ef}} \quad \text{(multiaxial)} \tag{2.5b}$$

where A is a material constant, Q is the activation energy and R is the universal gas constant. There are generally two types of diffusion creep, depending on the activation energy, i.e. whether the diffusion paths are predominantly through the grain boundaries (grain boundary diffusion), termed Coble creep, or through the grains themselves (bulk diffusion or lattice diffusion), termed Nabarro-Herring creep [7]. Since Coble creep involves relatively low activation energy, it dominates at low stresses and temperatures (<$0.6T_m$, T_m is the melting point). Besides the activation energy, diffusion-controlled creep also depends on the grain size d, which is a characteristic length scale independent of stress in this process. Coble creep strain rate is inversely proportional to d^3, while Nabarro-Herring creep strain rate is inversely proportional to d^2, thus Coble creep dominates in fine grained materials [11]. When the grain size is very large (~500μm), another lattice diffusion mechanism may dominate, termed Harper-Dorn creep, whose strain rate is independent of d [11].

b) Dislocation-controlled creep

At high stresses (~$10^{-3}G$), the enhanced driving force enables frequent dislocation motion, and thus the creep is dominated by dislocation motion. One possible feature of dislocation-controlled creep is that dislocations can rearrange themselves into cell-like structures by climb, a time-dependent diffusion process requiring thermal activation. The average cell size is reported to be inversely proportional to the stress [11]. Deformation can occur as a result of diffusional flow across the cells, similar to Nabarro-Herring creep but with the characteristic length scale changed to the stress dependent cell size. Besides this self-diffusion, atoms can also diffuse down the cores of dislocations, termed dislocation core diffusion, which involves the volume fraction associated with dislocation density (defined as the total dislocation length in a crystal divided by the crystal volume, which is proportional to σ^2). The above mechanism leads to a power-law relationship (only the simplest empirical one is shown here):

$$\dot{\varepsilon}^{ss} = A\sigma^m \exp\left(-\frac{Q}{RT}\right) \quad \text{(uniaxial)} \tag{2.6a}$$

$$\dot{\varepsilon}_{ij}^{\ ss} = A\sigma_{ef}^{\ m} \exp\left(-\frac{Q}{RT}\right)\frac{3s_{ij}}{2\sigma_{ef}} \quad \text{(multiaxial)} \tag{2.6b}$$

where *m* is power-law parameter (3 for self-diffusion, 5 for dislocation core diffusion, but actually may possibly have a value up to 10). Dislocation core diffusion may dominate at relatively low temperatures and high stresses due to the larger exponent.

When the stress is very high (>10^{-3}G), some researchers have occasionally observed a power-law breakdown phenomenon, which may be due to the transition from dislocation climb-controlled to dislocation glide-controlled creep [11]. In order to consider both power-law and power-law breakdown, an exponential form with hyperbolic *sine* function has been used in some analytical models, which will be presented later in section 2.2.4.

As the diffusion-controlled creep tests with relatively low stresses are time-consuming, most of the current available data from EDF Energy for the Type 316H stainless steels are from the power-law regime. Therefore, only the dislocation-controlled creep mechanism will be considered in the following sections.

2.1.2.2. Primary stage creep

The kinetics of primary creep is governed by the same processes as that of stationary or steady state creep, and with the same temperature and stress dependence. However, during the primary stage the strain rate is often observed to gradually decrease towards the steady state value (Figure 2.1), indicating that the primary strain rate is not a unique function of stress and temperature but is also dependent on the state of the material, which can be described in terms of a set of state variables S_k. These variables characterize the current material state and require associated considerations for their evolution, as the solid strains or as the time passes. The constitutive response can be written in the following form:

$$\dot{\varepsilon}_{ij} = f(\sigma_{ij}, T, S_k) \tag{2.7}$$

$$\dot{S}_k = f_k(\sigma_{ij}, T, S_k) \tag{2.8}$$

The evolution of each state variable is given by the second equation as a function of stress, temperature and the state itself.

a) Time hardening and strain hardening

Most early studies of primary creep have taken the basic equation (Eq. (2.6)) for steady state creep and have associated it with a time-hardening function (time t as the state variable) or strain-hardening function (strain ε as the state variable). Alternatively, other similar laws are also available, such as Andrade and Garofalo [8]. For simplicity, only the time hardening

and strain hardening theories are described here. With the addition of two different state variables, the two theories can be respectively given by

$$\dot{\varepsilon} = f(\sigma, T, t) = A\sigma^{m} t^{m_1} \exp\left(-\frac{Q}{RT}\right) \qquad \text{(uniaxial)} \qquad (2.9a)$$

$$\dot{\varepsilon}_{ij} = f(\sigma_{ij}, T, t) = A\sigma_{ef}{}^{m} t^{m_1} \exp\left(-\frac{Q}{RT}\right)\frac{3s_{ij}}{2\sigma_{ef}} \qquad \text{(multiaxial)} \qquad (2.9b)$$

$$\dot{\varepsilon} = f(\sigma, T, \varepsilon) = A\sigma^{m} \varepsilon^{m_2} \exp\left(-\frac{Q}{RT}\right) \qquad \text{(uniaxial)} \qquad (2.10a)$$

$$\dot{\varepsilon}_{ij} = f(\sigma_{ij}, T, \varepsilon_{ef}) = A\sigma_{ef}{}^{m} \varepsilon_{ef}{}^{m_2} \exp\left(-\frac{Q}{RT}\right)\frac{3s_{ij}}{2\sigma_{ef}} \qquad \text{(multiaxial)} \qquad (2.10b)$$

where m_1, m_2 are constants. The strain rate depends only on the current state while the strain depends on its entire history. The deformation-mechanism map for primary stage creep is similar to that of the stationary stage but the boundaries separating different regimes may change as the creep strain accumulates with time [11].

b) Competition between hardening and recovery

In the dislocation-controlled creep regime, the creep strain rate is known to be determined by a competition between hardening and recovery of dislocation structures, with hardening associated with the storage or accumulation of dislocations generated during deformation, and with recovery, the opposite process, associated with the removal or rearrangement of dislocations by thermal-controlled climb and/or dynamic annihilation [12]. McLean and co-workers [13-16] proposed a widely accepted concept of creep with regard to the competition. The concept considered the dislocation density as the material state variable and assumed that dislocations formed during plastic deformation exist in a three-dimensional network, which was later confirmed by detailed microscopy studies [4]. During primary creep, initially the

rate of recovery cannot catch up with the rate of hardening, so the dislocation density gradually increases, which causes the creep rate to decrease. As the average dislocation network mesh size decreases with increasing dislocation density, the hardening gradually slows down while recovery due to thermally-controlled climb and annihilation of dislocations accelerates. Eventually a dynamic balance is achieved between the effect of hardening and recovery [17], which is then the stationary stage. As a result, the creep strain rate becomes constant and the state variable representing the dislocation density becomes unchanged.

2.1.2.3. Tertiary stage creep

The onset of the tertiary stage is a sign that dramatic microstructural change or localized damage has occurred in the material, which is the reason for the progressively increasing creep strain rate (Figure 2.1). Generally, many researchers [18-23] have identified two principle categories of damage leading to final failure:

(a) Intrinsic softening due to changes in the material microstructure, in particular the vast accumulation of dislocation density.

(b) Reduction of internal load-bearing section due to the initiation and development of cavities and cracks.

Rounded and wedge shaped voids are seen mainly at grain boundaries and can coalesce to form large cavities. The mechanism of void formation (or cavitation) involves grain boundary sliding which occurs under the action of shear stresses acting on the boundaries. The contribution increases with increasing temperature, stress and decreasing grain size. In order to fully understand the material behaviour in the tertiary stage, a comprehensive investigation of creep deformation of the first two stages are prerequisite. However, the present research will not consider damage and failure mechanisms in the tertiary stage.

2.1.3. Current model and critical problem in EDF Energy

The above theory is based on the condition of constant stress. However, the real AGR components are currently experiencing non-steady conditions and changes to the operating envelope may lead to long-term changes in stress and temperature. During some complex thermal/mechanical cyclic loading, the AGR components may even experience a combined plasticity and creep deformation.

From limited data collected from some simple tests (e.g. uniaxial with step changes in load [24]), it has been found that the strain hardening theory lies closer to the data than time hardening, thus EDF Energy has been using, developing and applying the strain hardening model for Type 316H stainless steel and other power plant materials. With the strain as the state variable, the model is simple to use in real engineering applications and is able to deal with stress change condition, with the rule of transitions between different creep curves at different stresses simply based on the state trajectory or strain history [8]. However, EDF Energy has found that the model is not universally applicable but sometimes underestimates or overestimates the creep strain rate after a change of stress. Further, it should be noted that materials do not always exhibit the standard creep curves as schematically shown in Figure 2.1. Depending on the thermal/mechanical loading history, phenomena that are more complicated may be observed, e.g. no secondary stage, inverse primary stage (creep rate increases with time), etc. Most importantly, in the creep curves shown in Figure 2.3 of solution-treated Type 316H stainless steels at the typical operation temperature (550^{o}C), phenomenon of multiple minima (red dashed arrows) or multiple stationary stages at some relatively low stresses has been observed. Such phenomenon cannot be reproduced by the simple model. Other issues that are not considered by the empirical strain hardening model include thermal aging, or the effect of pre-strain and cyclic straining [2]. Therefore, all these deficiencies and other problems may require a prerequisite and clear understanding of the

dominant plasticity/creep deformation mechanisms under various conditions and how the plasticity and creep influences each other. This necessitates the identification of different state variables as well as their evolution laws.

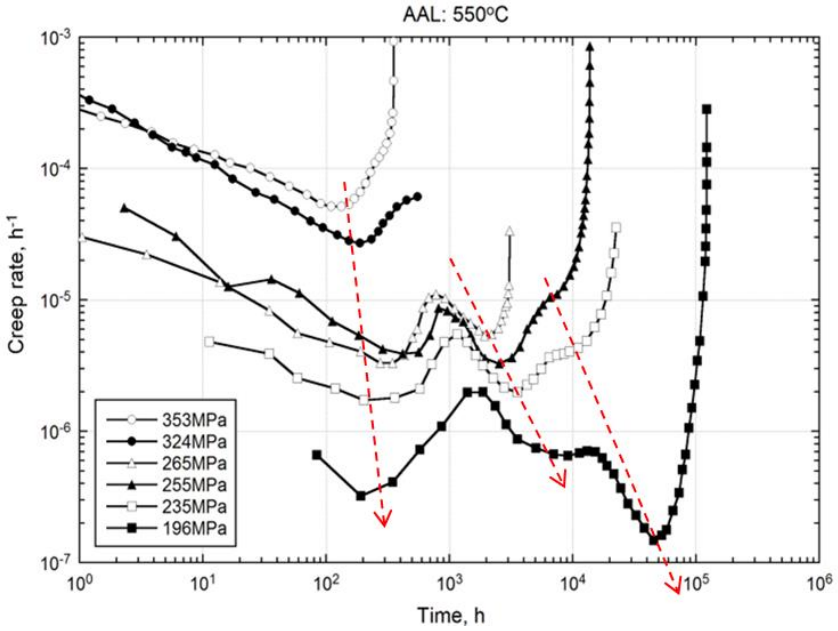

Fig. 2.3. Creep rate vs time curves of solution-treated Type 316H stainless steel at different stresses at 550°C. Red dashed arrows show some multiple minima at different stresses. AAL is a designation of the tested specimen. Figure comes from [25]

2.2. Literature review

Understanding dominant deformation mechanisms with different material states is crucial for the establishment of physical based constitutive models applicable to various conditions. In many cases, multiple mechanisms may simultaneously operate and contribute to the overall strength of the material. This section gives an overview of different strengthening and softening mechanisms of engineering alloys like 316 stainless steels, associated with the dislocation-controlled creep regime (Figure 2.2). Different dislocation motion modes at elevated temperatures are then introduced, followed by the concepts and distinguishing features of the internal stress and internal resistance to dislocation motion. Finally, emphasis is put on several previously used typical models related to plasticity/creep deformation, ranging from empirical to physical.

2.2.1. Strengthening and softening effect

2.2.1.1. Strengthening mechanisms

The strengthening effect refers to the resistance of materials to plastic deformation. There are various mechanisms of enhancing the strength of materials, from single crystals to polycrystals, from pure metals to engineering alloys. Incorporation of second constituents into a pure metal offers a very flexible means of strengthening. Impurity atoms can aggregate in a variety of forms and sizes, from randomly dispersed individual solute atoms to large second-phase precipitate particles. These different forms of dispersion, as different strengtheners, result in different interactions with dislocations. The consequent strength is a combination of these mechanisms.

a) Lattice resistance

The most fundamental resistance to dislocation motion through a crystal lattice is from the lattice itself, often called the Peierls-Nabarro strength [26]. Its magnitude varies on the basis of crystal structure and can be different for different slip systems, with a potentially large contribution for B.C.C. materials and a small contribution for F.C.C. materials ($\sim 10^{-6}G$) [27]. Although addition of alloying elements will increase the Peierls-Nabarro strength [28], it is beyond the concern of this thesis, since other contributions are more significant in F.C.C. 316 stainless steels.

a) Forest dislocation strengthening

Dislocations can be generated before or during deformation at all temperatures [28]. All the dislocations form a three-dimensional network or forest. Usually the dislocations can be divided into mobile and immobile dislocations, depending on the likelihood of glide on any

slip plane. The most frequently encountered obstacles for a moving dislocation on its slip plane are forest dislocation junctions which are intersections with dislocations on other slip planes (Figure 2.4). The stress needed to move a mobile dislocation may depend on both short-range interactions, such as dislocation intersections, and long-range interactions with both near and distant dislocations [29, 30]. As the dislocation density increases with multiplication, the mobility of mobile dislocations decreases, i.e. further dislocation movement is retarded, which is the most commonly seen hardening effect. To characterise the hardening process, the principal problem is the need for a mechanistic understanding of the evolution of the dislocation microstructures.

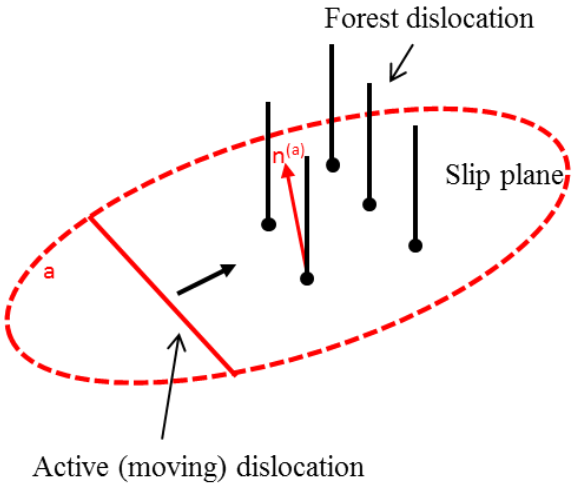

Fig. 2.4. A schematic illustration of an active dislocation moving on its slip plane; The junctions of other forest dislocations intersecting this slip plane serve as the obstacles to the moving dislocation.

Thermal exposure facilitates the diffusion of atoms and vibration of dislocations, which enhances the climb and thermally activated glide motion of dislocations thus obstacles can be bypassed more easily than that at ambient temperature. At very high temperatures, this can even lead to frequent multiplication and thus fast formation of cell-like substructures, consisting of dislocation walls and channels between walls [11]. The trapped dislocations in the walls become immobile that result in a reduction of mobile dislocation density and thus

the creep rate. Moreover, some internal stress may also arise and retard further movement of mobile dislocations since the immobile dislocations in the walls are impenetrable obstacles.

c) Solid solution strengthening

For engineering alloys, another strengthening is achieved by the process of solution heat treatment and quenching. Solution heat treatment involves heating the material to a suitable temperature, holding for sufficient time to induce all constituents to enter into solution. The quenching is to preserve the constituents in solution by rapidly cooling to usually near room temperature. As a consequence, solute atoms are trapped in the lattice, either substitutional or interstitial depending on their size [31]. Substitutional is when large atoms replace solvent atoms in their lattice positions (like *Cr* and *Ni*), while interstitial is when small atoms occupy interstitial sites between solvent atoms (like *C* and *N*) (Figure 2.5).

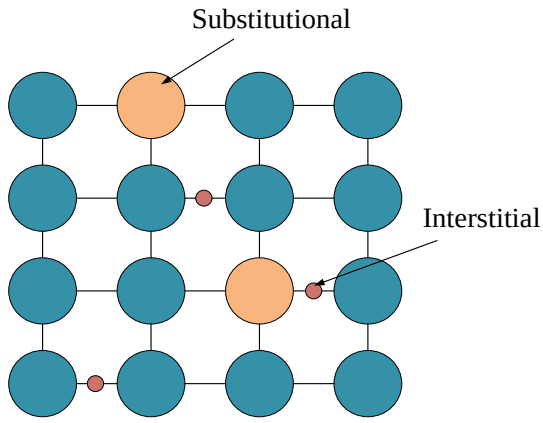

Fig. 2.5. A schematic diagram of the substitutional and interstitial solute atoms trapped in the solute lattice in an engineering solid solution

When solute and solvent atoms differ in size, local stress fields are created (compressive when the solute atom is larger than the solvent atom and tensile when the solute atom is smaller). Depending on their relative locations, solute atoms will either attract or repel dislocations in their vicinity. This allows the solute atoms to relieve either tensile or compressive strain in the lattice, which in turn puts the dislocations in a lower energy state.

Such attraction or repulsion of dislocations by solute atoms contributes to the strength of the material [27, 32, 33].

At elevated temperatures, although such a strengthening effect may be reduced due to increased diffusion mobility of solutes or precipitation process (to be introduced below), it may also facilitate the formation of solute clusters or clouds at energetically favourable sites, in particular, defects like dislocations, and can be dragged along with gliding dislocations, resulting in an additional strengthening in a form of a drag force on gliding dislocations [33].

d) Precipitation strengthening

Precipitation processes are significantly influenced by temperature, chemical composition and thermo-mechanical treatment history. The initially solution-treated state of austenitic stainless steels is thermodynamically unstable and changes in their microstructure can be made to occur by thermo-mechanical treatment [34]. Discrete particles of different phases in solid state can form in the supersaturated matrix. For Type 316 stainless steel, thermal ageing promotes precipitation of carbides (mainly $M_{23}C_6$, *M* refers to metallic elements) and other more stable intermetallic phases like Laves (Fe_2Mo), sigma ($FeCr$) and Chi ($Fe_{36}Cr_{12}Mo_{10}$) phases [34, 35]. These precipitates grow heterogeneously in defect-rich regions where the preferable nucleation sites are grain boundaries and matrix on intragranular dislocations [34-37], but unlike solute atoms, are relatively immobile [38].

Intragranular precipitates have been observed to retard dislocation glide and climb motion and also cell formation [39, 40]. Dislocations moving through the matrix can either cut through the intragranular particles (small or coherent particles) or bypass them (large or incoherent particles). The latter process is more commonly observed by transmission electron microscopy [41, 42] and is generally called Orowan bowing [43]. The degree of strengthening of Orowan bowing depends on the particle distribution or dispersion in the

matrix, which is inversely proportional to the mean inter-particle spacing [44, 45]. Thus a closely-spaced dispersion of precipitates has a larger strengthening effect than a widely spaced dispersion, which is similar to the operation of a Frank-Reed source [46]. The role of intergranular precipitates regarding the interaction with dislocations is less significant within the dislocation creep regime. However, depletion of solute elements in the matrix by the precipitation process, both intragranular and intergranular, may reduce the solute strengthening effect.

At elevated temperatures, besides the continuous nucleation and growth of different phases described above, particles may even coarsen (to be introduced later in the softening mechanism, section 2.2.1.2) so that large particles absorb small ones and grow. All these may change the particle distribution and the degree of Orowan bowing. In addition, the bypassing mechanism for intragranular precipitates may change due to the increased climb mobility of dislocations [47]. This is described in detail in section 2.2.2.

e) Strengthening-mechanism map

A strengthening-mechanism map for 316 stainless steel has been proposed by Aplin and D'Angelo [48], shown in Figure 2.6. This map is a more detailed form of the Frost and Ashby deformation-mechanism map (Figure 2.2) in the dislocation-controlled creep (power-law) regime. This map focuses on the variation of the dominant strengthening mechanisms within different temperature and stress ranges. Although the data used in the construction of Figure 2.6 are limited to short-term data, this map provides an insight into the selection of appropriate material state variables, which are associated with different microstructural elements and deformation mechanisms.

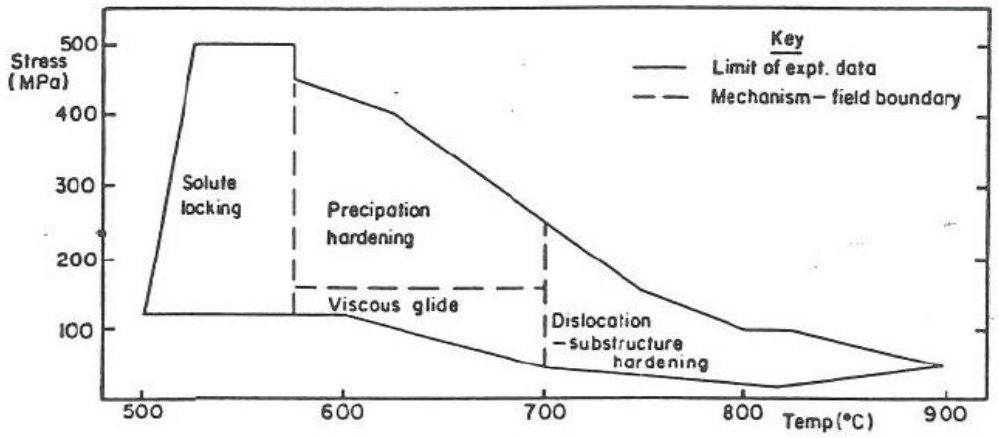

Fig. 2.6. Strengthening-mechanism map proposed by Aplin and D'Angelo [48]. The solid line is the limit of the considered experimental data and the dashed line represents the rough boundary of different mechanisms

The map covers the temperature range (470-650^{o}C) and most of the stress range (100-300MPa), where it is observed that solid solution and precipitation may dominate the creep response depending on the microstructural state. A different terminology, solute locking, is used in the map to describe the solute strengthening by thermal solute drag. Note that some forms of the solute hardening (or effect of thermal solute drag) may dominate the creep response at higher temperatures (580-700^{o}C) and low stresses, which is termed viscous glide. This is presumably because the majority of solute atoms still remain in solution at this stage, but at higher stresses, the precipitation process will accelerate at the expense of solute atoms in the matrix or more precipitates nucleate at the early stages of a test [48].

At very high temperatures (>700^{o}C), the most important structural changes that take place during creep deformation are likely to be the dislocation substructure formation (cell-like structures or subgrain formation), partly due to the enhanced dislocation climb motion or mobility of the dislocations. Precipitates can coarsen rapidly at these temperatures and solute atoms that remain in the matrix are very mobile. As a result, solute atoms and precipitates may not contribute significantly to the strengthening [48]. For the temperature range of interest in this thesis, dislocation substructure formation is not considered to be an important

mechanism. However, it is worthwhile investigating its strengthening effect in the future since the boundaries separating different mechanisms in Figure 2.6 may vary with different material states.

2.2.1.2. Softening mechanisms

Softening mechanisms, or the attenuation of the strengthening effect, is most commonly observed as a reduction of the strength during inelastic deformation. The softening mechanisms can be generally divided into two categories: dislocation-based softening (recovery) and precipitate-based softening (particle coarsening).

a) Dynamic and static recovery of dislocation structure

Recovery is a process by which deformed grains can reduce their stored energy by the removal or rearrangement of defects (primarily dislocations) in their crystal structure to a lower energy configuration [49]. The rearrangement refers to the alignment of dislocations into ordered arrays where their individual contribution to the stored energy is reduced by the overlapping of their strain fields, like dipoles and low angle tilt boundaries [12]. Recovery processes can be divided into dynamic recovery and static recovery. Both types will result in the reduction of dislocation density in the network.

Dynamic recovery is generally the annihilation of dislocations, i.e. dislocations with opposite signs can cancel out each other by slip or cross-slip motion on the same slip plane. According to this feature, dynamic recovery is understood to be mostly influential during frequent cyclic loading, where the possibility for the annihilation increases due to the generation of many dislocations with opposite signs [10]. The model of dynamic recovery introduced by Kocks, Mecking and Estrin (KME-model) [10, 50, 51] has been extensively applied, which gives the evolution of dislocation density (ρ) with plastic shear strain (γ^p) as:

$$\frac{d\rho}{d\gamma^p} = k_1\rho^{1/2} - k_2\rho \tag{2.11}$$

where k_1, k_2 are parameters defined as length-ratio [50]. The production term $k_1\rho^{1/2}$ is associated with storage of moving dislocations which become immobilized after having travelled a distance proportional to the average spacing between dislocations. The dynamic recovery term, $-k_2\rho$ is based on an assumption that the stored dislocations can break past their pinning points and be recovered everywhere in the structure [51].

Static recovery, also known as a time-dependent network coarsening process [4], is a relatively slow rearrangement process of dislocation structure associated with thermally-controlled climb. Dislocation climb occurs by the diffusion of atoms and vacancies to or away from the site of the dislocation line thus provides the dislocation additional mobility to move out of its slip plane. Therefore, climb motion largely facilitates the dislocations to bypass obstacles, like forest dislocation junctions. As a consequence, the mesh grows in the dislocation network, where long dislocation segments grow while small ones shrink and the line tension of the dislocations provides the driving force for climb [52]. At the current stage, models of network coarsening process driven by this dislocation-core-diffusion-controlled climb are not available in the literature. However, Lagneborg has proposed an approximate expression of the growth rate of the average mesh size ($\bar{\lambda}$) in the dislocation network driven by lattice diffusion [4, 16, 52, 53], analogous to grain growth theory [54]

$$\frac{d\bar{\lambda}}{dt} = \frac{M\Gamma}{\bar{\lambda}} \tag{2.12}$$

where M is the climb mobility and Γ is the dislocation line tension, or the line energy of the dislocation. Since it is understood that $\bar{\lambda}$ is inversely proportional to $\rho^{1/2}$ [4, 52, 55-57], as the mesh size increases by static recovery, the dislocation density decreases, leading to softening of the material. Although this theory captures the basic physics of network coarsening, it does

not capture the rate-controlling process, which is diffusional transport from a site to another, rather than the vacancy emission and absorption considered in grain growth theory. The deficiencies of the theory are to be discussed in detail in Chapter 6.

b) Particle coarsening

When equilibrium is approached for the precipitation of a certain phase, it is commonly found that the precipitate microstructure continues to change with the passage of time, where the precipitates coarsen by the larger particles growing at the expense of the smaller particles, thus increasing the number of larger-sized particles. This observed phenomenon, similar to the dislocation network coarsening, is called particle coarsening or Ostwald Ripening [58, 59], which is shown in Figure 2.7. The kinetics of particle coarsening is temperature and time dependent.

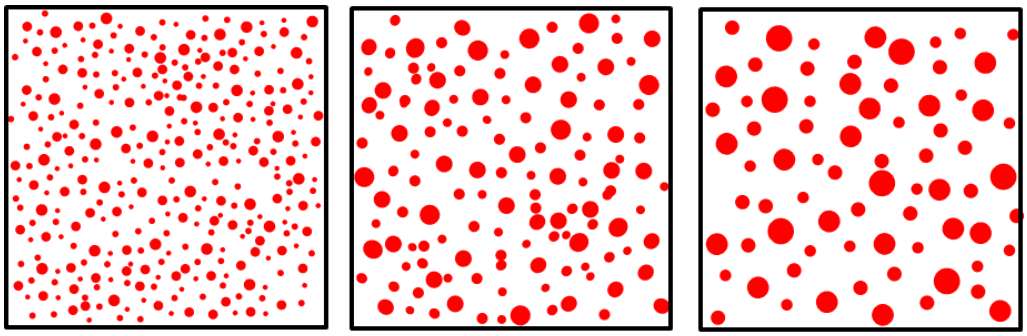

Fig. 2.7. A schematic diagram of particle coarsening, or Ostwald-Ripening process with the passage of time. (a) Precipitation in the supersaturated solid solution. (b) and (c) The large particles grow while the small ones shrink

This thermodynamically-driven spontaneous process occurs because of the interfacial free energy and the strain energy contained in the structure [60]. Large particles are more energetically favoured than small ones due to the greater volume to surface area ratio [61]. Thus large particles represent a lower energy state with lower interfacial energy. Atoms on the surface of small particles will tend to detach and diffuse through solution and then attach to the surface of larger particles. As a result, the number of smaller particles continues to

shrink, while that of larger particles continues to grow. During the coarsening process, the volume fraction of the particles is always assumed to be constant [58], thus as the small particles vanish with time, the mean inter-particle spacing will gradually increase, which thus attenuates the precipitation strengthening, or softens the material.

It should be noted that the precipitation of new stable phases may combine with gradual dissolution of old metastable phases due to the competition for solute atoms [62]. It has been found that the average sizes of the stable phases are much larger than the metastable phases, thus such phase transformations may have a similar softening effect to particle coarsening, with respect to the gradual increase of the mean inter-particle spacing [36]. However, coarsening can occur even when a single precipitate phase is present in the material [63]. Both phenomena may overlap and occur simultaneously [64].

2.2.2. Dislocation motion at elevated temperatures

Dislocations can either glide or climb at elevated temperatures. Thermally activated glide and climb facilitates the obstacle bypassing and further glide motion of dislocations, which then generates plastic strain. A gliding dislocation on its slip plane can meet multiple types of obstacles as described above, i.e. forest dislocation junctions, solute atoms and precipitates. Understanding the detailed mechanism of how dislocations interact with different microstructural elements is essential to the investigation of material creep behaviour. Three interaction modes are described in this section, respectively unzipping movement, particle bypassing and solute drag.

2.2.2.1. Obstacle strength and critical shear stress

Before we introduce different interaction modes between dislocations and obstacles on its slip plane, a prerequisite is to mechanistically quantify the resistance to dislocation motion of

each type of obstacles, which often refers to its strength. Friedel [53] gives an illustration of the obstacle strength associated with the shear stress required for a dislocation segment to bow and break away from one pair of obstacles, which is written as inversely proportional to the spacing between obstacles:

$$\tau = \frac{Gb}{\lambda}\cos\left(\frac{1}{2}\phi_c\right) \tag{2.13}$$

where G is the shear modulus, b is the length of the Burgers vector, λ is the spacing or length of the dislocation segment separated by two obstacles and ϕ_c is a critical angle for breakaway between the arms of the dislocation segments at an obstacle. The breakaway criterion requires that the angle between the arms of dislocation segments is equal to ϕ_c. In terms of Eq. (2.13), the obstacle strength lies in the range from 0 to 1 and $\phi_c \sim 0$ is for strong obstacles, such as precipitates, while $\phi_c \sim \pi$ is for very weak obstacles, such as solute atoms. Dislocation junctions are also weak obstacles but have a medium strength [32].

Further, as mentioned in section 2.2.1, thermal exposure may reduce the energy barrier of obstacles to dislocation glide motion and enhance vibration and diffusion mobility of dislocations, leading to the thermally activated glide and climb motion of dislocations [11]. Both processes indicate that, at elevated temperatures, even when the applied stress is lower than the critical shear stress, it is still possible for dislocations to bypass obstacles, glide and penetrate the whole slip plane. The effect of these will be modelled in detail in Chapter 6.

2.2.2.2. Unzipping movement

Eq. (2.13) is only an idealized expression of strength or critical shear stress for one pair of obstacles, or for regular array of obstacles along the dislocation line, in which case, the critical shear stress can be defined as the shear stress required for a dislocation to penetrate

the whole slip plane. In reality, given a single slip plane with a random distribution of obstacles with uniform strength, the influence from neighbouring segment bowing between the next pair of obstacles along the line cannot be ignored. As a result, the critical shear stress in Eq. (2.13) should be related to the mean spacing of all obstacles on the slip plane and the breakaway criterion for individual pairs of obstacles reduces to only the magnitude of the angle between the arms of dislocation segments $\phi = \phi_c$.

For weak and intermediate obstacles like solid solution and dislocation junctions, Foreman and Makin [44] have found that as the gliding dislocation propagates through a random array of these obstacles, a series of adjacent obstacles along the line satisfying the breakaway criterion are able to be bypassed in turn or simultaneously, which is regarded as consecutive breakaway or unzipping movement (Figure 2.8) [44]. Their obtained expression of critical shear stress is consistent with the modification of Eq. (2.13) by Friedel for weak and intermediate obstacles, who considers that as the dislocation segment breaks away from a weak or intermediate obstacle it does not bow out appreciably and consequently does not make contact with any new obstacles.

$$\tau = \frac{Gb}{\lambda}\left\{\cos\left(\frac{1}{2}\phi_c\right)\right\}^{3/2} \tag{2.14}$$

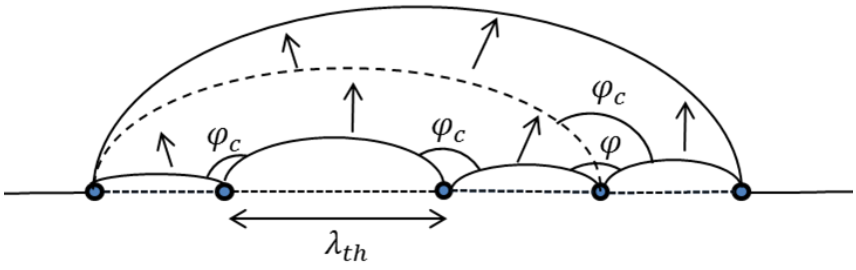

Fig. 2.8. A mobile dislocation and its breakaway from weak or intermediate obstacles on its slip plane; the blocked dislocations can break away from the obstacles once the included angles between the arms are equal to the critical angle ϕ_c.

This unzipping movement continues until the gliding dislocation finds a configuration where it is unable to move. Once the stress increases further, the dislocation can bow out and break away from the obstacles and propagate again. The effect of unzipping is to reduce the critical shear stress required for an obstacle to be bypassed, or to increase the area swept out by each released dislocation (Figure 2.9) and thus increase the strain increment that is obtained by a certain stress increment [44]. Note that although the unzipping movement is intrinsically an athermal process, it can be enhanced at elevated temperatures due to thermally activated glide and climb as mentioned above. For obstacles like forest dislocation junctions, the climb-controlled recovery leads to the coarsening of dislocation network, as described in section 2.2.1, which may reduce the number of obstacles and thus increase the mean spacing between all the obstacles.

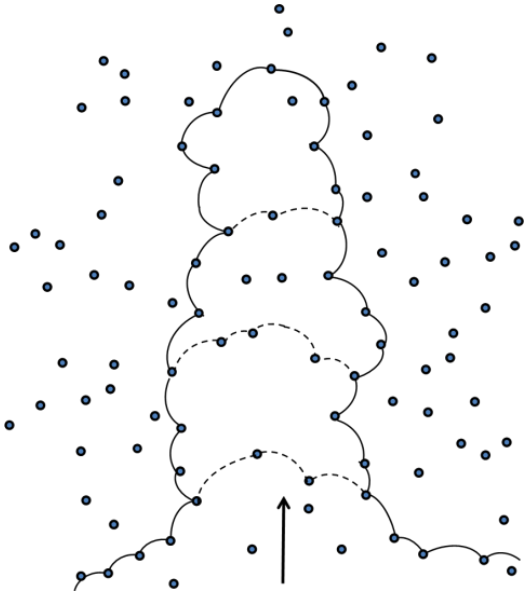

Fig. 2.9. Unzipping movement of dislocations in a random array gliding in the direction indicated by the black arrow, which is modified from [44]; the dashed curves are some intermediate positions of dislocation segments

2.2.2.3. Particle bypassing

a) Orowan bowing

Of all types of obstacles, precipitate particles sampled by the dislocation lines in the slip planes often can be divided into two groups. The first group consists of small and/or coherent precipitates that can be easily cut by the dislocations thus the breakaway angle ϕ_c is large and the strength or resistance is small. The second group consists of large and/or incoherent precipitates that are oftern regarded as strong non-deformable obstacles which can be overcome only when $\phi_c \sim 0$ in Eq. (2.13), of which the process is often called Orowan bowing [53]. Here we focus on the latter case associated with Orowan bowing. As a consequence, the dislocation bypassing process is characterized by encircling movements (with the dislocation bent into a semi-circular arc between precipitates) and closed dislocation loop formation before breakaway (Figure 2.10) [65]. In the 316 stainless steels considered in this thesis, the particles are simply idealized as with spherical shape. It should be noted that the effect of the precipitate morphology on dislocation motion is significant only for materials with a very high volume fraction of precipitates, such as nickel based superalloys [66].

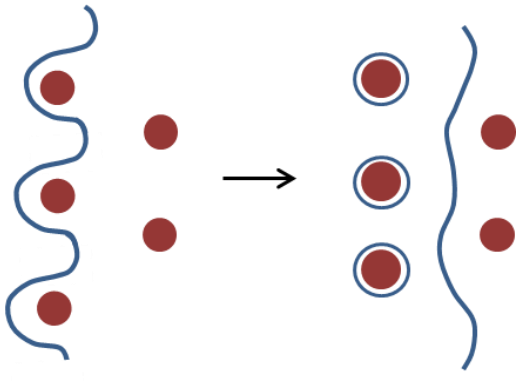

Fig. 2.10. The Orowan bowing bypassing mechanism, leaving loops encircling each particle [65]

Following Orowan [43] and also Forman and Makin [44], the critical shear stress or Orowan stress τ_p required for a dislocation to bow out and bypass strong obstacles, such as precipitates, can be expressed simply by setting $\phi_c = 0$ in Eq. (2.13). Then

$$\tau_p = \frac{Gb}{L_p} \tag{2.15}$$

where L_p is the inter-particle spacing, identical to the length of the dislocation segment blocked between two particles (Eq. (2.13)). The Orowan stress is roughly equal to the stress required to bend a dislocation segment to a semicircle with the diameter L_p. For a random distribution of precipitates, the simulations of Foreman and Makin [44] have shown that the corresponding Orowan stress is associated with the average inter-particle spacing (still use L_p here) multiplied by a statistical randomness factor 0.84, which is consistent with the expressions derived by other researchers, such as Kocks [67] and Ashby [68], using a variety of analytical approximations.

$$\tau_p = 0.84\frac{Gb}{L_p} \tag{2.16}$$

b) Secondary slip

The dislocation loops on a slip plane around the precipitates after a dislocation line has bypassed them (shown in Figure 2.10) are often called Orowan or primary loops, and the corresponding plane is called the primary plane. These loops together produce large stresses in the neighbourhood of the particles. Ashby [46] demonstrated that this Orowan mechanism of accommodation only occurs for the first 2 or 3 dislocations that bypass a precipitate. It then becomes more energetically favourable for plastic flow to be accommodated by prismatic loops punched out from the particles on secondary slip planes [46, 69]. Some experimental evidence can be found in support of this mechanism [70]. A discussion of different types of prismatic loop formation is given by Brown and Stobbs [71], who support

Ashby's proposal [46] that the secondary slip process is more energetically favourable [46]. A schematic of the origin of Ashby-type secondary slip around a single spherical particle in a plastically deformed matrix is shown in Figure 2.11 and is described below.

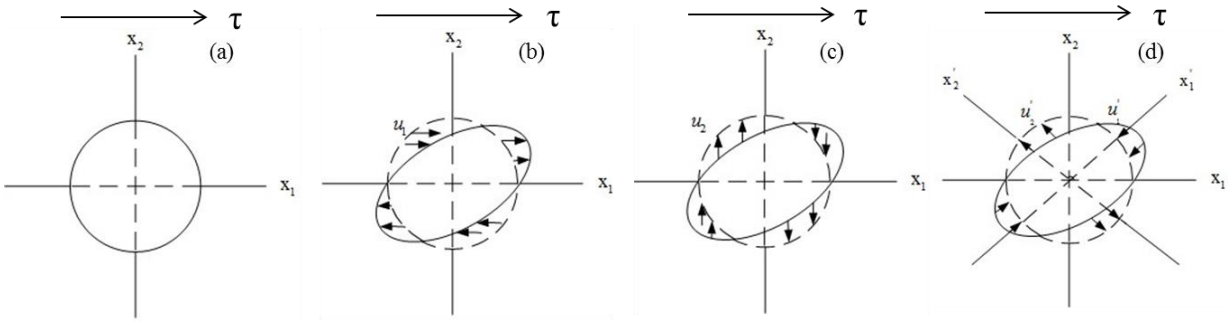

Fig. 2.11. Origin of Ashby-type secondary slip around a single spherical precipitate [62]; (a) A precipitate in a matrix with the shear stress τ ; (b) The matrix undergoes a uniform shear displacement u_1 when the precipitate is removed from its hole, leading to the distorted hole; (c) To replace the particle in the hole, a secondary shear displacement u_2 at the particle-matrix interface is needed if the precipitate is to be elastically distorted only; (d) Alternatively, the matrix can be displaced by prismatic punching to give displacements u_1' and u_2' parallel to new axes x_1' and x_2'

When a rigid spherical particle (Figure 2.11a) is removed from its original hole, the hole is free to deform and distorts into an ellipsoidal shape shown in Figure 2.11(b) due to the uniform primary plastic shear displacement u_1 caused by the shear stress along the x_1–axis in the matrix. If the initially separated rigid sphere is to be reinserted in the hole, this requires the elimination of the displacement incompatibilities, which can be achieved in two distinct ways. A secondary shear displacement u_2 at the particle-matrix interface along the x_2–axis normal to x_1–axis is needed if the particle is to be maintained only elastically distorted (Figure 2.11c), i.e. to restore the ellipsoid to the original shape of a sphere. As an alternative, a different slip pattern along two new directions x_1' and x_2' (may simply make angles of 45^o with the old axes in Figure 2.11d) can occur to restore the spherical shape. The latter slip pattern seems to be favoured by the experimental results [46]. As a result, geometrically necessary dislocations, i.e. prismatic loops, which also represent the amount of secondary slip,

are punched out around the particles on the secondary slip systems, consisting of two types, respectively “interstitial” loops (like those produced by condensation of interstitial atoms) and “vacancy” loops (like those produced by condensation of vacancies, Figure 2.12). These loops serve as additional obstacles retarding further dislocation motion on all slip planes.

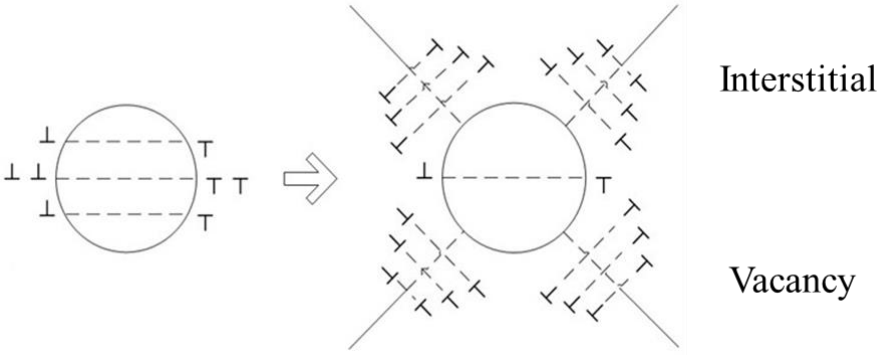

(a) (b)

Fig. 2.12. A schematic illustration of the generation of secondary loops (interstitial and vacancy loops). At (a) shear in the primary slip system has left primary Orowan loops round the particle. At (b) secondary slip has occurred by the nucleation and glide of secondary prismatic loops which will contribute to the hardening. The primary slip plane is horizontal and perpendicular to the page

c) Climb-controlled bypassing

Orowan bowing is a fast and time-independent process and can occur at any temperature provided the breakaway criterion is satisfied. At elevated temperature, when the Orowan process is inhibited (e.g. the applied shear stress is much lower than the Orowan stress in Eq. (2.16)), while particle bypassing can also occur with the aid of thermally activated glide motion of dislocations, as mentioned before, it can also be achieved gradually through dislocation diffusion-controlled climb [47]. McLean [47] has discussed three modes of dislocation climb around particles, respectively local climb, general climb and cooperative climb, each of which gives rise to a threshold stress [47, 72], a stress below which the particular climb mechanism cannot operate. Above the threshold stress, the work done by the dislocation as it glides and bypasses the particle is greater than the increase in line energy of

the dislocation as it climbs around the particle [73]. Unlike the Orowan bowing process, all these climb-controlled bypassing processes do not involve dislocation loop formation.

Figure 2.13(a) shows the mode of local climb, which assumes that climb only occurs local to the particle-matrix interface, i.e. the dislocation segment between particles remains in the slip plane [47]. This mode may operate when the volume fraction of particles is low so that the climb force on the dislocation segment at the particle due to the shear stress is amplified [47]. The threshold stress τ_{LC} has been reported by McLean,

$$\tau_{LC} \approx 0.7\tau_{OB} \tag{2.17}$$

where τ_{OB} is the Orowan stress associated with Orowan bowing, given by Eq. (2.16). Another expression, which has been reported by Shewfelt and Brown [74] using a computer simulation for dislocations bypassing a random distribution of particles, similar to that described by Foreman and Makin [44], shows that

$$\tau_{LC} = 0.32\frac{Gb}{L_p} \approx 0.4\tau_{OB} \tag{2.18}$$

Eq. (2.18) has been verified by Arzt [73, 75], who used a simple analytical model taking into account a random intersection height of dislocations on the particles.

Lagneborg [76] has opposed the local climb theory. He argued that the sharp dislocation bends at the point of particle contact implied by local climb are unstable high-energy configurations, which are therefore unlikely to occur. Based on this, he proposed a different climb mode, general climb (Figure 2.13b), which involves only a small increase in dislocation line length when portions of the dislocation away from the particle are allowed to relax or unravel by diffusion and leave the slip plane, smoothly connecting the portion which is forced to climb over the particle for geometrical reasons [47, 72, 75, 76]. As a consequence, the threshold stress for general climb would be smaller than that for local climb, but the rate

is much slower since it requires a longer length of dislocation to climb. McLean [47] has reported the threshold stress of general climb τ_{GC} as follows

$$\tau_{GC} = \tau_{OB} f^{1/2} / 2^{1/4} \qquad \text{for high stresses} \qquad (2.19a)$$

$$\tau_{GC} = \tau_{OB} f^{3/2} / 2^{5/4} \qquad \text{for low stresses} \qquad (2.19b)$$

where f is the volume fraction of particles. Arzt and Ashby [75] have reported a different expression for general climb

$$\tau_{GC} \approx 0.04 \frac{Gb}{L_p} \approx 0.05 \tau_{OB} \qquad (2.20)$$

Both Eq. (2.19) and Eq. (2.20) show a lower threshold stress than that for local climb (Eq. (2.18)), provided that, for the case of Eq. (2.19), the particle volume fraction is small (<20%). Note that at this volume fraction, 20%, Eq. (2.20) is close to Eq. (2.19b) and Eq. (2.19a) is close to Eq. (2.18). This may indicate that, at a given applied stress, which climb mode dominates largely depends on the volume fraction of particles. At some transition volume fractions, the climb velocities of dislocations for these modes will be generally equal [47, 73].

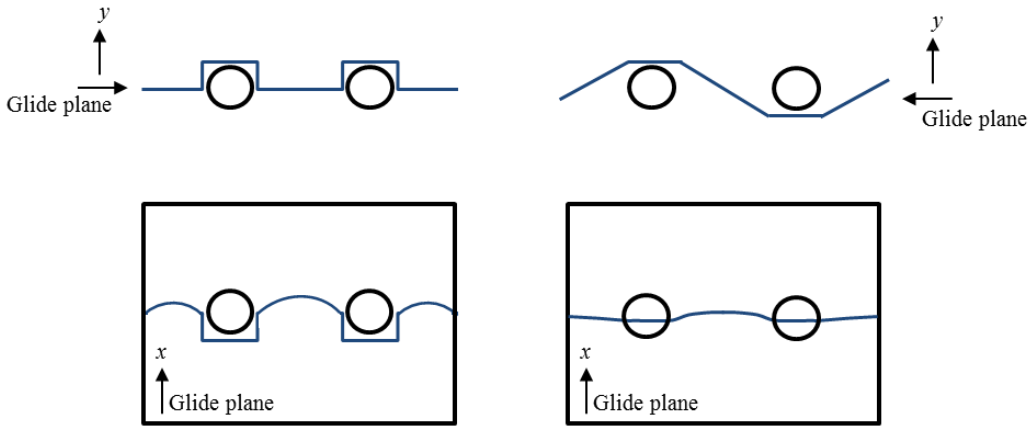

Fig. 2.13. Schematic illustrations of dislocation configurations for (a) local climb and (b) general climb around spherical particles in a single slip plane

Local climb and general climb are just two extreme cases. Evans and Knowles [72] have considered an intermediate geometry, i.e. cooperative climb, where the ends of the

dislocation segment are attached to network nodal points or fixed in space while the other segments between particles are allowed to climb (Figure 2.14). Such a configuration involves the minimum increase of dislocation line length but involves the maximum climb distance compared with the other two modes. No simple expressions of the threshold stress associated with cooperative climb have ever been reported.

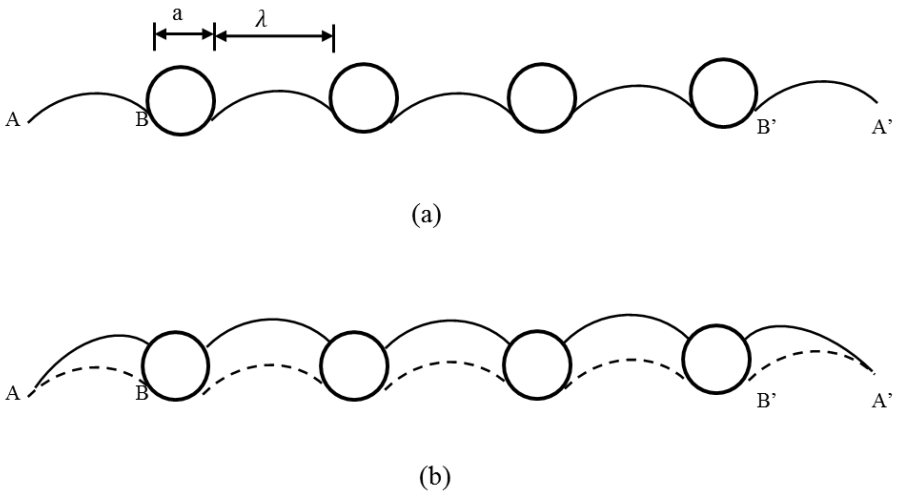

Fig. 2.14. Schematic illustration of the cooperative climb of dislocation segment AA' over a group of particles. (a) before climb, dislocation entirely stays in its slip plane. (b) after climb to top of particles only segments AC and C'A' have changed in length.

2.2.2.4. Solute drag

At ambient temperatures, dislocation motion around a random distribution of solute atoms in the matrix can be described by the unzipping process described earlier. Since solute atoms are weak obstacles, dislocation lines remain relatively straight as they propagate through the random array. At elevated temperatures, the solute atoms are partially mobile and can easily diffuse to the dislocation cores and form a solute cloud or atmosphere which pins the dislocations, which can then be dragged along with the gliding dislocations (Figure 2.15) [33]. As a consequence, the dislocation velocity or mobility is reduced since the rate-controlling factor is the average or effective diffusion rate of the solute atoms in the cloud [33]. This may enhance the rate of multiplication or reduce the rate of recovery of the dislocation structure

[77]. In fact, the effect of solute drag is more pronounced when the temperature is intermediately high (around 500^{o}C for 316 stainless steels shown in Figure 2.6) [48, 78, 79]. This is because at much lower temperatures, the solute atoms remain fixed in the lattice, while at much higher temperatures, the solute atoms can either be depleted by precipitation, or become extremely mobile and can readily keep up with the mobile dislocations with minimal driving force.

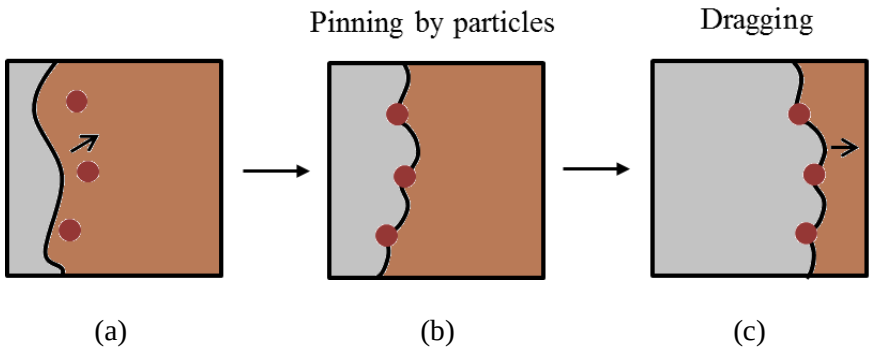

Fig. 2.15. Solute drag movement: (a) a gliding dislocation meets some mobile solute atoms; (b) mobile atoms diffuse to the dislocation core and pin the dislocation; (c) mobile solute atoms are dragged along with the gliding dislocation

2.2.3. Internal resistance and internal stress

According to sections 2.2.1 and 2.2.2, the material internal state can be described by the microstructural state, the change of which can be characterized by the evolution of microstructure during deformation, especially at elevated temperatures. In the literature, two terms have been used frequently, respectively the internal resistance or internal stress, to mechanistically describe the material internal state. However, it is evident that the distinction between the two terms in literature is often confusing and unclear [80]. This section seeks to clarify these two terms according to their physical origin, which benefits the selection of appropriate state variables and the understanding of how the change in the internal state may influence the subsequent dislocation motion, as described in the last section.

2.2.3.1. Internal resistance

The material internal resistance is essentially a material property, referring to the intrinsic resistance to dislocation motion and thereby the inelastic deformation. It is not a "stress" but "strength". Macroscopically, the yield strength can be used to provide a measure of the internal resistance in a bulk material, but care needs to be taken since the yield strength is often a combined result of the internal resistance and internal stress (to be illustrated later) [81]. To physically understand the origin of the internal resistance, it is more appropriate to view this term on each crystallographic plane. Based on the theory of crystal plasticity theory applied at the length-scale of a single slip plane, the internal resistance is the critical resolved shear strength (CRSS), or critical shear stress described above, illustrating the impediment of dislocation glide motion [82]. According to sections 2.2.1 and 2.2.2, the CRSS is characterised essentially by the distribution of different types of obstacles in the slip plane, i.e. the three-dimensional forest dislocation junctions, the solid solution elements and the secondary phase precipitates. Generally, a dislocation encounters an identical distribution of obstacles no matter what the direction of motion is, thus the internal resistance has an isotropic feature. Different strengthening and softening processes within the material associated with the evolution of microstructure may change both the type and magnitude of the internal resistance [83-87], thereby leading to the change in the micro- and macroscopic yield strength.

2.2.3.2. Internal stress

The term of "internal stress" has been used frequently in the literature. Other similar terminologies include back stress [88], friction stress [89, 90], threshold stress [91] and residual stress [92]. However, many of these terms according to their meanings in the literature should be somehow classified into the internal resistance terms considering the

definition described above. For example, the term of “threshold stress” has been used which must be overcome in order for dislocations to bypass dispersed precipitates [47, 88, 93]. Similarly, the term “friction stress”, which has been used to interpret the dislocation interaction with particles [94] or solute atoms [32], is an internal resistance.

The appropriate definition of the internal stress in this work, different from the material property of internal resistance, is the real stress which basically helps maintain the internal self-equilibrium of a material when there is no external stress [80]. Thus the internal stress is similar to the definition of residual stress and is understood to occur and accumulate during plastic deformation. Hereby the internal stress has a kinematic or directional feature. Within a polycrystalline material, based on the length-scale over which they vary and self-equilibrate, the classification of the residual stresses is Type I (macro-), Type II (meso-) and Type III (micro-) [95, 96]. Type I residual stresses self-equilibrate over a length-scale comparable to the macroscopic dimension of the component. Type II residual stresses self-equilibrate over a length-scale comparable to a few grains and are discontinuous from grain to grain. This type of meso-scale residual stress is a result of strain incompatibility or misfit between grains, created by the orientation dependent elastic and plastic anisotropy [96-98]. Type III residual stress is associated with the misfit stresses between matrix and microstructure elements at the micro-scale. This stress reduces quickly with distance but still satisfies the self-equilibrium condition. Accordingly, the term of “back stress” used in some works to describe the impediments to dislocation motion from the heterogeneous distribution of dislocations, such as the cell walls, grain boundaries and small-scale heterogeneities like dislocation loops and tangles [99, 100], should be all revealed as genuine measures of Type III residual stresses following the definition in this work.

2.2.3.3. The Bauschinger effect

The Bauschinger effect is one of the most important manifestations of the kinematic or directional feature, or the internal stress defined above [80]. It is normally observed that after forward deformation, either in tension or compression, it is easier to deform in reverse deformation than it is to deform in continued forward deformation. An example is depicted in Figure 2.16, where the tensile yield strength along the curve O'B is higher than the compressive yield strength along the dotted curve O'D (equivalent to the curve O'C but is inverted, i.e. the magnitudes of the changes in stress and strain with respect to O' are plotted, to provide an easier comparison with the tensile curve O'B) for materials with pre-tensile strain history (loaded along the curve OA and unloaded along the line AO'). In the literature, the Bauschinger effect is often characterised by two distinct quantities: transient softening and permanent softening stresses, which relate to the magnitudes of σ_{ts} and σ_{ps} as shown in Figure 2.16. The transient softening stress σ_{ts} refers to the immediate difference in the flow stress between tensile and compressive curves, while the permanent softening stress σ_{ps} refers to the observed long-term difference between the two curves. Both stresses can be measured respectively at a small and large strain offset from the starting point O'. However, care needs to be taken on the definition of permanent softening stress since "long term" only refers to a relative time scale. The mechanism of the Bauschinger effect has been naturally considered to be the assistance on the movement of dislocations by different types of internal stresses when the load is reversed [101]. Therefore, distinguishing between internal resistance and internal stress, and understanding how the internal stress evolves with deformation are vital to assessing the material plastic and creep behaviour.

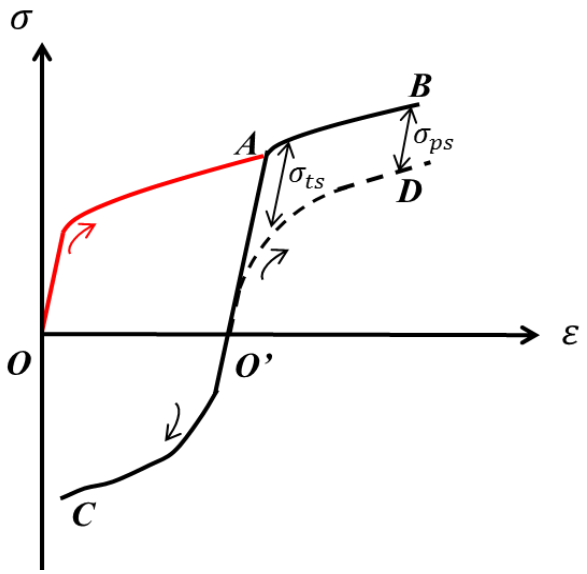

Fig. 2.16. Schematic diagram of Bauschinger effect, showing the prior tensile deformation history (loaded along the curve OA and unloaded along the line AO') and the continued (tensile, curve O'B) and reversed (compressive, curve O'C re-plotted as O'D) straining of the material.

2.2.4. Analytical constitutive models

A wide range of constitutive laws exist in the literature describing the inelastic response of materials. These laws can be divided into three broad groups, which we refer to as empirical, phenomenological and physical models. Empirical models are largely obtained by fitting arbitrary functions to the experimental data. The models are simple but the choice is limited by certain thermodynamic constraints [78]. A typical example of this is the Chaboche model and its extensions [6, 102]. Phenomenological models tend to adopt a similar structure to the empirical ones, but the choice of state variables, evolution laws and also fitting procedures are aided by an understanding of the perceived underlying mechanisms of deformation. Two such models will be briefly introduced in this section, mainly developed by Miller [99, 103, 104] and Dyson [105, 106] respectively. Physical models, or mechanistic models, are mainly based on state variables to characterize the hardening and recovery behaviour by capturing the evolution of mechanical state based on the understanding of deformation mechanisms. Examples of such models in terms of the multiplication of dislocations and evolution of the

dislocation density have been reviewed by Kocks and Mecking [107]. Some specific models established by Gibbs [108], Lagneborg and his co-workers [3, 4, 16, 52] from different aspects of dislocation structures are introduced.

2.2.4.1. Chaboche's model

In metal physics, a yield surface is defined in stress space as the separator convex surface between elastic and plastic regions. The size and location of the surface is commonly described in terms of two types of variables: isotropic and kinematic hardening variables. The isotropic variable accounts for the growth in size or expansion of the yield surface (the increase of internal resistance), while the kinematic variable accounts for its translation, often involving the internal stress and allowing for a description of the Bauschinger effect [6]. The yield surface and the two hardening types in multiaxial stress space are shown in Figure 2.17.

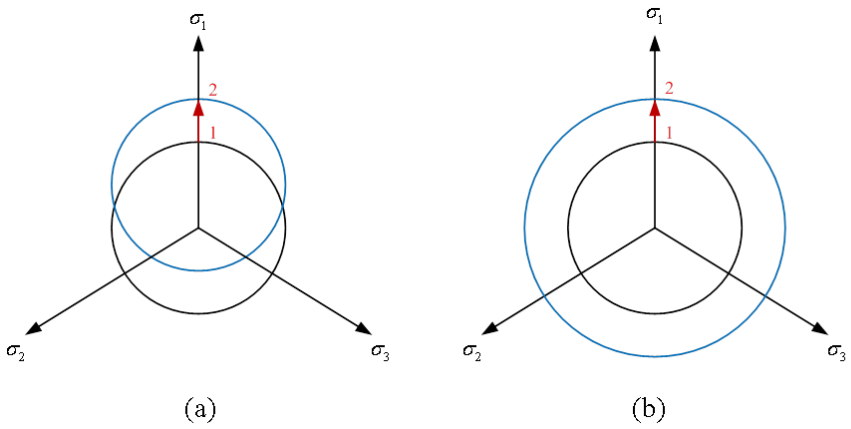

Fig. 2.17. Schematic representations of hardening in multiaxial condition: (a) kinematic (b) isotropic [102]. The black circle is the original yield surface while the blue circle is the updated yield surface.

The yield criterion is given by ($f > 0$ represents the inelastic domain)

$$f = \sqrt{\frac{3}{2}(s_{ij} - \chi_{ij})(s_{ij} - \chi_{ij})} - L - k \tag{2.21}$$

where k is the initial size of the yield surface, and $L+k$ represents the current size. χ_{ij} represents the current location of the centre of the yield surface in stress space. The unified cyclic plasticity and viscoplasticity model proposed by Chaboche [6] is based on a decomposition of the non-linear kinematic hardening rule proposed by Armstrong and Frederick [109], who simulated the multiaxial Bauschinger effect by using a non-linear internal stress evolution equation with dynamic recovery

$$\dot{\chi}_{ij} = \frac{2}{3} C_1 \dot{\varepsilon}_{ij} - C_2 \chi_{ij} \dot{p} \tag{2.22}$$

where C_1 and C_2 are both constants determined from uniaxial tests, $\dot{p}$ is the rate of effective plastic strain accumulation $\dot{\varepsilon}_{ef}$. Chaboche also gives the evolution law of L in Eq. (2.21) with hardening and recovery and $\dot{L} = \dot{\chi}_{ij} = 0$ during steady state creep. The general constitutive law is a power function

$$\dot{p} = \left(\frac{f}{D} \right)^n = \left(\frac{\sqrt{\frac{3}{2}(s_{ij} - \chi_{ij})(s_{ij} - \chi_{ij})} - L - k}{D} \right)^n \tag{2.23}$$

where D is an isotropic drag stress proportional to L and n is a material constant. Chaboche's model can be expanded to include a series of kinematic variables and more recovery terms to optimize the fitting of experimental data. For example, Chaboche proposes

$$\dot{\chi}_{ij} = \sum \chi_{ij}^{\ k} \qquad \dot{\chi}_{ij}^{\ k} = \frac{2}{3} C_{1k} \dot{\varepsilon}_{ij} - C_{2k} \chi_{ij}^{\ k} \dot{p} - G_{2k} \chi_{ij}^{\ k} \tag{2.24}$$

where the summation is over all specified kinematic variables $\chi_{ij}^{\ k}$ and the constants G_{2k} depend on the material and temperature. However, random addition of more state variables and recovery terms is also the main defect of Chaboche's model, with insufficient support from detailed physical processes.

2.2.4.2. Miller's model

The MODel of MATerial (MATMOD) family, established by Miller and co-workers [99, 103, 104], is based on the concept of dislocation-controlled visco-plasticity with inclusion of the solute drag mechanism. In the MATMOD, besides isotropic (D) and kinematic hardening (χ_{ij}) terms, an additional state variable F_{sol} related to the solute drag effect is included [103].

$$\dot{\varepsilon}_{ij} = f(\sigma_{ij}, T, D, \chi_{ij}, F_{sol}) \tag{2.25}$$

where F_{sol} represents the thermally interactive solute strengthening with isotropic terms. Different from Chaboche's model, there is no initial yield strength in MATMOD and the rate function is written in the form of a hyperbolic sine

$$\dot{p} = \theta(T)\left[\sinh\left(\frac{\sqrt{\frac{3}{2}(s_{ij}-\chi_{ij})(s_{ij}-\chi_{ij})}}{\sqrt{D(1+F_{sol})}}\right)^{3/2}\right]^{n} \tag{2.26}$$

where $\theta(T)$ is a temperature dependent function. The main specificity of Miller's model is the development of the drag stress and internal stress. The isotropic drag stress D is divided into D_ρ and D_λ to represent strengthening of forest dislocations and cell/subgrains respectively [100]. The internal stress term χ_{ij} is divided into χ_{ij}^{A} and χ_{ij}^{B} to represent long range and short range internal stresses arising from stable entities and metastable dislocation configurations respectively [99]. Meanwhile, the interactions between D_ρ and χ_{ij}^{B}, D_λ and χ_{ij}^{A} are also considered. All these factors obey a hardening/dynamic recovery/static recovery format similar to Chaboche's model. The unified MATMOD model has a broad range of application due to the comprehensive consideration of various phenomena. However, despite some simplicities made in an improved "physical-phenomenological" model [104], the broad

scope may come at the expense of practicability with too complex equations and too many material constants.

2.2.4.3. Dyson's model

The model proposed by Dyson [105, 106], focusing on precipitation hardened alloys, combines an Arrhenius law with the simplest hyperbolic *sine* function in Miller's model.

$$\dot{p} = A\exp\left(-\frac{Q}{RT}\right)\sinh\left(\frac{\sqrt{\frac{3}{2}(s_{ij}-\chi_{ij})(s_{ij}-\chi_{ij})}}{D}\right) \tag{2.27}$$

By understanding the precipitate-bypassing mechanism and the effect of dislocation substructure as additional barriers, Dyson utilized a new state variable of mobile dislocation density to illustrate dislocation-precipitate interactions. The isotropic hardening term D measures the strength of obstacles impeding dislocation motion. It consists of two aspects, dislocations (σ_d) and particles (σ_p)

$$D = \sqrt{{\sigma_p}^2 + {\sigma_d}^2} \tag{2.28}$$

where σ_d depends on the current dislocation density. The root mean square represents the interaction between the dislocation network and precipitates. Meanwhile, Dyson also used two kinematic hardening terms as internal stresses, respectively arising from Orowan loops around precipitates and the polarity of the dislocation substructure, i.e. the long range internal stress in Miller's model due to the incompatibility between dislocation walls (hard regions) and channels (soft regions). Dyson's model is simpler than Miller's and has been successfully used in modelling nickel-based superalloys [18, 19], but poorly in 316 stainless steels [106]. Part of the reason for poor agreement in 316 stainless steels may be the overemphasis of the strengthening effect from precipitates. Dyson assumed that all dislocations were initially

trapped at precipitates and very few could escape, which is not reasonable for 316 stainless steels due to much lower volume fraction of precipitates than that in nickel-based superalloys.

2.2.4.4. Gibbs' model

In contrast to the empirical and phenomenological models described above, Gibbs' theory of creep takes the well-known Orowan expression to determine the strain rate:

$$\dot{\varepsilon} = \rho b v \tag{2.29}$$

where ρ is the dislocation density, b is the length of the Burgers vector and v is the average velocity of dislocations. Gibbs' model also takes the dislocation density as the state variable, which evolves in a similar way to that described by Kocks and Mecking (Eq. (2.11)). The model combines the features of both thermally activated glide and climb-controlled recovery and it assumes that the velocity of mobile dislocations and hence the strain rate are determined entirely by the rate of thermal activation at local obstacles [108]. The most popular choice of local obstacles to glide has been alternate vacancy-emitting and vacancy-absorbing jogs in the screw components of glide dislocations [108]. As a result, v is given by

$$v = \frac{\pi D_l}{4l} \exp\left\{\frac{(\tau - \tau_\rho) l b^2}{kT}\right\} \tag{2.30}$$

where D_l is the lattice diffusivity, l is the spacing of defect-emitting jogs, k is the Boltzmann constant and τ_ρ is the long-range internal stress assumed to arise from a density of immobilized dislocations ρ_μ, written by the Taylor-type expression

$$\tau_\rho = 0.4 G b \sqrt{\rho_\mu} \tag{2.31}$$

Gibbs' model has focused only on simple and limited dislocation mechanisms and has only been used to describe the behaviour of pure metals due to incomplete consideration of other microstructural elements.

2.2.4.5. Lagneborg's model

The physical model proposed by Lagneborg and his co-workers [3, 4] focuses on a distribution of dislocation link lengths, i.e. a dislocation network structure. Here a dislocation link is defined as the segment between two obstacles or pinning points on its slip plane. Each link is associated with a critical shear stress regarded as the corresponding internal resistance. Most parameters in the model are related to the microstructural state variables such as the dislocation density, the change of which can be determined by pure geometric or physical expressions. In this work, we aim at understanding the underlying physics of deformation thus physical models are to be chosen and developed. Compared with other physical models, the proposed distribution of dislocation link lengths in Lagneborg's model is an elaborated framework and is the physical basis of this thesis. The framework is described and developed in detail in Chapter 3.

Further, note that physical models can be developed for the whole macroscopic polycrystalline material (continuum framework) or for each individual crystal (crystal based framework). Despite the greater complexities involved in the model formulation for the latter approach compared with the former, a crystal based framework is employed here and allows complicated boundary conditions for each crystal to be dealt with efficiently and flexibly and inclusion of physically based evolution laws for the microstructure at the levels of elementary shear slip systems, such as the degree of dislocation multiplication on different slip systems (self- and latent hardening behaviour). In the following chapters, we start from construction and validation of an athermal plasticity model for a single crystal and the whole polycrystal and then incorporate enhancements at elevated temperatures into the athermal model to constitute a comprehensive model for creep deformation.

Chapter 3

An athermal plasticity model for a single crystal

3.1. Introduction

Physical dislocation models, e.g. dislocation network models, have been proposed [110, 111] to characterize the hardening and/or recovery behaviour, by capturing the evolution of the dislocation structure during plastic or creep deformation. These models consider the dislocation structure of a deformed crystalline solid as a complex three-dimensional array of dislocation links arranged in a network, where a dislocation link is defined as the dislocation segment between two pinning points. A given grain will contain a distribution of link lengths. Lagneborg and Forsen [3] and Ostrom and Lagneborg [4] investigated for the first time the detailed evolution of the distribution of link lengths from a physical description of the glide motion of mobile dislocation links. Such a distribution is frequently described by an instantaneous distribution function [3, 4, 56, 57, 112, 113]. A typical distribution was derived by Wang et al [114], assuming that different slip systems uniformly orient in three-dimensional space and all configurations are equally probable, which also minimizes the total entropy. However, such a distribution function only considers a static structure without any external stress. The rate process is based on the athermal Orowan bowing [43] and Friedel's thermally activated network coarsening kinetics [53]. This model has been further extended to illustrate primary and steady-state creep processes, e.g. Ajaja [57]; Shi and Northwood [17]. Among these extensions, Ardell and Przystupa [115] provided a elaborated statistical analysis of the dislocation interaction and the evolution of the distribution. However, all these above models have allowed the existence of links with infinite length in the network, which is

physically unrealistic. In addition, none of these models have systematically accounted for the contributions of different types of obstacles to dislocation motion in engineering alloys, as described in section 2.2.2. Most importantly, previous evolution laws of the distribution function have not distinguished between different dislocation structures on different crystallographic planes, thus the hardening or recovery behaviour described by these models was simplified to be isotropic, i.e. the same for all slip planes.

This chapter establishes an athermal plasticity model for a single crystal, with the principal concern of the kinetics of slip and the evolution of microstructure on different crystallographic planes within a single crystal. The model extends the previous dislocation link length models by considering: (1) a two-dimensional dislocation link length distribution structure on each elementary slip plane; (2) the distinction between self- and latent hardening behaviour in terms of different evolution processes of the dislocation distribution on different crystallographic planes of individual grains; (3) athermal contribution to strengthening from precipitation and solid solution as well as their effects on the plastic response. The aggregate behaviour for the whole polycrystal is considered in Chapter 4. Some validations of the athermal model are shown and discussed in Chapter 5.

3.2. Athermal dislocation link length model

3.2.1 Structure of dislocation link length distribution

This section first establishes a two-dimensional distribution function to describe the distribution of dislocation link lengths on each elementary slip plane within a single crystal. This is done using a statistical approach (details can be found in **Appendix A**), based on the fact that the distribution of links is related to the distribution of pinning points on the slip plane since, initially, all the links are pinned by two points, with each point also connected to

two links. The pinning points in the model only refer to the forest dislocation junctions, which are the intersections of links from other slip planes. Given a slip plane with N_d randomly distributed pinning points per unit area, assume that a link connects each point to its nearest neighbour. The two-dimensional distribution function $\phi(\lambda)$ can be written as

$$\phi(\lambda) = \frac{2\pi\lambda}{L_d^{\,4}} \exp\left(-\frac{\pi\lambda^2}{L_d^{\,2}} \right) \tag{3.1}$$

where $\phi(\lambda) \cdot \Delta\lambda$ equals the number of pinning points per unit area with spacing in the range λ and $\lambda + \Delta\lambda$, or the number of potential links per unit area with lengths in the same range. $L_d = N_d^{-1/2}$ is the mean spacing of the pinning points on the slip plane. A schematic illustration of $\phi(\lambda)$ is shown in Figure 3.1. The curve is truncated at the link length close to the mean spacing, which is to be explained in the next section. The form of Eq. (3.1) is similar to the distribution function obtained by Wang et al, [114] for a 3-D distribution of links. The analysis of **Appendix A** is more straightforward than that presented by Wang et al [114] and it relates to a 2-D plane, rather than a 3-D body. Note, in the current context, different planes can have different distributions of link lengths.

The pinning points exert an athermal shear resistance to the connected link, which is understood to be inversely proportional to the link length [3]. In the athermal problem, the link can be released from the pinning points and glide without the help of recovery only when the resolved shear stress τ (RSS) seen by the link approaches the shear resistance.

$$\lambda = \frac{\alpha_d G b}{\tau} \tag{3.2}$$

where α_d is a dimensionless constant determining the average strength of the pinning points blocking the links, depending on the breakaway angle of a single obstacle from the two connected links (Eq. (2.13)) [44]; *G* is the effective shear modulus parallel to the slip plane and *b* is the length of the Burgers vector. According to Friedel [53], for a general obstacle, α_d

lies in the range from 0 to 1. In F.C.C crystals, theoretical and experimental estimates suggest that $\alpha_d \approx 0.35 \pm 0.15$ for forest dislocation junctions [116].

In terms of Eq. (3.2), the initiation of plastic flow on a single slip plane indicates the presence of a limited or threshold link length λ_{th}. Accordingly, at any instance, the overall range of the link lengths on the slip plane should be limited from 0 to λ_{th}, not to infinity [56, 117]. Therefore, within the distribution of pinning points described by Eq. (3.1), only the pinning points with spacing less than λ_{th} are connected with links, sessile or active shown in Figure 3.1, while links longer than λ_{th} cannot occur and are designated virtual or inactive links in Figure 3.1. Thus the actual distribution of dislocation link length is a truncation of the distribution shown in Figure 3.1.

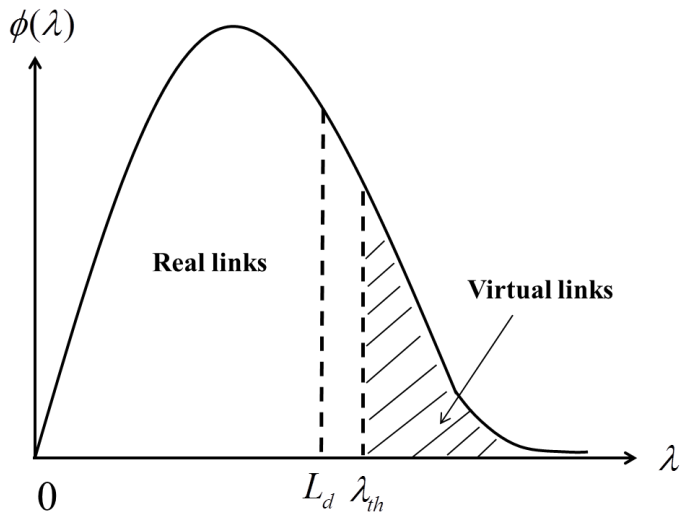

Fig. 3.1. The distribution of pinning points on a single slip plane and the associated truncated distribution of dislocation link length; λ is the distance between two pinning points and is also the link length between them. $\phi(\lambda)\Delta\lambda$ is the number of pinning points per unit area with distance (or number of links with length) between λ and $\lambda + \Delta\lambda$. L_d is the mean spacing and λ_{th} is the current maximum or threshold link length separating sessile and virtual links

This figure also shows that the mean spacing L_d is similar, but not identical, to the mean free path of dislocation glide (equivalent to the average link length $\bar{\lambda}$) described in the

literature [3, 4, 16, 52, 56, 57, 112, 113, 115]. It is reasonable to assume that all the slip planes within the single crystal have an initially identical distribution of pinning points and link lengths described by Eq. (3.1). However, further plastic deformation of the crystal may lead to a variation of the distributions on different slip planes.

3.2.2. Kinetics of dislocation slip

Theories of hardening of crystalline solids consider dislocation movement against the resistance provided by obstacles. Lagneborg and Forsen [3] described dislocation motion in terms of long waiting times at obstacles and occasional spurt-like movements of dislocation links between obstacles. Thus at any instant, all the dislocation links in the network can be considered as immobile and held up at obstacles, i.e. no links are long enough to glide freely. Once the resolved shear stress (RSS) increases and activates the threshold links, free glide motion occurs on the slip plane. The number of mobilized threshold links ΔN_m per unit area can be expressed as

$$\Delta N_m = \phi_{th} \left| \Delta \lambda_{th} \right| \tag{3.3}$$

where $\phi_{th} = \phi\left(\lambda_{th}\right)$ is the threshold value of the 2-D distribution function. These activated links overcome the pinning points and then continue to glide and sweep out an area before being blocked and partitioned into shorter links by some other pinning points (either pre-existing or newly created) and become immobile again. A schematic showing the motion of a single released threshold link is shown in Figure 3.2. Further glide only occurs when the RSS increases and mobilizes more links.

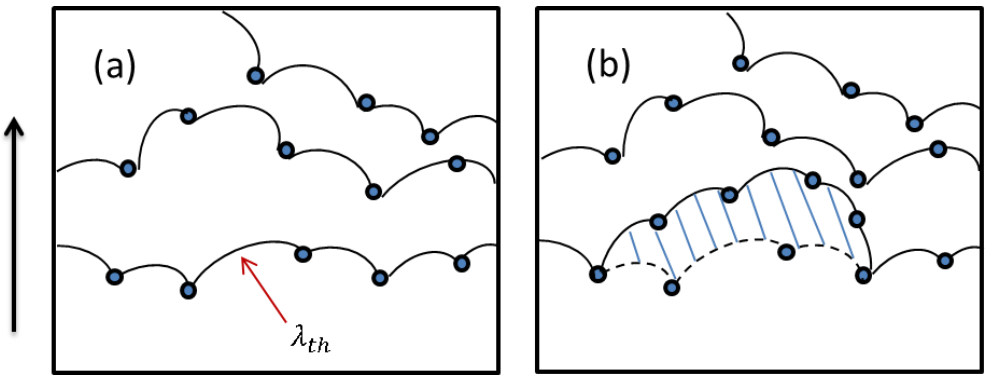

Fig. 3.2. A schematic diagram of the kinetic motion with dislocation links (a) before release and (b) after release and blocking on a single active slip plane, where the solid points are pinning points on this plane and the shaded area is the area swept out by the released threshold dislocation link.

If the area swept out by each mobile link is *s*, the generated shear strain increment $\Delta\gamma$ on the corresponding slip plane by all the mobilized links can be written as

$$\Delta\gamma = s\Delta N_m = s\phi_{th}\left|\Delta\lambda_{th}\right| \tag{3.4}$$

where the sign of $\Delta\gamma$ depends on the sweeping direction. For the sweeping area *s* of each mobile link, Lagneborg and Forsen [3] have assumed that each released link always expands to a circular loop with radius proportional to the average link length $\bar{\lambda}$. This suggests that the sweeping area decreases as $\bar{\lambda}$ decreases during dislocation multiplication. However, according to the simulation of Foreman and Makin [44] of dislocations bypassing a random distribution of obstacles on a slip plane, the opposite has been found. In their framework, a critical resolved shear strength τ_d (CRSS) is defined as the shear stress required for a dislocation to penetrate the whole slip plane (i.e. the sweeping area *s* tends to infinity) and is inversely proportional to the mean spacing defined previously

$$\tau_d = \frac{\alpha_d G b}{L_d} \tag{3.5}$$

This suggests that the sweeping area *s* should be a function of L_d / λ_{th} as shown in Figure 3.3. Simulations in which we have followed Lagneborg's suggestion and assumed that the

sweeping area is proportional to $\bar{\lambda}^2$ produce a stress-strain curve that exhibits substantially more hardening than observed experimentally. Similarly, expressions for the sweeping area based on Freidel's "unzipping" model also result in too high a rate of hardening. Rather than attempting to devise a model in which the sweeping area is a function of L_d / λ_{th}, we adopt a pragmatic approach in which we assume that the sweeping area is zero if $L_d < \lambda_{th}$ and is greater than zero if $L_d \approx \lambda_{th}$, i.e. the response is equivalent to a classical athermal plasticity model. The evolution of the distribution of link lengths is then used to provide relationships for the rates of evolution of self- and latent hardening as described below.

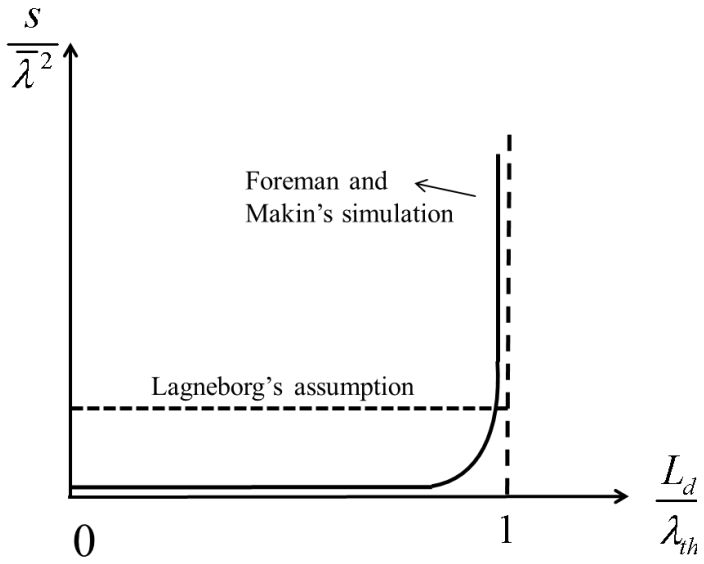

Fig. 3.3. A schematic feature of the magnitude of the sweeping area (comparison between Lagneborg's assumption and Foreman and Makin's simulation)

3.2.3. Hardening with dislocation multiplication

Dislocations interact with each other and multiply as they glide along a slip plane. Hardening of each slip plane is associated with the evolution of the distribution of pinning points and is characterised by the addition of new junctions or dislocation links, which decreases the mean spacing and increases τ_d in Eq. (3.5). In general, the multiplication processes consist of the multiple release of links, expansion and mutual partitioning or

network refinement [115]. Hardening on a slip plane by the increase of the number of pinning points on the same plane is called self-hardening while that by multiplication on other intersecting planes is called latent hardening. Note that self-hardening involves all three processes, while latent hardening only involves mutual partitioning or network refinement.

In previous dislocation link length models it is generally assumed that the hardening is isotropic and plastic flow is not considered at the scale of individual slip systems (see for example [3, 4]). Here we establish a crystal plasticity framework and consider plastic deformation on all slip systems in a body. We employ a simple statistical framework following Ardell and Przystupa [115] to distinguish between self- and latent hardening. In the following sub-sections, only one active slip plane is considered, while cases with multiple active slip planes can be simply analysed by superposition.

3.2.3.1. Dislocation network refinement

Network refinement describes the stage when the mobilized or threshold links on a single active slip plane cut some pinning points and are partitioned into shorter segments and become new members of the network. In the model, network refinement refers to interactions (or cuts) between the gliding and network links, not between gliding links themselves since they only occupy a relatively small population of the total number of interactions. If each threshold link cuts j intersecting links on average at each step, the total number of cuts per unit area is $j\Delta N_m$. Thus the increase in the total number of links in the network is simply $2j\Delta N_m$ since each cut results in the destruction of two links with the formation of four new links. Note that only half of these $2j\Delta N_m$ links belong to the self-hardened plane while the other half lie in the latent hardened planes. Since all the slip planes are equally oriented, it is statistically assumed that each of the latent hardened planes obtains $j\Delta N_m/(m-1)$ new links

on average, where m is the number of slip planes in the single crystal. In other words, $j\Delta N_m/(m-1)$ links on each latent hardened plane are cut on average. Thus considering Eq. (3.4), the relationship between the plastic shear strain increment $\Delta\gamma$ and the increase of number of pinning points on the self-hardened plane (ΔN_{self}) and latent hardened planes (ΔN_{latent}) can be written as

$$\Delta N_{self} = j\Delta N_m = \frac{j}{s}\Delta\gamma \tag{3.6a}$$

$$\Delta N_{latent} = \frac{j\Delta N_m}{m-1} = \frac{j/s}{m-1}\Delta\gamma \tag{3.6b}$$

For F.C.C. crystals, m=4.

3.2.3.2. Multiple release and expansion

Foreman and Makin [44] found that the dislocation lines blocked at weak obstacles like forest dislocation junctions may remain relatively straight as they frequently move through the array. Each activated threshold link has the possibility to grow longer by coalescing with adjacent consecutively released links with various lengths, even ones that are shorter than the threshold length. Such multiple releases of links may generate new gliding links, which may bypass multiple pinning points simultaneously in an unzipping motion until a new equilibrium condition is satisfied by the network refinement process. An intermediate process is shown in Figure 3.4, where the long link λ_f is grown from multiple releases of shorter links.

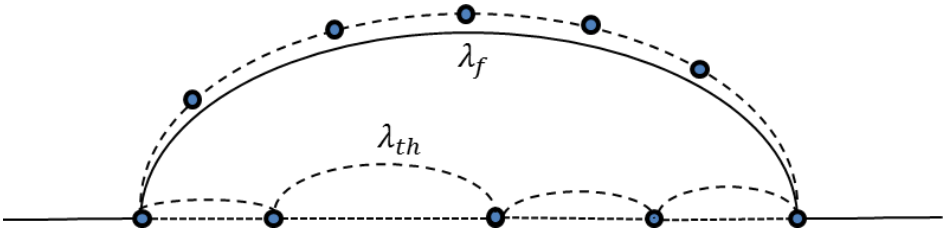

Fig. 3.4. Dislocation multiplication process; λ_{th} is the original length of the gliding link and λ_f is the length of the new gliding link before cut, grown from consecutively released multiple adjacent links

The multiple release of links leads to an additional loss in the distribution of links only on the planes with self-hardening, but it is expected that the number of newly generated links by network refinement is larger than those lost by this unzipping process. This can be incorporated into Eq. (3.6a) simply by introducing a scale factor κ ($\kappa < 1$)

$$\Delta N_{self} = (1-\kappa)\, j \Delta N_m = j_s \Delta N_m \qquad \text{or} \qquad \Delta N_{self} = \frac{j_s}{s} \Delta\gamma \tag{3.7}$$

Here $j_s / s = (1-\kappa)\, j / s$ is regarded as a combined coefficient for self-hardening, while j / s in Eq. (3.6b) is regarded as a combined coefficient for latent hardening. Note that on average the number of cuts for each mobile link is proportional to the area it sweeps. Thus both the proportionalities are fitting constants in the model.

3.2.3.3. Evolution of the distribution function

The distribution function established in Eq. (3.1) is based on the similarity between the number of links and the number of pinning points. We employ the same similarity argument here, and equate the increase of the number of links on a slip plane to the increase of the number of pinning points on the same plane. Considering that the pinning points on a single slip plane can originate from pre-existing junctions or newly formed junctions from cross-slip or the bowing of dislocations on other intersecting slip planes, such a simplification avoids consideration of the detailed origins of the pinning points but retains the basic physics of the

evolution process. Since the distribution function in Eq. (3.1) is a unique function of the mean spacing, or the number of pinning points N_d, updating N_d with Eqs. (3.6b) and (3.7) also updates the distribution of pinning points or link lengths, as shown in Figure 3.5, with different truncations at different threshold link lengths during work hardening. Eqs (3.6b) and (3.7) provide the fundamental relationships for the determination of the rates of self- and latent hardening associated with slip on a given slip plane. These are treated as independent relationships and they allow different distributions of link lengths to evolve on different slip planes.

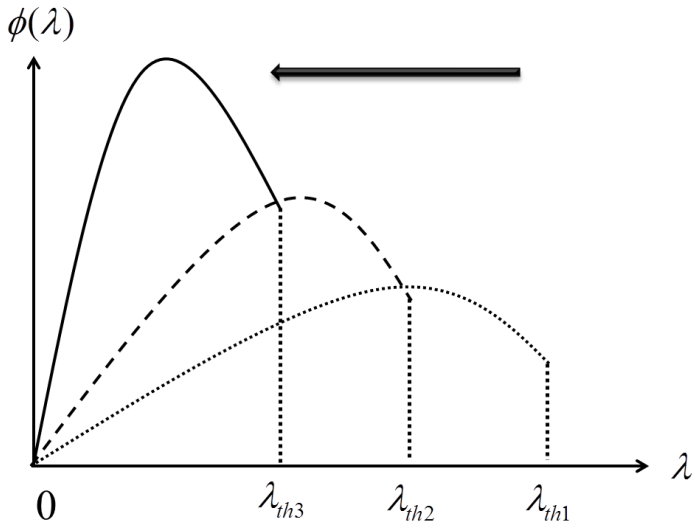

Fig. 3.5. Evolution of the distribution of link length, equivalent to the distribution of pinning points with the truncation by the threshold link length; the evolution of the distribution on self-hardened planes and latent hardened planes may vary.

3.2.4. Issues not covered in the present model

Compared with previous dislocation link length models, a volume constancy condition used to constrain the evolution of the shape of the three-dimensional distribution function during deformation [3, 118] is not considered in the present model. Since all the derivations described above are based on an understanding of the underlying physics, it is not necessary to specify a relationship of this type.

Moreover, the dynamic recovery effect, which is understood to be the spontaneous annihilation process taking place between mobile and sessile links with opposite signs, is not considered in any of the dislocation link length models. In the current model, since dynamic recovery mainly occurs on the active or self-hardened slip planes and reduces the number of mobile links on the corresponding planes [107], it is regarded as implicitly contained when tuning the self-hardening and latent hardening coefficients in Eqs. (3.6) and (3.7). In addition, dynamic recovery is more significant during cyclic loading than monotonic loading [106], thus detailed consideration of dynamic recovery is not necessary at this stage, where we are primarily interested in the material response under monotonic loading.

3.3. Athermal precipitation strengthening

3.3.1. Structure of precipitates distribution

The presence of precipitates in the material provides extra obstacles to dislocation glide motion apart from forest dislocation junctions and solute atoms (to be described in section 3.4). To understand athermal precipitation strengthening, we first describe the state variables associated with precipitates. Here some idealisations of the precipitate structure are used in the model: (1) the precipitates are considered to be hard and unfractured particles, i.e. they are much stronger than the matrix and cannot be plastically deformed when the matrix is deformed; (2) the shape of the precipitates is simplified as spherical thus no orientation effect needs to be considered. This is because the effect of different morphologies on the internal stress at the surface of the particle may die out at a distance of about the particle diameter due to St Venant's principle. Therefore, if the mean size or radius for all the particles is r_p and the number of particles per unit volume is N_p, the volume fraction f_v can be calculated by

$$f_v = \frac{4}{3}\pi r_p^{\,3} N_p \tag{3.8}$$

On a two-dimensional slip plane, Argon [27] has derived the mean radius and area fraction of multiple spherical particles, considering random intersections of these particles on the slip plane (Figure 3.6a).

$$\langle r \rangle = \int_0^{r_p} r_p \left[1 - \left(\frac{z}{r_p} \right)^2 \right]^{1/2} \frac{dz}{r_p} = \frac{\pi}{4} r_p \tag{3.9a}$$

$$\langle A \rangle = \pi \langle r^2 \rangle = \pi \int_0^{r_p} r_p^{\,2} \left[1 - \left(\frac{z}{r_p} \right)^2 \right] \frac{dz}{r_p} = \frac{2\pi}{3} r_p^{\,2} = \frac{32}{3\pi} \langle r \rangle^2 \tag{3.9b}$$

Further, the mean inter-particle spacing L_p can be expressed as

$$L_p = \sqrt{\frac{\langle A \rangle}{f_A}} = \langle r \rangle \sqrt{\frac{32}{3\pi f_A}} = r_p \sqrt{\frac{2\pi}{3 f_A}} \tag{3.10}$$

where f_A is the area fraction of particles on the slip plane. Eq. (3.10) is equivalent to Friedel's formulism [53] given that $f_A = f_v$. In fact, this equivalency is reasonable if we consider a thin slab of material of thickness *dx* and area $L_p^{\,2}$ which contains a single particle of area <*A*> (Figure 3.6b)

$$f_A = \frac{\langle A \rangle}{L_p^{\,2}} = \frac{\langle A \rangle \cdot dx}{L_p^{\,2} \cdot dx} = f_v \tag{3.11}$$

Note that the mean spacing on a slip plane L_p is also related to the number of particles per unit area N_A ($L_p = N_A^{-1/2}$), N_A can be determined by considering Eq. (3.8) and Eq. (3.10)

$$N_A = 2 r_p N_p \tag{3.12}$$

All the derivations above show a relationship between a three-dimensional distribution of precipitates within each individual grain and a two-dimensional distribution regarding each single slip plane within the grain.

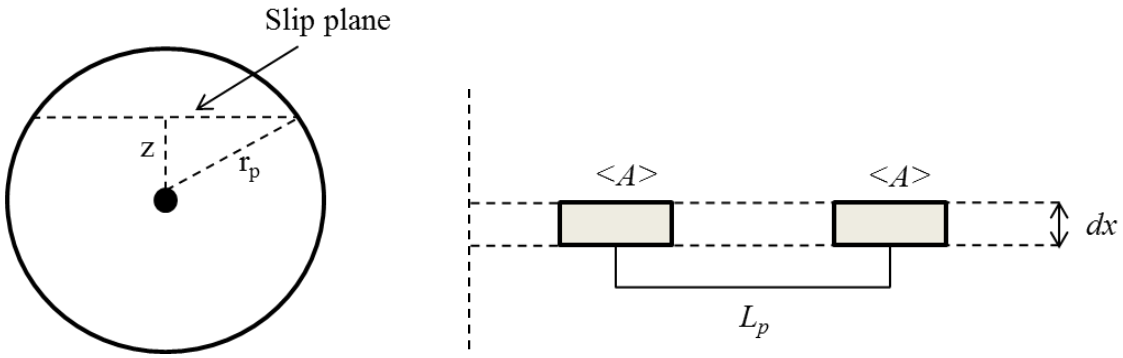

(a) (b)

Fig. 3.6. (a) A spherical particle intersecting a slip plane at a random position; r_p is the mean radius of the particle and z is the distance between the slip plane and the centre of the particle; (b) A random intersection on two particles with an averaged intersection area <A> for each particle

3.3.2. Contribution to internal resistance

As described in section 2.2.2, the precipitation strengthening depends on the nature of the dislocation-precipitate interaction on the active slip planes. At ambient temperature, the undeformable precipitates can only be bypassed by dislocations via the Orowan bowing process. The critical bypassing shear strength, or Orowan strength, taking into account a random distribution of precipitates on a slip plane has been shown in Eq. (2.15), which represents the internal resistance associated with precipitates.

In addition, as straining proceeds, the secondary slip process relieves the stress concentration at particles through the formation and storage of geometrically necessary dislocations in the form of prismatic loops around the particles, as described in section 2.2.2 (see Figures 2.11 and 2.12) [119]. The amount of secondary slip is considered to be the number of secondary loops punched out per unit volume. A qualitative analysis is presented here related to the secondary loop formation and the associated influence on each slip plane.

As is shown in Figure 3.7, a plastic shear strain γ, moving plane A relative to B is achieved by the passage of *n* dislocations. From the geometry of this process

$$nb = 2r_p\gamma \tag{3.13}$$

In secondary slip, this displacement is achieved by punching out *n** prismatic loops in each of the four secondary slip directions (Figure 2.12). Therefore,

$$n^* = \frac{n}{4} = \frac{r_p\gamma}{2b} \tag{3.14}$$

Note that prismatic loops generated from plastic shear strains on different slip planes do not cancel each other out, but interact with each other. Thus if all the active slip planes are considered, in practice, $n^* = r_p\sum\gamma/2b$. Therefore, the total number of additional prismatic loops in the network can be calculated as

$$4n^* \cdot N_p = \frac{2r_p\sum\gamma}{b} \cdot \frac{3f_v}{4\pi r_p^{\,3}} = \frac{3f_v\sum\gamma}{2\pi b r_p^{\,2}} \tag{3.15}$$

Further, if each prismatic loop is simplified as one link, the number of additional links *n'* on each slip plane is just the two-dimensional projection of Eq. (3.15), which is the same for all the slip planes.

$$n' = \frac{3f_v\sum\gamma}{2\pi b r_p^{\,2}} \cdot b = \frac{3f_v\sum\gamma}{2\pi r_p^{\,2}} \tag{3.16}$$

According to section 3.2.3.3, *n'* is also considered simply as the number of additional pinning points or forest dislocation junctions on the slip plane. Therefore, precipitates contribute to the internal resistance on each slip plane in two ways, the Orowan bypassing strength and the number of additional pinning points generated by the prismatic loops. Since the distribution of precipitates is considered to be identical on all the slip planes, the associated contribution to the internal resistance will also be identical on all the slip planes.

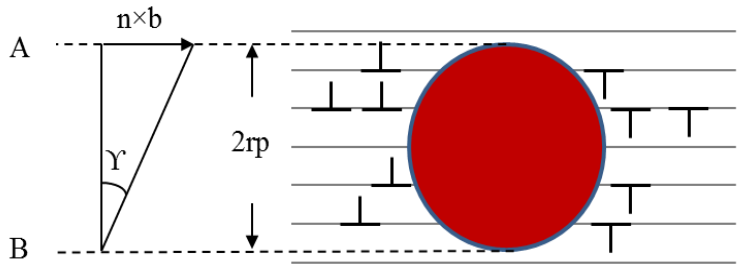

Fig. 3.7. A shear strain γ on a pack of slip planes deposits *n* primary dislocation loops around the particle of radius r_p

3.3.3. Contribution to internal stress

During plastic deformation, since the particles/precipitates are plastically stronger than the soft matrix, more and more stress is carried by the particles. This stress in the particles will remain even in the unloaded state. For a slip plane containing an area fraction f_A of intersecting precipitates, the stress balance on the slip plane in the unloaded state is

$$\tau_m^r(1-f_A)+\tau_p^r f_A=0 \tag{3.17}$$

where τ_p^r and τ_m^r are residual stresses in the precipitates (or at the particle-matrix interface) and matrix respectively, where τ_p^r is manifested as the attraction or repulsion from the particles to the surrounding loops and vice versa. According to section 2.2.3, τ_p^r and τ_m^r are Type III internal stresses. To determine τ_m^r in the matrix, as part of the driving force for further dislocation glide motion during loading, τ_p^r needs to be calculated. Note that the stress carried by the particles τ_p^r is independent on whether there are loops surrounding the particles. However, in practice, we can determine the stress τ_p^r in a simple way of determining the stress exerted on them by the prismatic loops. Since the stress close to a loop resembles that from a straight dislocation and falls off rapidly with distance [46, 120], we can reasonably assume that τ_p^r is exerted from each single particle to the nearest loop. This internal stress τ_p^r

is analysed here based on Kroupa's work [120], who took into account the average force exerted by one prismatic loop opposing the glide of a straight dislocation in its slip plane.

Ashby [46] states that the secondary slip extends outward from one particle to a distance comparable to the inter-particle spacing. Each new loop punched out forces the existing loops closer to each other. Consider a stack of n^* loops, shown in Figure 3.8, the outermost of which is fixed because it has reached the mid-point between particles or because of an earlier intersection with a glide dislocation. The mean spacing between loops, L_l, scales with the distance between particles (consider Eqs. (3.10) and (3.14))

$$L_l = \frac{L_p - 2r_p}{2n*} = \frac{\left(L_p - 2r_p\right)b}{r_p\gamma} = \frac{b}{\gamma}\left(\sqrt{\frac{2\pi}{3f_A}} - 2\right) \tag{3.18}$$

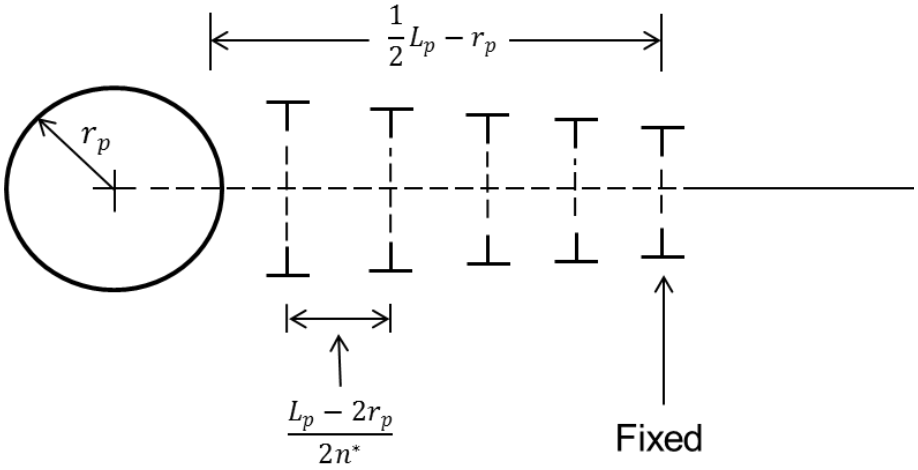

Fig. 3.8. A stack of prismatic loops exerts a stress in the particle-matrix interface which opposes the creation of another loop. This stress is roughly equal to that exerted by the nearest loop.

The opposing stress exerted by the nearest prismatic loop is expressed by Kroupa as

$$\sigma_l = \frac{\alpha_l G b}{L_l} = \frac{\alpha_l G\gamma\left(\sqrt{3f_A}\right)}{\sqrt{2\pi} - 2\sqrt{3f_A}} \tag{3.19}$$

where α_l is a strength constant (assumed here as equal to the average strength for forest dislocation junctions in Eq. (3.2)). According to Ashby [46] and Kroupa [120], each stack of

loops behaves like a spring, in tension along the x_1' direction in Figure 2.11(d) (i.e., attracts vacancy loops) and in compression along the x_2' direction in Figure 2.11(d) (i.e. opposes interstitial loops). Therefore, if all the four directions with punched-out loops are considered, the stress state at particle-matrix interface described by Eq. (3.19) is illustrated in Figure 3.9(a), which is equivalent to a pure shear stress state (Figure 3.9b).

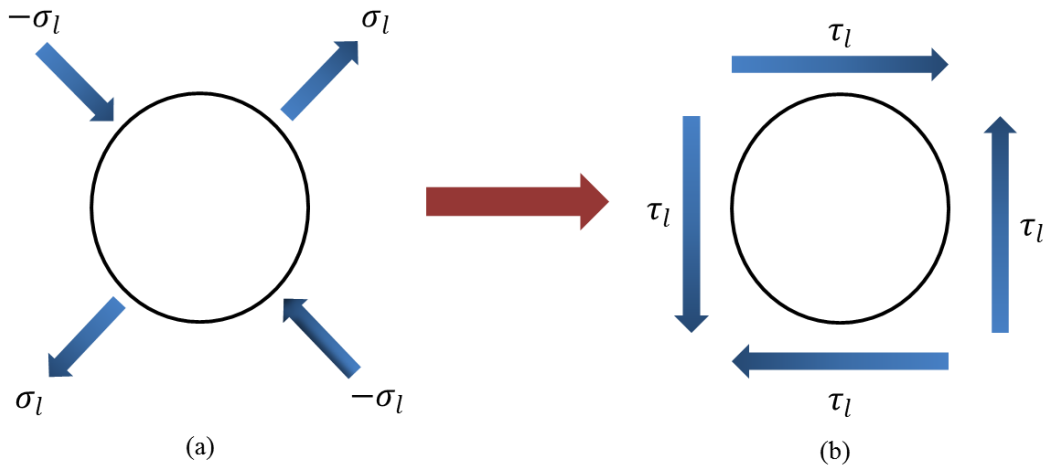

Fig. 3.9. The stress state of a single particle; (a) Attractive and repulsive stresses associated with different types of dislocation loops; (b) The equivalent pure shear stress state of the particle

Therefore, τ_m^r can be determined by substituting Eq. (3.19) into Eq. (3.18).

$$\tau_m^r = -\frac{f_A}{1-f_A}\tau_p^r = -\frac{f_A}{1-f_A}\tau_l = -\frac{\sqrt{3}\alpha_l G\gamma f_A^{3/2}}{(1-f_A)\left(\sqrt{2\pi}-2\sqrt{3f_A}\right)} \tag{3.20}$$

Considering that $f_A = f_v << 1$ in stainless steel, τ_m^r can be simplified as

$$\tau_m^r \approx -0.7\alpha_l G\gamma f_A^{3/2} \tag{3.21}$$

Eq. (3.21) indicates that τ_m^r on a single slip plane is linearly proportional to the plastic shear strain γ on the same plane. Finally, note that the accumulated Type III internal stress influences not only on the active slip planes, but has components acting on other slip planes, which will be presented in Chapter 4.

3.4. Athermal solid solution strengthening

3.4.1. Structure of solute atoms distribution

Another type of obstacle that can exist in a material, in addition to dislocation junctions and precipitates, is solute elements. The athermal strengthening effect of solute elements refers to the interaction forces or energy barriers on the dislocation line due to the presence of immobile solute atoms of different sizes. These obstacles can be weaker, but more plentiful compared with the other two microstructural elements, and partly overlap [44]. The distinguishing feature of the strengthening by solute atoms is the combination of repulsive and attractive interaction forces experienced by dislocations [27]. As a result, the dislocation line here is not pinned by these impurity atoms but instead becomes wiggly, adjusting its configuration to conform to the interaction forces produced by the immobile atoms (see Figure 3.10).

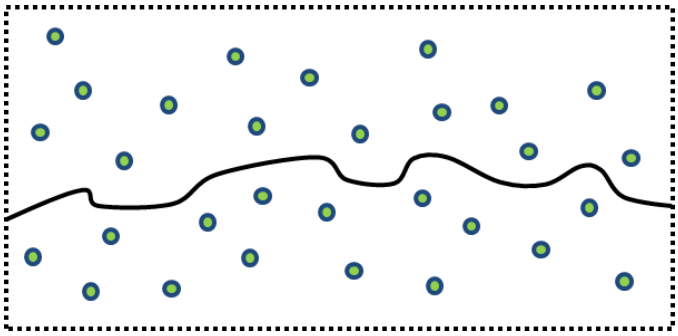

Fig. 3.10. Wiggly configuration of a dislocation line around impurity solute atoms

3.4.2. Solute bypassing strength

Similar to the simulation by Foreman and Makin [44], the athermal resistance (or CRSS) on a single slip plane with a random distribution of solute atoms is considered to be inversely proportional to the mean spacing L_s of the solute atoms on the plane:

$$\tau_s = \frac{\alpha_s G b}{L_s} \tag{3.22}$$

where α_s is the average strength related to the critical breakaway angle for solute atoms. The mean spacing L_s can be calculated from the solute concentration, or number density c of all the impurity atoms, in the material:

$$L_s = \sqrt{\frac{1}{cb}} \tag{3.23}$$

Substituting Eq. (3.23) into Eq. (3.22), the CRSS for athermal solute strengthening is

$$\tau_s = \alpha_s G b (cb)^{1/2} \tag{3.24}$$

The variation of the distribution of solute atoms on different slip planes is ignored, thus athermal solute strengthening is simplified as isotropic on all the slip planes.

3.5. Combination of strengths from the three mechanisms

Sections 3.2~3.4 have separately illustrated the distribution and the strengthening effects associated with three microstructure elements, respectively forest dislocation junctions, precipitates and impurity solute atoms. The athermal critical resolved shear strength (CRSS) for each type of element on a single slip plane is determined. In practice, a gliding dislocation on a slip plane encounters a combination of all three types of obstacles, as shown in Figure 3.11. Therefore, it is the combined strength that retards the moving dislocation.

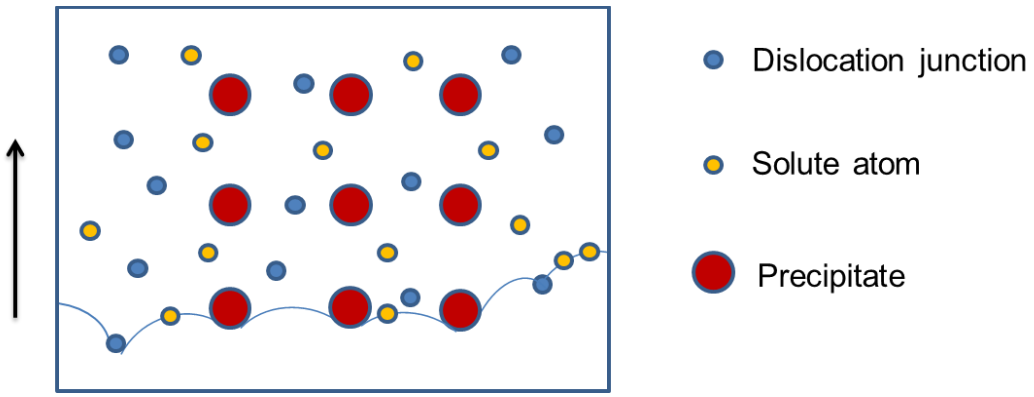

Fig. 3.11. A schematic diagram of the network with three predominant types of obstacles, respectively forest dislocation junctions (blue points), impurity solute atoms (green points) and precipitates (red circles); the blue line represents several dislocation links retarded by these obstacles

The overall CRSS τ_{cr} on a given slip plane is determined by a combination of Eqs. (3.5), (2.15) and (3.24). A general widely rationalized theory of the combination of any two kinds of strengths (τ_1 and τ_2) is given in the literature as [32, 121, 122]

$$\tau_t^{\,q} = \tau_1^{\,q} + \tau_2^{\,q} \tag{3.25}$$

where τ_t is the combined strength, q is an exponent whose value varies between 1 and 2 depending on details of the mechanisms involved. In athermal problems, Dong et al [32] has examined the strength of different combinations of obstacles with various breakaway angles as defined in Foreman and Makin's analysis [44] and various number densities. The results show that the linear superposition rule or additive strengthening (q=1) is valid when the number densities of the two obstacles differs by more than a factor of 3, otherwise a transition from additive (q=1) to geometric mean or quadratic rule (q=2) prevails [32, 106].

For Type 316 stainless steels, based on some experimental findings not shown here, the combined CRSS on a single slip plane is formulated simply using the quadratic rule

$$\tau_{cr} = \sqrt{\tau_d^{\,2} + \tau_p^{\,2}} + \tau_s \tag{3.26}$$

where τ_d is the athermal strength of forest dislocation junctions (Eq. (3.5)), τ_s is the athermal strength of impurity solute atoms (Eq. (3.24)), τ_p is the precipitates bypassing strength (Orowan strength, Eq. (2.15)). Such combination can also be found in [123]. Since the distribution of solute atoms and precipitates does not evolve at ambient temperature, both τ_s and τ_p in Eq. (3.26) are constants thus the continuous hardening or the increase of τ_{cr} on the slip plane is only characterised by the increase of τ_d due to the continuous multiplication of dislocations.

3.6. Summary

In this chapter, an athermal plasticity model for a single crystal is established, with specific emphasis on the detailed dislocation hardening mechanism on each slip plane associated with three types of obstacles, forest dislocation junctions, precipitates and impurity solute atoms.

For forest dislocations, a two-dimensional distribution function of dislocation link lengths or pinning points on a single slip plane is derived. The critical shear strength of the slip plane with randomly distributed pinning points is shown to be inversely proportional to the mean spacing of all the pinning points. Plastic shear strain is generated by the motion of mobile or threshold links. Hardening behaviour is described by the detailed dislocation multiplication processes, consisting of three stages: multiple release of links, expansion and network refinement. The details of these stages may vary on different slip planes and the corresponding evolution of the distribution functions as well as the critical shear strengths are used to distinguish the extent of self- and latent hardening on the different slip planes.

For precipitates, a simple linear periodic array of spherical particles is incorporated on each slip plane. The contribution to the athermal resistance by precipitation has been quantified, consisting of three aspects: (1) the modified Orowan strength in terms of the actual random distribution of particles [67]; (2) the distribution of secondary dislocation loops punched out between particles adding to the total number of forest dislocation junctions; and (3) the stress carried by the particles as the Type III internal stress.

For atoms in solid solution, their contribution to the athermal resistance is analysed using a similar formulation to that for the precipitates and forest dislocation junctions. Finally, an appropriate form of the overall combined critical resolved shear strength (CRSS) of a single slip plane is determined, taking into account the potential variation in the number density of all the three types of obstacles in Type 316 stainless steels.

Finally, all the key equations within this chapter are summarized below:

(1) Critical resolved shear strength of each individual type of obstacle

$$\tau_d = 0.35 \cdot \frac{Gb}{L_d} = 0.35 \cdot Gb\sqrt{N_d}$$

$$\tau_p = 0.84 \cdot \frac{Gb}{L_p} = 0.84 \cdot \frac{Gb}{r_p}\sqrt{\frac{3f_v}{2\pi}} = 0.84 \cdot \frac{Gb}{r_p}\sqrt{\frac{3f_A}{2\pi}}$$

$$\tau_s = \frac{\alpha_s Gb}{L_s} = \alpha_s Gb\left(cb\right)^{1/2}$$

(2) Combined critical shear strength of the three types of obstacles

$$\tau_{cr} = \sqrt{{\tau_d}^2 + {\tau_p}^2} + \tau_s$$

(3) Self- and latent hardening with dislocation multiplication

$$\Delta N_{self} = \left(1-\kappa\right) j\Delta N_m = \frac{j_s}{s}\Delta\gamma$$

$$\Delta N_{latent} = \frac{j\Delta N_m}{m-1} = \frac{j/s}{m-1}\Delta\gamma$$

(4) Contribution to number density of forest dislocation junctions from precipitates

$$n' = \frac{3f_v\sum\gamma}{2\pi {r_p}^2}$$

(5) Contribution to Type III micro-scale internal stress on individual slip planes from precipitates

$$\tau_m^r \approx -0.7\alpha_l G\gamma {f_A}^{3/2}$$

Chapter 4

A three-dimensional multi-scale self-consistent model for the polycrystalline aggregate

4.1. Introduction

For metallic polycrystalline materials like austenitic stainless steels, the macroscopic deformation is dependent on the microscopic behaviour of each individual grain. Given an applied load history, the local elastic and plastic anisotropy of differently oriented grains within the polycrystal leads to a variation in the micro-mechanical lattice response, whose evolution will depend on the detailed anisotropic flow, hardening and recovery laws for different slip systems in the body. The development of the local mismatch between grains during plastic deformation will lead to the accumulation of intragranular residual stresses (Type II as described in section 2.2.3), which has a considerable effect on damage development within the material [97, 98]. Therefore, understanding the local micro-scale variation between different grains or lattices plays an important role in assessing and improving the performance of such materials. This requires knowledge of the link between the behaviour of individual grains and the polycrystalline aggregate.

Various models linking the individual grain and aggregate polycrystalline responses have been proposed or developed to predict quantitative and qualitative features of elasticoplastic behaviour of polycrystalline materials, such as the Taylor model [124], which assumes that all grains experience identical strain, but elastic anisotropy plays no role in the model. Self-consistent models have been used extensively, which employ solutions of the classical Eshelby inclusion problem [125, 126], where each individual grain is regarded as an

ellipsoidal inclusion embedded in a macroscopically homogeneous medium. Typical examples of such models can be traced back to Hill [127-129] and K.B.W. model presented by Kroner [130], Budiansky and Wu [131]. They proposed the relationship between the misfit strain and the plastic behaviour of the inclusion. Difference between Hill's model and K.B.W. model has been discussed by Hutchinson [132], where K.B.W. model has assumed constant elastic moduli for individual grains, i.e. the interaction with the continuum matrix is purely elastic, while Hill's model has taken into account the change of instantaneous or tangent moduli for the polycrystal during plastic deformation to model the elastic-plastic interaction. However, the tangent moduli at each instant time may vary during different types of loading due to the real anisotropy of the material, thus the appropriate choice of the moduli is of great importance in Hill's model. Further, Hill [127-129] and Hutchinson [132] have combined the self-consistent approach with a crystal plasticity model and a simplified dislocation slip mechanism to elaborate the hardening behaviour of each grain. Examples of the use of these self-consistent models on evaluating neutron diffraction measurements can refer to [97, 133]. However, all these models lack consideration of detailed evolution of dislocation structure associated with slip processes in individual grains, thus the work hardening behaviour is only reflected in an empirical way.

In this chapter, an athermal three-dimensional multi-scale self-consistent approach for polycrystalline aggregates is established by incorporating the athermal part of the dislocation link length model established in Chapter 3 into a crystal based plasticity and self-consistent framework. For the interaction between individual grains and the continuum matrix, we simply assume purely elastic interaction, following K.B.W. model, to avoid the issue of the choice of tangent moduli. The model consists of three sub-models, which describe the response from the macro- to the micro-scale, namely: continuum, crystal plasticity and dislocation link length models. This chapter introduces the crystal plasticity and continuum

framework. This self-consistent model is able to capture the detailed interaction not only between each individual grain and the surrounding matrix (mismatch), but also between slip planes (self- and latent hardening), which has been discussed in Chapter 3.

4.2. Crystal based plasticity framework

A crystal based plasticity framework is used to determine the plastic strain increment of each individual grain within the polycrystal [107]. For a F.C.C crystal, each grain contains four slip planes and each slip plane has three slip directions, giving a total of twelve slip systems. If $\overline{n}^{\beta}(n_1^{\beta}, n_2^{\beta}, n_3^{\beta})$ is the normal to a slip plane and $\overline{s}^{\beta}(s_1^{\beta}, s_2^{\beta}, s_3^{\beta})$ is one of the slip directions associated with the slip system β ($\beta = 1 \sim 12$), the total plastic strain increment $\Delta\varepsilon^{p}$ can be obtained by adding all the shear strain increments $\Delta\gamma^{\beta}$ on all the active slip systems within the grain [107, 134]

$$\Delta\varepsilon^{p} = \sum_{\beta}^{12} \Delta\gamma^{\beta} sym(\overline{n}^{\beta} \otimes \overline{s}^{\beta}) \tag{4.1}$$

where $sym\left(\overline{n}^{\beta} \otimes \overline{s}^{\beta}\right)$ is the Schmid factor of slip system β and $\otimes$ represents the dyadic product. According to the conventional rate-independent models, five slip systems (five equations plus the plastic incompressibility condition) are needed to determine a three-dimensional plastic strain in each crystal (totally six components), selection of which may require certain detailed rules. For numerical simplicity, following Asaro and Needleman [134] and Hutchinson [82], a power-law relationship is employed between the shear strain increment $\Delta\gamma^{\beta}$ on the slip system β and the RSS τ^{β}, within a prescribed time step Δt

$$\Delta\gamma^{\beta} = \Delta\gamma_0 \left| \frac{\tau^{\beta} + \left(\overline{\tau}_m^{r}\right)^{\beta}}{\tau_{cr}^{\beta}} \right|^{p} \operatorname{sgn}\left(\tau^{\beta} + \left(\overline{\tau}_m^{r}\right)^{\beta}\right) \tag{4.2}$$

where τ_{cr}^{β} is the CRSS of the slip system β, expressed in the form of Eq. (3.26). p is a rate sensitivity exponent and $\Delta\gamma_0 = \dot{\gamma}_0 \Delta t$ is a reference shear strain increment. $\left(\bar{\tau}_m^r\right)^{\beta}$ is the overall Type III internal stress on the slip system β caused by the prismatic punching associated with precipitates, which has been described in Chapter 3. A large value of p ($p \to \infty$) is chosen in the simulation presented in this thesis (p=600), indicating that the dislocation slip only occurs on slip system β when $\tau^{\beta} + \left(\bar{\tau}_m^r\right)^{\beta}$ approaches τ_{cr}^{β}. Use of such rate-dependent model with the large exponent facilitates the automatic selection of the active slip systems at each time step. In addition, note that if the overall stress in the single crystal is denoted as σ^a, the current RSS τ^{β} on the slip system β is also linked with σ^a through the corresponding Schmid factor

$$\tau^{\beta} = \left[sym\left(\bar{n}^{\beta} \otimes \bar{s}^{\beta}\right)\right]^T \sigma^a \tag{4.3}$$

The determination of $\left(\bar{\tau}_m^r\right)^{\beta}$ takes into account the internal stress on all the slip systems since the Type III internal stress on the active slip systems (Eq. (3.21)) also influences other slip systems by its resolved components. Note that the normal stress σ_m^r caused by the Type III internal stress on all the slip systems can be expressed as

$$\sigma_m^r = \sum_{\beta=1}^{12} \left(\tau_m^r\right)^{\beta} sym\left(\bar{n}^{\beta} \otimes \bar{s}^{\beta}\right) \tag{4.4}$$

where $\left(\tau_m^r\right)^{\beta} = -0.7\alpha_l G\gamma^{\beta} f_A^{3/2}$ for slip system β. Therefore, $\left(\bar{\tau}_m^r\right)^{\beta}$ can be calculated in a way similar to Eq. (4.3) [135]

$$\left(\bar{\tau}_m^r\right)^{\beta} = \left[sym\left(\bar{n}^{\beta} \otimes \bar{s}^{\beta}\right)\right]^T \cdot \sum_{\beta=1}^{12} \left(\tau_m^r\right)^{\beta} sym\left(\bar{n}^{\beta} \otimes \bar{s}^{\beta}\right) \tag{4.5}$$

Furthermore, for F.C.C. crystals, it is understood that the coplanar slip systems {1,2,3}, {4,5,6}, {7,8,9} or {10,11,12} belonging to the same slip plane have identical CRSS and

experience the same hardening (the increase of CRSS) [136]. The activation of any coplanar system leads to plastic flow on the whole slip plane. Therefore, the above crystal plasticity model is consistent with the construction of the dislocation distribution and the rates of self- and latent hardening derived in Chapter 3 for different slip planes. In reality, the plastic shear strain increment $\Delta\gamma$ on a single slip plane described in Eq. (3.4) is simply the sum of the shear strain increments on all the active coplanar slip systems on the corresponding planes.

4.3. Continuum model for polycrystalline aggregate

For a polycrystalline material, the orientations of individual grains tend to be random if the material has not been subjected to any significant prior deformation history. Thus, even if each individual grain is anisotropic, the property differences tend to average out and, overall, the material is isotropic. In other words, the polycrystal formed by grains with random orientations can be regarded as isotropic at length scales sufficiently larger than the size of the crystallites, i.e. no preferred texture. This approximation of isotropic polycrystalline aggregate is reasonable based on the weak texture observed in materials similar to that employed in this study [137, 138].

With the above established constitutive response of each individual grain, the collective response of the polycrystalline aggregate can be obtained by the continuum self-consistent scheme [125, 139], which establishes the relationship between the response of each individual inhomogeneous grain and the bulk response of the polycrystalline aggregate when the grain contains a stress-free misfit strain. Each individual grain of a polycrystal is regarded as a spherical inclusion surrounded by an infinite homogeneous matrix that has the same isotropic properties as the macroscopic random array of polycrystals, i.e. the probability that a grain has a given orientation is the same for all possible orientations. Only small deformation is considered in this work, thus no lattice rotation is incorporated.

4.3.1. Model of elasticity

4.3.1.1. Original homogeneous inclusion

Eshelby obtained the solution for the elastic field of an ellipsoidal inclusion with a stress-free misfit strain ε^t embedded in an infinite isotropic or homogeneous matrix (Figure 4.1). In the current context, the misfit strain is an inelastic strain (plastic strain or thermal strain, etc).

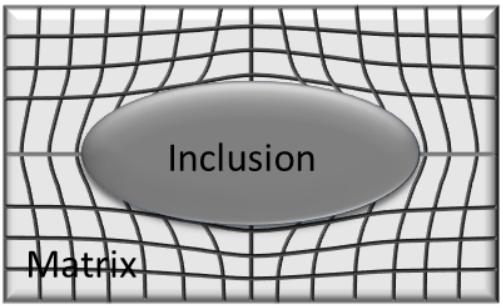

Fig. 4.1. Schematic of an ellipsoidal inclusion embedded in a homogeneous matrix. The inclusion has a mismatch with the surrounding matrix

If the inclusion is homogeneous (with the same elastic constants as the matrix), the total strain in the inclusion is obtained as

$$\varepsilon^i = S^i \varepsilon^t \tag{4.6}$$

where $\varepsilon^i = [\varepsilon_{11} \quad \varepsilon_{22} \quad \varepsilon_{33} \quad \gamma_{23} \quad \gamma_{13} \quad \gamma_{12}]^T$ is the total inclusion strain composed of the elastic strain and the misfit strain. S^i is the Eshelby tensor, which depends only on the geometry of the inclusion and Poisson's ratio (ν_i) of the matrix [125, 139]. The Eshelby shape tensor for a spherical inclusion is given by

$$S^i = \begin{bmatrix} \frac{7-5\nu_i}{15(1-\nu_i)} & \frac{5\nu_i-1}{15(1-\nu_i)} & \frac{5\nu_i-1}{15(1-\nu_i)} & 0 & 0 & 0 \\ \frac{5\nu_i-1}{15(1-\nu_i)} & \frac{7-5\nu_i}{15(1-\nu_i)} & \frac{5\nu_i-1}{15(1-\nu_i)} & 0 & 0 & 0 \\ \frac{5\nu_i-1}{15(1-\nu_i)} & \frac{5\nu_i-1}{15(1-\nu_i)} & \frac{7-5\nu_i}{15(1-\nu_i)} & 0 & 0 & 0 \\ 0 & 0 & 0 & \frac{2(4-5\nu_i)}{15(1-\nu_i)} & 0 & 0 \\ 0 & 0 & 0 & 0 & \frac{2(4-5\nu_i)}{15(1-\nu_i)} & 0 \\ 0 & 0 & 0 & 0 & 0 & \frac{2(4-5\nu_i)}{15(1-\nu_i)} \end{bmatrix} \tag{4.7}$$

Thus the elastic strain in the inclusion can be written as

$$\varepsilon^e = \varepsilon^i - \varepsilon^t = \left(S^i - I\right)\varepsilon^t \tag{4.8}$$

where I is the unity matrix. The stress field of the inclusion σ^i can be then calculated based on Hooke's law

$$\sigma^i = L^i\left(\varepsilon^i - \varepsilon^t\right) = L^i\left(S^i - I\right)\varepsilon^t \tag{4.9}$$

where L^i is the elastic stiffness matrix of the homogeneous inclusion or the macroscopically isotropic polycrystalline matrix. Given a macroscopically applied stress σ, the total strain in the inclusion becomes

$$\varepsilon^i = C^i T\sigma + S^i\varepsilon^t \tag{4.10}$$

where C^i is the compliance matrix $C^i = \left(L^i\right)^{-1}$ and T is the orientation matrix of the grain described by the angles that the outward normal to the faces of the cubic unit cell of the local F.C.C. grain make with the axes of the global co-ordinate system. Finally, considering Eq. (4.9), the total stress in the inclusion subject to the external stress σ can be written as

$$\sigma^i = L^i\left(S^i - I\right)\varepsilon^t + T\sigma \tag{4.11}$$

4.3.1.2. Real inhomogeneous inclusion

For a real inhomogeneous inclusion or an inhomogeneity or an anisotropic grain with a different elastic stiffness matrix L^a ($C^a = \left(L^a\right)^{-1}$ is the compliance matrix) from the matrix, if the inhomogeneity has a real misfit strain ε^{ta}, its elastic field (σ^a, ε^a) can be written as

$$\begin{aligned} \sigma^a &= L^a\left(\varepsilon^a - \varepsilon^{ta}\right) \\ \varepsilon^a &= C^a\sigma^a + \varepsilon^{ta} \end{aligned} \tag{4.12}$$

Since the Eshelby tensor cannot be used for anisotropic inclusion, its elastic field can be simulated by an equivalent inclusion method, where an equivalent homogeneous inclusion with a properly chosen misfit strain ε^{t*} is used to satisfy the equivalence relationship [139]

$$\sigma^a = \sigma^i, \varepsilon^a = \varepsilon^i \tag{4.13a}$$

$$\sigma^a = L^a\left(\varepsilon^a - \varepsilon^{ta}\right) = L^i\left(\varepsilon^i - \varepsilon^{t*}\right) = L^i\left(S^i - I\right)\varepsilon^{t*} \tag{4.13b}$$

Further, given the applied stress σ, similar to Eq. (4.11), the stress of the inhomogeneous inclusion is obtained as

$$\sigma^a = \sigma^i = L^i\left(S^i - I\right)\varepsilon^{t*} + T\sigma \tag{4.14}$$

Considering Eq. (4.12), the total strain of the inhomogeneity can be further expressed as

$$\begin{aligned} \varepsilon^a &= C^a L^i\left(S^i - I\right)\varepsilon^{t*} + C^a T\sigma + \varepsilon^{ta} \\ &= \varepsilon^i = C^i T\sigma + S^i\varepsilon^{t*} \end{aligned} \tag{4.15}$$

Thus, the relationship between the real misfit strain ε^{ta} in the anisotropic grain and the chosen misfit strain ε^{t*} in the equivalent inclusion can be derived as

$$\varepsilon^{ta} + \left(C^a - C^i\right)T\sigma = \left[C^a L^i\left(I - S^i\right) + S^i\right]\varepsilon^{t*} \tag{4.16}$$

Note that the misfit strain ε^{ta} is physically caused by the plastic deformation of the grain, thus $\varepsilon^{ta} = 0$ during elastic deformation and ε^{t*} is then solved as a function of σ, allowing the

elastic field in each grain to be derived, with respect to a local co-ordinate system co-incident with the outward normal to the faces of the unit cell:

$$\sigma^a = \left\{ \left\{ \left[I - \left(S^i \right)^{-1} \right]^{-1} C^i - C^a \right\}^{-1} \left(C^a - C^i \right) + I \right\} T\sigma = H^a T\sigma \tag{4.17a}$$

$$\varepsilon^a = \left\{ C^i + \left\{ \left(C^a - C^i \right)^{-1} C^a L^i \left(S^i \right)^{-1} - L^i \right\}^{-1} \right\} T\sigma = K^a T\sigma \tag{4.17b}$$

where H^a and K^a are the quantities in the braces. Note that if the individual grains are isotropic elastically, H^a reduces to the unity matrix I and Eq. (4.17a) simply rotates the stress from the global to the local co-ordinate system. Similarly, K^a reduces to the compliance matrix $C^a = C^i$ and Eq. (4.17b) gives the homogeneous elastic strain with respect to the local co-ordinate system. The initially unknown isotropic stiffness tensor L^i can be obtained from the elastic strain in all the grains of the polycrystal (Eq. (4.17b)) by using the virtual work principle (to be presented in section 4.3.3).

4.3.1.3 Orientation matrix

The orientation matrix T in the above derivations, also known as the transformation or rotation matrix, is described by the Euler angles in this work. All the rotations are on right-handed Cartesian coordinates and anticlockwise, so correspondingly, there are three rotation matrices (T_1, T_2, T_3). A general orientation can be written as $T = T_3 T_2 T_1$. An example of the stress/strain transformation with a rotation around the *z*-axis in the Cartesian coordinates can be written as

$$\begin{Bmatrix}\sigma_{11}\\ \sigma_{22}\\ \sigma_{33}\\ \tau_{23}\\ \tau_{13}\\ \tau_{12}\end{Bmatrix}=T_z\begin{Bmatrix}\sigma_{xx}\\ \sigma_{yy}\\ \sigma_{zz}\\ \tau_{yz}\\ \tau_{xz}\\ \tau_{xy}\end{Bmatrix} \quad \text{and} \quad \begin{Bmatrix}\varepsilon_{11}\\ \varepsilon_{22}\\ \varepsilon_{33}\\ 1/2\gamma_{23}\\ 1/2\gamma_{13}\\ 1/2\gamma_{12}\end{Bmatrix}=T_z\begin{Bmatrix}\varepsilon_{xx}\\ \varepsilon_{yy}\\ \varepsilon_{zz}\\ 1/2\gamma_{yz}\\ 1/2\gamma_{xz}\\ 1/2\gamma_{xy}\end{Bmatrix} \tag{4.18}$$

$$T_z=\begin{bmatrix}\cos^2\psi & \sin^2\psi & 0 & 0 & 0 & 2\sin\psi\cos\psi\\ \sin^2\psi & \cos^2\psi & 0 & 0 & 0 & -2\sin\psi\cos\psi\\ 0 & 0 & 1 & 0 & 0 & 0\\ 0 & 0 & 0 & \cos\psi & -\sin\psi & 0\\ 0 & 0 & 0 & \sin\psi & \cos\psi & 0\\ -\sin\psi\cos\psi & \sin\psi\cos\psi & 0 & 0 & 0 & \cos^2\psi-\sin^2\psi\end{bmatrix}$$

where ψ is the rotation angle around the *z*-axis. Note that for strain transformation, all the components are mathematical strains. To be consistent with the constitutive law where all the components are engineering strains, the corresponding rotation matrices for engineering strain need to be determined. Suppose an engineering-tensor interchange matrix *R* is defined:

$$R=\begin{bmatrix}1&0&0&0&0&0\\ 0&1&0&0&0&0\\ 0&0&1&0&0&0\\ 0&0&0&2&0&0\\ 0&0&0&0&2&0\\ 0&0&0&0&0&2\end{bmatrix} \qquad \begin{Bmatrix}\varepsilon_{xx}\\ \varepsilon_{yy}\\ \varepsilon_{zz}\\ \gamma_{yz}\\ \gamma_{xz}\\ \gamma_{xy}\end{Bmatrix}=R\begin{Bmatrix}\varepsilon_{xx}\\ \varepsilon_{yy}\\ \varepsilon_{zz}\\ \varepsilon_{yz}\\ \varepsilon_{xz}\\ \varepsilon_{xy}\end{Bmatrix}=R\begin{Bmatrix}\varepsilon_{xx}\\ \varepsilon_{yy}\\ \varepsilon_{zz}\\ 1/2\gamma_{yz}\\ 1/2\gamma_{xz}\\ 1/2\gamma_{xy}\end{Bmatrix} \tag{4.19}$$

The rotation matrix *T* for the engineering strain can be determined in the following way

$$\begin{Bmatrix}\varepsilon_{11}\\ \varepsilon_{22}\\ \varepsilon_{33}\\ \gamma_{23}\\ \gamma_{13}\\ \gamma_{12}\end{Bmatrix}=R\begin{Bmatrix}\varepsilon_{11}\\ \varepsilon_{22}\\ \varepsilon_{33}\\ 1/2\gamma_{23}\\ 1/2\gamma_{13}\\ 1/2\gamma_{12}\end{Bmatrix}=RT\begin{Bmatrix}\varepsilon_{xx}\\ \varepsilon_{yy}\\ \varepsilon_{zz}\\ 1/2\gamma_{yz}\\ 1/2\gamma_{xz}\\ 1/2\gamma_{xy}\end{Bmatrix}=R\cdot T\cdot R^{-1}\begin{Bmatrix}\varepsilon_{xx}\\ \varepsilon_{yy}\\ \varepsilon_{zz}\\ \gamma_{yz}\\ \gamma_{xz}\\ \gamma_{xy}\end{Bmatrix}=T^{-T}\begin{Bmatrix}\varepsilon_{xx}\\ \varepsilon_{yy}\\ \varepsilon_{zz}\\ \gamma_{yz}\\ \gamma_{xz}\\ \gamma_{xy}\end{Bmatrix} \tag{4.20}$$

Therefore for an anticlockwise transformation, the stress is transformed by T but the strain needs to be transformed by T^{-T}.

4.3.2. Model of plasticity

During macroscopic plastic deformation, incompatible plastic mismatch strains accumulate between grains, i.e. $\varepsilon^{ta} \neq 0$ in Eq. (4.16). Kroner [130], Budiansky and Wu [131] have expressed the mismatch between each grain and the surrounding matrix as (in incremental form)

$$\Delta\varepsilon^{ta} = \Delta\varepsilon^{p} - T^{-T}\Delta E^{p} \tag{4.21}$$

where $\Delta\varepsilon^{p}$ is the plastic strain increment in an individual grain determined by Eq. (4.1) with respect to the local co-ordinate system and ΔE^{p} is the macroscopic plastic strain increment of the bulk polycrystal with respect to the global co-ordinate system, which can be determined from the plastic strain increments in all the grains of the polycrystal with the virtual work principle (see section 4.3.3). As a result, ε^{t*} in Eq. (4.16) cannot be solved as an explicit function of σ. Instead, it can be solved as a function of ε^{ta} during macroscopic unloading ($\sigma = 0$), where

$$\Delta\varepsilon^{ta} = \left[C^{a} L^{i} \left(I - S^{i} \right) + S^{i} \right] \Delta\varepsilon^{t*} \tag{4.22}$$

Further, this is then used to derive the change of the intragranular residual stress and the elastic strain field ($\Delta X^{a}, \Delta\varepsilon_{r}^{e}$), defined with respect to the local co-ordinate system.

$$\Delta X^{a} = L^{i} \left(S^{i} - I \right) \left[C^{a} L^{i} \left(I - S^{i} \right) + S^{i} \right]^{-1} \Delta\varepsilon^{ta} \tag{4.23a}$$

$$\Delta\varepsilon_{r}^{e} = C^{a} \Delta X^{a} \tag{4.23b}$$

The intragranular residual stress ΔX^{a}, according to the definition in section 2.2.3, is a Type II internal stress. Finally, the total stress in each grain during plastic deformation is updated by

the combined contribution from the applied stress increment (by Eq. (4.17a)) and from the accumulation of residual stress (by Eq. (4.23a)) at each step.

$$\Delta\sigma^a = H^a T \Delta\sigma + \Delta X^a \tag{4.24}$$

Eqs. (4.3) and (4.24) then update the RSS at each step.

4.3.3. Aggregate behaviour

The aggregate behaviour here consists of two parts, respectively the determination of the initially unknown isotropic stiffness tensor L^i and the macroscopic plastic strain increment in Eq. (4.21) by the volume average method [140].

Consider a polycrystal which is subjected to a small macroscopic total strain increment ΔE (with elastic part ΔE^e and plastic part ΔE^p). The principle of virtual work states that the work done by any virtual external stress Σ^* on the polycrystal is equal to the volume average of the work done by all the individual grains

$$\Sigma^* \Delta E = \frac{1}{V}\int_V \sigma^* \Delta\varepsilon dV \tag{4.25}$$

where V is the volume of the polycrystal, σ^* is the virtual grain stress in equilibrium with Σ^* and $\Delta\varepsilon$ is the grain strain increment, which is compatible with ΔE. During elastic deformation, consider a uniform virtual stress field $\Sigma^* = \sigma^*$. Combined with Eq. (4.17b), Eq. (4.25) can be expressed as

$$\Delta E = \frac{1}{V}\int_V \Delta\varepsilon dV = \frac{1}{V}\int_V K^a T dV \cdot \Delta\sigma \tag{4.26}$$

Since $\Delta E = C^i \Delta\sigma$ and the isotropic elastic compliance matrix C^i for the polycrystal is contained in K^a, C^i can be determined by iteration. During plastic deformation, consider the case where there is no external stress, thus only the macroscopic plastic strain part exists for

the polycrystal. However, we will expect a microscopic distribution of residual elastic strain $\Delta\varepsilon^e$ and residual stress ΔX^a. Therefore, Eq. (4.25) becomes

$$\Sigma^* \Delta E^p = \frac{1}{V}\int_V \sigma^* (\Delta\varepsilon^e + \Delta\varepsilon^p) dV = \frac{1}{V}\int_V \sigma^* C^a \Delta X^a dV + \frac{1}{V}\int_V \sigma^* \Delta\varepsilon^p dV \quad (4.27)$$

Due to the symmetry of the compliance matrix C^a for a F.C.C. single grain, the first integral in Eq. (4.27) can be rearranged into

$$\frac{1}{V}\int_V \sigma^* C^a \Delta X^a dV = \frac{1}{V}\int_V \Delta X^a \varepsilon^* dV \quad (4.28)$$

where $\varepsilon^* = C^a \sigma^*$ is the grain strain caused by the virtual stress σ^*. If σ^* is obtained from the elastic problem by Eq. (4.17a), $\sigma^* = H^a T \Sigma^*$, ε^* is compatible. Therefore, the residual stress ΔX^a in Eq. (4.28) can be regarded as in equilibrium with zero external stress, i.e. Eq. (4.28) is equal to zero. As a result, only the second integral in Eq. (4.27) needs to be considered

$$\Sigma^* \Delta E^p = \frac{1}{V}\int_V \sigma^* \Delta\varepsilon^p dV \quad (4.29)$$

The explicit expression of ΔE^p can be obtained by choosing a simple form of Σ^*. For example, for the component of ΔE^p_{11}, we can choose a unit virtual stress along the "11" direction, $\Sigma^* = [1,0,0,0,0,0]^T$. Therefore

$$\Delta E^p_{11} = \frac{1}{V}\int_V \frac{H^a T \Sigma^*}{\Sigma^*_{11}} \Delta\varepsilon^p dV = \frac{1}{V}\int_V H^a T \Sigma^* \Delta\varepsilon^p dV \quad (4.30)$$

All the other components can be determined using a similar method.

4.4. Summary

This chapter extends the established athermal physical dislocation link length model described in Chapter 3 into a crystal based plasticity framework for each individual grain

within the polycrystalline aggregate. The plastic strain increment of individual grains is obtained by adding all the shear strain increments on all the active slip systems.

Further, the self-consistent scheme captures the interaction between slip planes (self- and latent hardening) and that between each individual grain and the surrounding isotropic matrix (mismatch). Intragranular residual stress accumulates in each grain as the mismatch develops during plastic deformation. The behaviour of the bulk polycrystalline aggregate is determined from the volume average of all the randomly distributed grains of the polycrystal by the virtual work principle.

The combination of Chapter 3 and Chapter 4 constitutes a complete athermal deformation model for polycrystalline materials. A summary of all the key equations in this chapter is given below, followed by a flowchart (Figure 4.2) of the calculation procedure of the comprehensive athermal model.

(1) Overall Type III micro-scale internal stress on individual slip systems taking into account the influence from the Type III internal stress on all the other slip systems

$$\left(\overline{\tau}_m^r\right)^\beta = \left[sym\left(\overline{n}^\beta \otimes \overline{s}^\beta\right)\right]^T \cdot \sum_{\beta=1}^{12}\left(\tau_m^r\right)^\beta sym\left(\overline{n}^\beta \otimes \overline{s}^\beta\right)$$

(2) Plastic shear strain increment of individual slip systems

$$\Delta\gamma^\beta = \Delta\gamma_0 \left| \frac{\tau^\beta + \left(\overline{\tau}_m^r\right)^\beta}{\tau_{cr}^\beta} \right|^p \operatorname{sgn}\left(\tau^\beta + \left(\overline{\tau}_m^r\right)^\beta\right)$$

(3) Relationship between the resolved shear stress (RSS) on individual slip systems and the total stress within the same grain

$$\tau^\beta = \left[sym\left(\overline{n}^\beta \otimes \overline{s}^\beta\right)\right]^T \sigma^a$$

(4) Plastic strain increment of individual grains

$$\Delta\varepsilon^p = \sum_{\beta}^{12} \Delta\gamma^\beta sym(\bar{n}^\beta \otimes \bar{s}^\beta)$$

(5) Total elastic response of individual grains during elastic deformation

$$\sigma^a = \left\{ \left\{ \left[I - \left(S^i\right)^{-1} \right]^{-1} C^i - C^a \right\}^{-1} \left(C^a - C^i\right) + I \right\} T\sigma = H^a T\sigma$$

$$\varepsilon^a = \left\{ C^i + \left\{ \left(C^a - C^i\right)^{-1} C^a L^i \left(S^i\right)^{-1} - L^i \right\}^{-1} \right\} T\sigma = K^a T\sigma$$

(6) Type II meso-scale internal stress increment and its contribution to the total grain stress during plasticity

$$\begin{aligned} \Delta X^a &= L^i \left(S^i - I\right) \left[C^a L^i \left(I - S^i\right) + S^i \right]^{-1} \Delta\varepsilon^{ta} \\ &= L^i \left(S^i - I\right) \left[C^a L^i \left(I - S^i\right) + S^i \right]^{-1} \left(\Delta\varepsilon^p - T^{-T} \Delta E^p\right) \end{aligned}$$

$$\Delta\sigma^a = H^a T\Delta\sigma + \Delta X^a$$

(7) Aggregate behaviour of the whole polycrystal

$$\Delta E = \frac{1}{V} \int_V \Delta\varepsilon dV = C^i \Delta\sigma \qquad \text{(elasticity)}$$

$$\Sigma^* \Delta E^p = \frac{1}{V} \int_V \sigma^* \Delta\varepsilon^p dV \qquad \text{(plasticity)}$$

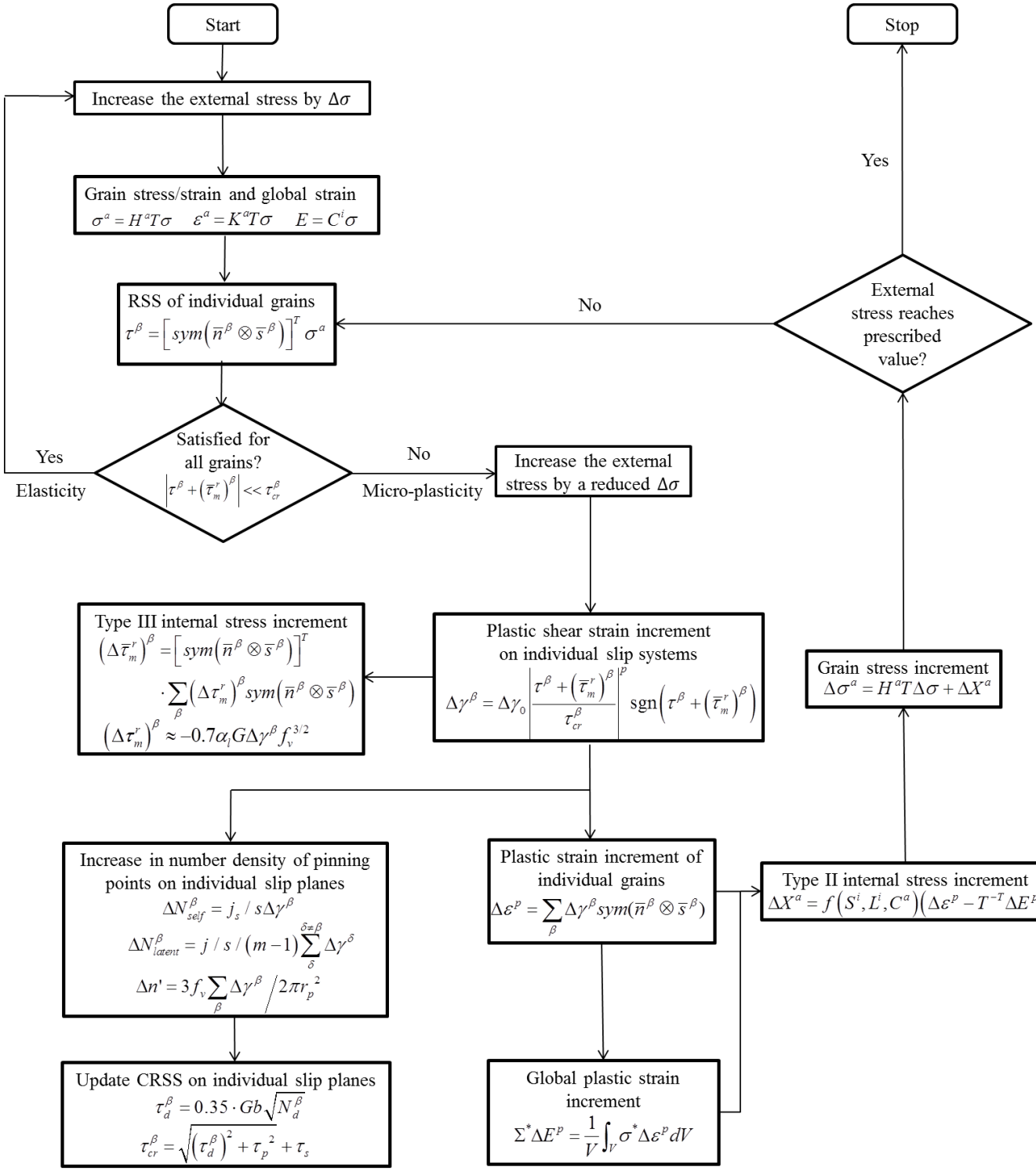

Fig. 4.2. Flowchart of the implementation procedure of the athermal model

Chapter 5

Application I: Self-consistent modelling for the evaluation of lattice response of austenitic stainless steel during time-independent plastic deformation

5.1. Introduction

In recent years, the advanced non-destructive, time-of-flight neutron diffraction (ND) technique has been extensively used to measure the *in situ* evolution of micro-scale lattice strains for different subsets of grains within a range of polycrystalline materials during macroscopic deformation [97, 98, 133, 138, 141, 142]. It captures the change of spacing of lattice planes, thus measuring the elastic response, whose evolution depends on the micro-plastic response of each grain. At the same time, many constitutive models and/or finite element analysis have been used [97, 98, 141] to simulate the relationship between the behaviour of individual grains and that of the polycrystalline aggregate to predict and understand the micro-scale behaviour of such materials. However, to date, no previous studies have systematically compared the model prediction with micro-scale ND measurements to identify the dominant lattice deformation mechanisms. In addition, none of these models have considered the detailed hardening mechanism associated with different microstructure elements.

This chapter applies the athermal multi-scale self-consistent model established in Chapters 3 and 4 to evaluate the macroscopic behaviour and microscopic lattice deformation of Type 316H F.C.C. polycrystalline austenitic stainless steel under uniaxial loading at ambient temperature. Principal focus is on how the change in Type II and/or Type III internal/residual

stress fields influences the microscopic lattice response and/or the macroscopic behaviour. Availability of the data measured by *in situ* neutron diffraction offers the opportunity to identify the most appropriate form of the constitutive relationship for the individual grains. The application of the model towards the athermal deformation behaviour is the foundation and pre-requisite of the further application on creep deformation behaviour of the material, which is to be presented in detail in Chapter 7.

5.2. Neutron diffraction experiment

The neutron diffraction experiments on Type 316H stainless steels were conducted with Dr Bo Chen as part of the collaboration with University of Bristol.

5.2.1. Sample description

The material of interest is an ex-service Type 316H F.C.C. austenitic stainless steel supplied by EDF Energy with a typical chemical composition or solute concentration given in Table 5.1. The thermal-mechanical history of this material includes in-service operation of 65,015 h exposed at temperatures between 490 ℃ and 530 ℃ and an additional thermal ageing at 550 ℃ for 22,100 h. The grain size for this material was measured to be 87±9 μm. Both inter- and intra-granular $M_{23}C_6$ carbide precipitates were present in this thermally aged material but their size and volume fraction were unknown. Based on some relevant simulation and experimental work [36, 143, 144], the mean size (radius of equivalent spherical particles) and volume fraction of intragranular particles are estimated to be 60 nm and 0.009, while those of intergranular particles (mainly carbides) are ignored since they do not disturb dislocation motion within the matrix. The very small volume fraction of precipitates indicates that the material is essentially a single phase F.C.C. polycrystalline

stainless steel. The three anisotropic elastic constants C_{11}, C_{12} and C_{44} of a single F.C.C. crystal of Type 316H stainless steel are listed in Table 5.2 (the alternative parameters E, ν and G represent Young's modulus, Poisson's ratio and shear modulus), with respect to the local co-ordinate system. The texture of similar specimens has been measured to be weak (a near random distribution of grain orientations [137, 138].

A symbol "EXLA" is used to describe the "Ex-service plus Laboratory Aged" material. The experiment consisted of two parts, involving two different groups of specimens. The first group was the original as-received specimens, designated EXLA1. This group was simply subjected to uniaxial tensile loading at ambient temperature in the first part of the experiment to measure and evaluate different lattice responses both parallel (axial) and perpendicular (radial) to the loading direction. Further, the second group referred to the same as-received specimens, designated EXLA2, but with some prescribed residual stress field by initially pre-straining the specimens at 550^{o}C up to a true stress of 250 MPa and then cooled and unloaded. This group was subjected to either uniaxial tensile loading (corresponding specimens designated EXLA2-1) or uniaxial compressive loading (corresponding specimens designated EXLA2-2) at ambient temperature in the second part of the experiment to assess the effect of deformation history on the subsequent macroscopic behaviour and microscopic lattice response parallel (axial) to the loading direction. A particular interest of the second part of the experiment is the macroscopic Bauschinger effect and the associated micro-plasticity.

Tab. 5.1. Chemical composition (wt.%) of Type 316H stainless steel

C	Si	Mn	P	S	Cr	Mo	Ni	Cu	N	Fe
0.07	0.61	1.65	0.025	0.007	16.6	2.33	13.6	0.26	0.025	Bal.

5.2.2. *In situ* measurement

The macroscopic deformation data employed in this chapter was generated using a strain gauge and the load cell on the loading rig, while the microscopic data was generated using the neutron diffraction (ND) technique, with measurements of the lattice response of this material subjected to uniaxial tensile loading obtained from experiments conducted on either the ENGIN-X instrument at ISIS, UK [98, 141, 145] or at Los Alamos National Laboratory, USA [97, 133, 138], while measurements of the material subjected to uniaxial compressive loading were obtained from experiments conducted on POLDI at SLS, Switzerland [146]. The experiment is introduced briefly below. For the detailed description of the experimental procedure, one can refer to [97, 98, 133, 138, 141, 145, 146].

Figure 5.1 illustrates and compares schematically the experimental setup of the *in situ* uniaxial tension and compression tests at ambient temperature [146]. Each group of specimens was loaded at a constant strain rate. The neutron diffraction technique measures the changes in the lattice spacing compared with the stress-free lattice spacing of different crystallographic planes with Miller indices {*hkl*}, which can be transformed into the changes of elastic lattice strain.

$$\varepsilon_{hkl} = \frac{d_{hkl} - d_{hkl}^{0}}{d_{hkl}^{0}} \tag{5.1}$$

where ε_{hkl} is the elastic lattice strain for the {*hkl*} planes, d_{hkl} is the current lattice spacing under a stressed condition and d_{hkl}^{0} is the stress-free lattice spacing. Each ND measurement represents the average value within each oriented grain family such that the members in the family have planes with the same Miller indices {*hkl*} diffracting to the detector (Figure 5.2a). The gauge volume used in the experiment ensured enough intensity for each collection. Since the neutron diffractometer is based on the concept of time-of-flight, many diffraction peaks can be measured simultaneously [147]. A typical measurement of different diffraction peaks

of each specimen is shown in Figure 5.2(b). Based on this, in the present work, we focus on the evaluation of data on three typical grain families, respectively {220}, {111} and {200}.

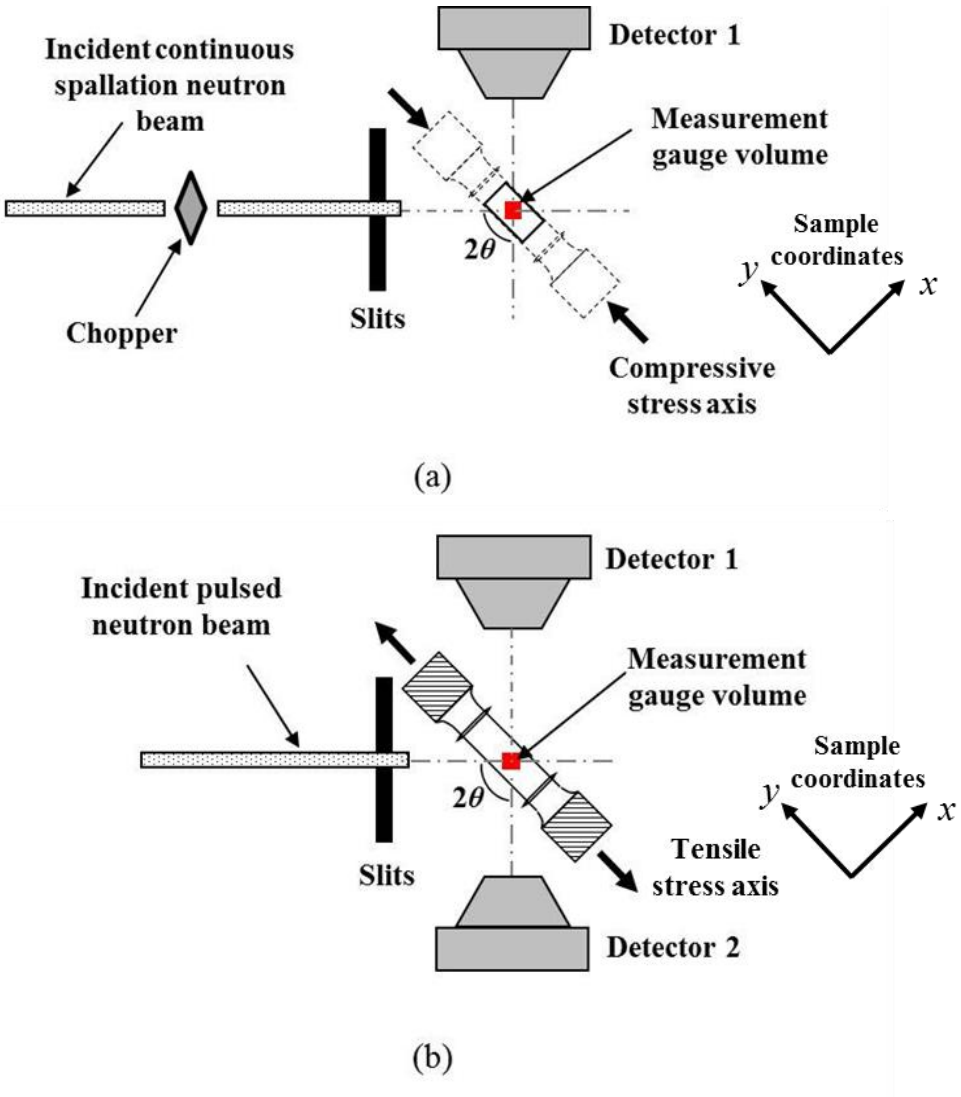

Fig. 5.1. Arrangement of the stainless steel specimens in the neutron diffraction instruments to measure the lattice strains of different subsets of grains within the gauge volume, between the incident and the diffracted beams: (a) *in-situ* compressive tests; (b) *in-situ* tensile tests. Two detectors in (b) allow the measurement of both axial (parallel, *y*-axis of the sample coordinate system) and radial (perpendicular, *x*-axis of the sample coordinate system) response with respect to the loading direction, while (a) only measures the axial (parallel) response. The figure is obtained from [146]

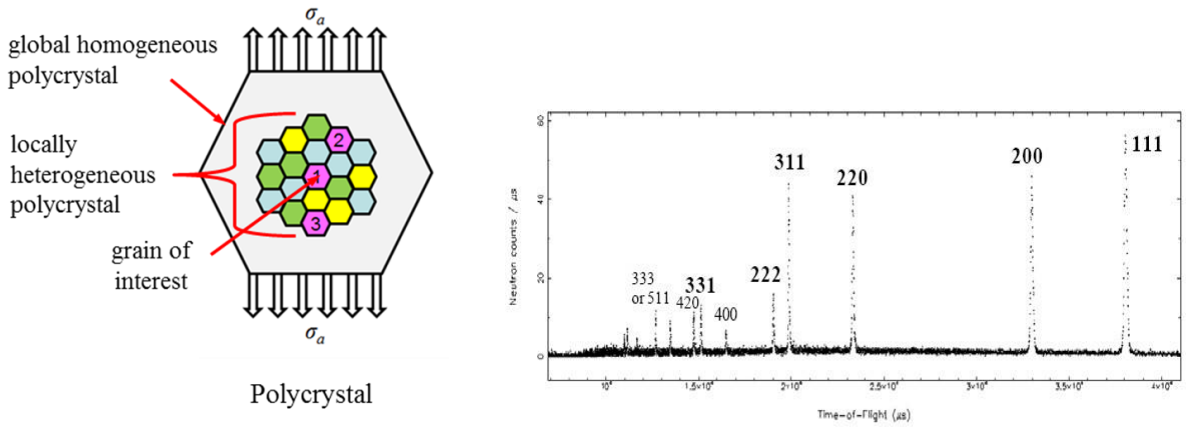

Fig. 5.2. (a) Arrangement of individual grains (1, 2 and 3) which exhibit the same crystallographic orientation in a locally heterogeneous polycrystal where an external stress, σ_a, was applied to the material. (b) A typical measurement of different diffraction peaks of each specimen [145].

Note that the applied loading direction in Figure 5.1 differs from the incident beam by 45^o, which allows a simultaneous collection of elastic lattice strains both parallel (axial) and perpendicular (radial) to the loading direction by the two detectors (detector 1 for axial and 2 for radial, Figure 5.1a) in the uniaxial tension test. However, in the uniaxial compression test, due to the limitation of the instrument, only one detector was applicable, measuring only the axial response (Figure 5.1b). An extensometer was attached to each specimen to measure the macroscopic strain of the whole polycrystalline material.

An incremental loading history was used in the experiments with alternative loading and unloading steps [97, 98, 138, 145, 146]. Use of these loading histories ensured the measurement of both the elastic lattice strain during loading and residual elastic lattice strain after unloading. Figure 5.3 shows a typical incremental tensile loading history.

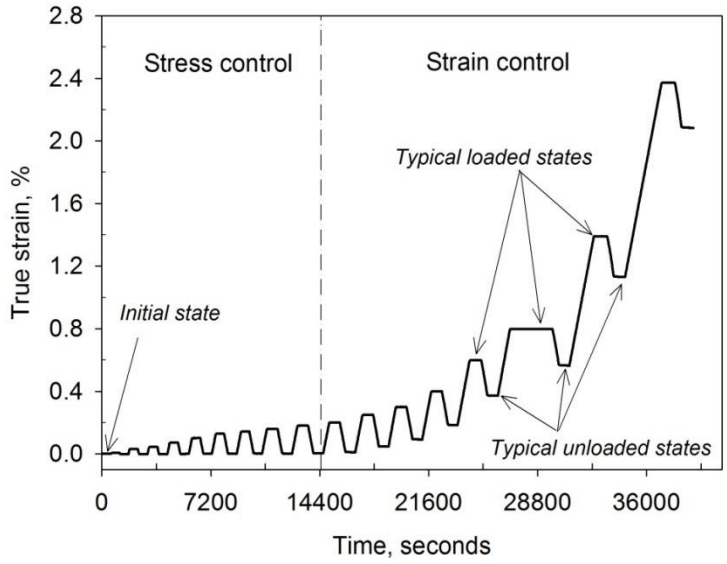

Fig. 5.3. An incremental tensile loading history at ambient temperature, consisting of alternative loading and unloading steps. Change from stress control to strain control in the experiment is because of the onset of macroscopic plastic deformation

5.3. Simulation procedure of as-received specimen

In the simulation in this chapter, we first present the procedure and corresponding results and evaluation of as-received specimens (EXLA1), while those of pre-strained specimens (EXLA2) are to be presented later. In the first part of the simulation for as-received specimens EXLA1, the external stress was increased from zero in small increments, with different increments employed during elastic and elastoplastic deformation. A sensitivity study has been conducted (not shown here) on the effect of different numbers of randomly oriented grains as representative for the whole polycrystalline material, with each orientation matrix (function of Euler angles) generated by Matlab. The results show that a selection of 100 randomly oriented grains can be reasonably efficient in calculation without losing too much accuracy in the matrix homogenization. Further, note that individual subset of grains with specific orientation (e.g. {220}, {111} or {200}) was implemented and simulated separately from the 100 representative grains, but the interaction with neighbouring matrix (composed by the 100 grains) remains the same for each individual grain. For each subset of

grains contributing to the axial (radial) response, all the members have a given common orientation parallel (perpendicular) to the loading axis but are randomly oriented with respect to other directions, thus each subset possesses almost a transversely isotropic elastic property. 12 symmetrically oriented grains were selected to represent each subset of grains.

Initially, all slip planes for all representative grains within the polycrystalline material (as well as the specific subset of grains of interest) were assumed to have identical distribution of dislocation links and other microstructure elements, thus with identical critical resolved shear strength (CRSS) on all the slip systems. At each step, the stress in each individual grain was updated using Eq. (4.17a) and the plastic strain increment calculated using Eqs. (4.1) and (4.2). The macroscopic plastic strain increment for the polycrystal was then obtained using the virtual work procedure described in section 4.3.3. The development of this incompatible plastic strain field results in a change in the intragranular residual stress or Type II internal stress field. This was calculated using Eq. (4.23a), allowing the further update of the total intragranular stress with Eq. (4.24). During plastic deformation, the dislocation link length distributions on the slip planes of each grain were updated using Eqs. (3.1), (3.6) and (3.7) and the CRSS was updated using Eqs. (3.6), (3.7) and (3.26). The accumulation of plastic shear strain on active slip systems results in the development of the Type III internal stress originated from the prismatic dislocation loops surrounding precipitates, which was calculated by Eqs. (3.21) and (4.5). This process was repeated until the maximum stress level achieved in the experiments was reached.

The values of the physical parameters used in the simulations are shown in Table 5.2. Three parameters (the initial number of pinning points on each slip plane N_0, the self-hardening coefficient j_s/s and the latent hardening coefficient j/s) were selected to provide the correct macroscopic stress-strain curve shown in Figure 5.4. Measurements from different researchers are shown in the figure. All other parameters were determined from geometric or

physical requirements. For the athermal precipitation strengthening described in Eq. (2.15), the mean inter-particle spacing L_p was calculated by the estimated volume fraction (0.009, equal to the area fraction as illustrated in Eq. (3.11)) and mean size (60 nm, radius of equivalent spherical particles) using Eq. (3.10). $\tau_p \approx 21$ MPa was then obtained. For the athermal solute strengthening described in Eq. (3.24), α_s has been estimated to be 0.000457 for austenitic stainless steels by taking into account the size misfit between impurity atoms and matrix atoms and the associated maximum force a single solute atom exerts on the dislocation [33]. $\tau_s \approx 37$ MPa was then obtained by taking all the solute elements in Table 5.1 as obstacles to dislocation motion. Depletion of solute atoms and the associated reduction of athermal solute strengthening by the limited precipitation in the material have been found to be negligible. The resulting model was then used to predict the evolution of the microscopic lattice strain and residual lattice strain during uniaxial tensile loading at ambient temperature.

Note that in Figure 5.4, the macroscopic stress-strain curves measured by different groups are similar, except for the curve from [98], which is lower than other curves. Such difference from other groups has also been reflected in the measurement of lattice strain, which will be shown and discussed later. Here we have calibrated our model (tuned the three fitting parameters) on the majority of macroscopic stress-strain data (Figure 5.4).

Tab. 5.2 Material parameters of 316H austenitic stainless steels used in the simulation

Parameter	Value	Parameter	Value
C_{11} [a]	198 GPa	$\Delta\gamma_0$	1
C_{12} [a]	125 GPa	p	600
C_{44} [a]	122 GPa	α_d	0.35
E	101.3 GPa	j_s/s	4.0×10^{14}
v	0.39	j/s	2.0×10^{15}
G	122 GPa	N_0	2.4×10^{13}
b	2.5×10^{-10} m	τ_s	37 MPa
		τ_p	21 MPa

[a] Data are taken from Kamaya [148]

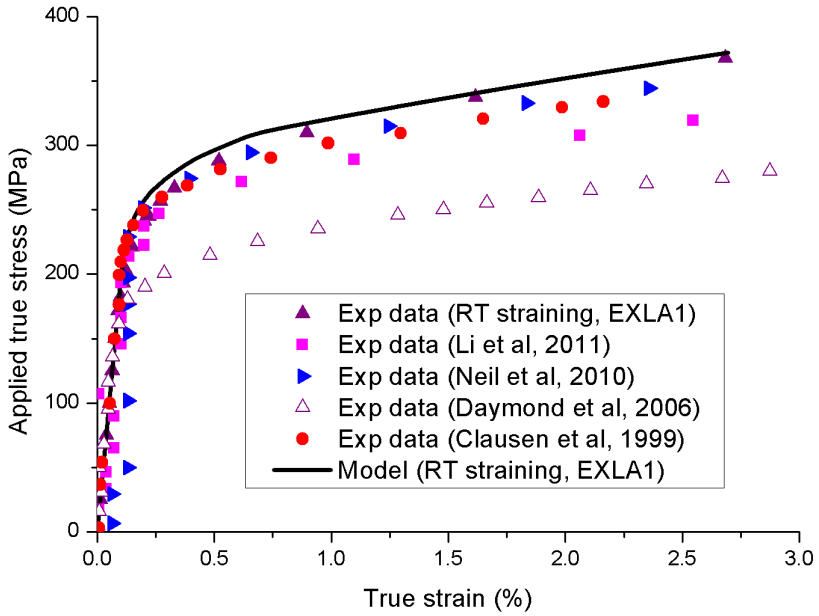

Fig. 5.4. Measured and simulated macroscopic polycrystal stress-strain response of Type 316H austenitic stainless steel subjected to uniaxial tension at room temperature (RT) for EXLA1 specimens.

5.4. Measurement and prediction of as-received specimen

5.4.1. Lattice response along axial direction

Figure 5.5 compares the measured and predicted results of the total lattice strain and the corresponding residual lattice strain evolution for the three grain families, {220}, {111} and {200}, parallel to the loading direction (axial response, corresponding to the *y*-axis of the sample co-ordinate system in Figure 5.1b). The residual lattice strain is plotted against the macroscopic plastic strain. Measurements from different researchers are also shown in the figure. The model prediction in Figure 5.5 is for the response averaged across all members of a given grain family, i.e. those grains with the corresponding crystallographic plane normal to the loading axis. However, the measured response is averaged over a wider range of grains, which will be examined and discussed later. The general trends for all the grain families observed in the experiment are predicted by the model. Simulation in which we ignore the contribution from the precipitates predict almost the same results [149], indicating an insignificant contribution from the small volume fraction of precipitates for this specimen.

Different subsets of grains show a linearly increasing lattice strain followed by a nonlinear response, especially in the {220} and {200} grain families (lattice response of {111} grain family is observed to be essentially linear). Note that the lattice response of {200} grain family measured by Daymond and Bouchard [98] exhibits an earlier occurrence of nonlinearity (lattice response of {220} grain family is not available in their paper). Since transitions or deviation from linearity indicate the occurrence of micro-yielding, which can be correlated with the evolution of the residual lattice strain, this will be discussed in the next section. Despite the general trend, however, the model predicts that all members of each grain family demonstrate an identical lattice response, especially the same plastic strain along the loading direction, indicating no variation about the average. This is due to the symmetry of the members of each grain family with respect to the loading direction. As a result, the measurements are, to some extent, independent of which grains within the family are sampled in the experiments. There is, however, some variations in ND measurements along the axial (loading) direction obtained by different groups.

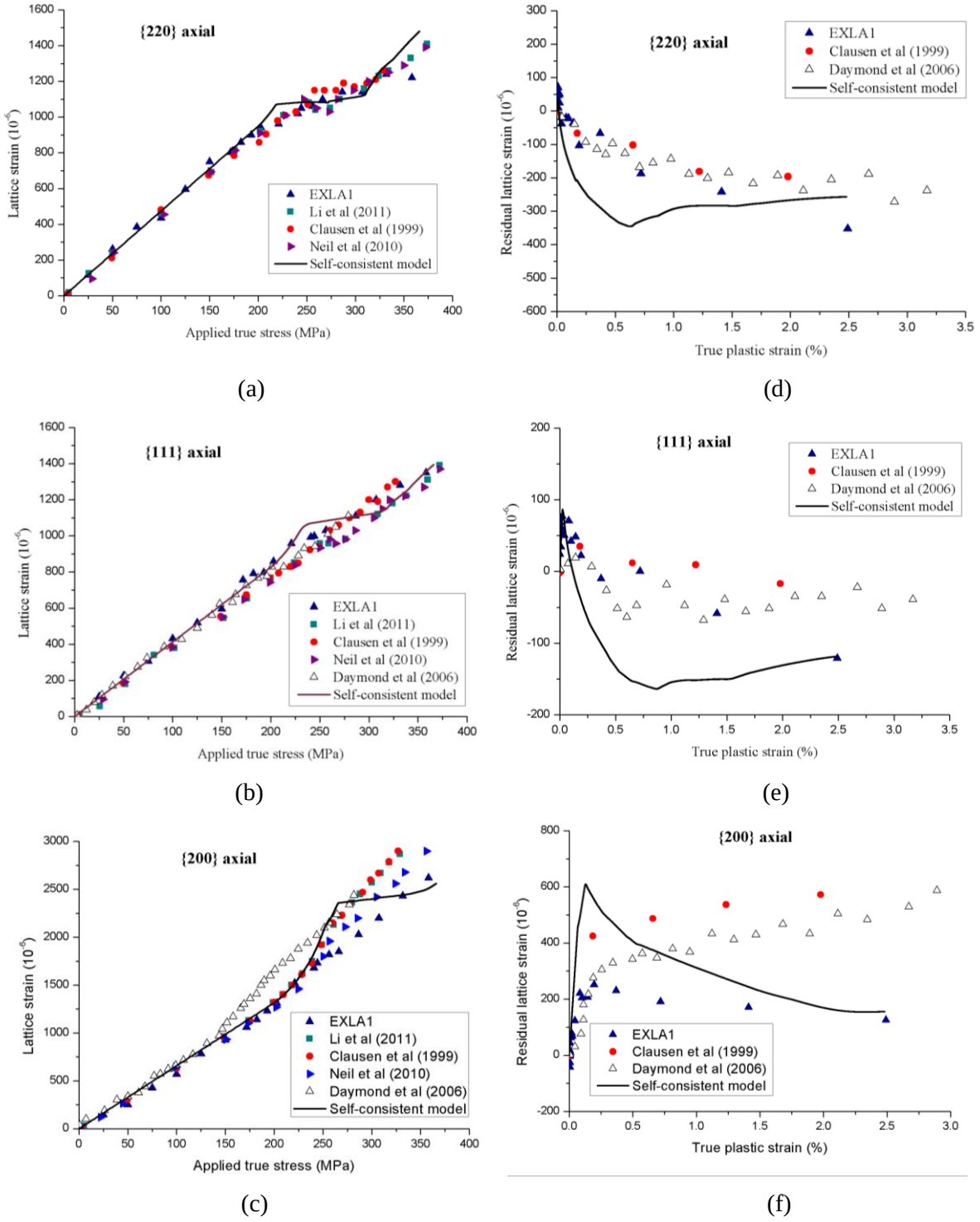

Fig. 5.5. Measured and predicted averaged results of lattice strain and residual lattice strain evolution along the *axial* direction (*y*-axis of the sample co-ordinate system in Fig. 5.1b): (a) and (d) {220} grain family lattice strain and residual lattice strain; (b) and (e) {111} grain family lattice strain and residual lattice strain; (c) and (f) {200} grain family lattice strain and residual lattice strain. Data was measured by different investigators for the same grain family within the same polycrystalline materials. The residual lattice strain is plotted against the macroscopic true plastic strain measured by the strain gauge at each unloading step.

Compared with the model prediction, the experimental data for all the grain families shown in Figure 5.5 demonstrates smoother transitions in the slope. This may be explained in three aspects. Firstly, the model does not take into account the effect of the orientation of neighbouring grains, which has been discussed by Clausen [97]; it takes the average response of all possible neighbours. Secondly, the model has assumed an initial zero residual stress state for each individual grain. In practice, non-identical and asymmetric residual stress state can exist in individual grains, introduced during processing or by some preloading and unloading histories before the specimen is tested. Thirdly, to provide a sufficient presentation or neutron density of each reflection plane within the gauge volume used in the experiment, in reality, the detector (Figure 5.1b) measures a range of grains across a slight spread of the orientation, i.e. those grains with the plane normal slightly deviated from the measured plane normal are also counted as members of the measured grain family. Such spread of orientation may be up to ~8^{o} from the perfect alignment. In reality, the last aspect of these has been taken into account in all the previous simulations [97, 98, 133, 138, 141], which may explain why the predictions of axial lattice responses of individual grain families from these groups seem to be more successful using different constitutive models. Altogether, the above three aspects demonstrate that, in practice, members of a given grain family may not always experience the same lattice response.

We have refined the model to take into account the last two aspects described above. Note that the original predicted axial response of the {200} grain family deviates most from the experimental results (Figure 5.5), which is also reflected in the relatively larger scatter of the data. We therefore focus on this particular grain family when evaluating the effects of an initial residual stress and the spread of orientation about specified outward normal in the measurement of lattice strains. It should be emphasized that the consideration of the spread of orientation is not for simply reproducing the results shown by different groups, but we want

to highlight the effect of this factor comparing with the results shown in Fig. 9.

5.4.2. Refinement of the axial lattice response

5.4.2.1. The spread in orientation

We first consider the spread of the orientation of the {200} grain family, where the spread angle is chosen to be 8^o, which is typical of that employed experimentally. The result averaged over grains with this spread of orientations, together with the original result with perfect alignment, is shown in Figure 5.6(a) and (d), respectively for the evolution of lattice strain and residual lattice strain. The effect of considering a spread of angles is to significantly smooth any transition, with different members of the grain family yielding at different instants during the loading history. The updated results shown in Figure 5.6 (a) and (d) now have become very similar to the predictions by other researchers *[97, 98, 133, 138, 141]*.

5.4.2.2. The initial residual stress state

We now examine the effect of an initial non-zero residual stress states on the response of the {200} grain family, which are introduced by tensile or compressive preloading along different directions. Here we ignore the effect of the spread in orientations considered above; the combined effect of the two will be examined in section 5.4.2.3. Three preloading axes (PA) are chosen, 0^o, 30^o and 90^o around the *z*-axis of the sample coordinates shown in Figure 5.1(b), where 0^o preloading is the same as the original uniaxial loading while a 90^o preloading makes the axial grain family resemble a radial grain family. For each case, the polycrystal is pre-strained, either in tension or compression, to a prescribed stress within the plastic region and then unloaded. Then it is reloaded in tension along the original uniaxial direction (*y*-axis

in Figure 5.1b) with the original identical CRSS on all slip systems for all grains, i.e. we use the prior loading to only introduce a residual stress state and keep all other aspects of the model the same. An equivalent uniaxial stress of 280MPa (absolute value) is chosen for each preloading direction. The reason for selecting this value is to set up a significant residual stress in each individual grain while at the same time avoiding micro-yielding of some grains at the beginning of reloading. In order to more fully evaluate the effect of residual stress, we examine the effect of scaling the residual stress determined in this way (using a scaling factor ***S*** in the range -1 to 1). The results are shown in Figure 5.6(b) and (e), where ***PA*** refers to preloading axis. The model predicts that the variation of the initial residual stress state can shift the axial lattice response of the grain family. Note that less sharp transitions are observed for 30^o and 90^o preloading compared with 0^o preloading. This is because members in the axial grain family are not symmetric with respect to the 30^o and 90^o preloading axes, thus a non-uniform residual stress state develops during preloading, leading to non-identical responses of each member during reloading.

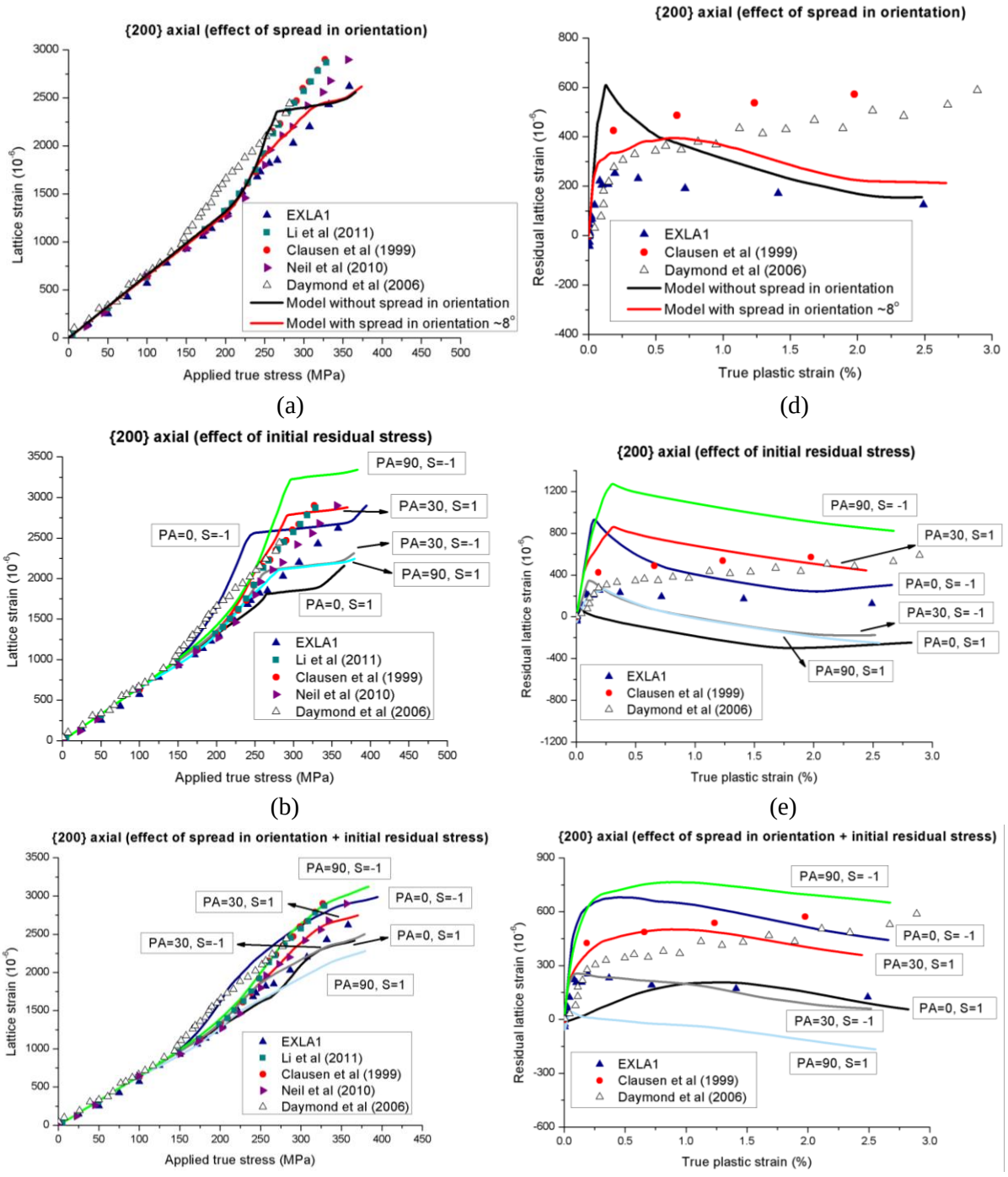

Fig. 5.6. Effect of spread in orientation and initial residual stress on the lattice response of {200} grain family along the *axial* direction of EXLA1 specimen. (a) and (d): effect of spread in orientation of outward normal to the lattice planes on the evolution of lattice strain and residual lattice strain; the spread of angle is chosen to be 8°. The original result without spread in orientation is also shown. (b) and (e): effect of initial residual stress introduced by preloading along different directions on the evolution of lattice strain and residual lattice strain. Within the labels, **PA** refers to preloading axis and **S** refers to scale. The maximum value of preloading is equivalent to uniaxial 280MPa. For simplicity, only one source of data is shown. (c) and (f): combined effect of initial residual stress and spread in orientation on the evolution of lattice strain and residual lattice strain. The setting of spread angle and initial residual stress remains the same.

5.4.2.3. The combined effect of initial residual stress and spread in orientation

Here we examine the combined effects of initial residual stress and spread of orientation of outward normal to the lattice planes. The predicted results are shown in Figure 5.6(c) and (f), where the spread and initial residual stress conditions remain the same as above. Features of both shifting and smoothing of the axial response are observed and the results cover the full spread of experimental data with the experimental results of different investigators explained in terms of different initial internal residual stress fields. Taking the data of the {200} axial grain family of EXLA1 specimen as an example, it is found that a spread angle of 8^o plus 30^o compressive preloading gives the closest match to the data. Here we have evaluated the effect of a residual stress on the lattice strain, but it can also influence the detailed form of the global stress-strain curve. Since parameters within the model were determined by fitting the uniaxial response, we need to examine whether the presence of residual stresses changes the quality of the fit. Figure 5.7 shows the refined global stress-strain curve taking into account the effect of the residual stress. The quality of the fit is similar to that with no residual stresses.

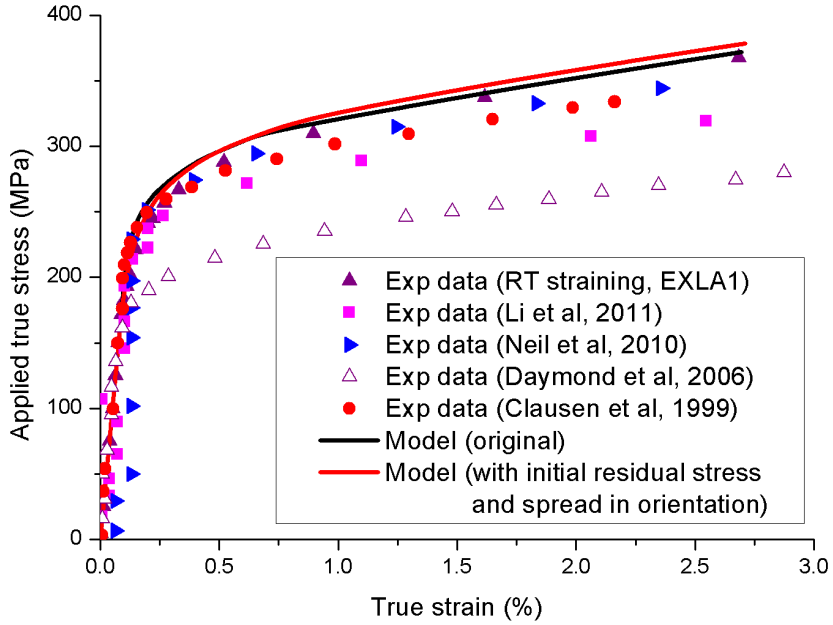

Fig. 5.7. Refined global stress-strain curve with initial residual stress field (30^{o} compressive preloading, scale=-1) and a spread angle of 8^{o}. The original fitted stress-strain curve is also shown.

5.4.3. Lattice response along radial direction

The measured and predicted evolution of lattice strain and residual lattice strain of the three grain families along the radial direction (*x*-axis of the sample co-ordinate system in Figure 5.1b) of EXLA1 specimen are plotted in Figure 5.8. In order to highlight an additional contribution to the spread in data, we do not consider a spread in orientation of lattice plane normal or the effect of an initial residual stress. Therefore, members of a given grain family considered here only refer to the grains with perfect alignment. Again, the model prediction was compared with the measurements obtained by different groups.

Compared with the axial lattice response shown in Figure 5.5, while the axial lattice response in the elastic regime is consistent between investigators (see Figure 5.5 or 5.6), large scatter or weak consistency is observed in the data along the radial direction. Such weak consistency of radial grain families has also been reflected in the poorer agreement of the predictions by different groups [97, 98, 133, 138, 141] compared with their predictions of axial grain families, although each of their analysis has considered the spread in orientations.

In reality, different from axial grain families, the model has predicted variations in the response of individual members in each radial grain family, which are presented in Figure 5.6 (a)-(c). This is because some grains which are members of a given grain family that diffract to the radial detector are not within the grain family with the same Miller indices {*hkl*} that diffract to the axial detector, i.e. the two detectors in Figure 5.1 are sampling the responses of different groups of grains. Therefore, members of each radial grain family are not symmetric with respect to the loading direction. As a result, measurement on a "family of planes" is perhaps a more appropriate term than that associated with a "family of grains". With this additional contribution, although the averaged response is smooth (members do not yield at the same time) and reasonably captures the general trend, Figure 5.8 demonstrates that: (a) there is more significant scatter in the experimental results in the elastic-plastic regime because experiments conducted by different investigators could have sampled the response of different members of a given radial grain family; and (b) the variation of the predicted response for different members of a radial grain family spans the full range of experimental data. More effort could be taken to refine the radial lattice response by considering the spread of lattice plane normal and initial residual stress to probe the appropriate initial state of each radial subset of grains, but there may be many combinations of these factors that reproduce the experimental results. However, together with the refinement in the axial family described earlier, the important messages in this work are that: care needs to be taken when explaining measurements of lattice responses on similar materials, since the two detectors are sampling different grains; and the initial state can be influential.

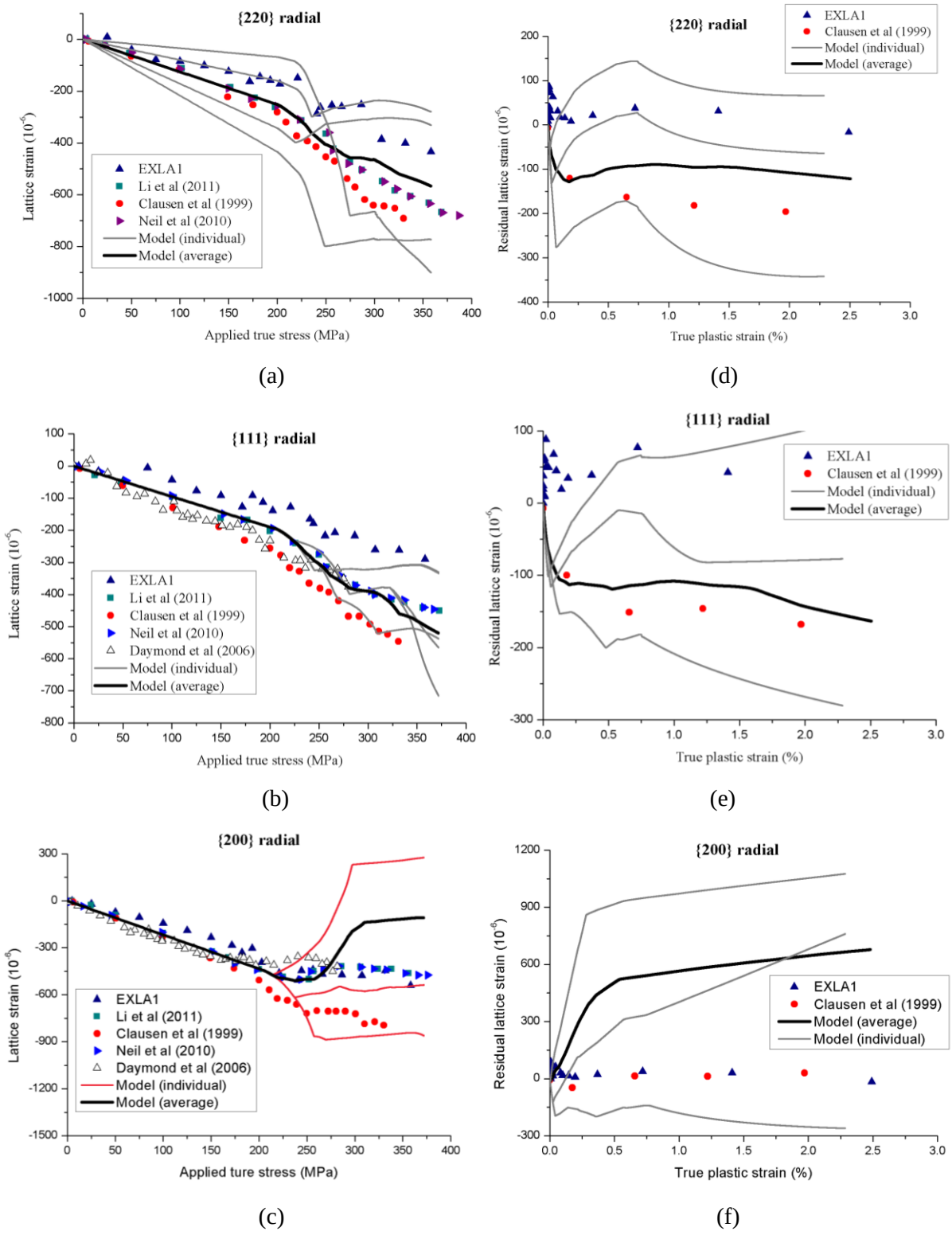

Fig. 5.8. Measured and predicted averaged results of lattice strain and residual lattice strain evolution along the *radial* direction (*x*-axis of the sample co-ordinate system in Fig. 5.1b) of EXLA1 specimen: (a) and (d) {220} grain family lattice strain and residual lattice strain; (b) and (e) {111} grain family lattice strain and residual lattice strain; (c) and (f) {200} grain family lattice strain and residual lattice strain. Data was measured by different investigators for the same grain family within the same polycrystalline materials. The residual lattice strain is plotted against the macroscopic true plastic strain measured by the strain gauge at each unloading step.

Further, from the experimental perspective, the responses of different grain families (both axial and radial) are described in terms of diffraction elastic constants (DEC), where the diffraction Young's modulus is defined and measured as the slope of the applied stress over the elastic lattice strain of each axial family of grains while the diffraction Poisson's ratio is defined and measured as the ratio of the radial elastic lattice strain over the axial elastic lattice strain at the same applied stress level [97, 98, 145]. However, although the diffraction Young's modulus of each family of grains measured from the axial lattice response in elastic regime shown in Figure 5.6 exhibits consistency among different researchers, it is not a physical Young's modulus of the family since the intragranular stress is not identical to the macroscopically applied stress. In addition, as mentioned above, a given axial family of grains is not identical to the corresponding radial family of grains with same Miller indices, thus diffraction Poisson's ratio is also not a physical measurement.

5.5. Simulation procedure of pre-strained specimen

We now consider the response of the pre-strained specimens EXLA2. The particular interest for this group is on the effect of prior deformation history on the macroscopic Bauschinger effect and associated microscopic lattice response. Although the specimens EXLA2 and EXLA1 have identical chemical composition (Table 5.1), they may be cut from different positions in the structural components or may have experienced different service histories. Thus their initial states, in particular, residual stress states, can be different. However, the initial residual stress state of individual grains, as discussed above for refinement in the EXLA1 specimen, is ignored in this part of simulation because the pre-straining tends to wipe out any pre-existing residual stress and set up a new residual stress state that the subsequent response will be insensitive, or weakly sensitive, to the original state.

Here the initial condition of the EXLA2 specimens before high temperature pre-straining (550^{o}C up to 250 MPa) remained the same as that of the EXLA1 specimen before the refinement, i.e. the distributions of all microstructure elements were assumed to be identical on all slip planes for all grains within the polycrystalline materials, leading to an identical CRSS on all slip systems. Meanwhile, the update procedure of each stress/strain term as well as the values of the parameters (Table 5.2) also remained the same as that for specimen EXLA1. The change of the population of precipitates during high temperature pre-straining was ignored due to the short duration of the test, which would not provide sufficient time for further nucleation and growth of particles to occur. Thus both τ_s and τ_p were assumed to be constant throughout the simulation. However, it should be noted that the modulus is temperature-dependent [3, 11]. According to Frost and Ashby [11],

$$G = G_0\left(1+\frac{T-300}{T_M}\cdot\frac{T_M}{G_0}\frac{dG}{dT}\right) = G_0\left(1+\frac{T-300}{T_M}\cdot Y\right) \tag{5.1}$$

where T is the current temperature (not to be confused with the orientation matrix used in Chapter 4), G_0 is the shear modulus at 0K, T_M is the melting temperature and Y is a temperature-dependence factor. For 316 stainless steels, T_M=1810K and Y= -0.81 [11]. Young's modulus was also found to follow similar temperature dependence. Therefore, since all contributions to the CRSS in the model are proportional to the shear modulus, the CRSS needs to be scaled with the temperature-dependent modulus when the temperature changes. In addition, while the plastic mismatch strain for each individual grain developed during high temperature pre-straining remained the same, the Type II and Type III internal/residual stresses also need to be scaled with the shear modulus (Eqs. (4.23a) and (3.21)).

The resulting model was then used to predict the evolution of the microscopic lattice strain and residual lattice strain for this group during subsequent uniaxial tensile or compressive loading at ambient temperature. The macroscopic Bauschinger effect was also evaluated.

5.6. Measurement and prediction of pre-strained specimen

5.6.1. Macroscopic response

Figure 5.9 compares the measured and predicted results of the macroscopic response of the specimens subjected to room temperature (RT) uniaxial reloading in tension (EXLA2-1) and compression (EXLA2-2), following high temperature (HT) tensile pre-straining at 550^{o}C. All the data in this section can be found in [146]. For comparison, the compression data (EXLA2-2) is shown using absolute values. The sharp increase of the initial yield stress observed in the RT tensile stress-strain curve (red line in Figure 5.9), compared with the HT pre-straining stress-strain curve (black line in Figure 5.9), is due to the scale of the CRSS through the temperature-dependent shear modulus. Again, the results (also the predicted microscopic lattice responses shown later) are almost the same when we ignore the contribution of the precipitates to the constitutive response, showing a weak contribution from precipitates due to the small population. The difference between the tensile (red line) and compressive (blue line) stress-strain curves is due to different roles of the developed Type II residual stresses from high temperature tensile pre-straining in these two specimens, which will be discussed in detail in the next section.

Further, while the trend regarding the transient softening (defined in Figure 2.16) is observed and predicted by the model, the permanent softening is unclear in the experiment due to the limited data. However, from the extended macroscopic stress-strain curves shown in Figure 5.10 beyond the scope of measurements, it is observed that the compressive stress-strain curve asymptotes towards the tensile stress-strain curve, indicating the absence of permanent softening of the EXLA2 specimens.

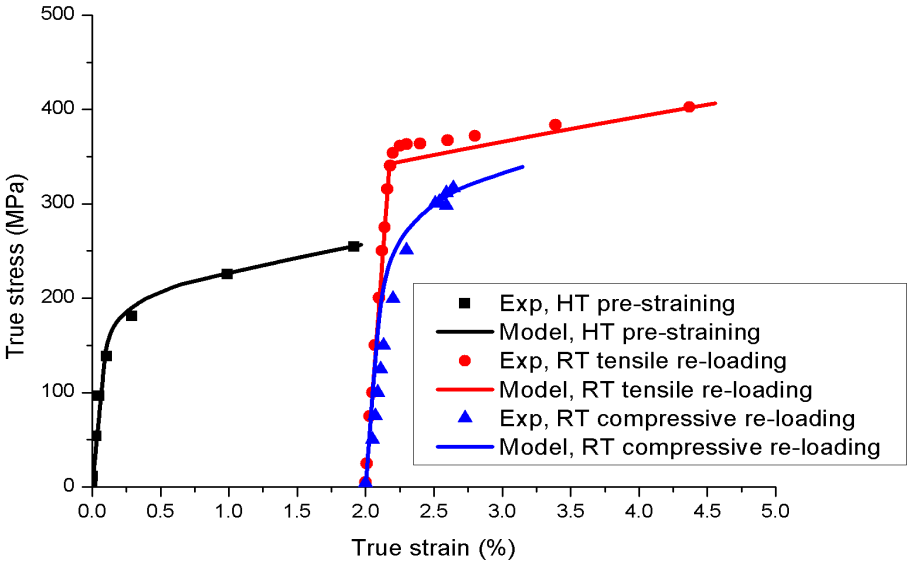

Fig. 5.9. Comparison of experimental data and model prediction in terms of macroscopic stress-strain relationship for EXLA2 specimens; the figure shows the high temperature (HT, 550^{o}C) tensile pre-straining and the subsequent reloading in tension (EXLA2-1) and compression (EXLA2-2) at room temperature (RT). Data and prediction for EXLA2-2 is shown in absolute value.

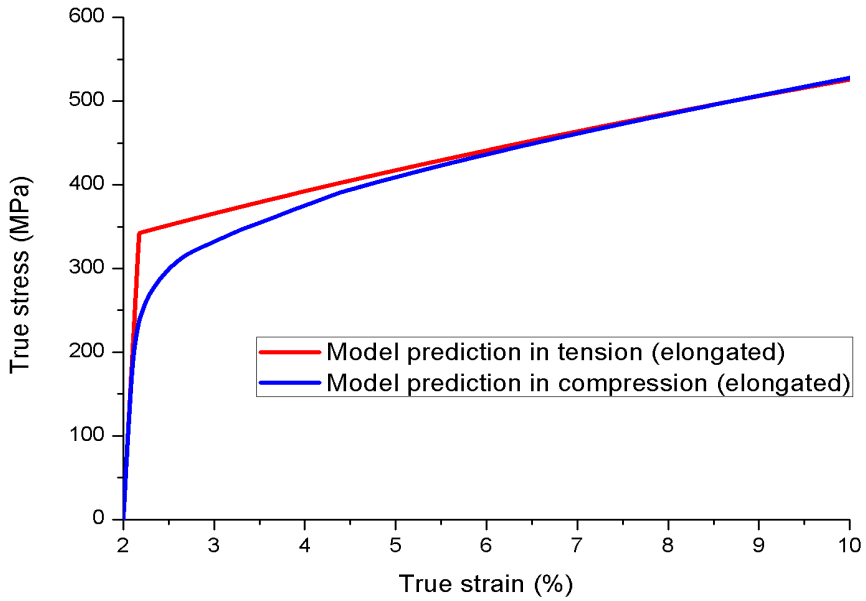

Fig. 5.10. Model predicted extended macroscopic stress-strain curves subjected to tensile or compressive reloading at ambient temperature. Result of the EXLA2-2 (compressive) specimen (blue line) is shown in the absolute value.

5.6.2. Lattice response along axial direction

Figure 5.11 compares the measured and predicted results of the total lattice strain and the corresponding residual lattice strain evolution for the three families {220}, {111} and {200}

of the EXLA2 specimens parallel to the loading direction (axial response, corresponding to the *y*-axis of the sample co-ordinate system in Figure 5.1a), subjected to room temperature (RT) tension (EXLA2-1) or compression (EXLA2-2). The residual lattice strain is plotted against the macroscopic plastic strain. Data and predicted results for EXLA2-2 specimens (compression) are again shown using absolute values to compare with those for EXLA2-1 specimens (tension). Both the data and predictions are for the response averaged over all members of a given family. The general trends for all the three families within both EXLA2-1 and EXLA2-2 specimens observed in the experiment are predicted by the model. Similar to the axial response of the EXLA1 specimens shown in Figure 5.5(a)-(c), the model predicts an identical axial lattice response for all members of each family, and discontinuous changes in the slopes of the lattice response of each family illustrated in Figure 5.11(a)-(c), as before, indicate the occurrence of micro-yielding. Note that the predicted sharp transitions in the slope are likely to be smoothed by taking into account a combined effect of the spread in orientation and an initial residual stress state (before the high temperature pre-straining), according to the refinement analysed for the EXLA1 specimen along axial direction (section 5.4.2). However, as mentioned above, in order to highlight the internal processes that are responsible for the Bauschinger effect, we do not consider further refinement on the response in this section as discussed before.

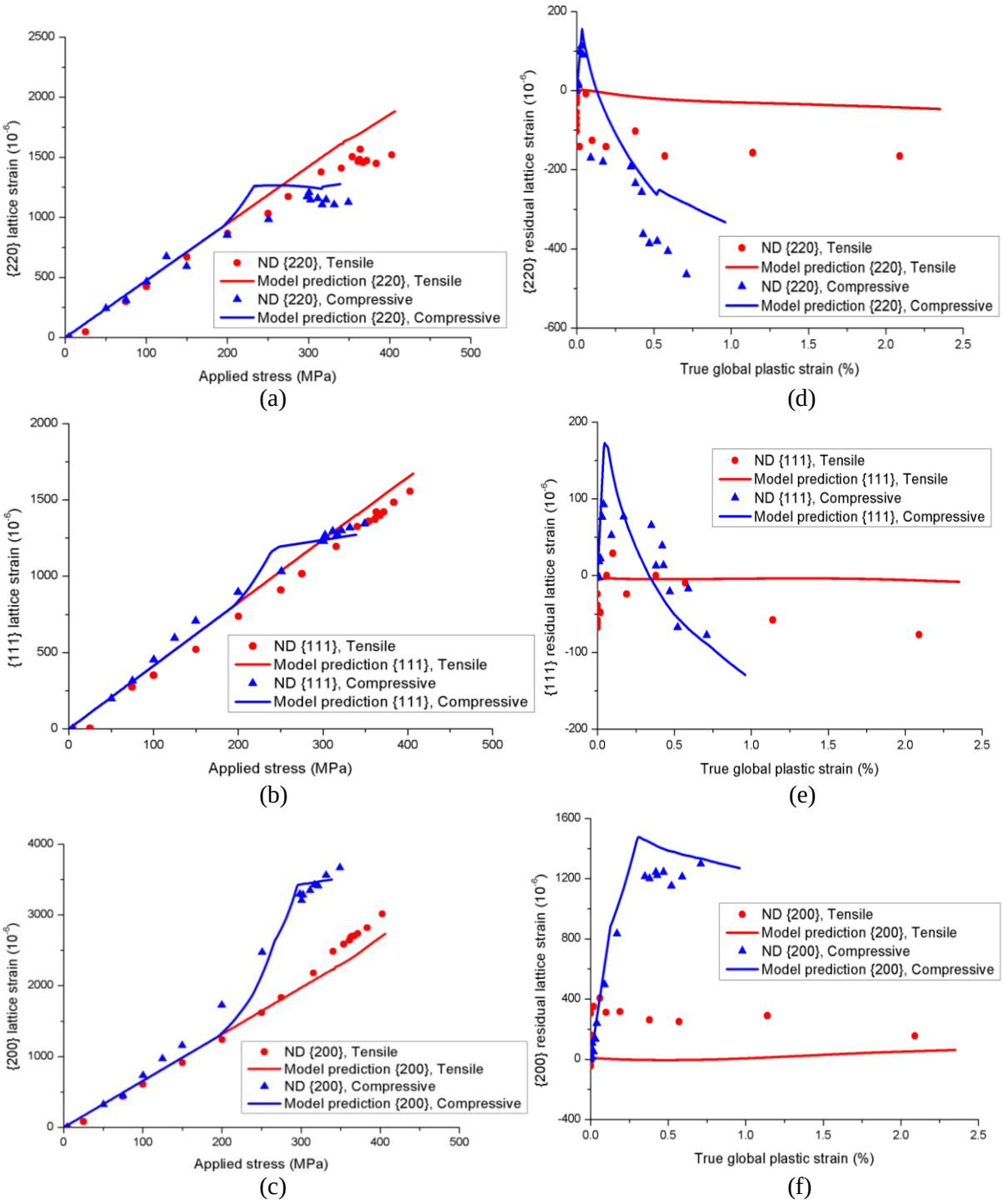

Fig. 5.11. Measured and predicted averaged results of lattice strain and residual lattice strain along the *axial* direction (*y*-axis of the sample co-ordinate system in Fig. 5.1a) of EXLA2-1 (tensile) and EXLA2-2 (compressive) specimens: (a) and (d) {220} grain family lattice strain and residual lattice strain; (b) and (e) {111} grain family lattice strain and residual lattice strain; (c) and (f) {200} grain family lattice strain and residual lattice strain. Data and predictions for EXLA2-2 (compressive) specimen (blue) are shown in the absolute value. The micro- residual lattice strain is plotted against the macroscopic true plastic strain measured by the strain gauge at each unloading step.

Following the extended macroscopic stress-strain curves shown in Figure 5.10 beyond the scope of measurements, the corresponding extended microscopic lattice response are shown in Figure 5.12. Compared with Figure 5.11(a)-(c), it is observed that the slope of lattice response of each of the three families of the EXLA2-1 (tensile) specimen always remain linear and parallel to the original elastic lines, while that for each family of the EXLA2-2 (compressive) specimen is observed to experience discontinuous changes but eventually become parallel to the original elastic lines. All these phenomena shown in Figures 5.11 and 5.12 are attributed to the development of Type II residual stress state in different specimens during deformation, which will be discussed in detail in the next section.

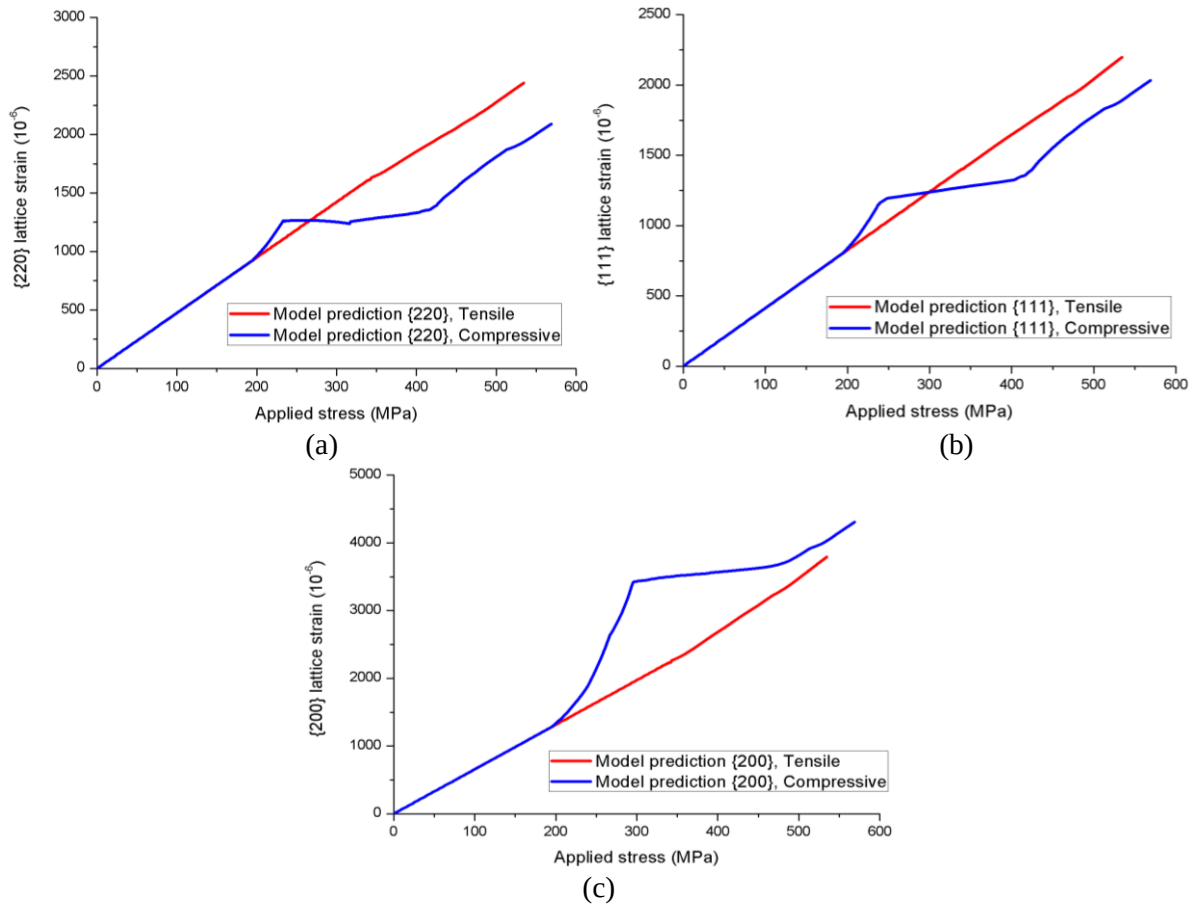

Fig. 5.12. Model predicted extended microscopic response subjected to uniaxial tensile or compressive reloading; (a) {220} grain family; (b) {111} grain family; (c) {200} grain family. Predictions of the EXLA2-2 (compressive) specimen (blue lines) are shown in the absolute value.

5.7. Discussion

5.7.1. The latent hardening of polycrystals

The effect of strain hardening, in particular latent hardening, on the development of nonlinear lattice strain observed in Figure 5.5 and Figure 5.11 has been emphasized by Li and O'Dowd [141]. Unlike the crystal plasticity model described here, empirical approaches have often been used in previous studies [97, 129, 132, 141] to describe the hardening effect (increase of CRSS) on each slip system. The incremental plastic response can be written in the form

$$\Delta\tau_{cr}^{\delta} = \sum_{\beta} h^{\delta\beta} \left|\Delta\gamma^{\beta}\right| \tag{5.2}$$

where $h^{\delta\beta} = q^{\delta\beta} h^{\beta}$ is the strain hardening matrix (no sum on β) and h^{β} is a hardening coefficient varying during deformation. $q^{\delta\beta}$ is a matrix capturing the latent hardening behaviour. $q^{\delta\beta}$ for F.C.C crystals is expressed as

$$q^{\delta\beta} = \begin{Bmatrix} K & qK & qK & qK \\ qK & K & qK & qK \\ qK & qK & K & qK \\ qK & qK & qK & K \end{Bmatrix} \tag{5.3}$$

where K is a 3×3 matrix fully populated by ones [136]. The diagonal terms represent self-hardening on coplanar systems and off-diagonal terms define the level of latent hardening on non-coplanar systems. The quantity q in Eq. (5.3) is the latent hardening ratio (LHR), with a single constant value frequently used [82, 97, 141]. However, other researchers have reported that the LHR changes during deformation [150]. The present dislocation link length model incorporated within the crystal plasticity framework models the evolution of LHR during plastic deformation, which can be calculated by loading a single grain along any single slip system. For the current model and using the values of the parameters as shown in Table 5.2,

the result is shown in Figure 5.13, whereby the LHR gradually decreases and eventually saturates with the accumulation of plastic shear strain. The transition occurs at a small value of plastic shear strain and is when all three slip systems on the slip plane are activated. The lattice response simulated with constant or variable LHR may not differ too much in the problems considered here given a small total strain, but may be significantly different during extensive plastic or cyclic loading.

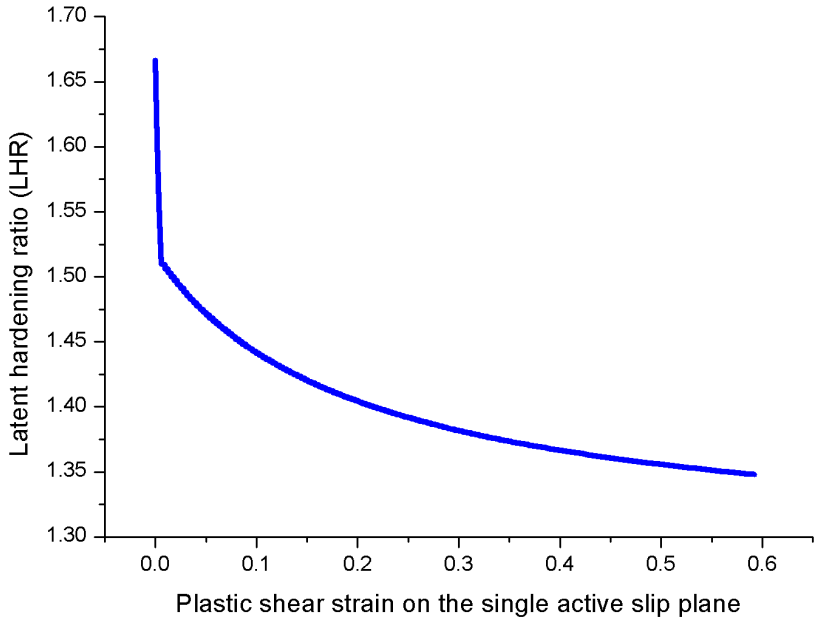

Fig. 5.13. Change of the latent hardening ratio (LHR) during single slip of a single crystal

5.7.2. The role of development of Type II intragranular residual stress in determining the nonlinearity

The Type II intragranular residual stress associated with the development of incompatible plastic strains plays an important role in explaining the multiple forward and backward inflections in the lattice response observed in Figures 5.5, 5.6, 5.8, 5.11 and 5.12. Here we mainly discuss the axial response in the two groups of specimens (Figures 5.5, 5.6, 5.11 and 5.12) and for simplicity ignore the effects of initial residual stress and any spread in lattice planes considered in the experiments.

For each of the three axial families of planes within the EXLA1 specimen, the small decrease in slope beyond the applied stress of approximately 200 MPa compared to the initial elastic portion of the curve suggests the onset of micro-yielding somewhere in the surrounding homogeneous matrix, prior to plastic deformation in the grain family under consideration. Load is transferred from the surrounding regions to the grain family, which deforms only elastically. This results in an increase in the slope of the lattice strain/stress curves of Figure 5.5(a)-(c) (see also Eqs. (4.23a) and (4.24)). This is also reflected in both the observed and predicted initial increase in the residual lattice strain in Figure 5.5(d)-(f). According to this, note that the macroscopic stress-strain curve measured by [98] (Figure 5.4) is lower than other curves, indicating an earlier micro-yielding in the matrix due to difference in the tested sample (e.g. a different initial residual stress state), this can also explain their measurement of {200} family of grains, which shows earlier deviation from linearity compared with other data (Figure 5.5c). The subsequent sharp increase in applied stress with minimal increase in lattice strain observed in Figure 5.5(a)-(c) indicates micro-yielding and plastic straining within the grain family of interest, with the load transferred to other grains within the body which are yet to yield. This leads to a sharp reduction of the Type II residual stress and related lattice strain as macroscopic plastic strain is accumulated (Figure 5.5d-f). The mismatch reaches a steady state once each family of planes deforms plastically almost at the same rate as the polycrystal itself. Consequently, the plastic strain increments generated in the individual members during each increment of loading are now compatible, i.e. $\Delta\varepsilon^{ta}$ defined in Eq. (4.21) is zero, i.e. the slope of the curve of Figure 5.5(a)-(c) for all families of planes then asymptotes towards the initial elastic slope.

For EXLA2 specimens, the results further support the above discussion on the Type II residual stress. For EXLA2-1 (tensile) specimen, in Figure 5.11(a)-(c), when the applied tensile stress is small, both the measurement and prediction show that the lattice strain

responses of the three families are elastic. Beyond yield, the model still predicts a slope similar to the elastic response for all the families. This indicates that a suitable Type II residual stress field has been achieved after the high temperature (HT) pre-straining that allows grains to deform compatibly plastically during room temperature (RT) tensile loading, giving rise to a sharp change in slope of the stress-strain curve at yield for EXLA2-1 as shown in Figure 5.9 (red line). This is also reflected by an almost zero value of the residual elastic lattice strain observed in Figure 5.11(d)-(f) (red lines) for all the three families. However, experimentally there is a more distinct increase in the slope for the {200} family in Figure 5.11(c), before it decreases again to become parallel to the elastic response line. The trend for the {220} family in Figure 5.11(a) is less clear, but there is evidently a sharper decrease in slope in the experimental result. According to the refinement carried out for the EXLA1 specimen in the last section, this discrepancy between the model and experiment could result from that, some grains within a given family, taking into account the spread in orientation, are still yet to yield. However, there could also be a number of other related physical processes: (i) the Type II residual stress between grains could have relaxed either during or after HT pre-straining; (ii) creep could have contributed to the inelastic deformation during the HT pre-straining; or (iii) the mechanism of plastic flow at HT is different to that at RT. In either case, the Type II residual stress generated by the pre-straining is different from that required to ensure compatibility of plastic deformation of the grains during loading at RT. The stresses therefore redistribute during the initial stages of plastic deformation until a suitable Type II residual stress state that gives rise to compatible plastic straining is established. As a result, the experimental stress-strain curve in Figure 5.9 shows a more gradual yielding process (i.e. there is a less sharp definition of yield) than predicted by the model.

In contrast, for the EXLA2-2 (compressive) specimen, the Type II residual stress state

established during HT pre-straining is significantly different to that which is required to give compatibility of plastic straining (the distribution and magnitude of the residual stresses in the grains are correct, but they have the wrong sign). Plastic flow therefore occurs much earlier in some grains than in others and the change in slope of the stress-strain curve (blue line in Figure 5.9) is less sharp, while the Type II residual stress state redistributes as the number of grains that deform plastically gradually increases. Therefore, the EXLA2-2 specimen exhibits similar trends in the macro- and microscopic behaviour (Figures 5.9 and 5.11, blue lines) as those for EXLA1 with no pre-strain history (Figures 5.4 and 5.5). At the strain level shown in Figure 5.9, a full steady state Type II residual stress state has not been achieved, which is consistent with the observation that the compressive stress-strain curve is asymptoting towards, but has not yet met, that for tensile loading. This also explains that the development of Type II intragranular residual stress during HT pre-straining leads to the transient softening, regarding Bauschinger effect, of the material. At high strains we would expect a Type II residual stress state to have been established that promotes compatible plastic deformation of the grains. The slopes of Figure 5.11(a)-(c) (blue lines) would then change back towards the initial elastic slope. This condition has been clearly seen for all the three families, shown in the extended macro- and microscopic curves in Figure 5.12.

5.7.3. The role of development of Type III residual stress in influencing the Bauschinger effect

The Bauschinger effect of the EXLA2 specimen (with initial high temperature (HT) pre-strain history) is predicted by the model. Note that only transient but not permanent softening is observed in the macroscopic behaviour of the material (Figures 5.9 and 5.10). In other words, the degree of the kinematic or directional feature predicted by the model is weak. Section 5.7.2 has discussed the relationship between the Type II intragranular residual stress

and the transient softening regarding the Bauschinger effect. This section evaluates the role of the Type III residual stress associated with precipitates and prismatic loops described in Chapter 3. According to Eqs. (3.21) and (4.5), the Type III residual stress is a function of the volume fraction of intragranular precipitates and the plastic shear strain on all the active slip systems. Therefore, we examine if the change of these two factors could lead to a change in the Bauschinger effect of the material. Here we only focus on the macroscopic behaviour.

5.7.3.1. The Type III residual stress with different volume fractions of intragranular precipitates

The Type 316H stainless steel specimens used in the experiment have been estimated to contain only 0.009 volume fraction of intragranular carbides with an average size of 60 nm. In practice, long-term creep deformation or thermal ageing of solution-treated 316H stainless steels at elevated temperatures could result in precipitation of other intragranular intermetallic phases, such as Laves and Chi phase [36], with the latter growing preferentially at very high temperatures (>700^{o}C). The ultimate or maximum volume fraction of these two phases, together with that of carbides, was calculated using the software *Thermo-Calc*, a thermodynamic calculation program, with the input of alloying elements shown in Table 5.1 and the phase diagram for stainless steels (detail is not shown here). Accordingly, two values of volume fraction were chosen in this section, respectively 0.05, referring to the total potential volume fraction of intra-carbide and intra-Laves, and 0.1, referring to a heavily aged material with complete precipitation of carbide and Laves plus some Chi phase. All these particles were treated equally as spherical and the mean radius for all particles was chosen to ensure the same mean inter-particle spacing calculated by Eq. (3.10) as that of the original specimen with estimated volume fraction of 0.009. The contribution to the internal resistance by the precipitates (Orowan bowing, Eq. (2.15) and number of prismatic loops, Eq. (3.16) at

same level of plastic strain) is therefore identical for all cases. Depletion of solute atoms was also calculated according to the *Thermo-Calc* results and the associated reduction of athermal solute strengthening by the enhanced precipitation in these two cases was found to be less than 2 MPa and was thus ignored.

In both cases, following the original experimental procedure, the materials were initially pre-strained at 550^{o}C up to the same strain level as the experiment (~2%). Only one parameter, the initial number of pinning points on each slip plane N_0, was changed to provide a similar macroscopic stress-strain curve during high temperature pre-straining as the original EXLA2 specimen (Figure 5.9). All other parameters remained the same. The resulting model was then used to predict the Bauschinger effect subjected to uniaxial tensile and compressive reloading at room temperature and the result is shown in Figure 5.14, compared with the results of the original EXLA2 specimen. It was found that the slope of both tensile and compressive stress-strain curves in the plastic region increases as the volume fraction of intragranular precipitates increases, indicating an increasing resistance to plastic flow by the increase of Type III residual stress (opposite to the applied shear stress, Eq. (4.2)). This is because a given load tends to be carried more and more by precipitates, i.e. less and less by the matrix, as the population of precipitates increases. Thus materials with larger populations of precipitates require more load to activate the dislocation glide motion to achieve a certain strain level. Meanwhile, the positions of the sharp change in slope of the stress-strain curve at yield during tensile loading remain almost the same in all cases, which is as expected since all cases are with the same pre-strain level and same mean inter-particle spacing, thus providing the same contribution to the internal resistance from precipitates. However, the Bauschinger effect, including both transient and permanent softening, becomes more pronounced as the volume fraction of precipitates increases. Compared with the original result for the EXLA2 specimen (solid blue and red curves in Figure 5.14), a larger population

of precipitates has resulted in a larger value of Type III residual stress during pre-straining, which will lead to even more grains deforming plastically at an early stage during reverse compressive loading. In other words, the enhanced Type III residual stress further drives the overall residual stress field away from a steady state. In addition, it should be noted that even for a very large volume fraction of precipitates, 0.1, the model still predicts the compressive curve asymptoting to the tensile curve, although delayed by the increase of Type III residual stress.

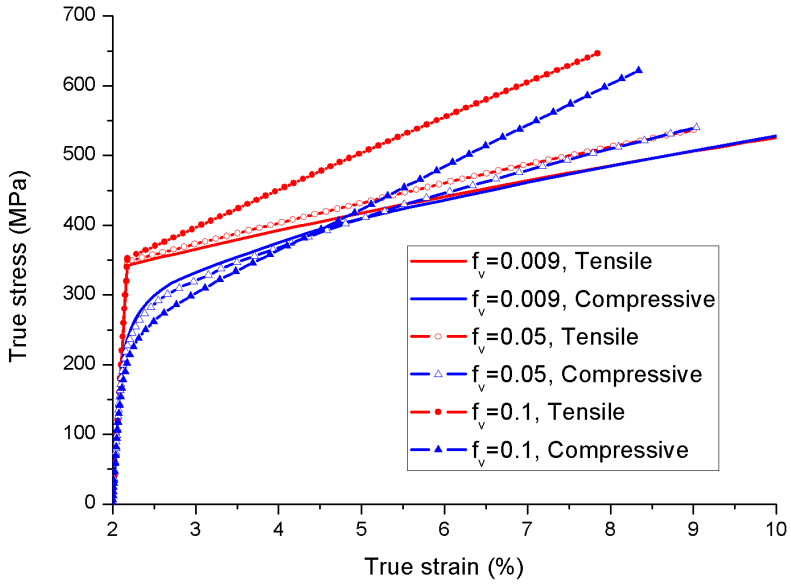

Fig. 5.14. Model predicted macroscopic stress-strain curves of materials with different initial volume fractions of intragranular precipitates, subjected to reloading in tension and compression at room temperature after high temperature (550^{o}C) tensile pre-straining; Predictions of the original specimen are also shown. The inter-particle spacings are the same for all the cases. Predictions for the compressive curves are shown in the absolute value.

5.7.3.2. The Type III residual stress with different high temperature pre-strain levels

In this case, we fixed the volume fraction of intragranular precipitates at 0.05 and the material was pre-strained at 550^{o}C up to different levels, 2%, 4% and 6%. The predicted macroscopic behaviour during subsequent reloading in uniaxial tension and compression at room temperature is shown in Figure 5.15. It is observed that the slope of both tensile and

compressive curves in the plastic region remains almost the same, independent of the HT pre-strain level. This is because at a fixed population of precipitates, the ratio of load carried by the precipitates and that carried by the matrix would remain the same during subsequent reloading. Meanwhile, note the difference between the tensile and compressive stress-strain curves after yielding is enhanced as the pre-strain level increases, showing a strong kinematic feature. This can be explained similarly as before that the larger the Type III residual stress accumulates during HT pre-straining, the more that it favours the plastic straining during reverse compressive loading and delays the achievement of a steady state in the residual stress state in the material that allows grains to deform compatibly plastically, or delays the asymptote between the compressive and tensile curves. This, combined with the results shown in Figure 5.14, however, may also indicate that there is actually no "permanent" softening in the material, given a very long term, according to the definition of permanent softening stress in the Bauschinger effect introduced in section 2.2.3.

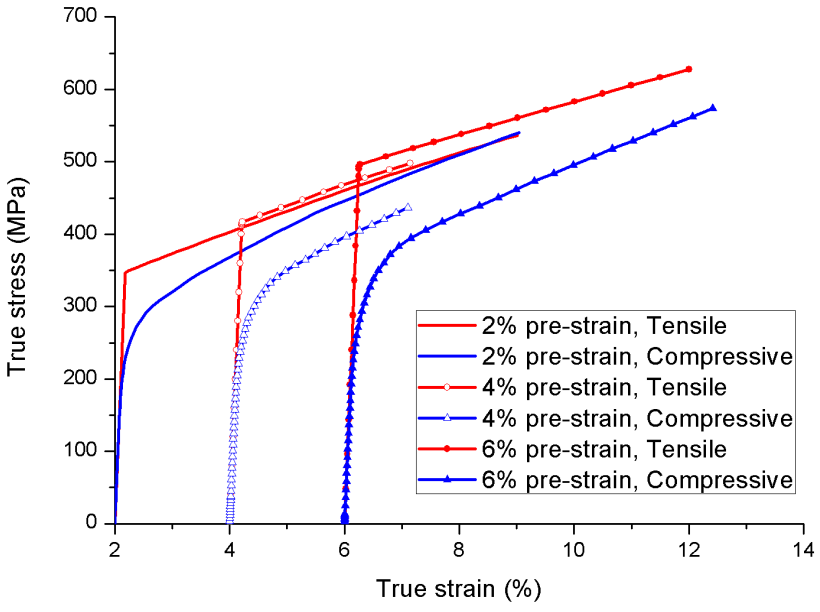

Fig. 5.15. Model predicted macroscopic stress-strain curves of materials with different high temperature pre-strain levels, subjected to reloading in tension and compression at room temperature after high temperature pre-straining (550^{o}C). The volume fraction of the intragranular precipitates is fixed at 0.05. Predictions for the compressive curves are shown in the absolute value.

Lastly, to understand whether the enhanced "permanent" softening observed in Figures 5.14 and 5.15 is related to the Type II residual stress, here we examine a material with a very large volume fraction (0.1) of intragranular precipitates. In this case, the Type III residual stress is ignored or deactivated throughout the simulation. The material was initially pre-strained at 550^{o}C up to a high level of 6%, followed by unloading and reloading in tension and compression at room temperature, as before. The result is shown in Figure 5.16. Compared with Figures 5.14 and 5.15 at the same strain lavel (e.g. ~10%), no "permanent" softening is observed. We then conclude that the Type II residual stress field is related only to the transient softening while the Type III residual stress field contributes to both transient and "permanent" softening.

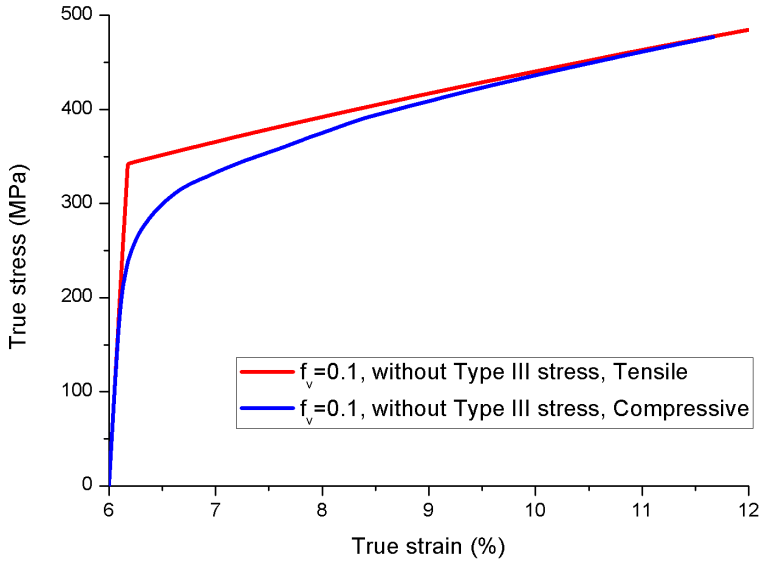

Fig. 5.16. Model predicted macroscopic stress-strain curves of a material with 0.1 volume fraction of intragranular precipitates and a high temperature (550^{o}C) pre-strain level of 6%, during subsequent room temperature reloading in tension and compression. The Type III residual stress is ignored in the simulation. Predictions for the compressive curves are shown in the absolute value.

5.8. Summary

This chapter applies the athermal multi-scale self-consistent model for individual grains and a polycrystalline aggregate established in Chapters 3 and 4 to the evaluation and explanation of the micro-scale lattice responses (measured by neutron diffraction (ND)

technique) and the macroscopic Bauschinger effect of a Type 316H polycrystalline austenitic stainless steel subjected to uniaxial tensile and/or compressive loading. Two groups of specimens are examined. The first group, EXLA1, are as-received ex-service specimens and the lattice responses of three different subsets of grains ({220}, {111} and {200}), both along axial and radial directions with respect to the uniaxial tensile loading direction, are evaluated. The consistency and scatter of data measured by different groups is also explained. The second group EXLA2 has the same service history as the EXLA1 specimen but has a further pre-strain history at 550^{o}C. Measurements of the axial lattice responses of the same three subsets of grains as well as the macroscopic Bauschinger effect during subsequent reloading in compression and tension at room temperature are evaluated. Most importantly, the role of Type II and Type III residual stress field in determining these macro- and microscopic behaviour is investigated. The main results and findings of the model are summarised as follows:

1. In general: The as-defined latent hardening ratio (LHR) evolves during plastic deformation. Use of a pure constant may generate similar results in this study but may induce problems during complex conditions, such as cyclic loading.
2. In general: For perfectly aligned members of each axial family of planes considered in this work, a trend of increase and then decrease can be observed in both the lattice strain and residual lattice strain evolution, which can be explained by the yielding sequence, i.e. the homogeneous matrix and then the family of planes itself. This also indicates the load transfer between different local regions during micro-yielding.
3. For EXLA1: Larger scatter is observed in radial response than in axial response. This is because the data generated at the radial detector is sensitive to the orientations of the grains that make up the family of planes sampled by the detector. The axial and radial

detectors in the experiment measure non-identical families of planes thus the diffraction elastic constants (DEC) are not physical measurements.

4. For EXLA1: The sharp transitions observed in the lattice response of each family of plane can be smoothed by taking into account the effect of the spread of orientations of lattice planes included in the experimental measurements and the initial residual stress state. Refinement by the combined effect of spread of normal to the grain families and initial residual stress can be used to probe the appropriate initial state of each family of planes.
5. For EXLA2: The development of the Type II intragranular residual stress during high temperature uniaxial tensile pre-straining leads to the transient softening phenomenon of the material, which is reflected from different macroscopic responses during subsequent uniaxial tensile and compressive reloading.
6. For EXLA2: The change in the volume fraction of intragranular precipitates and/or the pre-strain level in the material influence the accumulation of the Type III internal stress and also the macroscopic Bauschinger effect. However, in practice, there is no "permanent" softening provided a very long term, since the enhancement of the Type III residual stress is only able to delay but not eliminate the asymptote feature between the macroscopic tensile and compressive curves during reloading at room temperature after high temperature pre-straining.
7. For EXLA2: The Type II residual stress field is related only to the transient softening while the Type III residual stress field contributes to both the transient and relatively "permanent" softening.

Chapter 6

High temperature model enhancement

6.1. Introduction

As the temperature is increased, the kinetics of inelastic deformation of metallic materials may change. Mechanisms of thermally activated glide and/or climb may facilitate dislocations to bypass obstacles and slip to occur even when the applied shear stress is not able to activate the athermal bypassing mechanism as described in Chapter 3. Depending on the population of precipitates, the particle bypassing mechanism at elevated temperatures may change from glide-controlled Orowan bowing to climb-controlled bypassing as reviewed in Chapter 2, where compared with Orowan bowing, climb-controlled bypassing mechanisms can occur at lower stresses (Eqs. (2.16)~(2.20)) and do not involve the formation of dislocation loops, but may be much slower since the rate-controlling process involves the diffusional rearrangement of material. For solute atoms in the matrix, their enhanced mobility at elevated temperatures may allow the formation of solute clusters or clouds in or around the dislocation core, which then can be dragged along by mobile dislocations and control the kinetics of both glide and climb motion. The moving dislocations exert a drag force on the solute clusters; the same drag force is exerted by the clusters on the moving dislocations.

Also, the creep behaviour of metallic materials is understood to be a competition between hardening and recovery, both of which will change when the microstructural state evolves at elevated temperatures. Mechanistically, a complete understanding of creep deformation and mechanisms requires knowledge of how the evolution of microstructure influences the material's internal resistance and internal stress, as reviewed in Chapter 2. For forest

dislocations, climb-controlled recovery leads to dislocation network coarsening and redistribution of link lengths, where long links grow at the expense of short links. As a result, the total number of dislocation links as well as dislocation junctions or pinning points on each slip plane gradually decreases, leading to a gradual increase of the mean spacing between junctions, and gradual recovery of the dislocation strengthening effect (Eq. (3.6)). For precipitates, thermal ageing or high temperature creep deformation promotes the transformation of different precipitate phases, consisting of nucleation, growth and coarsening processes, during which the mean particle size, volume fraction and mean inter-particle spacing evolve, leading to a change in the Orowan strength and associated Type III internal stress, as well as other climb-bypassing strengths (Eqs. (2.16)~(2.18)). In addition, the precipitation process may also attenuate the effect of solute drag by depletion of solute atoms in the matrix.

This chapter is an enhancement of the athermal plasticity model constructed in Chapters 3 & 4, incorporating a number of mechanisms active at elevated temperatures. Basic physics of the processes responsible for the evolution of microstructure are considered, respectively dislocation network coarsening and phase transformation, which will allow detailed modelling of the evolution of the associated internal resistance and internal stress. This enhancement, combined with the athermal model established before, constitutes a complete constitutive model to investigate material behaviour at various temperatures. Application of this enhanced model to Type 316H stainless steels at elevated temperatures is to be presented in Chapter 7.

6.2. Kinetics of dislocation motion at elevated temperature

6.2.1. Thermally-activated dislocation glide

The first mechanism we consider that is active at elevated temperature is thermally activated glide, which states that the thermal exposure may reduce the energy barrier of obstacles to dislocation glide motion or enhance vibration of dislocations [11]. As mentioned in Chapter 2, this indicates that, at elevated temperatures, even when the resolved shear stress (RSS) is lower than the internal resistance (CRSS) on individual slip systems, dislocations may still be able to bypass some obstacles and sweep across a slip plane rapidly to generate some plastic shear strain until they encounter and are held at some other obstacles. This, however, cannot be simply described by the idealized power-law relationship of Eq. (4.2), where the exponent *p* has been assigned to be very large to simulate a rate-independent flow rule. Instead, some rate dependency needs to be considered, which can be simulated by reducing the exponent in the power-law relationship, but a more physical Arrhenius law is used here [11, 26, 151]

$$\dot{\gamma} = \dot{\gamma}_0 \exp\left(-\frac{\Delta F_0}{kT}\left(1 - \left| \frac{\tau + \bar{\tau}_m^r}{\tau_{cr}} \right| \right) \right) \operatorname{sgn}\left(\tau + \bar{\tau}_m^r \right) \tag{6.1a}$$

Or $$\dot{\gamma} = \dot{\gamma}_0 \exp\left(-\frac{\Delta F_0}{kT}\left(1 - \left| \frac{\tau + \bar{\tau}_m^r}{\tau_{cr}} \right|^g \right)^h \right) \operatorname{sgn}\left(\tau + \bar{\tau}_m^r \right) \tag{6.1b}$$

where $\tau + \bar{\tau}_m^r$ is the sum of RSS and Type III internal stress, as used in the crystal plasticity framework (Eq. (4.2)); $\dot{\gamma}_0$ is a reference shear strain rate, which is understood to be physically related to the dislocation vibration frequency and mobile dislocation density [11]; *k* is Boltzmann's constant; *T* is temperature; ΔF_0 is the total activation energy required to overcome obstacles without aid from external stress; the CRSS τ_{cr} is the flow strength which

forces the dislocation through the obstacle with no help from thermal energy [11]; note that τ_{cr} scales with temperature through the temperature-dependent shear modulus [141, 152]. g ($0 < g \leq 1$) and h ($1 \leq h \leq 2$) in Eq. (6.1b) are two empirical quantities describing a random distribution of shape of obstacle energy barrier, rather than a regular box-shaped one described by Eq. (6.1a). Different values of g and h have been discussed in the literature [11, 151] and here we simply adopt those optimized by Frost and Ashby [11] across the full range of obstacle types, where g=3/4 and h=4/3. In addition, in Eq. (6.1), Frost and Ashby [11] argued that the stress dependence of the exponential is much larger than that of the pre-exponential, thus $\dot{\gamma}_0$ can be treated as a constant and has been estimated to be 10^6/s for this thermally activated glide mechanism. However, their estimation is based on the use of total dislocation density within the material and atomic vibration frequency or Debye frequency (~10^{12} -10^{13}) [11, 153], as well as the use of an empirical flow strength that is much larger than the CRSS used in our framework at a given temperature. In reality, $\dot{\gamma}_0$ is physically more appropriately associated with the effective dislocation vibration frequency (much smaller than Debye frequency [26, 153, 154]) and mobile dislocation density (smaller than the total dislocation density). As a consequence, $\dot{\gamma}_0$ is here estimated to be ~1-10 /s. Given the value of CRSS used in our work, we expect our relationship (Eq. (6.1)) to predict a similar inelastic strain rate as that of Frost and Ashby [11].

For the total activation energy ΔF_0, an expression has been given by Frost and Ashby [11], $\Delta F_0 \approx \alpha_0 G_0 b^3$, where G_0 is the shear modulus at 0 K and for strong obstacles, such as large incoherent precipitates, $\alpha_0 = 2$, for medium strength obstacles, such as forest dislocations, $\alpha_0 = 0.2 \sim 1.0$, and for weak obstacles, such as solute atoms, $\alpha_0 < 0.2$. Ideally, three separate equations are needed as below for all three types of obstacles considered in this study, each of which has a separate value of α_0.

$$\dot{\gamma}_1 = \dot{\gamma}_0 \exp\left(-\frac{\alpha_{01} G_0 b^3}{kT} \left(1 - \left| \frac{\tau_1 + \overline{\tau}_m^r}{\tau_d} \right|^g \right)^h \right) \mathrm{sgn}\left(\tau_1 + \overline{\tau}_m^r \right) \tag{6.2a}$$

$$\dot{\gamma}_2 = \dot{\gamma}_0 \exp\left(-\frac{\alpha_{02} G_0 b^3}{kT} \left(1 - \left| \frac{\tau_2 + \overline{\tau}_m^r}{\tau_p} \right|^g \right)^h \right) \mathrm{sgn}\left(\tau_2 + \overline{\tau}_m^r \right) \tag{6.2b}$$

$$\dot{\gamma}_3 = \dot{\gamma}_0 \exp\left(-\frac{\alpha_{03} G_0 b^3}{kT} \left(1 - \left| \frac{\tau_3 + \overline{\tau}_m^r}{\tau_s} \right|^g \right)^h \right) \mathrm{sgn}\left(\tau_3 + \overline{\tau}_m^r \right) \tag{6.2c}$$

where τ_1, τ_2, τ_3 are sub-resolved shear stresses used to bypass the corresponding obstacle (τ_d: forest dislocations; τ_p: precipitates; τ_s: solute atoms), which combine to provide the total resolved shear stress (RSS). The dislocations must bypass these obstacles simultaneously to generate any considerable shear strain, this suggests that

$$\dot{\gamma}_1 = \dot{\gamma}_2 = \dot{\gamma}_3 \tag{6.3}$$

First consider the situation where $\alpha_{01} = \alpha_{02} = \alpha_{03} = \alpha_0$. Then Eq. (6.3) requires that

$$\frac{\tau_1}{\tau_d} = \frac{\tau_2}{\tau_p} = \frac{\tau_3}{\tau_s} = \frac{\tau}{\tau_{cr}} \tag{6.4}$$

where in the last term of this expression we have assumed that the combined response can be expressed by Eq. (6.1b). The question now is how the three RSS τ_1, τ_2 and τ_3 combine to give τ. We can simply assume that these RSS combine in the same way as for the athermal deformation described in Chapter 3, i.e.

$$\tau = \sqrt{{\tau_1}^2 + {\tau_2}^2} + \tau_3 \tag{6.5}$$

Then, making use of Eq. (6.4), we find that

$$\tau = \left(\sqrt{{\tau_d}^2 + {\tau_p}^2} + \tau_s \right) \cdot \frac{\tau}{\tau_{cr}} \tag{6.6a}$$

$$\text{i.e.} \quad \tau_{cr} = \sqrt{\tau_d{}^2 + \tau_p{}^2} + \tau_s \tag{6.6b}$$

Eq. (6.6b) is consistent with the way that the CRSS combine, as shown in Eq. (3.26), which can be substituted into Eq. (6.1b) to give the thermally activated glide response for the slip plane. When the three α_{0i} are not equal to each other, use of a similar procedure results in a cumbersome set of equations that are difficult to fit to and calibrate against experimental data. Here we adopt a pragmatic approach that retains the essential physics of the deformation process, and assume that for this more general case $\dot{\gamma}$ is given by Eq. (6.1b) with τ_{cr} given by Eq. (6.6b) (or Eq. (3.26)), but with α_0 treated as a fitting parameter (noting that $0.2 \le \alpha_0 \le 2$).

Further, in Chapter 4 we employed a power-law rate relationship (Eq. (4.2)) to approximate the athermal glide process by using a large value of the exponent *p*. An alternative use of this type of model is to use it to approximate the thermally activated glide process described by Eq. (6.1b). Then, in order to capture the behaviour over a stress range of practical interest, the exponent *p* must be a function of temperature and physical parameters contained in Eq. (6.1b). Kocks et al [151] found that a good approximation is obtained when $p \approx \Delta F_0 / kT$ for values of the RSS is close to the CRSS ($\tau \approx \tau_{cr}$).

6.2.2. Climb-controlled bypassing of particles

The second mechanism we consider here that is active at elevated temperature is the extended bypassing modes for impenetrable precipitates, including local climb, general climb and cooperative climb as described in section 2.2.3, when Orowan bowing is inhibited. These bypassing modes involve dislocation climb but do not result in the formation of dislocation loops. A threshold stress (Eqs. (2.16)–(2.20)) is required for each climb-controlled bypassing mode, which is related to the increase in dislocation line length or line energy as a section of dislocation climbs over a precipitate. The mode with the minimum increase in dislocation line

length (cooperative climb) gives rise to the smallest threshold stress, but it also involves more material to redistribute by diffusion than the other two climb-bypassing modes.

A simple thermodynamic analysis is used to derive the plastic shear strain rate associated with these climb bypassing processes, as presented in **Appendix B**, based on the derivation for climb-controlled dislocation network coarsening (see section 6.3). Only the local climb (LC) and general climb (GC) processes are considered since the rate of cooperative climb is expected to be very low for the material considered in this study. This approach assumes that the rate-controlling process for each climb bypassing mode is the dislocation-core-diffusion-controlled climb and once a dislocation climbs and bypasses the precipitates, it glides rapidly on the slip plane until it encounters and gets held at some new precipitates. Given a constant distribution of precipitates, the thermodynamic analysis approximately derives a linear relationship between the plastic shear strain rate and the applied shear stress.

Local climb:
$$\left(\dot{\gamma}_p\right)_{LC} = Y\left(\tau - \tau_{LC}\right)\frac{16 D_c \rho_m b^5}{r_p{}^2 kT}\,\mathrm{sgn}\left(\tau\right) \tag{6.7a}$$

General climb:
$$\left(\dot{\gamma}_p\right)_{GC} = Y\left(\tau - \tau_{GC}\right)\frac{32 D_c \rho_m b^5}{r_p L_p kT}\,\mathrm{sgn}\left(\tau\right) \tag{6.7b}$$

where $\left(\dot{\gamma}_p\right)_{LC}, \left(\dot{\gamma}_p\right)_{GC}$ are the plastic shear strain rate for the local climb (LC) and general climb (GC); accordingly, τ_{LC}, τ_{GC} are the threshold stress for the two processes, which scale with the Orowan stress (Eqs. (2.17) ~ (2.20)); Y can be treated here as a fitting parameter; r_p, L_p are the mean particle size and mean inter-particle spacing; D_c is the dislocation core diffusivity (or pipe diffusivity) and ρ_m is the mobile dislocation density. Therefore, at any instant time at elevated temperature, also taking into account the thermally activated glide motion described in the last sub-section, the dominant or rate-controlling process is the one which gives rise to the highest shear strain rate. The transition stress between different

processes can be simply determined by equating the corresponding rate relationships (Eqs. (6.1b), (6.7a) and (6.7b)). This feature is schematically illustrated in Figure 6.1, where the solid curve determines the dominant process across a range of applied shear stresses and the hollow points represent the position of transition stress.

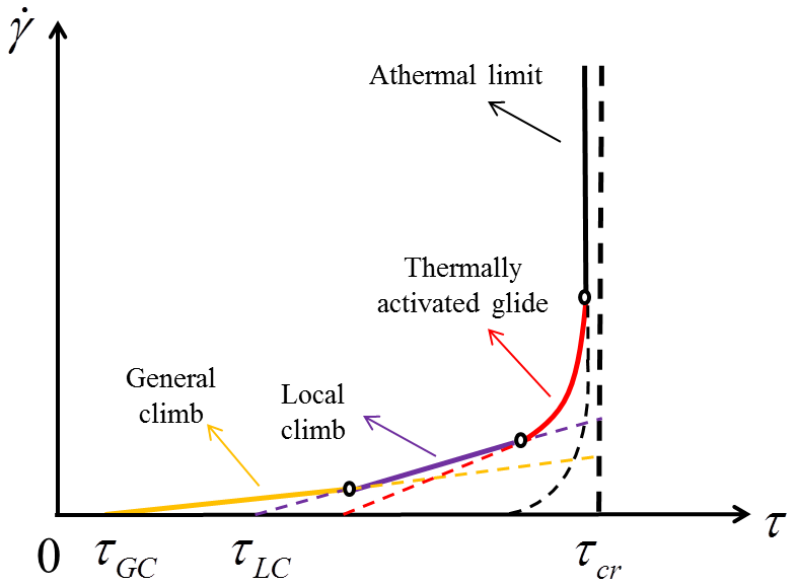

Fig. 6.1. Schematic illustration of the deformation kinetics across a range of shear stresses, taking into account the general climb (green), local climb (blue) and thermally activated glide (red) processes. τ_{LC}, τ_{GC} are the threshold stress for local climb and general climb. The actual dominant process is the one which gives rise to the highest shear strain rate (solid curve)

Further, it should be noted that the rate-controlling process may vary over time due to successive nucleation and growth of precipitates (see section 6.4), where both the mean size and mean inter-particle spacing would evolve, leading to a change in both the Orowan stress and threshold stress for climb bypassing processes. However, as can be seen in Figure 6.1, the climb bypassing process may only dominate when the applied shear stress is very low.

Finally, note that, in the derivation of Eq. (6.7), we have assumed that dislocations can glide rapidly between precipitates on the slip plane once they climb over and escape from the precipitates. In other words, the applied shear stress has been assumed to be greater than the combined strength of forest dislocation junctions and solute atoms thus the rate to bypass these two types of obstacles can be neglected. However, if this is not the case, use of a similar

procedure on combining the different kinetic processes (thermally activated glide and climb bypassing) is required to give the total response for the slip plane, as described in section 6.2.1. Such complexity is not considered in this work due to the different rate relationships established for different kinetic processes that would lead to a cumbersome set of equations.

6.2.3. Thermal solute drag—interactive solute strengthening

The third elevated temperature mechanism of interest relates to thermal solute drag process, or interactive solute strengthening [155, 156]. Different from precipitates, solute atoms have more mobility in the network at elevated temperatures and may either diffuse into and collect in a line along the core of continuously gliding (climbing) dislocations, or form atmospheres or clusters around dislocations. In either case, the mobile solutes can usually be dragged along by moving dislocations, impeding their motion. A detailed review of the process can be found in [156]. The effect of solute drag has been discussed extensively in a series of papers by Miller and his co-worker's and incorporated in their phenomenological model [104, 155, 156], which has been used to investigate the influence of solute drag on the plateaus and peaks in the shape of the flow stress/temperature curves of different materials [156, 157], and also the peaks in the creep rate vs stress curves of 316 stainless steels [157]. The physical basis of their models of solute drag is the theory of Cottrell and Jaswon [158], who proposed that this interactive solute strengthening is greatest at strain rates and temperatures where the velocity of the moving dislocations is close to that of the diffusing solute atoms. At low temperatures or high strain rates, the solutes cannot diffuse fast enough to keep up with the dislocations thus the solutes do not diffuse into the core or form a moving atmosphere around the dislocations. Conversely, at high temperatures or low strain rates, the solutes diffuse so rapidly that they do not impede the dislocation motion. Meanwhile, the

magnitude of the solute drag force is understood to be independent of the deformation history and thus only depends on the current temperature and strain rate [104, 155, 156].

In this sub-section, we incorporate the phenomenological model of solute drag developed by Miller and his co-worker's [155, 156] into our crystal plasticity framework. However, as mentioned in section 2.2.4, there are many parameters in their model, which make it complex and difficult to fit to experimental data. In addition, the detailed form of their model was chosen to simply reflect the features described above and was not derived from any particular mechanisitic theory of solute drag. Therefore, we do not employ the full version of their model, but present a reduced version which retains the essential physics of the process.

Following the work of Schmidt and Miller [77, 155], the solutes that are dragged along with moving dislocations enhance the strain hardening by increasing the effectiveness of all types of obstacles, concomitantly encountered by the dislocations, as barriers to deformation. Therefore, the thermally activated glide process (Eq. (6.1b)) is modified into

$$\dot{\gamma} = \dot{\gamma}_0 \exp\left(-\frac{\Delta F_0}{kT}\left(1 - \left| \frac{\tau + \bar{\tau}_m^r}{\left(1 + F_{sol}\right)\tau_{cr}} \right|^g \right)^h \right) \operatorname{sgn}\left(\tau + \bar{\tau}_m^r\right) \tag{6.8}$$

where the term F_{sol} is a variable defining the influence of solute atoms on the strengths of the obstacles. The term $\left(1 + F_{sol}\right)$ is introduced when solute atmospheres are present. The internal resistance of all obstacles is then enhanced. But when there is no solute cloud or the solute atoms are extremely mobile, Eq. (6.8) reduces to Eq. (6.1b) for thermally activated glide. Following Schmidt and Miller [155], the equation defining F_{sol} can be written as

$$F_{sol} = F_{sol,\max} \exp\left[-\left(\frac{\log\dot{\gamma} - \log\dot{\gamma}_{\max}}{B} \right)^2 \right] \tag{6.9}$$

where $F_{sol,\max}, \dot{\gamma}_{\max}, B$ are material constants. $F_{sol,\max}$ controls the height of the peak, which has been considered to be linearly proportional to the current concentration of solute atoms in the

matrix $\bar{c}$ [104, 156], i.e. $F_{sol,\max} = A\bar{c}$ where A is the proportionality. $\dot{\gamma}_{\max}$ is the magnitude of the shear strain rate at which the solute drag force reaches its maximum. Note that the nominal uniaxial strain rates $\dot{\varepsilon}, \dot{\varepsilon}_{\max}$ were used in the original model proposed by Schmidt. For the crystal plasticity framework employed here, we transform the relations in terms of $\dot{\gamma}, \dot{\gamma}_{\max}$ using the Schmidt factor as shown in Eq. (4.1).

While the solute contents controlling the interactive solute strengthening vary for different materials [77, 156], for 316 stainless steels, solute complexes or pairs (*Cr*-*C* [40] or *Mo*-*C* and *Mo*-*N* [159]) have been considered as being most responsible for the strengthening. In either case, it demonstrates that the solute drag in 316 stainless steels occurs largely due to the presence of interstitial elements, not substitutional, which has also been confirmed by Schmidt in general for iron alloys [77], but the force or rate would depend on the slowest substitutional elements. Therefore, the effect of solute drag in 316 stainless steels would attenuate by depletion of these solute elements arising from precipitation (see section 6.4).

6.3. Dislocation network coarsening

The following sections progressively discuss several evolution processes of the microstructure at elevated temperatures, which directly lead to a change of the associated internal resistance and/or internal stress. The first and most important evolution process is the dislocation-climb-controlled recovery or network coarsening process.

6.3.1. Deficiency of previous theory

Lagneborg has proposed a dislocation network coarsening model [4], where the three-dimensional network coarsening process is represented as the growth of the mesh-like structure consisting of links from different slip planes interconnecting each other [4, 55]. The

average mesh size in the network is often assumed to be identical to the average link length $\bar{\lambda}$ [55, 57, 115]. This model is analogous to grain growth [51] and has been used by many other researchers [55, 57, 115]. He assumes that the thermal recovery by growth of meshes is identical to Friedel's equation for the dislocation network speed of climb of the lines of the network [16, 52, 53] and the average link length grows in the following way

$$\dot{\bar{\lambda}} = M\Gamma\frac{1}{\bar{\lambda}} \tag{6.10}$$

where M is the climb mobility and Γ is dislocation line tension. However, Lagneborg's model has been criticized for not fully describing the network coarsening process [17]. In fact, during thermal-assisted dislocation climb or mesh growth, the work done can be dissipated by two processes: (1) vacancy emission and absorption and (2) diffusional transport from one site to another. The slowest process is the rate-controlling process. Kocks and Mecking [4] have argued that Friedel's grain growth law (Eq. (6.10)) only holds for dislocation network coarsening when (1) is the rate-controlling process, i.e. the speed of climb of the lines of the network is controlled by the rate of emission and absorption. However, since some constrained glide may contribute to the coarsening process, (2) may be the rate-controlling process. In addition, Ardell and Lee [112] have found that the linear relationship between $\dot{\bar{\lambda}}$ and $1/\bar{\lambda}$ is not consistent with experimental data and should be replaced by a power-law relationship. Therefore, in this section, we derive a more reasonable recovery law for mesh growth or network coarsening, using a simple thermodynamic kinetic analysis. Emphasis is put on the recovery of the state variable, i.e. the mean spacing L_d of all pinning points on individual slip planes.

6.3.2. Thermodynamic evolution of the dislocation distribution

In this and subsequent sections where we develop models for the evolution of microstructure we employ a variational principle described by Cocks et al [160, 161]. This provides a natural framework for modelling the range of situation examined in this thesis. It also provides a systematic approach for the development of simple models which capture the major physical processes. Consider a variational functional

$$\Pi = \Psi + \dot{\Phi} \tag{6.11}$$

where Ψ is the rate potential related to the kinetic processes (here it refers to dislocation climb motion) and $\dot{\Phi}$ is the rate of change of Gibbs free energy (here it refers to the rate of change of total dislocation line energy). Cocks et al [160, 161] demonstrate that the best approximation for the rate of evolution of the microstructure (the mean dislocation link length in the context) within the range of idealized geometries considered is that which minimises the functional Π (i.e. $\delta\Pi = 0$).

6.3.2.1. The Gibbs free energy

First, we identify a thin slab of material with thickness *dz* (Figure 6.2). Consider N_d as the number of pinning points per unit area on a slip plane (*x*-*y* plane in Figure 6.2). Assume that these pinning points are associated with dislocation segments of uniform length *dz* within the slab. Thus $N_d \times dz$ is the total length of dislocation associated with the slab of volume $dz \times 1$. Therefore, the dislocation density (ρ) associated with the pinning points can be defined as

$$\rho = \frac{N_d dz}{dz \times 1} = N_d \tag{6.12}$$

Eq. (6.12) shows that the number of pinning points per unit area is associated with the dislocation density (length per unit volume). Note that, in F.C.C crystals, there are four slip

planes with four different N_d (N_{d1}, N_{d2}, N_{d3}, N_{d4}). Thus if we assume that dislocations within all slabs of the type considered above are only associated one slip plane, the total dislocation density can be simply expressed as the arithmetic mean of the four quantities.

$$\rho = \frac{1}{4}\left(N_{d1} + N_{d2} + N_{d3} + N_{d4}\right) \tag{6.13}$$

According to Chapter 3, $L_d = N_d^{-1/2}$. Thus

$$\rho = \frac{1}{4}\left(\frac{1}{L_{d1}^{\ 2}} + \frac{1}{L_{d2}^{\ 2}} + \frac{1}{L_{d3}^{\ 2}} + \frac{1}{L_{d4}^{\ 2}}\right) \tag{6.14}$$

Therefore, the total Gibbs free energy or potential energy Φ and its rate $\dot{\Phi}$ is calculated as

$$\begin{aligned} \Phi &= \rho\Gamma = \frac{1}{4}\Gamma\left(\frac{1}{L_{d1}^{\ 2}} + \frac{1}{L_{d2}^{\ 2}} + \frac{1}{L_{d3}^{\ 2}} + \frac{1}{L_{d4}^{\ 2}}\right) \\ \dot{\Phi} &= -\frac{1}{2}\Gamma\left(\frac{1}{L_{d1}^{\ 3}}\dot{L}_{d1} + \frac{1}{L_{d2}^{\ 3}}\dot{L}_{d2} + \frac{1}{L_{d3}^{\ 3}}\dot{L}_{d3} + \frac{1}{L_{d4}^{\ 3}}\dot{L}_{d4}\right) \end{aligned} \tag{6.15}$$

where $\Gamma = \frac{1}{2}Gb^2$ is the dislocation line energy.

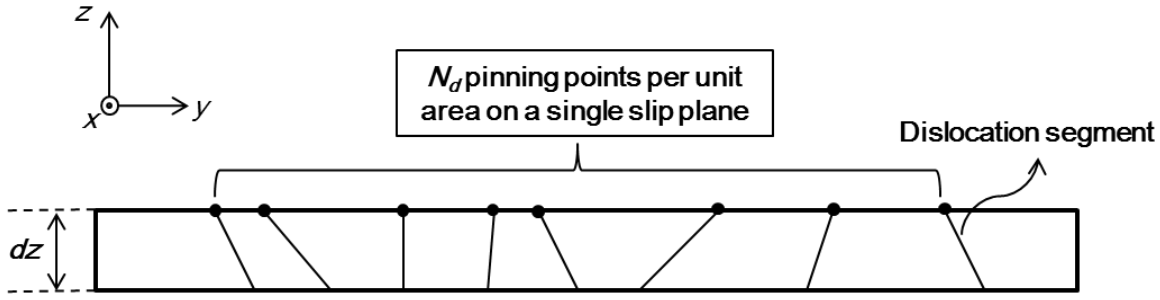

Fig. 6.2. A thin slab with thickness *dz*, containing N_d pinning points and $N_d \times dz$ total length of dislocation segments

6.3.2.2. The kinetic process

The kinetic process of network coarsening indicates that the pinning points can move as a result of glide, cross-slip or climb of dislocation segments. We assume that dislocations glide

freely and energy is only dissipated as a result of climb. It is simply assumed that half the links climb while the other half glide or cross-slip. Now consider two segments crossing a single slip plane (Figure 6.3a) with an average length $\bar{\lambda}_a$ and separated by the mean spacing L_d. Assume that atoms predominantly diffuse through the dislocation core, i.e. climb is controlled by dislocation pipe diffusion. Consider a small length *dx* on a segment, as shown in Figure 6.3(b). The magnitude of the rate of volume of atoms flowing into or out of the elemental length is

$$\frac{dV}{dt} = \left|\frac{dJ}{dx}\right| dx \cdot a_c \tag{6.16}$$

where a_c is the area of dislocation core and *J* is the volumetric flux, defined as the volume of atoms flowing through unit area per unit time. Assume that the dislocation segment climbs at a constant rate *v*, thus

$$\frac{dV}{dt} = |v| \cdot dx \cdot b \tag{6.17}$$

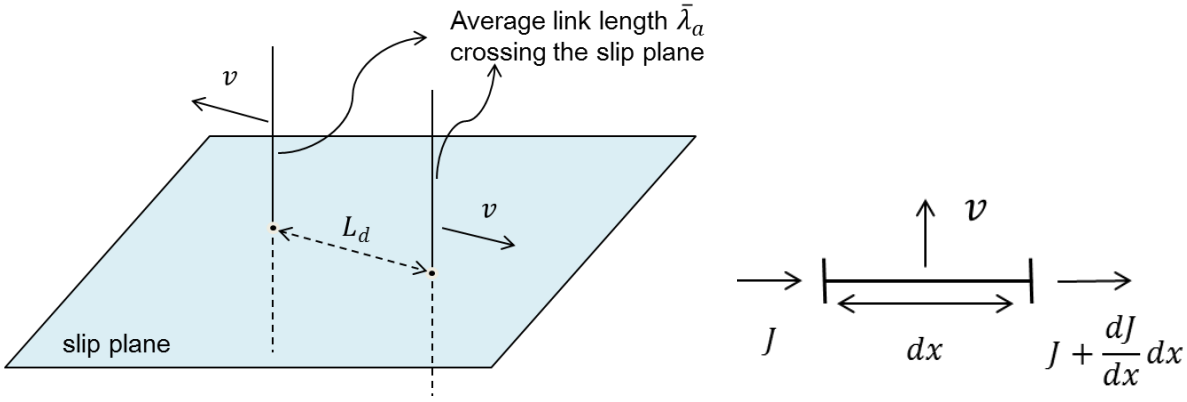

(a) (b)

Fig. 6.3. (a) Schematic of climbing (at a constant rate *v*) of two dislocation segments crossing a single slip plane with an average length $\bar{\lambda}_a$ and separated by L_d; (b) Diffusional flux across a small length *dx* on a segment by atoms diffusing dominantly through the dislocation core

Note that v is also associated with the rate of change of L_d on the slip plane ($v \approx \dot{L}_d / 2$ in terms of Figure 6.3a). Combination of Eqs. (6.16) and (6.17) determines the flux J

$$\left|J\right| = \frac{\left|v\right|b}{a_c} x + W = \frac{\left|\dot{L}_d\right|b}{2a_c} x + W \tag{6.18}$$

where W is an integration constant. Eq. (6.18) indicates that the flux varies along the dislocation segment. Now consider a representative dislocation segment of length $\bar{\lambda}_a$, the average link length. Further, assume that the flux J=0 at the centre of the link, x=0. Thus W=0. Therefore, the average flux on the dislocation segment can be simply calculated as

$$\left|\bar{J}\right| = \frac{2}{\bar{\lambda}_a} \int_0^{\bar{\lambda}_a/2} \left|J\right| dx = \frac{\left|\dot{L}_d\right| b \bar{\lambda}_a}{8a_c} \tag{6.19}$$

We can adopt alternative assumptions and approximations, but most reasonable approximations only change the constant in Eq. (6.19). According to Fick's law, the volumetric flux J can be expressed as

$$J = Mf \tag{6.20}$$

where $M = D_c \Omega / kT$ is the climb mobility (D_c: core diffusivity; $\Omega \approx b^3$: atomic volume; k: Boltzmann constant and T: temperature) and f is the thermodynamic driving force for diffusion—the negative of the gradient in the chemical potential. Note that the total length of the climbing segments per unit volume crossing the slip plane is of the order of $1/\bar{\lambda}_a^3 \times \bar{\lambda}_a = 1/\bar{\lambda}_a^2$ (it is not necessary to determine the detailed proportionality here; this will be addressed later). Therefore, the total volume V of the climbing dislocation segments per unit volume can be written as (taking into account that only half of the segments climb)

$$V = \frac{a_c}{2\bar{\lambda}_a^2} \tag{6.21}$$

Therefore, the rate potential Ψ_a for the climbing dislocation segments on this single slip plane can be determined by

$$\Psi_a = \int_V \frac{1}{2} f \cdot J dV = \int_V \frac{1}{2M} J^2 dV = \frac{1}{2M} \bar{J}^2 \cdot \frac{a_c}{2\bar{\lambda}_a^{\,2}} \tag{6.22}$$

Taking into account all the four slip planes, the overall rate potential can be obtained, considering Eq. (6.19), as

$$\begin{aligned} \Psi = \sum \Psi_a &= \frac{1}{2M}\left(\bar{J}_1^{\,2} \cdot \frac{a_c}{2\bar{\lambda}_{a1}^{\,2}} + \bar{J}_2^{\,2} \cdot \frac{a_c}{2\bar{\lambda}_{a2}^{\,2}} + \bar{J}_3^{\,2} \cdot \frac{a_c}{2\bar{\lambda}_{a3}^{\,2}} + \bar{J}_4^{\,2} \cdot \frac{a_c}{2\bar{\lambda}_{a4}^{\,2}} \right) \\ &= \frac{1}{2M}\left(\frac{b^2}{128a_c} \dot{L}_{d1}^{\,2} + \frac{b^2}{128a_c} \dot{L}_{d2}^{\,2} + \frac{b^2}{128a_c} \dot{L}_{d3}^{\,2} + \frac{b^2}{128a_c} \dot{L}_{d4}^{\,2} \right) \end{aligned} \tag{6.23}$$

Eq. (6.23) shows that the rate potential Ψ is independent of the precise definition of $\bar{\lambda}_a$. Finally, substituting Eqs. (6.15) and (6.23) into Eq. (6.11), the functional Π is (taking $a_c \approx 2b^2$ [11])

$$\begin{aligned} \Pi = \Psi + \dot{\Phi} &= \frac{1}{512M}\left(\dot{L}_{d1}^{\,2} + \dot{L}_{d2}^{\,2} + \dot{L}_{d3}^{\,2} + \dot{L}_{d4}^{\,2} \right) \\ &- \frac{1}{2}\Gamma\left(\frac{1}{L_{d1}^{\,3}} \dot{L}_{d1} + \frac{1}{L_{d2}^{\,3}} \dot{L}_{d2} + \frac{1}{L_{d3}^{\,3}} \dot{L}_{d3} + \frac{1}{L_{d4}^{\,3}} \dot{L}_{d4} \right) \end{aligned} \tag{6.24}$$

Using the principle $\delta\Pi = 0$, i.e.

$$\frac{\partial \Pi}{\partial \dot{L}_{d1}} = \frac{\partial \Pi}{\partial \dot{L}_{d2}} = \frac{\partial \Pi}{\partial \dot{L}_{d3}} = \frac{\partial \Pi}{\partial \dot{L}_{d4}} = 0 \tag{6.25}$$

and substituting M and Γ into Eq. (6.25), the change of the mean spacing on individual slip planes can be obtained, which is independent of the mean spacing on other slip planes:

$$\dot{L}_{di} = \frac{64 D_c G b^5}{kT} \cdot \frac{1}{L_{di}^{\,3}} \qquad (i=1\sim4) \tag{6.26}$$

Note that the fact that there is no interaction between the coarsening processes on the different slip systems is a direct consequence of our assumption that the total dislocation

density is simply an arithmetic mean of the contributions from the four families of slip planes. Other choices of relationship will, most likely, result in relationships where there is some coupling/interaction between the changes of link length on the different slip planes. We do not explore this further here, but Eq. (6.26) provides the simplest possible form of relationship for the recovery process. We can examine its suitability by examing its ability to model the influence of recovery on the creep process.

The recovery law of Eq. (6.26) gives a power-law relationship between $\dot{L}_{di}$ and $1/L_{di}$. Note that in addition to the no interaction of the climbing process on the different slip planes described above, many other simplifying assumptions have been used in the derivations of Eq. (6.26), such as the simplified calculation of the average flux on each climbing dislocation segment (Eq. (6.19)) and assuming that half the segment rearrange by climb. However, in reality, variation of these additional assumptions is understood to only change the constant in Eq. (6.26). Therefore, for general problems, we can take the following alternative expression

$$\dot{L}_{di} = \frac{W_c D_c G b^5}{kT} \cdot \frac{1}{L_{di}^{\ 3}} \qquad (i=1\sim4) \tag{6.27}$$

where W_c serves as a fitting parameter. Further, the reduction of the number of pinning points on individual slip planes can be directly obtained, considering that $L_d = N_d^{-1/2}$

$$\dot{N}_{di} = -\frac{2}{L_{di}^{\ 3}} \dot{L}_{di} = -\frac{2W_c D_c G b^5}{kT} \cdot \frac{1}{L_{di}^{\ 6}} = -\frac{2W_c D_c G b^5}{kT} \cdot N_{di}^{\ 3} \quad (i=1\sim4) \tag{6.28}$$

Eq. (6.28) can also be substituted into Eq. (6.13) to determine the reduction of the dislocation density.

6.3.3. Combination of hardening and recovery law

The hardening law in the athermal model developed in Chapter 3 shows that the mean spacing on individual slip planes decreases with increasing plastic strain as more pinning

points are introduced. It has been demonstrated that the rate of change of mean spacing on a given slip plane *i* depends on the mean spacing only on the same slip plane but also depends on the plastic shear strain rate on all the slip planes due to self- and latent hardening, i.e. a full relationship of the rate of change of the mean spacing can be written as

$$\dot{L}_{di} = -\frac{1}{2} N_{di}^{3/2} \cdot \dot{N}_{di} = -\frac{1}{2} L_{di}^{3} \cdot \left(\frac{j_s}{s} \dot{\gamma}_i + \frac{j}{3s} \sum_{k \neq i} \dot{\gamma}_k \right) \quad (i=1\sim4) \qquad (6.29)$$

where $\dot{\gamma}_i$ refers to the sum of all the plastic shear strain rates on the three slip systems on the slip plane *i*. Considering that the recovery law (Eq. (6.27)) describes an increase of L_{di} during the network coarsening process, the overall change of L_{di} on the slip plane *i* with combined hardening and recovery processes can be expressed as

$$\dot{L}_{di} = -\frac{1}{2} L_{di}^{3} \cdot \left(\frac{j_s}{s} \dot{\gamma}_i + \frac{j}{3s} \sum_{k \neq i} \dot{\gamma}_k \right) + \frac{W_c D_c G b^5}{kT} \cdot \frac{1}{L_{di}^{3}} \quad (i=1\sim4) \qquad (6.30)$$

Eq. (6.30) gives the overall evolution law of the state variable (L_{di}), which can then be used to determine the evolution of the corresponding internal resistance, or critical resolved shear strength (CRSS), contributed from forest dislocation junctions (Eq. (3.6)). During steady state creep, it is expected that the state variable becomes almost constant ($\dot{L}_{di} = 0$), i.e. a balance is reached between hardening and recovery.

Further, note that the rate of reduction of the number of pinning points described by Eq. (6.28) does not distinguish between general dislocation links or secondary loops surrounding the particles. In fact, given a total N_{di} dislocation links on the slip plane *i*, consisting of N_{li} loops, the rate of reduction of N_{li} can be simply expressed using a statistical approach

$$\dot{N}_{li} = \frac{N_{li}}{N_{di}} \dot{N}_{di} \qquad (i=1\sim4) \qquad (6.31)$$

The overall rate of change of N_{li} with combined hardening and recovery can be obtained, considering Eq. (3.16),

$$\dot{N}_{li} = \frac{3 f_v}{2\pi r_p^{\,2}} \dot{\gamma}_i - \frac{N_{li}}{N_{di}} \dot{N}_{di} \tag{6.32}$$

It is expected that during steady state of creep, $\dot{N}_{li} = 0$. In addition, since the Type III internal stress in the particles has been characterised as the stress exerted on the particles by the surrounding loops, as depicted in Chapter 3, this stress can be relieved by the recovery of dislocation loops, which, in reality, can be determined in terms of Eqs. (3.16) and (3.21)

$$\left(\dot{\tau}_m^r\right)_i = -0.7\alpha_l G \dot{\gamma}_i f_v^{\,3/2} = -0.7\alpha_l G \left(\frac{2\pi r_p^{\,2}}{3 f_v} \dot{N}_{li} \right) f_v^{\,3/2} \qquad (i=1\sim4) \tag{6.33}$$

Finally, as noted earlier, similar to the physics of self- and latent hardening on different slip planes (see Chapter 3), self- and latent recovery may also occur, especially if we consider the overlap of dislocation links between four slip planes, which may result in non-linear approximations of the dislocation density as shown in Eq. (6.13) and lead to a change in the final relationship in Eqs. (6.27) and (6.28). However, these complexities are not taken into account in this study to avoid introducing more complexity into the model.

6.4. Phase transformation at elevated temperatures

Besides the change of the state variables associated with dislocation structure, i.e. the mean spacing between forest dislocation junctions on the different slip planes, as considered in section 6.3, long-term thermal exposure and/or creep deformation leads to more complex evolution of microstructure, in particular, change of population of precipitates. This section describes a separate phase transformation model that captures the change of other state variables, such as the mean inter-particle spacing and mean radius of precipitates.

Generally, the relevant physical parameters describing the precipitates include (1) their crystallography; (2) their morphology; (3) their chemical composition; (4) their size

distribution (or simply mean size); (5) their volume fraction (the mean spacing can be directly obtained by (4) and (5) as shown in Eq. (3.11)); and (6) their number density [162]. However, for mechanical purposes, according to the athermal precipitation strengthening modelled in Chapter 3, we concentrate on how the last three aspects evolve during phase transformation at elevated temperature, which consists of three sub-processes, respectively nucleation, growth and coarsening, as described in Chapter 2. All other aspects are simplified in this study.

Various approaches have been proposed or developed to predict the evolution of different phases in metallic alloys during thermal treatments. Among them, the most well-known fundamental framework is the classical phase transformation model proposed by Avrami [60, 163] or more generally called the Johnson-Mehl-Avrami-Kolmogorov (JMAK) model, which simply assumes constant nucleation and growth rates to calculate the volume fraction of different phases that have transformed [60]. The model has been extended by different groups [62, 63, 123, 162], taking into account non-constant nucleation and growth rates of particles and the interaction between different phases. All these works are applicable only for evolution of precipitates during pure thermal ageing, while enhanced precipitation by creep has been discussed and modelled elsewhere in different ways [123, 164, 165].

In this section, we take the basic physics of the classical JMAK model for transformation of one or multiple phases and incorporate extensions, including non-constant nucleation and growth rates and the effect of creep loading. Following the geometric assumptions used in Chapter 3, all precipitates are considered to be spherical, i.e. they grow isotropically.

6.4.1. Precipitate nucleation and growth

6.4.1.1. JMAK phase transformation model

The JMAK theory describes how solids transform from one phase to another at constant temperature, incorporating an extended volume method to calculate the increment in the

volume fraction to be transformed, and to relate it to the current value of the transformed fraction. Here the extended volume means the volume of the new phase that would nucleate if the entire sample is still untransformed. Initially, particles are allowed to grow into each other, i.e. nucleation may occur even in the regions which have already transformed. During a time interval Δt, the new number of nuclei N_p that appear in a volume V is

$$N_p = V\dot{N}_p \Delta t \tag{6.34}$$

where $\dot{N}_p$ is the nucleation rate of precipitates per unit volume. The extended volume ΔV_p^e of the new phase in the time interval is

$$\Delta V_p^e = V\dot{N}_p \Delta t \cdot \frac{4\pi}{3}\left(\dot{r}_p \Delta t\right)^3 \tag{6.35}$$

where "e" refers to "extended" and $\dot{r}_p$ is the growth rate of the mean radius r_p of spherical particles. In fact, only a fraction of this volume is real, because some of the nuclei lie within previously transformed material, which is called impingement. If nucleation occurs randomly and homogeneously in the parent material, then the probability that any change in extended volume lies in the untransformed parent phase is proportional to the fraction of untransformed material at that instant. Thus the real change of volume in the time interval is

$$\Delta V_p = \left(1 - \frac{V_p}{V}\right)\Delta V_p^e \tag{6.36}$$

where V_p is the current volume of particles before the time interval Δt. Eq. (6.36) indicates a cease of particle growth at points of impingement and continuation unabated elsewhere. The simplifications of constant nucleation and growth rate in the original JMAK model [166] allows an easy integration of Eq. (6.35) over the entire time period and the final rearranged equation, considering Eq. (6.36), gives rise to the evolution of the volume fraction f_v

$$f_v = \frac{V_p}{V} = 1 - \exp\left(-Kt^4\right) \tag{6.37}$$

where $K = \pi \dot{N}_p \dot{r}_p^3 / 3$ is a constant. Eq. (6.37) depicts the basic characteristics of phase transformation, where the rate is slow at the beginning and the end of the process but rapid in between. In the JMAK theory, the theoretical maximum volume fraction that can be transformed by a single phase is 1, which can be attained when $t \to \infty$ in Eq. (6.37).

In some complex cases, simultaneous reactions can occur where multiple phases may transform from the parent phase. For each phase, only that formed in the untransformed parent phase will contribute to the real volume of the same phase. Thus on average, a fraction $\left(1 - \sum_{k=1}^{n} V_k \Big/ V\right)$ of the extended volume will be in previously untransformed material, where the sum is over all *n* phases that have transformed. It follows that the extended volume of *i* (Eq. (6.36)) can be written as

$$\Delta V_i = \left(1 - \sum_{k=1}^{n} V_k \Big/ V\right) \Delta V_i^e \qquad (i=1\sim n) \tag{6.38}$$

However, in such cases, the evolution of the volume fraction of each phase can only be determined numerically and the maximum volume fraction of each phase that can be transformed is less than 1.

6.4.1.2. Classical nucleation theory

One of the most significant extensions of the traditional JMAK model is the incorporation of classical nucleation theory (non-constant nucleation rate) based on the change in Gibbs free energy G^* or the activation energy associated with the formation of a precipitate in a supersaturated solid solution, which has been reviewed by Christian [60]. Given precipitates with spherical shape, G^* is simply given by

$$G^* = \frac{4}{3}\pi r_c^3 G_v + 4\pi r_c^2 \chi \tag{6.39}$$

where r_c is the critical radius of stable nuclei, χ is the interfacial energy of the precipitate and G_v is the chemical driving force for precipitation. Thermodynamics tells us that the critical radius of the stable nuclei can be determined such that the Gibbs free energy is minimized

$$\frac{\partial G^*}{\partial r_c} = 0 \rightarrow r_c = -\frac{2\chi}{G_v} \tag{6.40a}$$

$$G^* = \frac{16\pi\chi^3}{3G_v^{\ 2}} \tag{6.40b}$$

Expressions for the chemical driving force G_v have been given elsewhere [27, 123, 164]

$$G_v = -\frac{kT}{v_m}\ln\left(\frac{\bar{c}}{c_{eq}}\right) \tag{6.41}$$

where v_m is the molecular volume of the concerned phase, $\bar{c}$ and c_{eq} are respectively current and equilibrium solute concentration in the matrix, referring to the component of the phase. Note that for compound phases, $\bar{c} = \Pi \bar{c}^i$ (and $c_{eq} = \Pi c_{eq}^i$) refers to the product of current (equilibrium) solute concentration of all components of the phase (e.g., for the carbide $M_{23}C_6$, $\bar{c} = \bar{c}^M \cdot \bar{c}^c$ and $c_{eq} = c_{eq}^M \cdot c_{eq}^c$) [164]. Our formulation of the nucleation rate is based on this theory. For a detailed explanation, one can refer to [60, 123, 162, 164]. These studies give

$$\dot{N}_p = N_{site} Z \beta^* \exp\left(-\frac{G^*}{kT}\right)\exp\left(-\frac{t^{in}}{t}\right) \tag{6.42}$$

where N_{site} is the number density of potential nucleation sites per unit volume, Z is called the Zeldovich factor, representing the probability that a nucleus with a size corresponding to the top of the nucleation barrier will continue to grow to form the new phase, i.e. not dissolve; β^* is the condensation rate of atoms in a particle with critical radius, or the rate at which molecules attach to the nucleus causing it to grow; t^{in} is an incubation time and $\exp\left(-t^{in}/t\right)$

relates to the achievement of a steady state nucleation. Expressions of Z, β^* and t^{in} have been given in the literature [60, 123, 162, 164].

$$Z = \frac{v_m}{2\pi r_c^{\,2}}\sqrt{\frac{\chi}{kT}} \tag{6.43a}$$

$$\beta^* = \frac{4\pi r_c^{\,2} D^i c^i}{a_m^{\,4}} \tag{6.43b}$$

$$t^{in} = \frac{2}{\pi\beta^* Z^2} \tag{6.43c}$$

where a_m is the lattice parameter of the parent phase and D^i and c^i are respectively the bulk diffusivity and concentration of the rate-controlling solute elements in the matrix, in relation to the components of the precipitate phase.

6.4.1.3. Parabolic growth theory

The assumption of constant growth rate used in the traditional JMAK model has been understood to be valid only when the growth is very fast so that the interface of a particle almost moves at a constant speed [60]. Another important extension is the non-constant growth rate, following Zener's growth law [167], which physically describes that the growth rate of particles is dependent on the gradient of solute concentration (present only in the immediate vicinity of the precipitate interface [62]); thus the growth rate is controlled by solute diffusion. In fact, the constant growth rate can be explained using Zener growth theory when there is always an oversupply of solute elements in the matrix (extensive supersaturation), then the gradient of solute concentration can be approximated to be constant.

For this approach, we simply focus on the mean radius $\bar{r}_p$ of the spherical precipitates and ignore the particle size distribution. According to Zener's theory [167], $\bar{r}_p$ can be written as

$$\bar{r}_p = \alpha_\lambda \sqrt{D^i t} \tag{6.44}$$

where "*i*" here indicates the rate-controlling component and α_λ is a dimensionless growth coefficient depending on the gradient of solute concentration. An approximate approach has been widely used to determine α_λ, assuming that the solute concentration c^i changes at a constant rate from c^i_{eq} at the particle-matrix interface to $\bar{c}^i$ in the matrix far away from the precipitate phase, as shown in Figure 6.4.

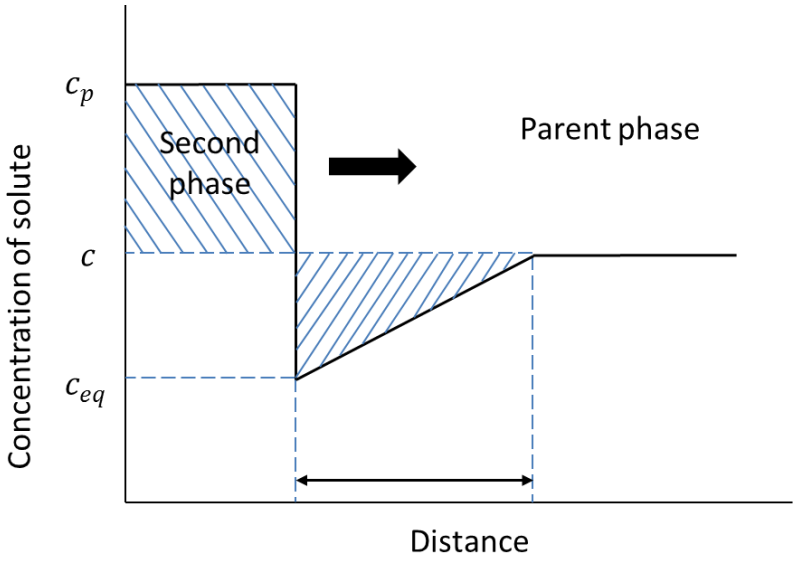

Fig. 6.4. The constant solute concentration approximation profile

Zener's analysis gives

$$\alpha_\lambda = \sqrt{2\left(\frac{\bar{c}^i - c^i_{eq}}{c^i_p - c^i_{eq}}\right)} \tag{6.45}$$

where c^i_p is the solute concentration in the precipitate phase. Eqs. (6.44) and (6.45) can be rearranged to determine the growth rate of the mean radius $\bar{r}_p$, which shows a parabolic feature [123, 162, 164]

$$\dot{\bar{r}}_p = \frac{D^i}{\bar{r}_p} \cdot \frac{\bar{c}^i - c^i_{eq}}{c^i_p - c^i_{eq}} \tag{6.46}$$

Further, during simultaneous nucleation and growth, Eq. (6.46) is modified, taking into account the formation of $\Delta N_p = \dot{N}_p \Delta t$ new nuclei with size r_c in the existing population of precipitates with mean radius $\bar{r}_p$ [123, 162, 164] to give

$$\dot{\bar{r}}_p = \frac{D^i}{\bar{r}_p} \cdot \frac{\bar{c}^i - c^i_{eq}}{c^i_p - c^i_{eq}} + \frac{\dot{N}_p}{N_p}\left(r_c - \bar{r}_p\right) \tag{6.47}$$

As the volume fraction and mean radius evolve during precipitation, as shown in Eqs. (6.38) and (6.47), the change of mean inter-particle spacing can be directly calculated by Friedel's model, i.e. Eq. (3.10).

6.4.1.4. Evolution of solute concentration

The precipitation process results in depletion of solutes from the matrix, thus the concentration decreases. If $\bar{c}_0^{\,i}$ is the initial concentration of element *i* in the matrix, the current concentration $\bar{c}^i$ can be calculated in the following way [62]

$$\bar{c}^i = \frac{\bar{c}^i_0 - f_v c^i_p}{1 - f_v} \tag{6.48}$$

The change of matrix composition during precipitation can affect subsequent nucleation and growth processes. In fact, a decrease of $\bar{c}^i$ leads to an increase of Gibbs free energy G^* in the system in terms of Eqs. (6.40b) and (6.41), and thus reduces the nucleation rate in Eq. (6.42). In addition, since $\bar{c}^i_p$ and c^i_{eq} are approximately constants for a given stable phase, a decrease of $\bar{c}^i$ also reduces the concentration gradient and thus the growth rate of $\bar{r}_p$ (Eq. (6.46)).

6.4.2. Particle coarsening

In the late stage of transformation of a given phase, the nucleation rate in the desaturated solid solution progressively decreases until the gradient of solute concentration becomes

almost zero. Afterwards the material experiences coarsening or Ostwald Ripening, during which large particles grow while small ones shrink and vanish, but the volume fraction of precipitates remains unchanged [58]. As a result, both the mean radius and mean inter-particle spacing increases. Given a dilute binary system where the maximum volume fraction that can be transformed is small, e.g. <30% [60], the most widely accepted theory to model the kinetics of diffusion-controlled coarsening of a given phase is the Lifshitz-Slyozov-Wagner (LSW) theory, which gives the mean radius of spherical particles after a time *t* [58]

$$\bar{r}_p^{\,3} = \bar{r}_0^{\,3} + Ct \tag{6.49a}$$

Or alternatively $$\left(\dot{\bar{r}}_p\right)_{coars} = \frac{C}{3\bar{r}_p^{\,2}} \tag{6.49b}$$

where $\bar{r}_0$ is the original radius before coarsening and $C = 8\chi V_m^{\,2} D^i c^i / 9RT$ is a coarsening parameter (with same definitions of *R*, χ, D^i and c^i as before and V_m is the molar volume of a given phase). Many attempts to improve the LSW theory have not fundamentally changed the cubic coarsening kinetics described in Eq. (6.49) [60, 168, 169]. Further, note that the volume fraction of precipitates is always constant during coarsening

$$f_v = \frac{4\pi}{3}\bar{r}_p^{\,3} N_p = cons \tag{6.50}$$

Thus a change of number density of precipitates during coarsening can be directly obtained as

$$\left(\dot{N}_p\right)_{coars} = -\frac{3N_p}{\bar{r}_p}\left(\dot{\bar{r}}_p\right)_{coars} \tag{6.51}$$

Note that the internal resistance for a wider dispersion of precipitates is lower than that of a narrower one, as illustrated in Chapter 2. Thus the precipitation nucleation and growth processes strengthen the material while the particle coarsening process softens the material. However, care needs to be taken when multiple phases transform consecutively (e.g. carbide and Laves phase in 316 stainless steels as described in Chapter 2). Unsynchronized

nucleation, growth and coarsening of different phases may lead to a very complex evolution process of the mean size and/or mean inter-particle spacing.

6.4.3. Effect of creep loading

One complexity, which can arise when modelling phase transformation, is the concomitant creep deformation which promotes or accelerates the phase transitions [36, 37, 123, 164, 165]. Note that creep deformation introduces more crystalline defects (notably dislocations) in the material than pure thermal ageing, thus terminologies in the literature describing the precipitation process with such complexity include stress-assisted or strain-induced precipitation, or heterogeneous precipitation on dislocations [123, 164, 165, 170]. Extensions of the phase transformation model described in sections 6.4.1 and 6.4.2 incorporating such superimposed plasticity/creep effect can be found in [123, 164]. Some qualitative overview about the effect of creep loading on phase transformation can be found in [165]. It is found, however, that regardless of the complexity in the developments of the phase transformation model, enhancement of the kinetics of precipitation due to creep may be regarded as a consequence of the following two aspects [37]:

(1) Dislocations provide more extensive heterogeneous and energetically favourable nucleation sites (reduced nucleation barrier, or Gibbs free energy, compared to homogeneous transformation), thus enhancing the nucleation rate;

(2) Dislocations act as short-circuit diffusion paths, where the exchange of solute between the precipitates can occur either by bulk diffusion, or by pipe diffusion through dislocation cores. This may lead to faster kinetics of precipitation during both growth and coarsening.

For simplicity, we do not incorporate the full complicated extensions in [123, 164] but retain the very simple elements that capture the basic physics. For aspect (1), the enhancement of nucleation rate by dislocations is accommodated by simply modifying the

Gibbs free energy G^* by introducing an adjustable parameter w (w<1), assuming that the heterogeneous nucleation barrier is proportional to the homogeneous barrier [164]

$$G^* = w\left(\frac{4}{3}\pi r_c^3 G_v + 4\pi r_c^2 \chi\right) \tag{6.52a}$$

$$G^* = w\frac{16\pi\chi^3}{3G_v^{\ 2}} \tag{6.52b}$$

We do not take into account the influence on the potential nucleation site since the rate dependence of the exponential is much larger than the pre-exponential in Eq. (6.42). Meanwhile, complexity of splitting w into two parameters to accommodate different changes in the surface and body of the nucleus due to heterogeneous nucleation is ignored. In relation to (2), diffusion can occur by dislocation pipe diffusion thus the effective diffusivity for both growth and coarsening processes can be expressed as a combination of bulk diffusivity D_L^i and pipe diffusivity D_p^i of the solute element "i" [11, 171]

$$D^i = D_L^i + a_c \rho D_p^i \tag{6.53}$$

Here $a_c \approx 2b^2$ is the area of the dislocation core, ρ is total dislocation density. Based on the above physics, it is understood that the effect of creep loading is more significant for intragranular than for intergranular precipitates, due to the change in dislocation population within the matrix. Therefore, in the simulations associated with phase transformation, which are to be presented in Chapter 7, we only focus on detailed intragranular precipitation but simplify intergranular precipitation to be independent of creep deformation. However, care needs to be taken with this simplification since solute atoms in the matrix can also be depleted during intergranular precipitation. Such depletion of solute atoms will result in a decrease of solute concentration, thus may reduce the effect of solute drag and change the kinetics of creep/plastic deformation, as described in section 6.2.3.

6.5. Summary

In this chapter, based on the athermal model for a single crystal established in Chapter 3, some enhancements at elevated temperature are incorporated and discussed, including the change in the deformation kinetics and extended evolution processes of the microstructure.

For the deformation kinetics, thermal exposure facilitates thermally activated dislocation glide motion and climb-controlled bypassing over particles (without formation of dislocation loops, compared with the Orowan bowing process), both of which demonstrate that the plastic shear strain can be generated even when the athermal deformation mechanisms are inhibited. The thermal solute drag process enhances the effectiveness of all kinds of obstacles as the solute atoms in the matrix diffuse down the dislocation core and are dragged along with mobile dislocations. This process is understood to be history independent and is a function of only the current strain rate and the current solute concentration of interstitial elements (in particular, carbon) for 316 stainless steels.

For the evolution of microstructure, the first part illustrates the climb-controlled recovery of the dislocation network, or recovery of the state variables associated with dislocation structure, i.e. the mean spacing between forest dislocation junctions on individual slip planes. A thermodynamic analysis is used to determine different recovery rates of the mean spacing on different slip planes. Combination of hardening and recovery laws determines the overall evolution of the state variables during creep. The second part refers to the transformation of multiple phases, consisting of nucleation, growth and coarsening processes, during which the state variables, in particular, mean inter-particle spacing and mean size of the different types of particles, may evolve. An extended JMAK phase transformation model is used to illustrate these processes, taking into account classical nucleation theory, a diffusion-controlled parabolic growth law and the traditional Oswald Ripening coarsening model. All these kinetics may be enhanced by external creep loading, compared with pure thermal ageing.

Finally, depletion of solute atoms in the matrix by precipitation process leads to a reduction in the solute concentration in the matrix and may reduce the extent of the solute drag process.

All the key equations within this chapter are summarized below:

(1) Thermally activated glide enhanced by solute drag

$$\dot{\gamma} = \dot{\gamma}_0 \exp\left(-\frac{\Delta F_0}{kT}\left(1 - \left| \frac{\tau + \overline{\tau}_m^r}{\left(1+F_{sol}\right)\tau_{cr}} \right|^g \right)^h \right) \operatorname{sgn}\left(\tau + \overline{\tau}_m^r\right)$$

$$F_{sol} = F_{sol,\max} \exp\left[-\left(\frac{\log\dot{\gamma} - \log\dot{\gamma}_{\max}}{B} \right)^2 \right]$$

(2) Plastic shear strain rate determined by dislocation climb bypassing over particles

Local climb: $$\left(\dot{\gamma}_p\right)_{LC} = Y\left(\tau - \tau_{LC}\right)\frac{16 D_c \rho_m b^5}{r_p{}^2 kT}\operatorname{sgn}\left(\tau\right)$$

General climb: $$\left(\dot{\gamma}_p\right)_{GC} = Y\left(\tau - \tau_{GC}\right)\frac{32 D_c \rho_m b^5}{r_p L_p kT}\operatorname{sgn}\left(\tau\right)$$

(3) Evolution of the mean spacing on individual slip planes between all the pinning points combining hardening and recovery of the dislocation network

$$\dot{L}_{di} = -\frac{1}{2} L_{di}{}^3 \cdot \left(\frac{j_s}{s}\dot{\gamma}_i + \frac{j}{3s}\sum_{k\neq i}\dot{\gamma}_k \right) + \frac{W_c D_c G b^5}{kT} \cdot \frac{1}{L_{di}{}^3}$$

(4) Precipitation nucleation, growth and coarsening

$$\dot{N}_p = N_{site} Z \beta^* \exp\left(-\frac{G^*}{kT} \right) \exp\left(-\frac{t^{in}}{t} \right)$$

$$\dot{\overline{r}}_p = \frac{D^i}{\overline{r}_p} \cdot \frac{\overline{c}^i - c_{eq}^i}{c_p^i - c_{eq}^i} + \frac{\dot{N}_p}{N_p}\left(r_c - \overline{r}_p \right)$$

$$\left(\dot{\overline{r}}_p\right)_{coars} = \frac{1}{3\overline{r}_p{}^2} \cdot \frac{8\chi V_m{}^2 D^i c^i}{9RT} \qquad \left(\dot{N}_p\right)_{coars} = -\frac{3N_p}{\overline{r}_p}\dot{\overline{r}}_p$$

The updated flowchart of the implementation of a general comprehensive creep model described in this chapter (combined with Chapters 3 &4) is shown in Figure 6.5, where the detailed equations are ignored in the figure.

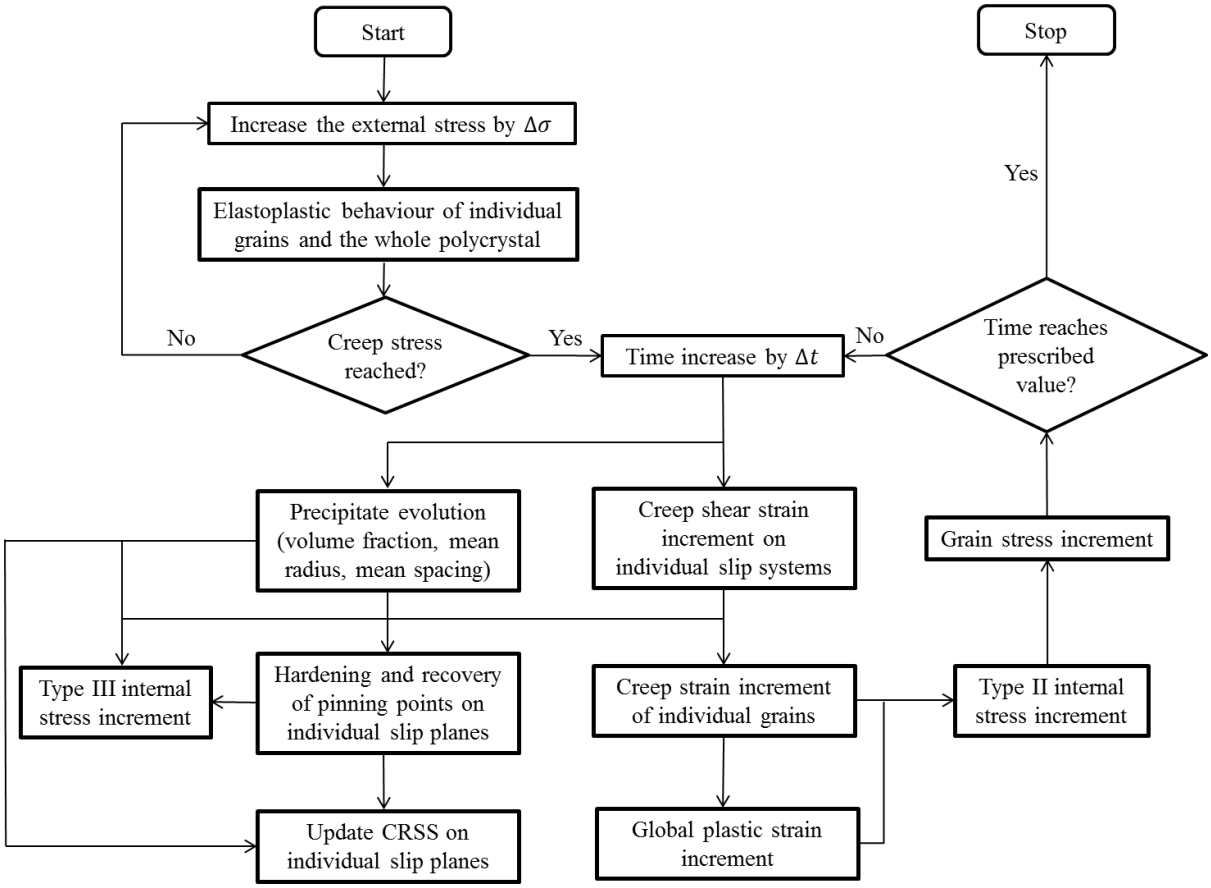

Fig. 6.5. Flowchart of the implementation procedure of the creep model. The block "elastoplastic behaviour of individual grains and the whole polycrystal" represents the same procedure described in Fig. 4.2

Chapter 7

Application II: High temperature behaviour of austenitic stainless steels under various stresses and/or temperatures

7.1. Introduction

In the literature, various experimental data related to the behaviour of Type 316H stainless steels at elevated temperatures are available. These data were collected during experiments at various temperatures and/or stresses, including monotonic plastic loading [157], creep deformation [25, 146, 172, 173], and microstructure characterisation [35, 36], where the last of these captured the evolution of populations of different precipitate phases during thermal ageing and/or creep. The specimens in these studies did not have identical initial conditions, some of which were ex-service or contained considerable populations of precipitates [146, 173], and others were initially solution treated to dissolve any precipitates [25, 36, 157, 172]. At the same time, extensive effort has been made to fit the data with different types of constitutive model and understand the underlying physical deformation mechanisms. Examples of these include use of Schmidt and Miller's unified phenomenological model [155], which has been applied extensively on different materials to a wide range of experiments like monotonic plastic loading and creep deformation. However, as mentioned in Chapter 2, the large number of fitting parameters may weaken the understanding of the underlying physics. Dyson's phenomenological model [105, 106] has been used to understand creep and relaxation of different materials, but was found to be more suitable to

materials with a very large volume fraction of precipitates, such as nickel-base superalloy. EDF Energy has examined a series of empirical models to evaluate creep and relaxation data of 316 stainless steels but none of the models is able to fit and explain all the observed results. Further, to date, none of the present constitutive models has systematically examined the influence of evolution of microstructure, in particular, precipitates, on the mechanical behaviour of materials at elevated temperatures.

This chapter attempts to evaluate the macroscopic behaviour of Type 316H polycrystalline austenitic stainless steels under various temperatures and/or stresses, using the combined multi-scale self-consistent model established in Chapters 3 & 4 and the high temperature enhancement of the model presented in Chapter 6. Emphasis is put on how the evolution of microstructure (forest dislocations, precipitates and solid solution) at elevated temperature influences the mechanical/creep properties of the material. Of all the available creep data, the applied stresses and temperatures were chosen such that creep deformation is in the dislocation creep regime for the material according to the Frost & Ashby deformation-mechanism maps [11]. The data measured at very high temperatures (>650^{o}C), which is out of the interested service range as described in Chapter 1, is not considered here.

7.2. Simulation I: Influence of creep deformation on materials Bauschinger effect

7.2.1. Brief introduction

Recall that in Chapter 5 we have evaluated the macroscopic Bauschinger effect of ex-service plus laboratory aged (EXLA) Type 316H polycrystalline austenitic stainless steel samples (EXLA2) with some high temperature (550^{o}C) tensile pre-strain history (loaded up to 250MPa, unloaded and cooled), using the athermal multi-scale self-consistent model

established in Chapters 3 & 4. The model predicts that the Type II and III residual stress fields play an important role in determining the observed Bauschinger effect. A suitable residual stress field established by high temperature tensile pre-straining leads to all individual grains deforming compatibly plastically in the specimen subjected to continued uniaxial tensile loading at ambient temperature (EXLA2-1), thus the stress-strain curve exhibits a sharp change in slope after yielding. However, in contrast, the residual stress field is significantly different to that which is required to give compatibility of plastic straining in the specimen subjected to reverse compressive loading (EXLA2-2). Plastic flow therefore occurs much earlier in some grains than in others while the residual stress field redistributes, and the stress-strain curve demonstrates a more gradual yielding process. Besides the transient softening phenomenon described above, the phenomenon of permanent softening is also explained as a relative definition dependent on the strain level that it is measured. It can only be delayed by the development of Type III residual stress associated with the particles and/or the surrounding dislocation loops (see Chapter 5).

In the neutron diffraction experiment conducted on ENGIN-X at ISIS, UK and on POLDI at SLS, Switzerland, the Bauschinger effect of some other specimens have also been tested, where these specimens have experienced an extended tensile pre-strain history, compared with the EXLA2 specimens in Chapter 5, consisting of high temperature (550^{o}C) creep deformation (250MPa) up to either the primary stage (~160h, designated EXLA3) or secondary stage (~1000h, designated EXLA4). These specimens were then subjected to either uniaxial tensile loading (EXLA3-1 and EXLA4-1) or compressive loading (EXLA3-2 and EXLA4-2) at ambient temperature, similar to the experimental procedure on the EXLA2 specimens with no pre-crept history. The entire loading history of these samples is schematically shown in Figure 7.1.

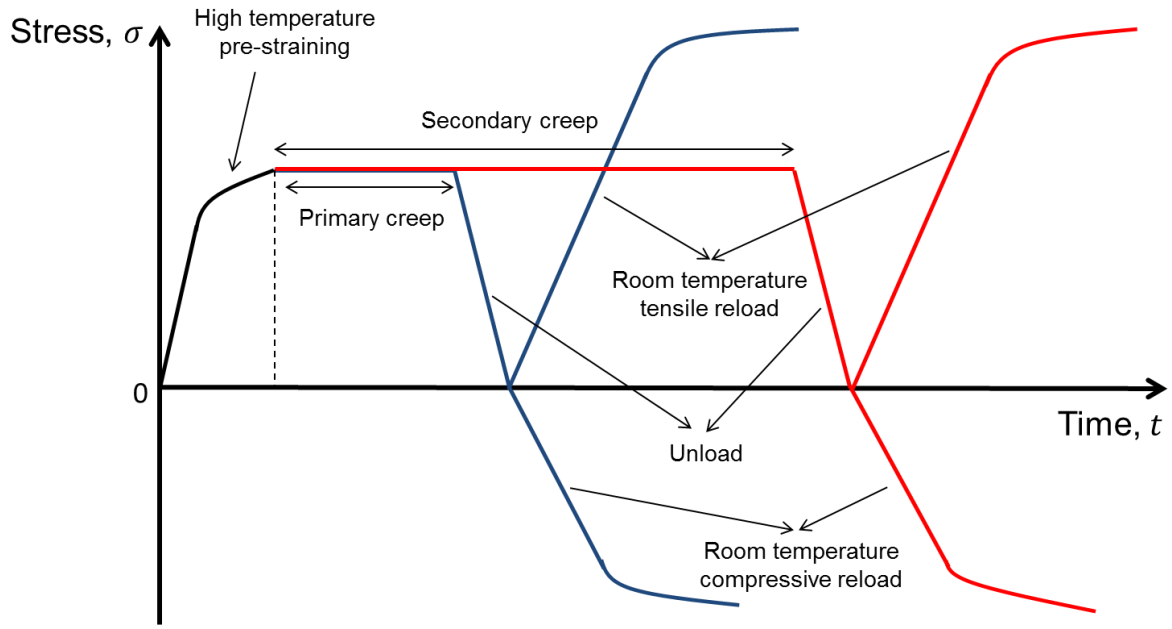

Fig. 7.1. A schematic diagram of the loading history of EXLA3 and 4 specimens; the black curve is the high temperature pre-straining, same as used in Chapter 5, and EXLA3 specimen further follows the blue lines and EXLA4 specimen further follows the red lines

This section consists of two parts. The first part examines the macroscopic Bauschinger effect of these EXLA3 and EXLA4 specimens. The key difference from the simulation on the EXLA2 specimens in Chapter 5 is the incorporation of the enhanced recovery model derived in Chapter 6 into the self-consistent model to simulate the creep deformation of the material. Here we focus only on the bulk response rather than the microscopic elastic lattice response since the change of elastic strain during creep deformation is understood (and is reflected in the neutron diffraction measurements) to be negligible. The second part extends the simulation in the first part by considering other creep tests conducted at different stresses on the same ex-service material.

7.2.2. Simulation procedure and material parameters

The material used in this simulation is the ex-service plus laboratory aged (EXLA) Type 316H polycrystalline austenitic stainless steel samples considered in Chapter 5, i.e. the initial

distribution of precipitates for each sample remains the same as that estimated in Chapter 5. Similarly, all slip systems for all grains within the polycrystalline materials were assumed to have identical critical resolved shear strength (CRSS) before commencement of any loading. The initial residual stress state is not considered here. For the first simulation on the EXLA3 and EXLA4 specimens, each group started from uniaxial pre-straining at 550^{o}C up to a macroscopic true stress of 250 MPa, followed by uniaxial tensile creep up to primary (~160h, EXLA3) or stationary (~1000h, EXLA4) stage at the same temperature and stress. Then each group was cooled and unloaded elastically with the developed CRSS and residual stress field remaining in the unloaded individual grains (which scale with the temperature-dependent modulus). Finally, the specimens were reloaded at ambient temperature, either in tension (EXLA3) or in compression (EXLA4), using the same procedure as that described in Chapter 5. During the simulation of creep, the applied stress remained the same but the CRSS on each slip system of each individual grain was updated using the combined hardening (Eqs. (3.6) and (3.7)) and recovery model (Eqs. (6.28) and (6.32)). The plastic shear strain rate was calculated by the rate-dependent flow rule (thermally activated glide, Eq. (6.1b)). While the update of the Type II residual stress of each grain remained the same as that in Chapter 5 using Eq. (4.23a), the Type III residual stress was updated using Eq. (6.33) as it recovers with the recovery of the dislocation structure. Phase transformation during these short-term creep deformations was ignored, as was the effect of solute drag due to the extensive depletion of carbon in the matrix by the precipitates. In these short-term tests, Orowan bowing dominates the contribution from the precipitates and the possibility of climb-controlled bypassing over particles does not need to be considered. Further, the recovery of dislocation structure was considered only during creep, and was ignored during the pre-straining at 550^{o}C before creep and reloading at ambient temperature in tension or compression. All strains were updated using the same approaches as described in Chapter 5. However, to be consistent throughout

the simulation in this section, the plastic shear strain rate during high temperature pre-straining and subsequent reloading was also calculated by the thermally-activated glide rule (Eq. (6.1b)) rather than the power-law relationship used in Chapter 5. The procedure adopted in the second set of simulations on the same ex-service materials at other stress levels remains the same, except the change in the preloading stress level at 550^{o}C.

The model was first used to fit the high-temperature pre-straining and creep curves and then to predict the macroscopic response of each specimen during subsequent uniaxial tension and compression at ambient temperature. Values of the physical parameters used in the simulations remain the same as shown in Table 5.2 and are summarized together with the new parameters required by the extended model in Table 7.1 (all values of stress or modulus are at room temperature and need to be scaled at 550^{o}C according to Eq. (5.1)). In the rate-dependent thermally activated glide rule of Eq. (6.1b), the reference shear strain rate $\dot{\gamma}_0$ is simply set to be 1/s as mentioned in section 6.2. The shape factors of energy barriers *g* and *h* were chosen to be *g*=3/4 and *h*=4/3, following Frost and Ashby [11]. For the activation energy ΔF_0, G_0 is obtained in terms of the shear modulus reported in the literature at room temperature. α_0 is fitted to be 1 for a combination of all types of obstacles. In the recovery model established in Chapter 6, the dislocation core diffusivity D_c for austenitic stainless steels at 550^{o}C was given by Frost and Ashby [11], 6.47×10^{-15} m^2/s, taking into account the dislocation core area $a_c \approx 2b^2$. While W_c in the model (Eq. (6.28) or Eq. (6.30)) was chosen to fit the creep curve.

Tab. 7.1 Material parameters of 316H austenitic stainless steels used in the simulation of creep deformation and its influence on materials Bauschinger effect

Parameter	Value	Parameter	Value
C_{11} [a]	198 GPa	τ_p	21 MPa
C_{12} [a]	125 GPa	τ_s	37 MPa
C_{44} [a]	122 GPa	j_s / s	4.0×10^{14}
E	101.3 GPa	j / s	2.0×10^{15}
v	0.39	W_c	40
G	122 GPa	D_c	6.47×10^{-15} m^2/s
G_0	139 GPa	a_0	1
b	2.5×10^{-10} m	g	3/4
α_d	0.35	h	4/3
N_0	2.4×10^{13}	$\dot{\gamma}_0$	1/s

[a] Data are taken from Kamaya [148].

7.2.3. Evaluation of materials Bauschinger effect

7.2.3.1. Creep at 250MPa stress

Similar to Figure 5.9 in Chapter 5, the simulated macroscopic responses of EXLA3 and EXLA4 during room temperature (RT) reloading in uniaxial tension (EXLA3-1 and EXLA4-1) and compression (EXLA3-2 and EXLA4-2) following high temperature (HT) uniaxial tensile pre-straining and tensile creep (primary or secondary) at 550^{o}C are shown in Figure 7.2, together with the experimental measurements. The corresponding measured and predicted creep curves are shown in Figure 7.3 separately. All these data can be found in [146], and all the compression data are shown using absolute values. The initial strain value of each specimen during RT reloading represents the total inelastic strain accumulated from HT pre-straining and creep. Note that some variability occurs in the experimental creep curves of these specimens (Figure 7.3), which has been attributed to variability in the service history of each tested specimen [146]. However, such variability in the creep curves is considered to be acceptable since all specimens show similar steady state creep rates. Therefore, to best compare our model predictions and the measurements during subsequent

RT reloading, the measured initial inelastic strain values accumulated from pre- HT creep for both EXLA3 and EXLA4 specimens have been modified to be consistent with the model predicted creep curve shown in Figure 7.4 at the correponding periods.

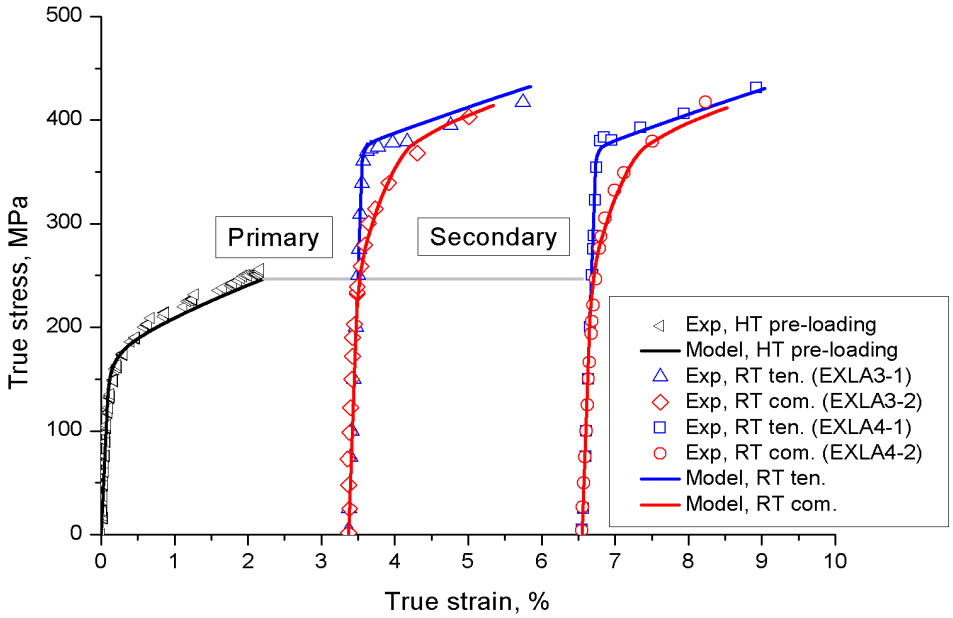

Fig. 7.2. Comparison between experimental data and model prediction in terms of macroscopic stress-strain relationship for pre-crept specimens (EXLA3 for primary stage and EXLA4 for secondary stage); the figure shows high temperature (HT, 550^{o}C) tensile pre-straining and subsequent reloading in tension (EXLA3-1 and EXLA4-1) and compression (EXLA3-2 and EXLA4-2) at room temperature (RT). The initial strain value for RT reloading accounts for the total inelastic strain accumulated during HT preloading and creep. Data and prediction for compression is shown in absolute value.

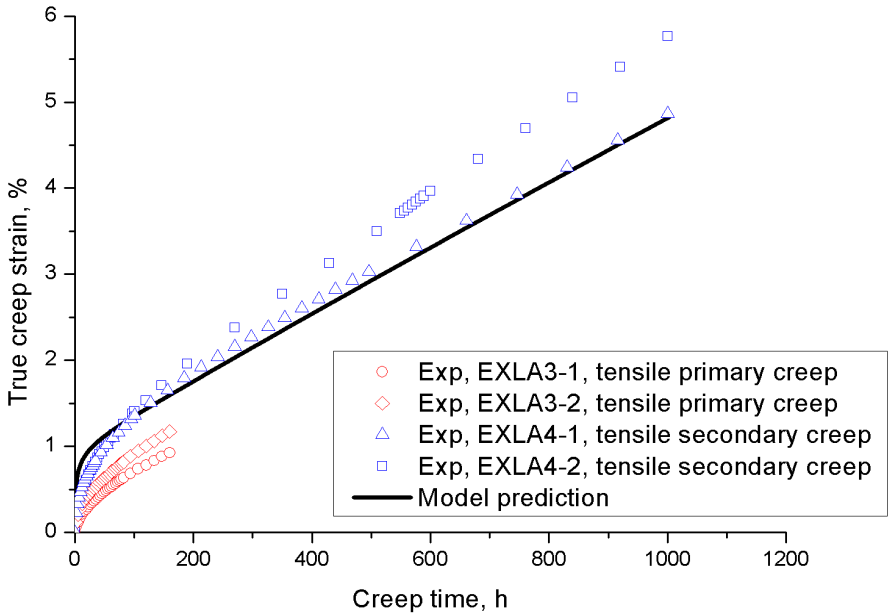

Fig. 7.3. Measured and predicted tensile creep curves for EXLA3 (160h) and EXLA4 (1000h) specimens. All these specimens were initially given the same HT pre-straining up to 250MPa external stress. Each group consists of two specimens subjected to the same creep test.

In Figure 7.2, compared with specimens without any pre-crept history (EXLA2 as used in Chapter 5), the transient softening is still observed and predicted in the specimens tested here, indicating a non-steady-state residual stress field for specimens subjected to compression (EXLA4). The mechanism in terms of the role of Type II residual stress field has been discussed in detail in Chapter 5. In addition, both predictions and experimental measurements of RT tensile curves demonstrate an increasing initial yield stress from EXLA2 (loading-up) to pre-crept specimens EXLA3 and EXLA4, but the increase of yield stress from EXLA3 (primary) to EXLA4 (secondary) is not significant. This feature is reproduced by the model, and is due to the continuous accumulation of dislocations and the development of the residual stress field during primary, and their gradual saturation towards the secondary stage. Further, a smooth transition following initial yielding is predicted by the model for both the pre-crept EXLA3 and EXLA4 specimens, rather than a sharp transition as observed for the EXLA2 specimen, which was not pre-crept, as shown in Figure 5.9. This indicates that the residual stress state redistributes or recovers within individual grains during creep deformation, and is different from that developed during HT plastic tensile pre-straining. A steady-state residual stress state is yet to be achieved again in the specimens during subsequent reloading.

7.2.3.2. Separation of isotropic and kinematic stress terms

In the literature, three empirical variables have been used to describe the evolution of inelastic deformation and evaluate the Bauschinger effect [146]: (i) an initial yield stress, σ_0, describing an isotropic resistance to create inelastic flow of material; (ii) a stress σ_{iso} describing the contributions to isotropic hardening; and (iii) a stress σ_{kin} describing the contributions to kinematic hardening. According to the definition, the flow stress at forward tensile loading σ_f and reverse compressive loading σ_r can be expressed as

$$\sigma_f = \sigma_0 + \sigma_{iso} + \sigma_{kin}$$
$$\sigma_r = -\sigma_0 - \sigma_{iso} + \sigma_{kin} \tag{7.1}$$

As a result, the isotropic and kinematic stress terms are given by

$$\sigma_{iso} = \frac{\sigma_f - \sigma_r}{2} - \sigma_0$$
$$\sigma_{kin} = \frac{\sigma_f + \sigma_r}{2} \tag{7.2}$$

For the Type 316H stainless steels employed in this study, the initial yield stress σ_0 was determined from the average value of the elastic limit obtained from the tested non-pre-strained specimens (e.g. EXLA1 in Chapter 5) [146]. For the EXLA2 (loading up), EXLA3 (primary) and EXLA4 (secondary) specimens, a small strain offset, $\varepsilon_{off} = 10^{-4}$, was used to determine point *A* on each tensile curve (corresponding flow stress σ_{f0}) and point *B* on each compressive curve (corresponding flow stress σ_{r0}), as schematically shown in Figure 7.4. These values were then used to calculate the isotropic and kinematic stresses in terms of Eq. (7.2) to evaluate the transient softening behaviour of each tested specimen [146].

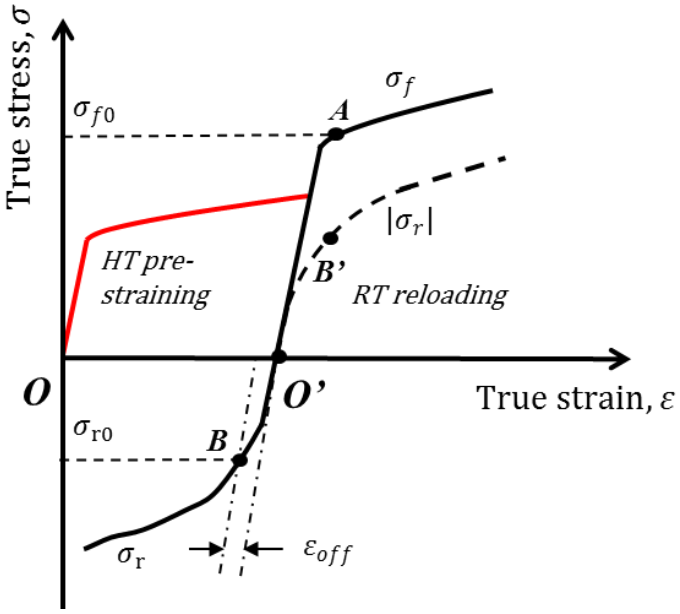

Fig. 7.4. Schematic diagram of the Bauschinger effect test, showing prior tensile creep deformation and continued (tensile) and reversed (compressive) straining at room temperature; A small strain offset ε_{off} is used to determine the isotropic and kinematic stress terms

The experimentally calculated evolution of isotropic and kinematic stress terms from the non-pre-strained condition through to the secondary pre-crept condition are shown in Figure 7.5(a). The horizontal axis refers to the total inelastic strain induced by high temperature pre-straining, including loading up and/or creep. Also shown in the figure are values predicted by the model, using the same approach described above (using Figure 5.9 for EXLA2, Figure 7.2 for EXLA3 and EXLA4). Note that a small difference of 2MPa, calculated from the experimental data for the reference non-pre-strained condition, is due to minor differences in σ_{f0} and σ_{r0} of several tested reference specimens [146]. It is found that the high-temperature pre-straining has resulted in an increase in both the isotropic and kinematic stresses. Subsequent primary creep pre-straining further enhances the isotropic stress but slightly reduces the kinematic stress. However, further creep pre-straining towards secondary stage does not change the values of these stresses significantly. This trend is well captured by the model. Compared with the result shown in Figure 7.2, this is understood to be consistent, in an empirical way, whereby the isotropic internal resistance (or CRSS) has developed during pre-straining and primary creep but has remained almost unchanged as secondary creep is approached, while the kinematic internal stress or residual stress state developed during pre-straining recovers during creep deformation, but then achieves a constant value.

A similar simulation with extended creep deformation has been carried out, where the material is allowed to creep for extended periods of 2000h and 4000h. The elongated creep curves are not shown here but we only focus on the evolution of the empirical isotropic and kinematic stresses due to this extended creep, which is shown in Figure 7.5(b). In the figure, the almost flat curves of both isotropic and kinematic stresses indicate nearly no change of the two stresses during the extended secondary stage, which is as expected since all state variables would have achieved a steady state at the beginning of this stage.

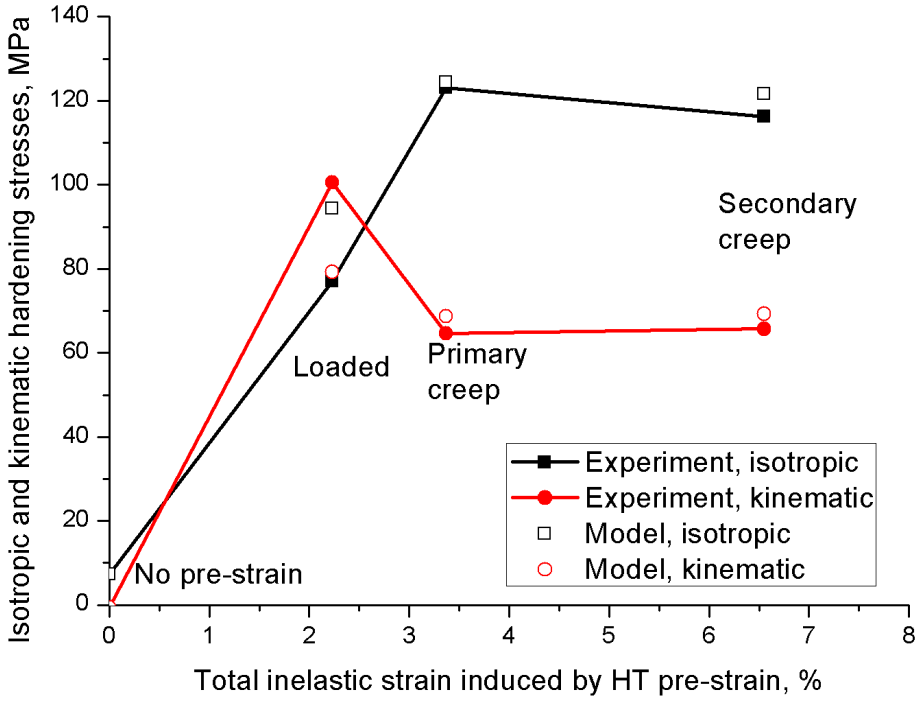

(a)

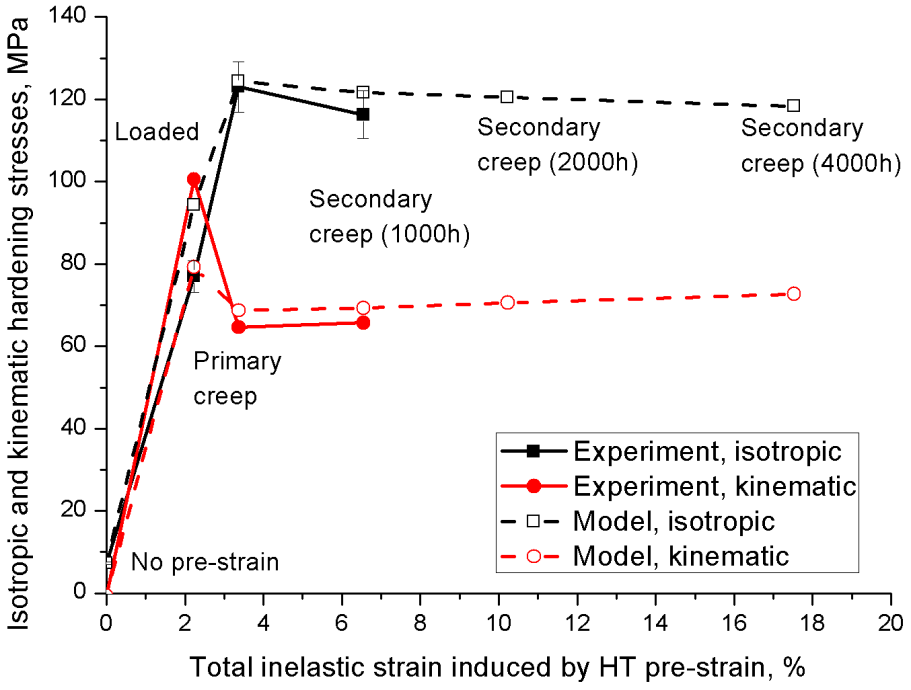

(b)

Fig. 7.5. Experimentally determined and model predicted evolution of the empirical isotropic and kinematic stresses. (a) The results are based on the macroscopic stress-strain curves illustrated in Figure 5.7 (EXLA2) and Figure 7.2 (EXLA3 and EXLA4); (b) Based on (a), some simulated results in materials with extended creep deformation are also shown.

7.2.3.3. Creep at other stresses

The above results and analyses are all based on creep deformation at 250 MPa, 550^{o}C. In this section, some additional creep curves of the same EXLA material tested at 550^{o}C but at other stresses (280 MPa and 320 MPa) are simulated. The only difference in this part is the different levels of plastic pre-straining experienced as the specimens are loaded up to the prescribed stress level. The measured and predicted creep curves are shown in Figure 7.6. Also shown in the figure are the results of the test conducted at 250 MPa discussed in the previous subsection, for comparison. It is found that the model successfully captures the increase of creep rate as the creep stress level increases.

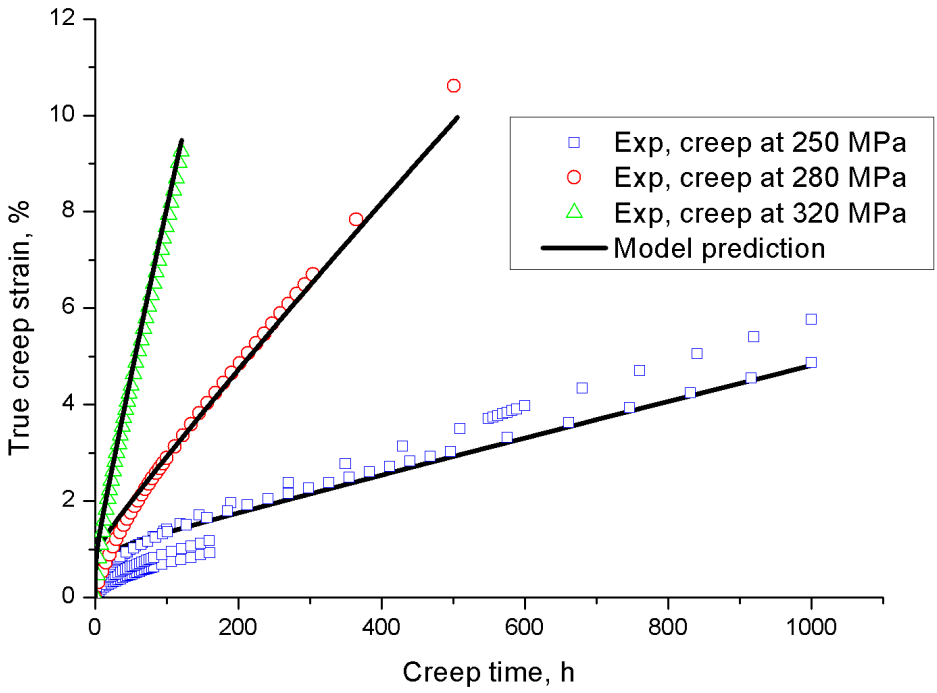

Fig. 7.6. Experimental and model predicted creep curves at different stresses.

Based on these simulated creep curves, the corresponding influence on the evolution of the empirical isotropic and kinematic stresses is also examined and is shown and compared in Figure 7.7. Extended creep deformation beyond the time shown in Figure 7.6 is also considered. It is found that the model predicts an enhancement of both isotropic and kinematic stresses as the creep stress increases, indicating a strong dependence on the level of

pre-straining. Both terms remain almost constant during secondary creep over an extended period, regardless of the creep stress level, which reflects the achievement of a steady state. Meanwhile, according to the study of the factors in determining materials Bauschinger effect, in particular, the Type III residual stress, as discussed in Chapter 5, the increase in the level of HT pre-straining would lead to an enhanced transient and relative "permanent" softening. This is successfully reflected in the predicted results, and is responsible for the difference between the isotropic and kinematic stresses being enhanced as the applied stress in increased (taking into account Eq. (7.2)).

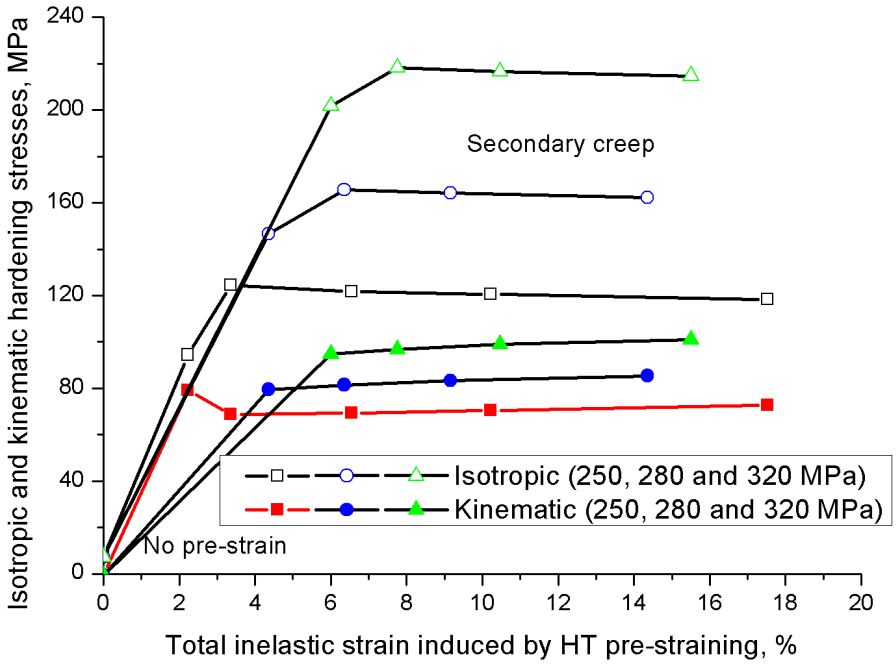

Fig. 7.7. Model predicted evolution of the empirical isotropic and kinematic stresses resulted from different levels of creep stresses, 250 MPa, 280 MPa and 320 MPa.

7.2.4. Summary

The influence of creep deformation on the Bauschinger effect of the EXLA Type 316H austenitic stainless steels is evaluated by using the multi-scale self-consistent model established in Chapters 3 and 4 combined with the recovery model of dislocation structure presented in Chapter 6. Phase transformation has been ignored in the short-term creep tests

and the effect of solute drag has not been taken into account in these EXLA specimens due to the extensive depletion of carbon in the matrix by the existing carbide precipitates. Key findings from these simulations consist of the following aspects:

- The critical resolved shear strength (CRSS) for individual slip systems of individual grains develops during high temperature pre-straining and subsequent primary creep, compared with the non-pre-strained condition, but it remains almost unchanged during secondary creep. This is consistent with the evolution process of the state variable towards a steady state, i.e. the number of forest dislocation junctions. Also during these stages, the population of precipitates and solute atoms does not change.
- The residual stress state of the individual grains also develops during high temperature pre-straining but may recover or redistribute during subsequent primary creep and remains almost unchanged during secondary creep. Once the residual stress recovers, it is different from that developed during high temperature pre-straining that ensures compatibility of plastic deformation for all grains during tensile reloading at ambient temperature. Therefore, the tensile reloading curves for pre-crept specimens exhibit a smooth initial yielding process rather than a sharp one and the full steady state residual stress field is yet to be achieved again during reloading.
- The evolution of physical CRSS and residual stress state can be correlated with the evolution of empirical isotropic and kinematic stress terms, calculated from the tensile and compressive reloading curves. At a given temperature, an increase of the stress level or level of high temperature pre-straining enhances the creep rate and the values of both isotropic and kinematic stresses, as well as the associated Bauschinger effect, and in particular, the transient softening behaviour. Both the isotropic and kinematic stresses saturate during secondary creep, regardless of the stress or high temperature pre-strain level.

- Understanding how the CRSS and residual stress state evolve during high temperature creep deformation is vital to assessing material behaviour during cyclic creep-fatigue loading.

7.3. Simulation II: Precipitation and phase transformation

7.3.1. Review of experimental measurement

So far in this study, the materials that have been evaluated are all in the ex-service condition (used in the AGR nuclear reactors at 490 ^{o}C - 530^{o}C for ~65,000 h) plus some laboratory ageing treatment (550^{o}C, ~22,000 h), in which a considerable population of precipitates has formed in the material both inter- and intragranularly. The presence of these precipitates changes the creep properties of the material compared with that of the initially solution annealed materials. In reality, substantial research has been carried out directly on solution annealed austenitic stainless steels, where the precipitates are yet to form during subsequent thermal ageing or creep loading. Since a number of deformation mechanisms are associated with the precipitates, i.e. Orowan bowing, dislocation climb-controlled bypassing, dislocation loop formation and associated Type III internal stress, etc, it is essential to understand how precipitates evolve or how different phases transform at elevated temperatures, and how this influences the creep behaviour of the material.

The National Institute for Materials Science (NIMS) from Japan has carried out a systematic experimental observation and investigation on the microstructural characteristics of long-term (up to 17 years) crept specimens of Type 316H austenitic stainless steels, regarding the evolution of precipitates and creep rupture at different temperatures (550^{o}C - 750^{o}C) [36]. All the tested specimens were initially given a solution treatment to dissolve any precipitates that are present into solution. During the long-term creep tests, both the specimen

head volume (with pure thermal ageing) and gauge volume (thermal ageing + creep) were examined; information that has been reported includes: evolution of chemical composition; Vickers hardness; mean size of different precipitate phases (available data of mean size is only in the head volume and over a limited range of temperatures); and most importantly, creep strain rate vs time curves at different stresses and/or temperatures, etc. Some relevant results are firstly reviewed in this section. Based on these results, some simplifications in the simulation are introduced.

7.3.1.1. Sequence of precipitation

The NIMS report provides a time-temperature-precipitation (TTP) diagram (Figure 7.8) for Type 316H stainless steels during pure thermal ageing, i.e. for the specimen head volume, which is similar to that reported elsewhere [37], where the multiple "C-shape" curves indicate the "beginning of nucleation" of a certain precipitate phase. However, care needs to be taken in interpreting this as the "beginning of nucleation", since it roughly refers to the time when the precipitate phase becomes experimentally observable and measurable, thus is dependent on the experimental technique employed.

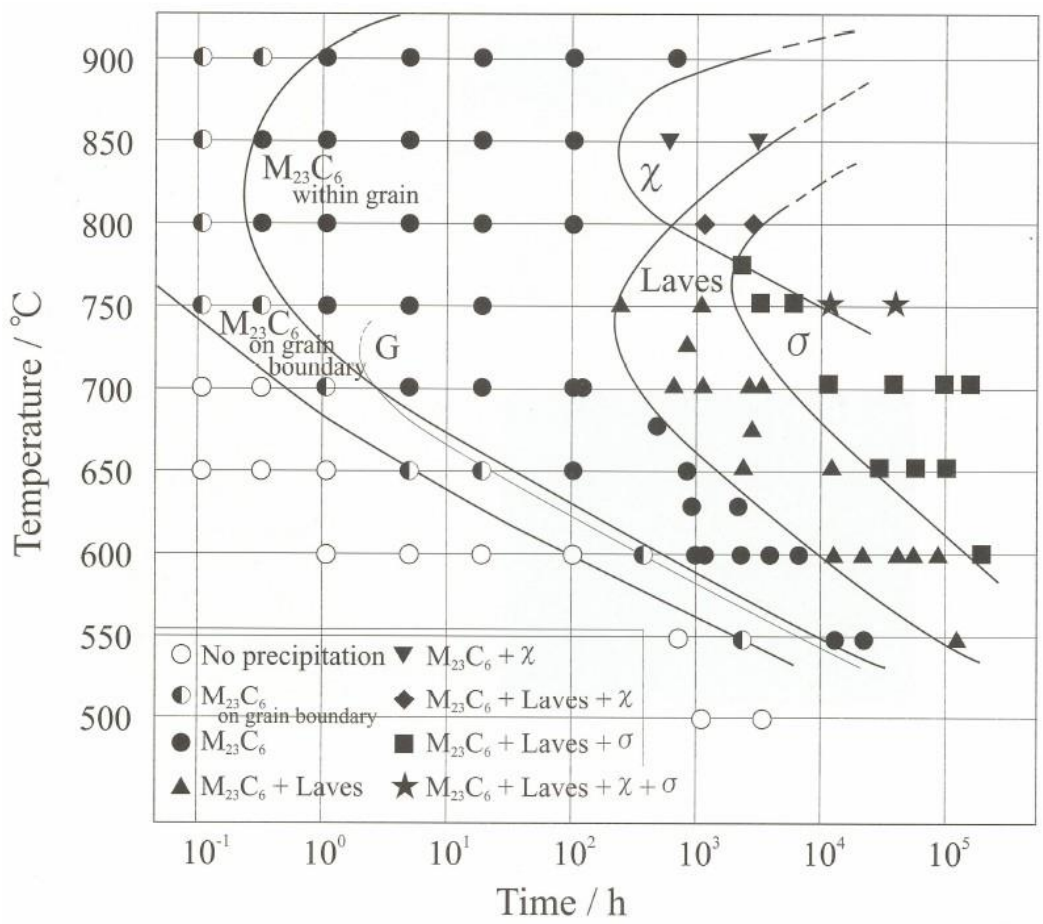

Fig. 7.8. Time-temperature-precipitation (TTP) diagram for specimen head volume (subjected to pure thermal ageing) of Type 316H stainless steels (map provided by NIMS report [36]). σ refers to sigma phase and χ refers to Chi phase.

According to this TTP diagram, thermal ageing promotes precipitation of carbides ($M_{23}C_6$) and intermetallic phases, such as Laves phase, sigma phase and Chi phase [34, 35]. More detailed studies of the morphology of these phases within similar materials have been conducted elsewhere [35, 37, 174, 175] and the results show that carbides appear to be the first major stable phase to form in this material, which can form both along grain boundaries (intergranular) and inside the matrix (intragranular). In addition, precipitation of Laves phase, mainly observed inside the matrix, then form at the expense of some carbides, because the intermetallic phase transformation can lower the *Cr* and *Mo* content in the matrix, thus increasing the carbon solubility [174, 175]. This is also reflected in the evolution of mean particle size (to be shown later), where the coarsening rate of carbides is observed to decrease,

but that of Laves phase is observed to increase as the temperature increases [36]. As the ageing time increases, precipitation of sigma phase occurs after the precipitation of Laves phase is complete [174], but is mainly observed on grain boundaries or triple junctions [35]. Very little information is available for the Chi phase. Overall, the precipitation sequence at service temperatures (below 700^{o}C) is found to be carbides → Laves → sigma → Chi, and such a sequence indicates a trend of increased stability. Note that in the TTP diagram in [37], it is found that the creep in the specimen gauge volume does not alter this sequence, but may lead to slightly earlier observation of each phase at each temperature. To simplify the problem, since the sigma phase is an intergranular phase that does not significantly interact with dislocations and both sigma and Chi phases either form at very high temperatures out of the concerned temperature range, or occur at low temperatures but only after an extensive period of ageing that almost exceeds the life expectation of the component, we only concentrate on carbide and Laves phase in the following.

7.3.1.2. Chemical composition

Figure 7.9 shows the evolution of chemical composition of carbide and Laves phase with ageing time in both specimen head and gauge volumes, provided by the NIMS report [36]. The variation of chemical composition with temperature is found to be negligible thus is not distinguished in Figure 7.9.

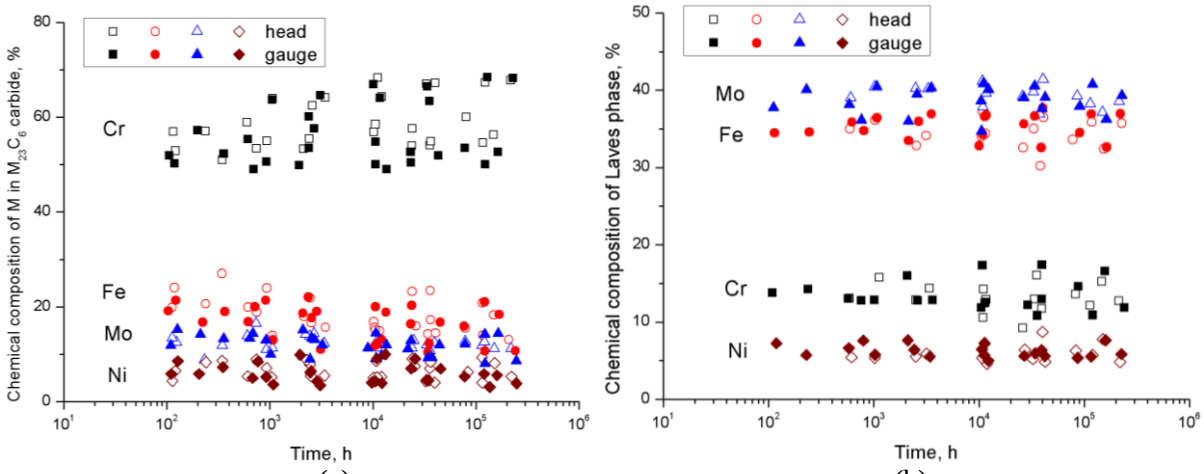

Fig. 7.9. Change in chemical composition of (a) *M* in $M_{23}C_6$ carbides and (b) Laves phase within grains in specimen head and gauge volume as a function of ageing time at different temperatures. The variation with temperature is found to be negligible and is not distinguished in the figure. It is assumed for each phase that Fe+Cr+Mo+Ni=100%. All data can be found in [36]

It is observed that both phases contain metallic elements of *Fe*, *Cr*, *Mo* and *Ni*, indicating a non unique chemical expression of each phase and some potential competition of these elements between the two phases. However, it should be noted that the dominant elements in each phase vary, where *Cr* is the major metallic element for carbides and *Fe-Mo* dominates in Laves phase. Therefore, the major chemical expression for carbides is $Cr_{23}C_6$ while that for Laves phase is Fe_2Mo, which has also been identified in the work carried out at Loughborough University [35]. In addition, it is seen that the chemical composition for both phases remains almost constant even over a long period of ageing or creep and no difference can be observed between the specimen head and gauge volume. Therefore, we simply regard both phases in this material as having stable compositions, while the competition of other minor metallic elements is only considered empirically (to be shown later).

7.3.1.3. Vickers hardness

Figure 7.10 illustrates the evolution of Vickers hardness, both in the specimen head and gauge volume, of initially solution-treated 316 austenitic stainless steels during thermal

ageing or creep, with data measured by NIMS at different temperatures and/or stresses [36]. Some additional data for the specimen head volume measured by Loughborough University [35] is also shown in the figure. It is found that the hardness of the head volume starts at a low value and gradually increases with ageing time. On the contrary, although the hardness of the gauge volume starts at the same level as that of the head volume, it increases more rapidly, up to a maximum value and then gradually decreases.

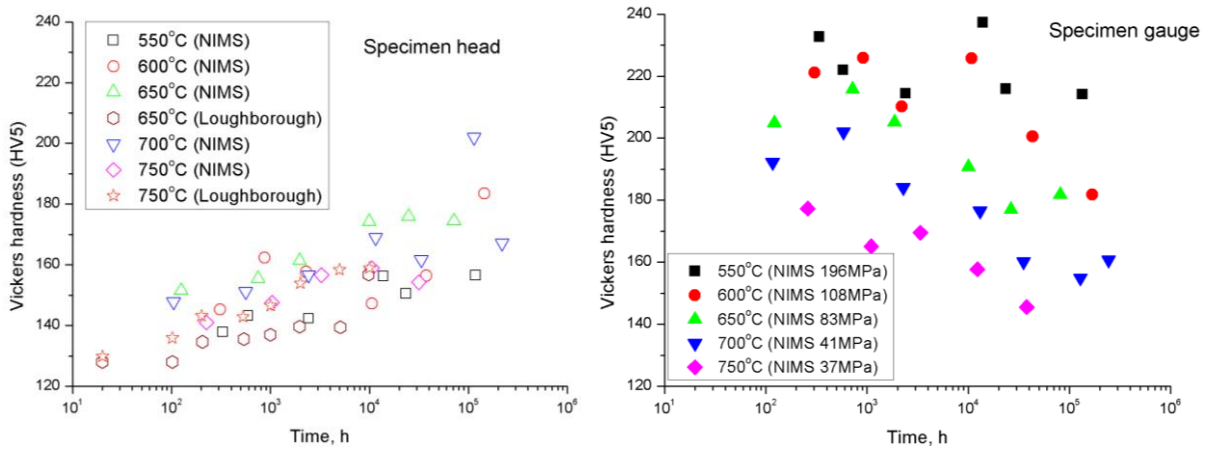

Fig. 7.10. Comparison of Vickers hardness versus time for specimens tested at various temperatures, (a) specimen head and (b) gauge volumes of Type 316H stainless steel. Some additional data for hardness of head volume measured by Loughborough University is also shown in (a). All data can be found in [36]

Hardness has been understood to be an indicator of the material's athermal yield strength [176]. For the material employed in this study, the athermal yield strength is contributed from combined forest dislocation junctions, precipitates and solute atoms as already shown in previous chapters. A separate study has been carried out (not shown here), which demonstrates that the reduction of athermal solute strengthening due to the depletion of solute atoms by precipitation in this material is negligible. Therefore, the increase of hardness or yield strength of the specimen head volume, subjected to pure thermal ageing, is likely to be associated with the decrease of mean inter-particle spacing caused by nucleation and growth

of precipitates, since the evolution of solid solution can be ignored and dislocation structure can recover thus the contribution to the yield strength from forest dislocation reduces. However, the high value of hardness for the gauge volume is likely to be attributed to additional forest dislocation junctions generated during high temperature pre-straining and creep and enhanced precipitation, while the subsequent decrease of hardness may be attributed to recovery of the dislocation structure and/or coarsening of precipitates.

7.3.2. Simulation procedure of phase transformation

This section simulates and evaluates the phase transformation process in solution-treated Type 316H austenitic stainless steel with the same chemical composition as given in Table 5.1, using the improved JMAK phase transformation model introduced in Chapter 6. In this simulation we only focus on evolution of precipitates during thermal ageing in the absence of creep, i.e. we only examine the microstructural data measured for the specimen head volume. For the specimen gauge volume subjected to thermal ageing plus creep deformation, relevant simulations are provided in section 7.4.

According to the temperature range of interest and life expectation of the material, we only examine the evolution of microstructure below 700^{o}C (500 ^{o}C ~650 ^{o}C) up to 5×10^{5} h (~60 years). As mentioned earlier, we limit our study to two intragranular phases, carbides ($Cr_{23}C_6$) and Laves phase (Fe_2Mo). For intergranular carbides, according to Faulkner's report to EDF Energy [144], they form and saturate rapidly even at relatively low temperatures (500^{o}C) with a maximum volume fraction around 0.8%. Therefore, in our simulation, we simply consider the initial state of the material as containing 0.8% volume fraction of intergranular $Cr_{23}C_6$ carbides. The depletion of corresponding solute elements can then be obtained regardless of the size of these intergranular carbides. Such depletion may influence the subsequent transformation of each intragranular phase.

At the beginning of the simulation, no precipitates were present inside the matrix. Both intragranular carbides and Laves phase were allowed to transform simultaneously. All the particles were idealized as spherical. At each time step Δt, the number of newly formed particles of each phase ΔN_p per unit volume was calculated using the classical nucleation theory (Eq. (6.42)) and the mean size of all the existing particles of each phase was updated using Zener's parabolic growth law (Eq. (6.47)). Then the increase of volume fraction of each phase was calculated using the traditional JMAK model (Eq. (6.38)), taking into account the potential impingement from both phases. Following these, the number density of each phase resolved on each slip plane (per unit area) and mean inter-particle spacing of all particles on the slip plane can be determined directly by Eqs. (3.12) and (3.10). Further, the current solute concentration ($\bar{c}^i$) in the matrix for the major elements of each phase (*Cr* and *C* in carbides, *Mo* in Laves) was updated using Eq. (6.48). This allowed further update of the nucleation rate (Eq. (6.42)) from the change of chemical driving force (Eq. (6.41)) and critical radius of stable nuclei (Eq. (6.40)), etc. For each phase, this process was repeated until the current solute concentration $\bar{c}^i$ of corresponding elements in the matrix reached the equilibrium value (c_{eq}^i), when the nucleation ceased and coarsening started. Afterwards, the volume fraction of each phase remained unchanged and the number of dissolved particles and the mean particle size were updated by the Ostwald Ripening or coarsening rate (Eqs. (6.51) and (6.49b)). Meanwhile, to avoid time-consuming calculations with short time steps and numerical instabilities with long time steps, the time step was optimized during the simulation by performing a logarithmic increment of the time step. Δt was chosen such that the critical radius r_c in Eq. (6.40) did not vary by more than 1% between each time step [162].

Values of the parameters used in this simulation are shown in Table 7.2. Seven parameters (nucleation site density, surface energy and molecular or molar volume of carbide and Laves phase, and a coarsening reduction factor for carbide) were selected to provide the best fit to

the data, where the surface energy and molecular volume were adjusted based on the values estimated in the literature [177-179]. The coarsening reduction factor was used to reduce the coarsening rate of carbides. This is based on the fact that the consequence of the formation of intermetallic Laves phase is the depletion of *Mo* and/or *Cr* in the adjacent matrix, which in turn leads to the increase in the solubility of carbon in the matrix and partial dissolution of the prior formed carbides. Other parameters were obtained for the literature, including bulk diffusivity and activation energy of *Cr* (rate-controlling element for carbide, diffusing much slower than *C*) [177, 180] and *Mo* (rate-controlling element for Laves, diffusing slower than *Fe*) [11, 181, 182] as well as the lattice parameter of the matrix phase of F.C.C stainless steel [183]. The initial solute concentration of all elements in the matrix is given in Table 5.1, while that in each phase and the equilibrium value in the matrix were obtained using *ThermoCalc*, a thermodynamic calculation program (details of which is not shown here).

The resultant model is then used to examine the direct outputs from the phase transformation process, i.e. mean particle size, number density, volume fraction and mean inter-particle spacing of both phases at various temperatures.

Tab. 7.2 Material parameters of 316H austenitic stainless steels used in the simulation of phase transformation

Parameter	Description	Unit	Phase or element	Value			
a_m	Lattice parameter for austenitic stainless steel	m		3.6×10^{-10}			
N_{site}	Nucleation site	m^{-3}	Carbide	1×10^{13}			
			Laves	5×10^{14}			
V_m	Molar volume	$m^3\ mol^{-1}$	Carbide	6×10^{-6}			
			Laves	2×10^{-6}			
χ_c	Surface energy	$J\ m^{-2}$	Carbide	0.3			
			Laves	0.25			
D_{V0}	Bulk diffusion pre-exponential term	$m^2\ s^{-1}$	Cr	1.5×10^{-4}			
			Mo	7.4×10^{-4}			
Q_{V0}	Bulk diffusion activation energy	$KJ\ mol^{-1}$	Cr	240			
			Mo	283			
$\bar{c}_0$	Initial solute concentration in the matrix	wt. %	Cr	0.166			
			C	0.0007			
			Mo	0.0233			
				500°C	550°C	600°C	650°C
c_p	Solute concentration in the particles	wt. %	Cr in carbide	0.68			
			C in carbide	0.051			
			Mo in Laves	0.5			
c_{eq}	Equilibrium solute concentration in the matrix	wt. %	Cr	0.0159			
			C	7.25×10^{-8}	2.92×10^{-7}	9.48×10^{-7}	2.97×10^{-6}
			Mo	0.0025	0.0046	0.0076	0.0116
C_f	Coarsening reduction factor		Carbide	1	1	0.3	0.03

7.3.3. Evaluation of phase transformation during thermal ageing

Figure 7.11(a) and (b) shows the evolution of the mean particle size of the carbides and Laves phase, as well as the overall results for both phases from 500°C-650°C. Available data at some temperatures is also shown in the figure. Corresponding results for the volume fraction and number density (per unit area) are presented respectively in Figure 7.11(c) and (d) and Figure 7.11(e) and (f). No data is available for these two outputs. In general, the results coincide with the time-temperature-precipitation (TTP) diagram shown in Figure 7.8.

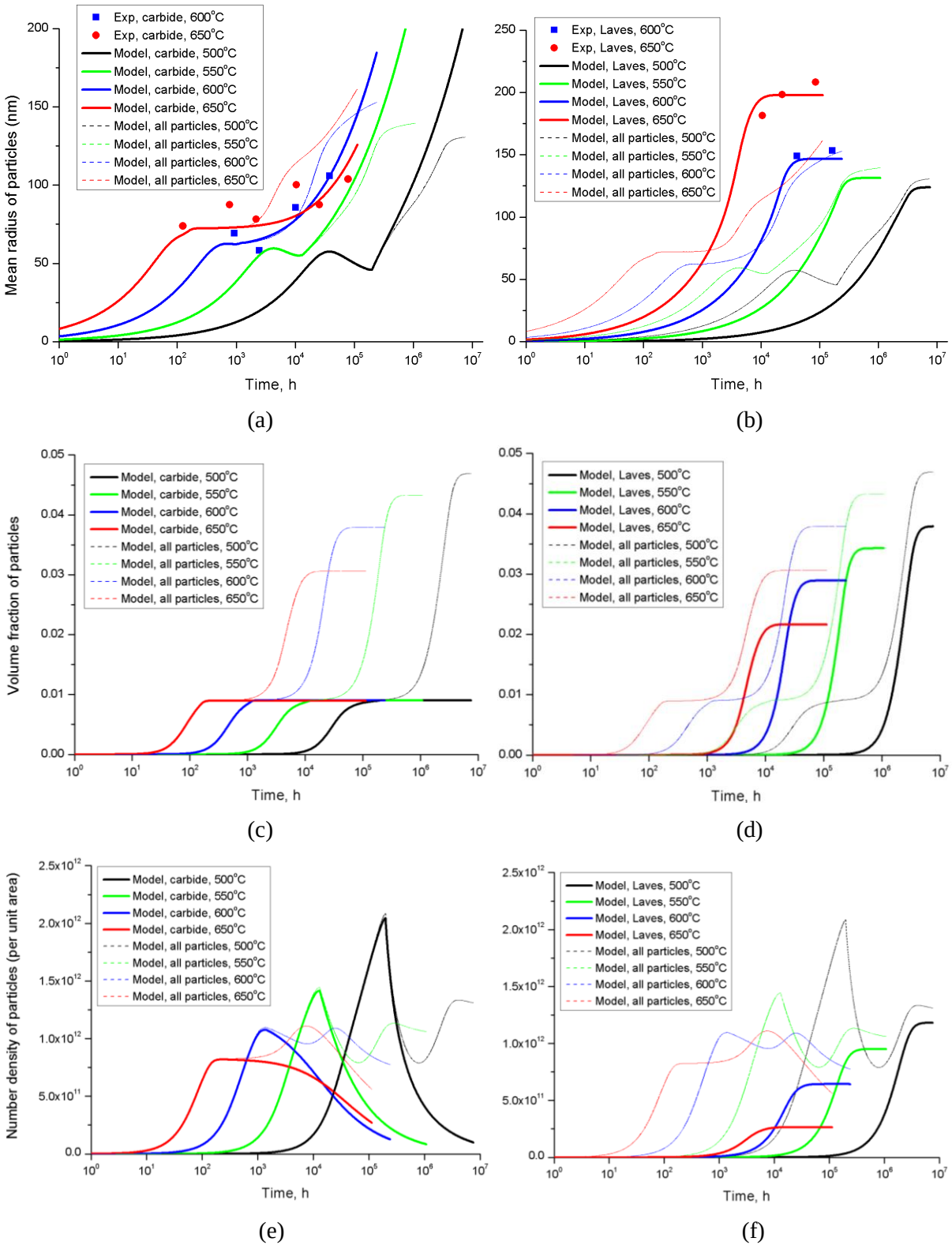

Fig. 7.11. Evolution of the mean particle size ((a) and (b)), volume fraction ((c) and (d)) and number density per unit area ((e) and (f) for carbide (corresponding results in (a), (c) and (e)) and Laves phase (corresponding results in (b), (d) and (f)), at various temperatures from 500°C to 650°C. The overall results for all particles are also shown in each figure.

In the figure, carbide is observed to transform and saturate much faster than Laves phase at each temperature. The maximum volume fraction that carbide can transform is much smaller than that of Laves phase, but it may give rise to more particles than Laves phase. Some decrease of the mean size can be seen for the carbides at low temperatures (550^oC and 500^oC) near saturation, which is due to a very slow rate of growth, while the nucleation of new nuclei is still incomplete (see Eq. (6.47)). The overall result for both phases resembles the result for the carbides at short times and gradually resembles that of Laves phase at long times, indicating that carbides dominate during the early stage of thermal ageing, but after they saturate, i.e. nucleation is complete, Laves phase becomes dominant. A further examination of the saturation values demonstrates a trend, whereby as the temperature is increased, we tend to observe fewer particles with a larger mean size after a given time.

The model captures the general trend observed experimentally. It is evident that after saturation different distributions of precipitates are obtained at different temperatures, which indicates that accelerated tests on a material at temperatures higher than that employed in service may not be able to reproduce an identical microstructural state to that obtained at the service temperature.

Figure 7.12 gives the evolution of concentration (mass percent) of *C*, *Cr* and *Mo* in the matrix during thermal ageing at various temperatures. Note that the initial concentrations of carbon and chromium in Figure 7.12(a) and (b) are smaller than those given in Table 5.1. This reduction is due to the consideration of 0.8% intergranular carbide at the beginning of the simulation. Concentration of all elements in the matrix decreases towards the equilibrium value (saturation), due to depletion by phase transformation. It should be noted that the equilibrium value of *Mo* differs significantly at different temperatures, as given in Table 7.2, calculated using *ThermoCalc*. This can be attributed to the large variation in the solubility of *Mo* in the matrix at different temperatures.

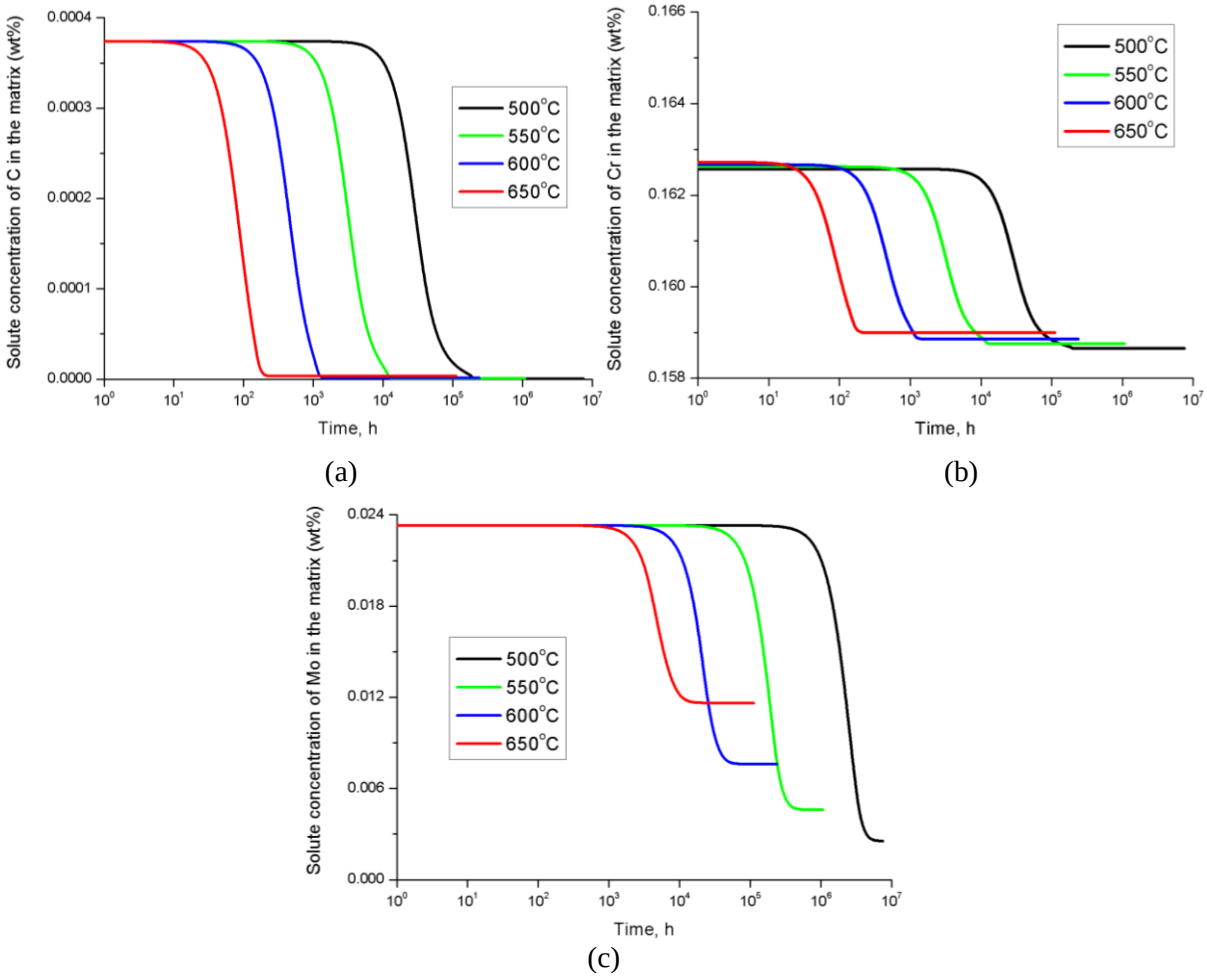

Fig. 7.12. Evolution of concentration of (a) *C*, (b) *Cr* and (c) *Mo* in the matrix phase during thermal ageing at various temperatures from 500°C to 650°C

Another important output from the phase transformation process is the mean inter-particle spacing, calculated from the number density per unit area (the overall result in Figure 7.11e and f) or from the mean size and volume fraction (the overall result in Figure 7.11a-d) as predicted by using Friedel's model Eq. (3.10) and shown in Figure 7.13(a). The corresponding Orowan bowing and climb bypassing strength, calculated by Eqs. (2.16), (2.18) and (2.20) are shown in Figure 7.13(b), taking into account the temperature-dependent shear modulus given by Eq. (5.1). Starting from solution treatment without any precipitate, it is expected that the mean spacing would start from infinity (the corresponding Orowan bowing and climb bypassing strength would start from zero). The results for the early stage at each temperature are not shown in the figure. For each phase, the number density decreases after

saturation. However, since carbide and Laves phase do not saturate at the same time, the evolution of mean spacing exhibits a complex feature, showing multiple minima in the intermediate period of ageing but eventually increasing after both phases have saturated.

According to previous chapters, all the results shown in Figures 7.11 – 7.13 demonstrate that the evolution of precipitates can influence the creep behaviour in the specimen gauge volume in several aspects, including the change in Orowan bowing and climb bypassing strengths as well as the Type III internal stress associated with the Orowan bowing process, and attenuation of the effect of solute drag due to depletion of solute atoms. However, care must be taken when applying these results to the specimen gauge volume since all precipitate phases have been considered so far as strong hard particles. Note that small particles may not be experimentally observable and may be easily cut by dislocations [48, 184]. Therefore, the real contribution of precipitates to creep may be much weaker.

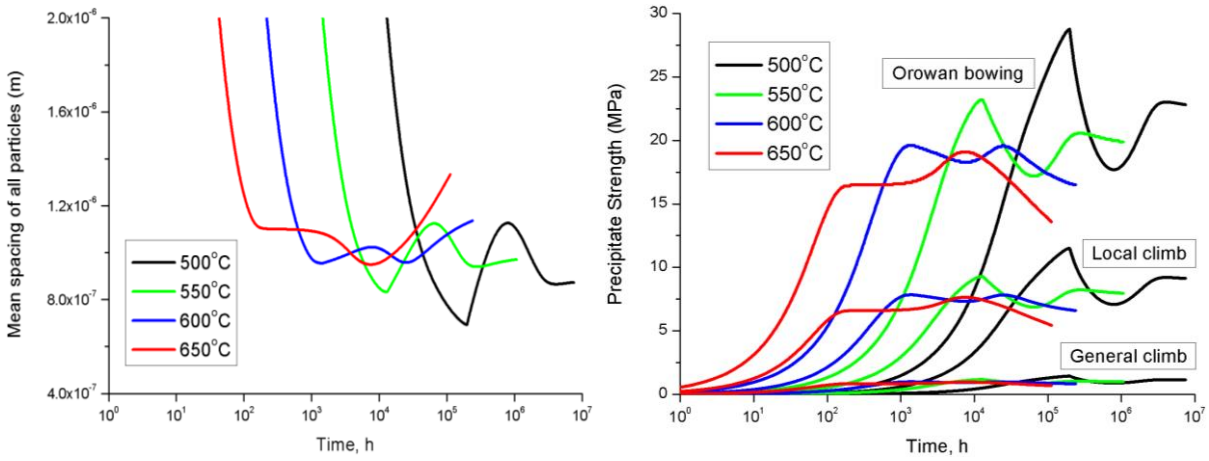

(a) (b)

Fig. 7.13. Evolution of (a) mean inter-particle spacing and (b) associated Orowan bowing and climb bypssing strengths at various temperatures from 500°C to 650°C

7.3.4. Summary

The phase transformation of solution-treated Type 316H austenitic stainless steels subjected to pure thermal ageing is evaluated in this simulation by using the improved JMAK phase transformation model introduced in Chapter 6. The effect of creep deformation is not considered. The findings are briefly summarized below:

- Carbides and Laves phase are major phases at typical service temperatures even over an extensive period of ageing. Both phases show stable chemical compositions ($Cr_{23}C_6$ for carbide and Fe_2Mo for Laves phase).
- The predicted occurrence of each phase at each temperature is consistent with that shown in the time-temperature-precipitation (TTP) diagram of Figure 7.8. Carbides transform faster than Laves phase, thus the dominant phase may switch from carbides during the early stage of ageing to Laves at a late stage. Due to different kinetics of transformation between carbides and Laves phase, the mean inter-particle spacing and the associated Orowan bowing and climb bypassing strengths evolve in a complex way. All these results demonstrate that accelerated tests on a material at temperatures higher than that in service may not be able to reproduce an identical microstructural state as that at the service temperatures.
- Understanding how different phases transform in the material at elevated temperatures is essential to assessing creep behaviour. Evolution of precipitates may change the Orowan bowing and climb bypassing strengths as well as the Type III residual stress associated with Orowan bowing. Depletion of solute atoms by precipitation may also attenuate the effect of solute drag. However, the practical contribution to creep strength by precipitates may be much weaker, particularly when taking into account that small particles can be easily cut by dislocations.

7.4. Simulation III: Creep curves with multiple secondary stages or minimum creep rates

7.4.1. Brief introduction

An interesting and important finding from the experiment conducted at NIMS on initially solution-treated (designated ST) Type 316H stainless steel specimens is that the material may not exhibit simple creep curves at some intermediate temperatures and stresses [25, 172], where multiple minima in the creep rate or multiple secondary stages can be observed in the creep rate vs time curves (e.g. Figure 2.3). Such a phenomenon is widely seen across a range of experiments on solution-treated specimens with similar chemical compositions and thermal histories. Figure 7.14 compares some creep rate vs time curves for two tested specimens with designation AAL and AAB, which were obtained at the same stresses and temperatures (550^{o}C-650^{o}C) [25, 172]. The chemical composition of the two specimens is shown in Table 7.3. It is found that, before the drastic increase of creep rate late in life, which indicates the tertiary stage, the phenomenon of multiple minima or secondary stages is observed in both specimens, but may not occur at all temperatures and stresses.

This section attempts to evaluate the creep rate vs time curves, in particular, the phenomenon of multiple secondary stages, by the combined model of creep and phase transformation that have been established so far in this thesis (Chapters 3, 4 and 6). According to section 7.3, different phases transform in the solution-treated (ST) specimens during the early stages of thermal ageing. This process can even be promoted by creep deformation. In this section, we intend to understand how, and to what extent, the evolution of the microstructural state can be correlated to the change in creep behaviour of the material. However, due to the variability or scatter in these creep curves (Figure 7.14), which may be due to different chemical compositions, we do not attempt to refine and fit each particular

curve, but only focus on the trends and explanation of the mechanism for the multiple secondary stages. In this section, we only take the specimen AAL as an example. Temperatures are limited to 550°C-650°C and only three curves with three different stresses are selected at each temperature.

Tab. 7.3. Chemical composition (wt.%) of two similar specimens of Type 316H stainless steel

Ref. code	C	Si	Mn	P	S	Cr	Mo	Ni	Cu	N	Fe
AAL	0.07	0.61	1.65	0.025	0.007	16.60	2.33	13.60	0.26	0.025	Bal.
AAB	0.05	0.52	1.51	0.021	0.001	16.42	2.34	13.21	0.14	0.034	Bal.

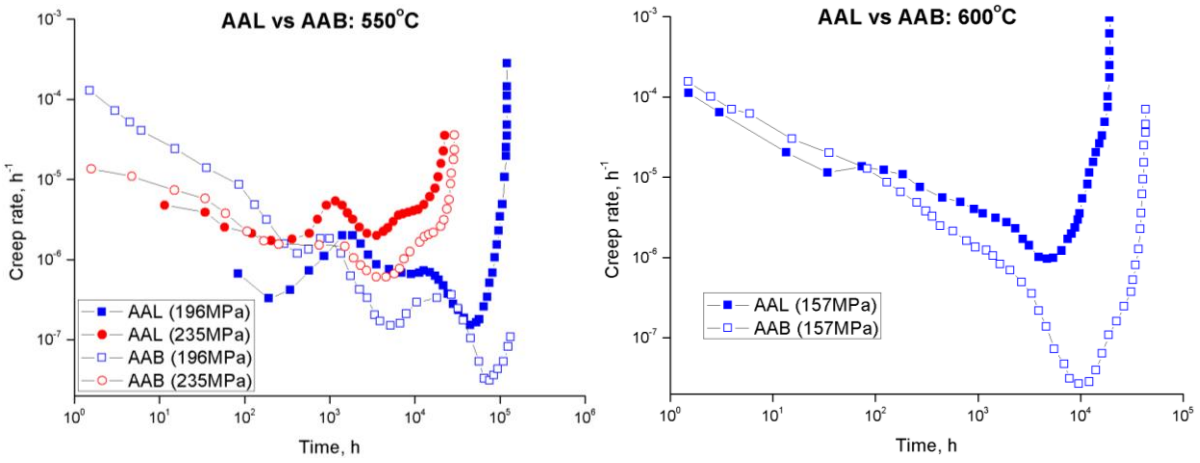

(a)

(b)

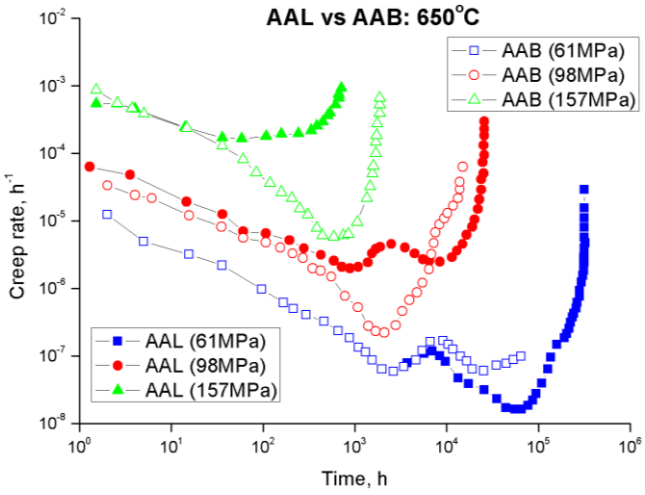

(c)

Fig. 7.14. Comparison of creep rate vs time curves of two Type 316H stainless steel specimens at (a) 550°C; (b) 600°C and (c) 650°C tested at the same stresses. AAL and AAB are the designation for the tested specimens. Data were extracted from [25, 172]

7.4.2. Identification of dominant mechanism(s) for multiple minimum creep rates

In order to identify the dominant mechanism(s) for the observed multiple minimum creep rates or secondary stages in the solution-treated (ST) specimens, it is critical to understand the reason for the increase of creep rate after each secondary stage, in particular, before the last secondary stage, because the very last increase in creep rate may be largely attributed to damage accumulation induced softening of the material. Based on all parts of the model that have been established, discussed and/or validated so far in this thesis, we propose that the candidate mechanism(s) for the multiple secondary stages may lie in the following aspects:

(1) Alternative competition or domination between hardening and recovery regarding the evolution of the dislocation structure;

(2) Complex evolution of the precipitate population, where the mean inter-particle spacing during phase transformation may evolve and exhibit multiple minima (see Figure 7.13);

(3) Reduced effect of thermal solute drag due to depletion of atoms in the solute clusters during phase transformation.

Here we examine these factors by undertaking a series of sensitivity studies.

7.4.2.1. Creep without phase transformation and solute drag

We start from creep without consideration of the effect of solute drag and phase transformation, thus we only examine factor (1) as described above. The material is solution-treated (ST), with the chemical composition shown in Table 7.3 (AAL). In this simulation, all slip systems for all grains within the ST polycrystal were assumed to have identical critical resolved shear strength (CRSS) before commencement of any loading. No initial residual stress was considered and no precipitates were present in the material. Similar to the

simulation procedure for the EXLA specimens described in section 7.2, the material was first subjected to uniaxial tensile pre-straining at each interested temperature up to the required stress, and then followed by uniaxial tensile creep. During the short-term monotonic pre-straining, the recovery of dislocation structure was ignored and the temperature effect considered is only the scale of the modulus, while the effect of thermal solute drag is to be incorporated later. All the stresses and strains were updated using the same approaches as described in section 7.2 except that we do not consider the Type III residual stress associated with particles. Finally, the obtained results of creep strain were transferred to creep strain rate.

Values of most parameters used in this simulation remain the same as shown in Table 7.1. Changes were made to three parameters: (1) the Orowan strength was not considered; (2) the initial number of pinning points per unit area (or initial dislocation density, Eq. (6.13)) was reduced to 1×10^{13} for solution-treated conditions, as measured by Morris and Harris [40]; (3) a_0 in the activation energy ΔF_0 in the thermally activated glide rule (Eq. (6.1b)) was set as 0.5, as used by Frost and Ashby [11], to simulate a weaker combination of obstacles (forest dislocations + solute atoms) than that in the EXLA specimens with considerable precipitates, where a value of **1** has been fitted and used.

The measured and simulated creep rate vs time curves for the ST specimens between 550^{o}C-650^{o}C at three different stresses are shown in Figure 7.15(a)-(c). It is found that the predicted curves deviate significantly from the data at 550^{o}C, but gradually approaches the data at higher temperatures. Predictions even fit reasonably well with the data at 650^{o}C. However, all these results show standard creep curves such that the rate of recovery gradually catches up with the rate of hardening from early stage of creep (primary) to later stage (secondary), leading to the eventual achievement of a dynamic balance. No complex competition between hardening and recovery occurs that can give rise to the multiple secondary stages, i.e. there must be some contribution from phase transformation and/or

thermal solute drag. Meanwhile, predictions and relevant data found in the literature [157] of an extended monotonic loading across a range of temperatures and strain levels are shown in Figure 7.15(d), plotted between the modulus-compensated flow stress and temperature. Monotonic loading at very high temperatures (>650^{o}C) are not considered. Note that, in the data shown in Figure 7.15(d), a gradually pronounced peak can be observed in the temperature range 400 ^{o}C to 600^{o}C as more and more plastic strain accumulates. Since precipitates formed during short-term monotonic loading can be ignored, this peak was attributed to the effect of thermal solute drag [157]. In fact, such an effect was found to be even more significant as the strain rate decreases to a very low level at these temperatures [157]. Therefore, all these results in Figure 7.15 indicate that, between 500^{o}C and 600^{o}C, we might expect thermal solute drag to make a significant contribution to the material creep response.

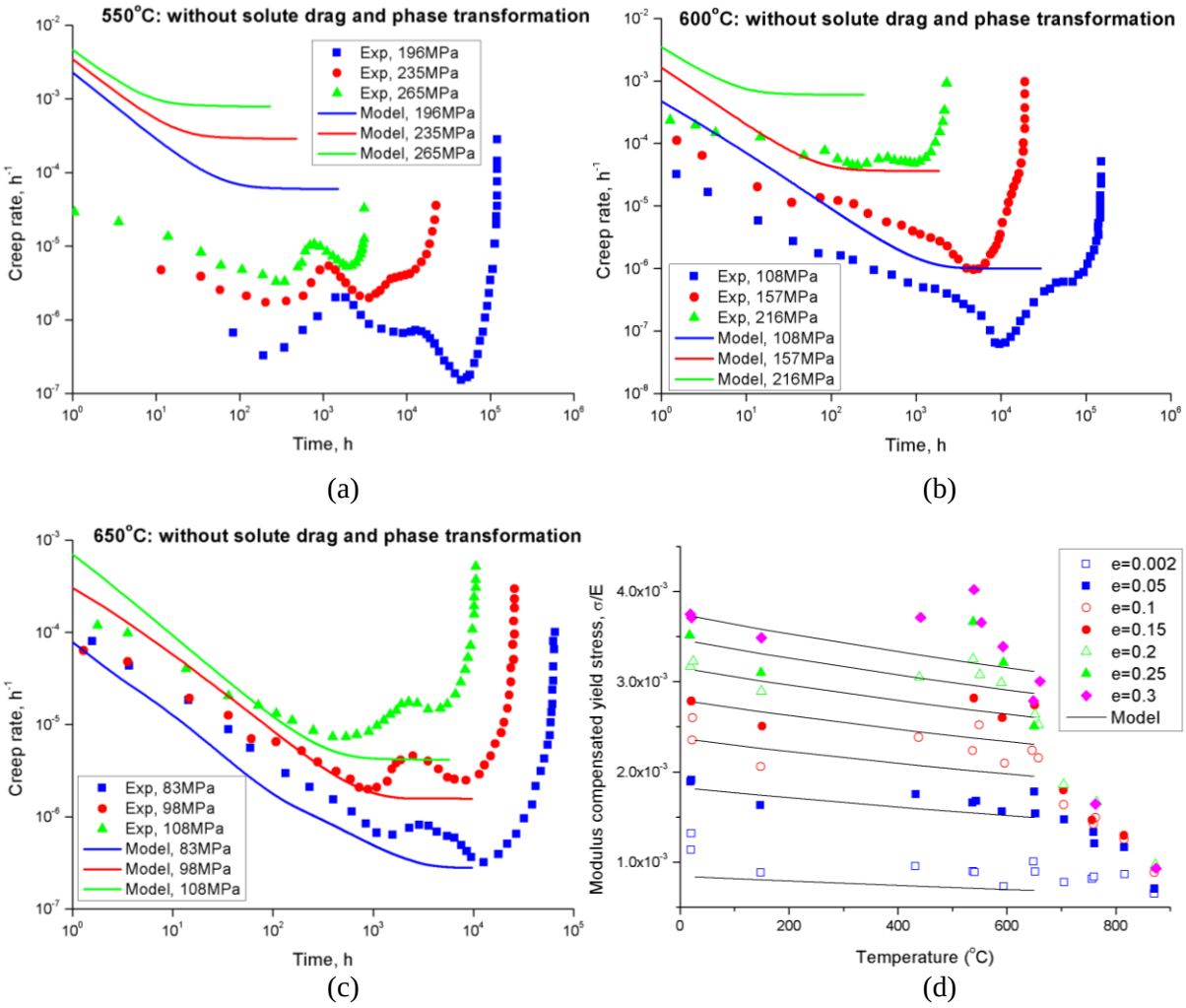

Fig. 7.15. Predictions and measurements of creep rate vs time curves at (a) 550°C; (b) 600°C and (c) 650°C, without considering thermal solute drag and phase transformation. Some extended monotonic pre-straining across a range of temperatures and strain levels is shown in (d), plotted between modulus-compensated flow stress and temperature

7.4.2.2. Creep with phase transformation but without solute drag

In the second part, we take into account the interaction between phase transformation and creep. This is to examine factor (2) as described earlier. The effect of solute drag is considered in the next section. The simulation procedure in this part is similar to section 7.4.2.1, except that at each time step during creep, both the carbide and Laves phases were allowed to transform, with increments of volume fraction, mean size, mean inter-particle spacing determined by the improved JMAK phase transformation model. All phases were

assumed to be strong particles that can only be bypassed. The Orowan bowing strength was updated using Eq. (2.16). This then modified the internal resistance on individual slip planes and led to the development of the Type III residual stress. At each time step, the shear strain rate on each active slip system was calculated by Eq. (6.1b). The climb-controlled bypassing mechanism is not considered in this simulation because for the applied stresses employed here at each temperature, the CRSS on each active slip system has developed during monotonic pre-straining before creep and it did not change significantly during creep, i.e. the contribution to the CRSS by phase transformation was limited. However, we may expect the climb bypassing mechanism to dominate if the applied stress decreases during creep, or if the applied stress is very low such that the phase transformation may lead to a considerable contribution to the CRSS.

Parameters used in the simulations of section 7.4.2.1 are also used here. Values of additional parameters are needed to describe the effect of creep loading on phase transformation, as illustrated in section 6.4.3. Diffusivity of *Cr* and *Mo* changes with accumulation of dislocations (see Eq. (6.53)), where the bulk diffusivity has been shown in Table 7.2 and the dislocation core (pipe) diffusivity of the two elements in 316 stainless steels was found or estimated based on [11, 185] and is not shown here. The dislocation density in individual grains was updated at each step using Eq. (6.13) by averaging the numbers of forest dislocation junctions on all the slip planes. The parameter w in Eq. (6.52) was kept the same for both carbide and Laves phases, where two values were chosen for comparison, 0.5 and 0.1. Further, to avoid any numerical instability, an additional issue is addressed here, such that a_0 was kept to be constant 0.5 throughout the simulation, although it is understood that the microstructural state (population of precipitates) may gradually evolve to a similar state as that in the EXLA specimens, in which a_0 has been fitted to be **1** (section 7.2). Note that even after the saturation of all the carbides and Laves phase in the material, there should

be at least some enhancements of the creep strength by the solute drag (to be simulated in the next section) from the remaining solute elements in the matrix, which has not been considered in previous simulations for the EXLA specimens. Therefore, the use of constant 0.5 for a_0 here could be reasonable.

Figure 7.16(a)-(c) presents the simulated creep rate vs time curves for the ST specimens between 550°C-650°C at three different stresses. For comparison, the curves with phase transformation that is not affected by creep (constant diffusivity and w=1) is also shown in the figure (designated w=1). However, in the simulated period at 550°C (Figure 7.16a), the effect of creep on phase transformation was found to be negligible thus is not shown in the figure. In fact, predictions at 550°C resemble the results shown in Figure 7.15(a) without consideration of phase transformation, indicating negligible contribution from precipitates at this temperature at this early period of creep. As the temperature increases, significant influence from phase transformation can be observed. At 600°C in Figure 7.16(b), compared with Figure 7.15(b), precipitation gradually enhanced the creep strength (reduced creep rate) of the material, which varies with different accelerated phase transformations. Some minima can be seen in the curves and the increase in creep rate is due to extensive particle coarsening (reduced Orowan bowing strength). However, since the mean inter-particle spacing evolved in a complex way as shown in Figure 7.13, the minimum creep rate may even occur earlier with less accelerated phase transformation (e.g. at 108MPa). Further, at 650°C in Figure 7.16(c), it was found that the phase transformation has caused a significant drop of the creep rate, i.e. a significant increase in the creep strength, which was even worse during accelerated phase transformations. Here we may expect the large drop to be eliminated by two aspects: (1) small precipitates do not contribute to Orowan bowing strength since they can be easily cut; in other words, the number of strong particles is small; (2) solute atoms diffuse very fast at this temperature, so that some amount of the solute bypassing strength described by Eq. (3.24)

may be negligible. However, as shown in section 7.3, a low number density of large particles tends to form at high temperatures. In addition, as can be seen in the strengthening-mechanism map proposed by Aplin and D'Angelo (Figure 2.6) [48], the mechanism of creep at 650^{o}C at the stresses considered in this simulation was found to be "viscous glide", indicating either not many observable precipitates, or a large inter-particle spacing for the precipitates, so that they do not directly influence the creep behaviour, at least during the short-term creep tests used to construct the map. However, such a feature of the precipitate population cannot be reflected in the simple phase transformation model employed here. As an alternative, in the following simulations in which we include the effect of solute drag, we simply do not consider the Orowan bowing strength at this temperature.

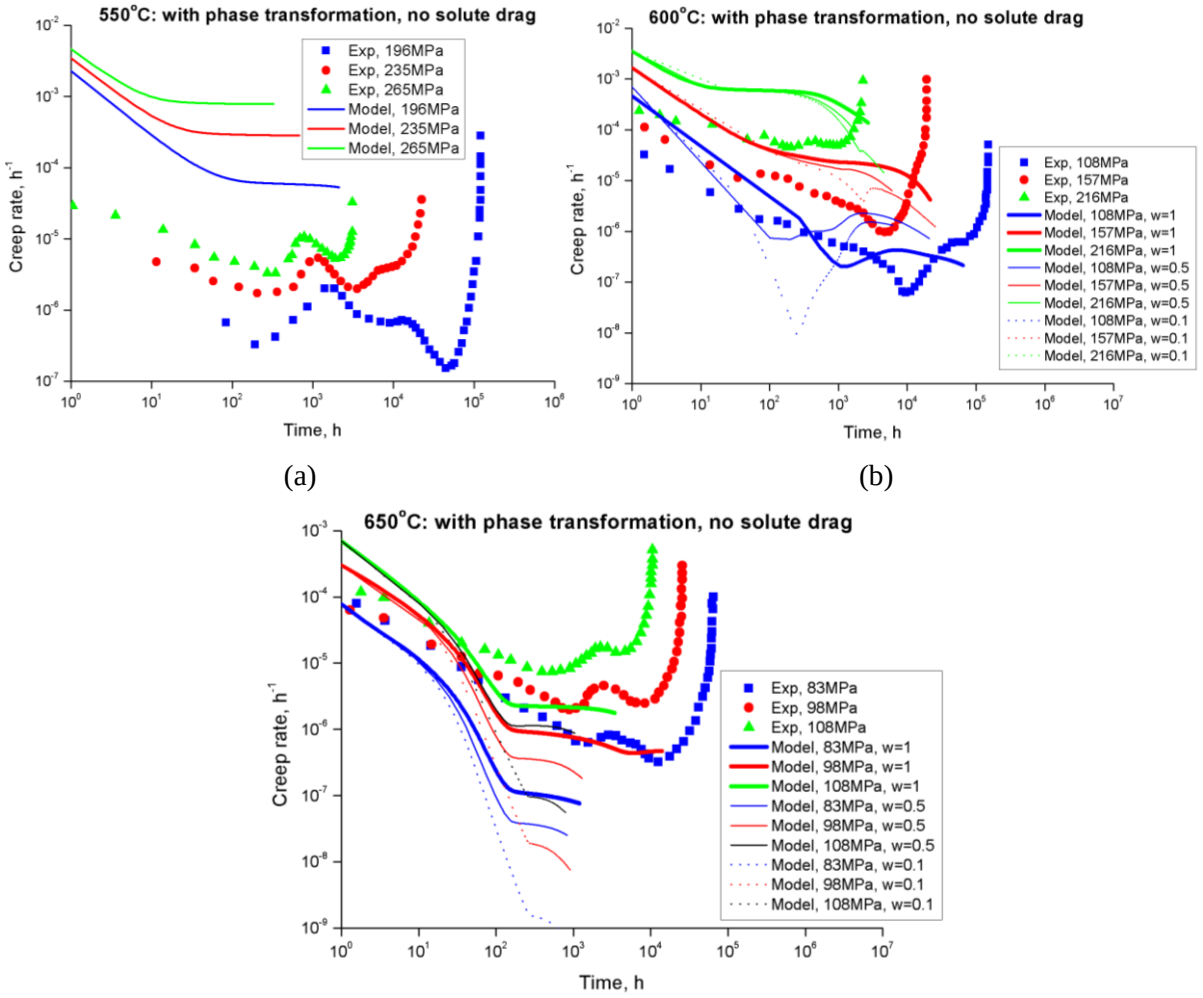

Fig. 7.16. Predictions and measurements of creep rate vs time curves at (a) 550°C; (b) 600°C and (c) 650°C, taking into account the interaction between creep and phase transformation. The curves with phase transformation that does not affected by creep are also shown in the figure (600°C and 650°C) as a comparison

7.4.2.3. Creep with phase transformation and solute drag

In this last part, we take into account the effect of thermal solute drag combined with phase transformation. Different from previous simulations, solute drag influences the material behaviour both during monotonic pre-straining and creep at elevated temperature, as can be seen in Figure 7.15(d). Following Schmidt and Miller [157], we assume that solute drag plays a role only at intermediate temperatures in a range 400°C to 650°C. We employ the same procedure and parameters as used in the last sub-section except that the shear strain rate at each time step was updated using Eq. (6.8), taking into account the enhancement of the CRSS

by the effect of solute drag (F_{sol}). For additional parameters associated with the solute drag (F_{sol}, expressed in Eq. (6.9)), $\dot{\gamma}_{\max}$ was given by Schmidt and Miller [157], where for 316 stainless steels, the maximum effect of solute drag has been found to be at $\dot{\varepsilon}_{\max} = 1\times10^{-9}$/s. $\dot{\gamma}_{\max}$ was then transformed from $\dot{\varepsilon}_{\max}$ using the Schmid factor in Eq. (4.1). $F_{sol,\max}$ has been shown to be a function of the current solute concentration $F_{sol,\max} = A\bar{c}$. Different solute complexes or pairs have been considered as responsible for the thermal solute drag effect, which include *Cr*-*C* [40] and *Mo*-*C* or *Mo*-*N* [159] complexes, thus $\bar{c}$ may most likely be related to the concentration of *Cr* and/or *Mo*. Note that the change of the concentration of *Cr* during phase transformation is found to be small (Figure 7.11b), here we simply assume $\bar{c}$ to be the concentration of *Mo*. *A* and *B* in Eq. (6.9) were chosen to fit the monotonic pre-straining data. It should be noted that the mass percent is used here as the concentration. For the enhanced phase transformation as affected by creep loading, we simply select *w*=0.5 as an example. Values of these additional parameters are summarized in Table 7.4.

Tab. 7.4 Additional parameters of 316H austenitic stainless steels used in the simulation of creep with phase transformation and solute drag

Parameter	Value	Parameter	Value
$\dot{\gamma}_{\max}$	2.5×10^{-9} s^{-1}	A	10
$\bar{c}(Mo)$	0.0233	B	8
w	0.5		

Figure 7.17 presents the updated results of extensive monotonic pre-straining across the same range of temperatures and strain levels as that shown in Figure 7.15(d). It is found that the updated fit considering the solute drag is much better than Figure 7.15(d) without consideration of solute drag (predictions are also shown in Figure 7.17) and the peak at these intermediate temperatures is captured by the model. It should be noted that the strain rate at monotonic pre-straining is relatively fast for the solute drag to make considerable change to

the monotonic loading curves, especially at low stress-strain levels, which cover the interested stress range employed in creep. However, the mechanism of solute drag indicates that a subtle change in monotonic pre-straining may lead to significant change in the creep response when the strain rate decreases extensively during creep. In fact, solute drag plays an important role such that it either enhances the creep strength (reduces the creep rate) as the creep rate decreases (see Eq. (6.9)), or enhances the creep rate as its effect attenuates as the concentration of *Mo* gradually decreases.

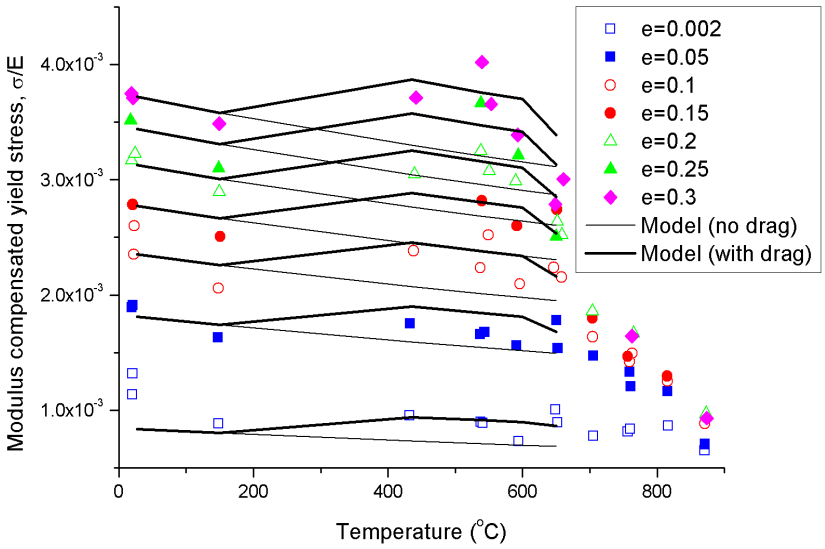

Fig. 7.17. Updated results of extended monotonic pre-straining across a range of temperatures and strain levels, considering the effect of solute drag; the results without consideration of solute drag are also shown.

Figure 7.18(a)-(c) presents the updated predictions of creep rate vs time curves for the ST specimens tested at 550°C-650°C at three different stresses. It should be noted again that the model does not predict the sharp increase of creep rate at very late stage of creep, which may refer to tertiary creep, because the model has not considered any damage accumulation. Here we start to interpret the results from higher temperatures. At 650°C in Figure 7.18(c), a bulge at each curve can be observed, and the model successfully predicts the occurrence of two minimum creep rates or secondary stages at almost the same time as the data. At this temperature, since we have ignored the Orowan bowing strength, the increase of creep rate is

purely caused by the reduced effect of solute drag, which almost coincides with the decrease of the concentration of *Mo*, and the subsequent decrease of creep rate is due to extensive dislocation multiplication (hardening) when solute drag has become weak. A new dynamic balance between hardening and recovery is yet to be achieved towards the second steady state. Further, the difference between the prediction and data originated from early stage of creep may be compensated by reducing the solute bypassing strength (Eq. (3.24)) since solute atoms may become mobile and diffuse fast at this temperature that they may not contribute to the strength significantly. However, we do not consider any further refinement here.

At 600^{o}C in Figure 7.18(b), the model predicts the occurrence of a bulge at relatively low stresses (108MPa and 157MPa), which does not occur in the data since damage may have started to accumulate after the first secondary stage. It is observed that the predicted secondary stage occurs earlier than the data at these two stresses, and the subsequent increase of creep rate is due to a combined effect of particle coarsening and depletion of *Mo*. Note that from the strengthening-mechanism map shown in Figure 2.6, at these two stresses at 600^{o}C, mechanism could still be "viscous glide". Therefore, if we follow the simulation carried out at 650^{o}C, where the Orowan strength contributed from phase transformation is ignored, the refined predictions are obtained and shown in Figure 7.18(d). It is then found that predictions at 108MPa and 157MPa approach the data and the increase of creep rate almost coincides with the data. However, the match between the prediction and data at higher stress (216MPa) in Figure 7.18(d) is found to be worse than that shown in Figure 7.18(b) at the same stress, indicating a contribution to creep strength by Orowan bowing strength, which is consistent with the strengthening-mechanism map shown in Figure 2.6, where the mechanism at this stress and temperature is found to be precipitation. Compared with the other two stresses, this may also indicate some significant influence of high stresses on the phase transformation.

At 550°C in Figure 7.18(a), the prediction shows poor agreement with the data. A large difference is observed at the early stage of creep and the model does not predict the occurrence of two secondary stages. In fact, the secondary stage is still yet to be achieved.

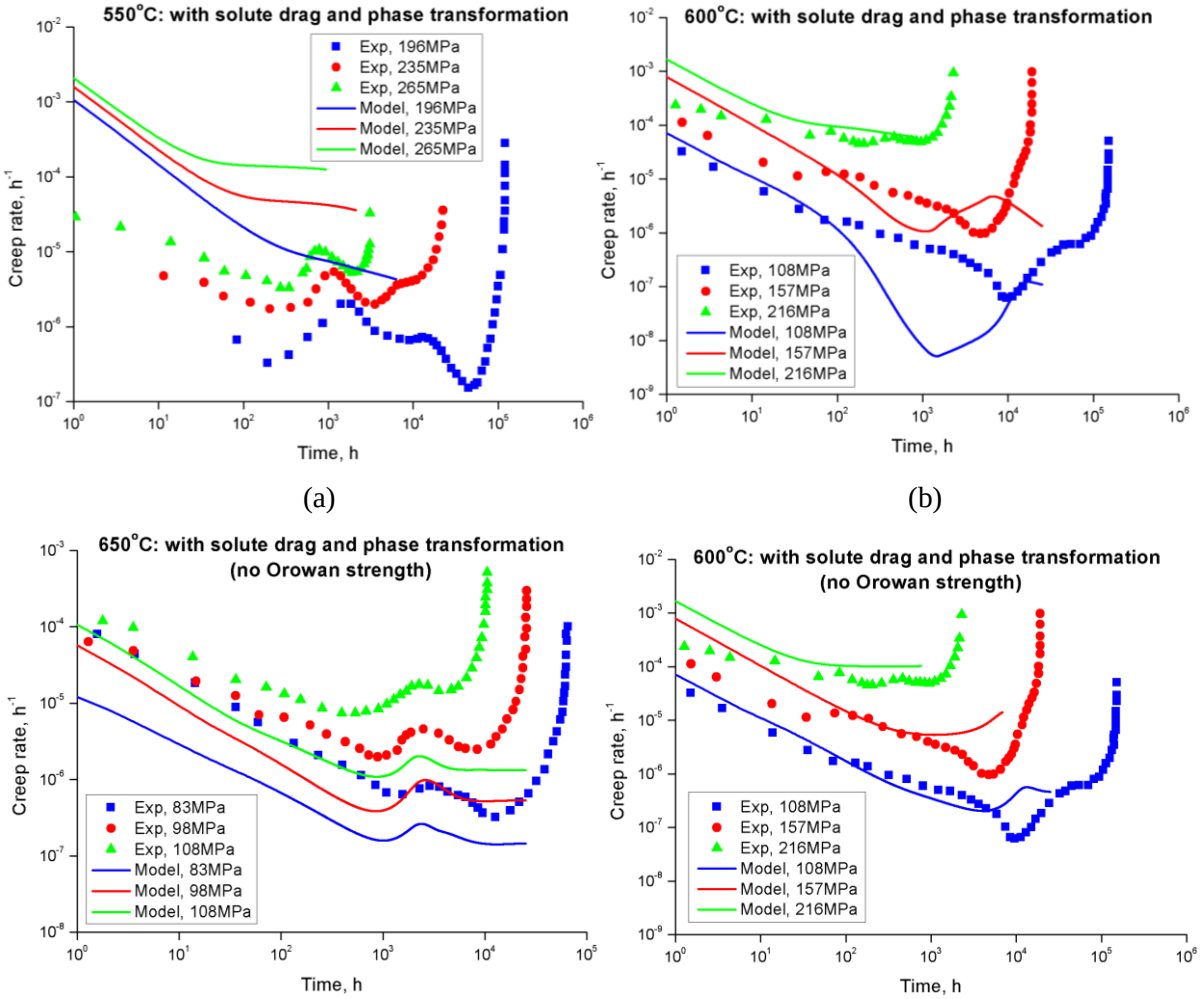

Fig. 7.18. Updated predictions of creep rate vs time curves at (a) 550°C; (b) 600°C and (c) 650°C. A refinement of the result at 600°C is presented in (d), by ignoring the Orowan bowing strength.

Here we try to explain this poor agreement at 550°C in the following aspects:

(1) The nucleation of precipitates can be largely dependent on the magnitude of strain-on-loading [40, 48], which has not been covered in the present phase transformation model. Since the stresses tested at 550°C are much larger than those at the other two higher

temperatures, more dislocations introduced by the extensive plastic monotonic pre-straining may significantly change the subsequent kinetics of the microstructure evolution and many precipitates may have already formed at the beginning of each creep test that contribute to the creep strength.

(2) The fitting parameter *A* in the solute drag model (Eq. (6.9)) may change with temperature [157]. Such change may be associated with the change in the size of the solute clusters surrounding moving dislocations, depending on the mobility of solutes at different temperatures. This may change the solute drag force or enhancement of the CRSS (Eq. (6.8)), leading to the change in the creep response at different temperatures.

(3) The chemical composition of carbides and Laves phase has been simplified, using their dominant elements. In practice, the majority of carbides formed at the very beginning of phase transformation could be $Fe_{23}C_6$ and such high amount of *Fe* is gradually replaced by *Cr* and/or *Mo* during subsequent ageing [186], which may not be manifested at higher temperatures due to fast kinetics of phase transformation at the beginning of the test. In addition, the dominant solute complexes or pairs for thermal solute drag may change at different temperatures between *Mo-C* and *Cr-C* as both have been reported [40, 159]. These subtle interactions are not covered in this phase transformation model.

In a sum, a more detailed microstructure study is further needed in order to calibrate and investigate in depth of the correlation between phase transformation and creep behaviour on this material.

7.4.3. Summary

The creep behaviour of initially solution-treated 316H stainless steels at various stresses and temperatures was evaluated in this section, using the combined model that has been established so far in this thesis. In particular, we have combined the creep model with the

enhancements of thermal solute drag and phase transformation and attempted to correlate the change in creep response and the evolution of microstructural state. The general trend of the multiple minimum creep rates or multiple secondary stages observed in creep rate vs time curves at some intermediate temperatures and stresses was captured by the model. The key findings out of this simulation are summarized below:

- The significant evolution of the microstructural state during thermal ageing and/or creep affects the mechanical properties of the material in many ways, including changes in the creep behaviour, temperature sensitivity and strain rate sensitivity.
- Mechanism of the complex phenomenon of multiple minimum creep rates or steady states is identified as being the combined effect of thermal solute drag and phase transformation. Evolution of microstructural state may change the deformation kinetics and break the dynamic balance between hardening and recovery that a new balance is yet to be achieved towards the second steady state.
- Care should be taken when combining the creep model with the phase transformation model since other mechanisms associated with more complex interactions between precipitation and creep may occur such as cutting of small precipitates, which does not contribute to the Orowan bowing strength and Type III internal stress. A more detailed study on microstructural evolution is further needed to investigate in depth of the correlation between phase transformation and creep behaviour of the solution-treated materials.
- Understanding the effect of thermal solute drag and phase transformation on the creep behaviour of the solution-treated material at elevated temperature is beneficial to the assessment of the evolution of materials' internal state and enables physical deformation modelling for a broader range of stress and temperature in the future.

Chapter 8

Conclusions and Future work

8.1. Conclusions

The creep deformation mechanisms of Type 316H austenitic stainless steels at various conditions (mechanical loading, temperature and microstructural state) are explored and investigated theoretically by developing a physically based multiscale state variable self-consistent model for polycrystalline materials, taking into account the evolution of different microstructural elements and a range of different internal strengthening and softening mechanisms. The model consists of continuum, crystal plasticity framework and dislocation link length model that allows the detailed distribution of dislocation structure, its evolution during plastic/creep deformation and the influence from other microstructural elements, such as precipitates and solute atoms, to be incorporated. The state variables are appropriately identified as the mean spacing between different types of obstacles. Evolutions of these different state variables are captured by the model through various processes, such as the dislocation multiplication (hardening) and network coarsening (recovery), the precipitation nucleation and growth and coarsening (Ostwald Ripening). The established model has been applied and validated on the evaluation of various available experimental data measured for Type 316H austenitic stainless steel specimens with initial conditions of either ex-service plus laboratory aged (EXLA) or solution treated (ST). The data covers a range of uniaxial tensile and compressive loading at ambient temperature, as well as phase transformation and/or creep at elevated temperatures. Different phenomena have been reasonably captured and interpreted by the model.

In conclusion, the multiscale self-consistent model captures the detailed interactions between different slip planes within individual grains, and between different grains within the polycrystal, and has been shown to be powerful in determining the deformation mechanisms associated with different mechanical behaviour of the material. While the model has been shown to be able to probe the appropriate initial conditions of the material before any commencement of loading (e.g. distribution of initial residual stress state within individual grains), it is clearly demonstrated that the nonlinear microscopic lattice response and macroscopic Bauschinger effect observed upon reloading at ambient temperature are attributed to the development of the Type II and/or Type III residual stresses. It is also shown that the material does not exhibit permanent softening, which should be a relative definition depending on the strain level that it is measured. Further, for the EXLA specimens, the state variables associated with forest dislocations (precipitates and solute atoms do not evolve) evolve during high temperature pre-straining and subsequent primary creep and saturate towards secondary creep. However, for the ST specimens, all the state variables may evolve, which is manifested in the phenomenon of multiple minima or multiple secondary stages observed in creep rate vs time curves over an extensive period of creep. The effect of thermal solute drag combined with the precipitate phase transformation has been considered as responsible for interpreting such complex phenomenon in the ST specimens. The results and analysis of this work are beneficial to the appropriate assessment of materials' internal state and further investigations of deformation mechanisms for a broader range of stress and temperature, which are critical for the life prediction and assessment of the structural components of AGRs nuclear reactors currently in service. Finally, this research can also be extended to other engineering alloys.

8.2. Future work

The future work is aimed at applying and/or improving the model developed in this thesis to extend the scope of the current research. In particular, further researches could be directed at several specific areas as follows.

8.2.1. Simulation of cyclic and creep-fatigue behaviour

The present research only considered simple loading conditions, such as monotonic tensile or compressive loading (Chapter 5) and uniaxial tensile creep (Chapter 7). During some complex conditions, such as cyclic loading, the dynamic recovery process associated with the annihilation of dislocations may become significant due to the production of a large number of dislocations with opposite signs. Thus it is more appropriate to model the dynamic recovery in detail separately rather than to couple the mechanism in the hardening as used in the present work (see Chapter 3). Further, the exposure at elevated temperature enhances the dislocation climb mobility thus may also enhance the dynamic recovery. This section attempts to understand and examine the creep-fatigue behaviour of Type 316H stainless steels subjected to cyclic loading at elevated temperature. To achieve this, the detailed investigation of the role of dynamic recovery as well as its influence on the evolution of internal resistance and internal stress during cyclic loading at elevated temperature is required.

8.2.2. Internal stress associated with the cell structure

The Type III internal stress has been discussed in Chapter 2 to be associated with the heterogeneous dislocation structures such as the secondary dislocation loops around the precipitates. Another dislocation structure that can contribute to the Type III internal stress, which is not considered in the current framework, is the dislocation cell structure, which is

formed when mobile dislocations frequently interact with each other and gradually get trapped to form dislocation walls, serving as impenetrable obstacles and resulting in the plastic deformation incompatibility between the walls and channels. The mechanisms of cell structure formation in impeding further dislocation motion include (1) the reduction of mobile dislocation density as being trapped in the walls; and (2) a Type III internal stress resulting from the incompatibility between the walls and channels. The cell structure is seen more frequently in pure metallic materials rather than engineering alloys since the precipitates existing in alloys are understood to be able to retard the formation of such dislocation substructure. However, as has been shown in the strengthening-mechanism map (Figure 2.6) in Chapter 2, the cell structure may also occur and dominate in 316H stainless steels at very high temperatures (>700^{o}C). Reasons for this can be (1) the extensive particle coarsening that reduces the strengthening effect associated with the precipitates; and (2) the increased diffusion mobility of solute atoms in the matrix that they do not form atmospheres or clusters to retard dislocation motion. Both of these factors may enhance the dislocation climb mobility and multiplication during creep, making the stainless steels behave like pure metallic materials. In addition, note that the particle coarsening can occur at any temperature given a certain time, thus the cell structure may also form at relatively low temperatures after long-term creep. Further, the formation of cell structure may be promoted by cyclic loading since it increases the chance for dislocations to interact with each other. Understanding the internal stress associated with the cell structure will broaden the model application to much higher temperatures and much longer term of creep.

A composite-type model [187, 188] has been proposed to describe the strain mismatch between a hard component representing the cell walls and a soft component representing the channels. The geometric illustration of such composite structure is simply shown in Figure 8.1. The model takes into account the loss of mobile dislocation density in the cell walls and

the large internal stress associated with the cell structure. This part of work will develop and implement such composite model into the current multiscale self-consistent model and evaluate the creep behaviour of the material at very high temperatures.

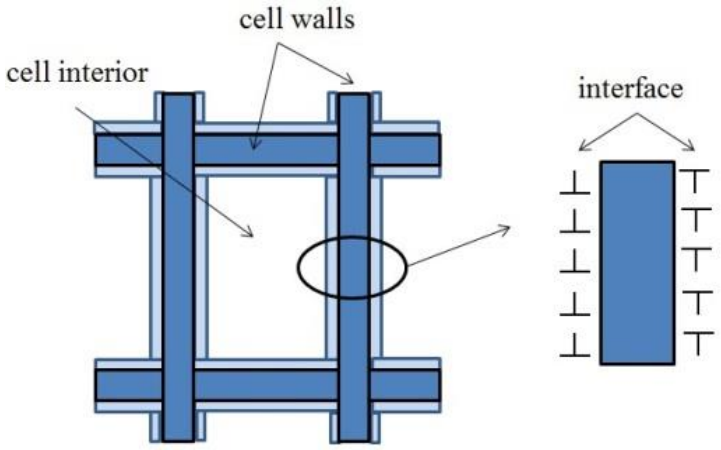

Fig. 8.1 Geometry of a cell structure cross-section with the interface layers [187]

8.2.3. Evaluation of stress relaxation

Apart from the creep data tested at constant load or constant strain rate, some stress relaxation data of the ex-service 316 stainless steels is also available in EDF Energy Ltd. The stress relaxation is defined as a gradual nonlinear decrease in the applied macroscopic stress with time under a fixed constant strain at elevated temperature (Figure 8.2). Understanding and explaining the stress relaxation data of the material is vital to the life assessment and prediction of the AGR nuclear reactors since the current non-steady changes in the operation mode of AGRs may involve such stress relaxation phenomenon.

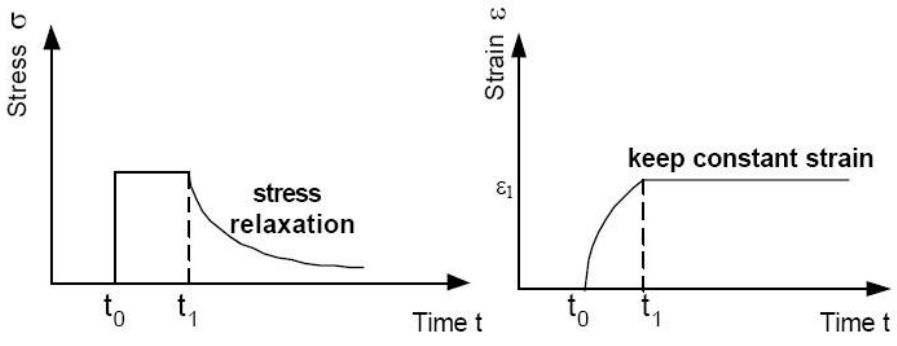

Fig. 8.2 A schematic diagram of stress relaxation

It has been understood that the creep strain may still accumulate at exposure of elevated temperature, thus the relaxation of stress is due to the transformation from the elastic strain to creep strain during the dwell of the total strain. However, the empirical creep models used by EDF Energy that can fit some creep data of the material have shown poor agreement in the stress relaxation data, indicating some changes in the deformation mechanisms. Having previously reviewed and studied the strengthening and softening mechanisms as well as deformation kinetics at various conditions in this thesis, this section applies the established multiscale self-consistent model to evaluate and interpret the available stress relaxation data of 316H stainless steels. The dominant mechanism(s) for stress relaxation will be identified.

8.2.4. Consideration of damage accumulation

The tertiary stage during creep deformation has been considered to be a process of rapid damage accumulation. There are many specific microstructural features that evolve during service, which can be reasons for the acceleration of creep rate in tertiary stage that leads to final failure. Strain softening process can be a type of damage related to dislocation activities. With continuous thermal recovery, climb-controlled dislocation motion will be more and more frequent thus more dislocation links will be released and glide, leading to the acceleration of creep rate. The cavitation or void growth seems to be another type. The cavities can grow by diffusion mechanisms such as grain-boundary diffusion and surface diffusion, or the combination of the two. The coalescence of cavities by diffusion can form micro-cracks and propagate further, which will result in final failure. After the detailed fundamental understanding of creep deformation, the study of damage mechanisms will be a significant extension of the current research.

References

[1] Advanced Gas-Cooled Reactors (AGR) http://wwwnucleartouristcom/type/gcrhtm.
[2] Spindler M. Discussion document-Creep constitutive models for type 316H. British Energy 2010.
[3] Lagneborg R, Forsen BH. A model based on dislocation distributions for work-hardening and the density of mobile and immobile dislocations during plastic flow. Acta Metall Mater 1973;21:781-90.
[4] Ostrom P, Lagneborg R. A recovery-athermal glide creep model. J Eng Mater-T Asme 1976;98:114-24.
[5] Blum W, Eisenlohr P, Breutinger F. Understanding creep - a review. Metall Mater Trans A 2002;33:291-303.
[6] Chaboche JL. A review of some plasticity and viscoplasticity constitutive theories. Int J Plasticity 2008;24:1642-93.
[7] Meyers MA, Chawla KK, Hosford WF. Mechanical behavior of materials. 2nd ed. Cambridge: Cambridge University Press; 2009.
[8] Penny RK, Marriott DL. Design for creep. 2nd ed ed. London: Chapman & Hall; 1995.
[9] Feehery WF, Barton PI. Dynamic optimization with state variable path constraints. Comput Chem Eng 1998;22:1241-56.
[10] Estrin Y, Mecking H. A Unified Phenomenological Description of Work-Hardening and Creep Based on One-Parameter Models. Acta Metall Mater 1984;32:57-70.
[11] Frost HJ, Ashby MF. Deformation-mechanism maps : the plasticity and creep of metals and ceramics. Oxford: Pergamon Press; 1982.
[12] Doherty RD, Hughes DA, Humphreys FJ, Jonas JJ, Jensen DJ, Kassner ME, et al. Current issues in recrystallization: a review. Mat Sci Eng a-Struct 1997;238:219-74.
[13] Mclean D. The physics of high temperature creep in metals. Reports on Progress in Physics 1966;29.
[14] Mclean D, Hale KF. The stress sensitivity of creep. Proceedings of the Symposim on Structural Processes in Creep 1961.
[15] Mitra SK, Mclean D. Work Hardening and Recovery in Creep. Proc R Soc Lon Ser-A 1966;295:288-95.
[16] Lagneborg R. Recovery Creep in Materials Hardened by a Second Phase. J Mater Sci 1968;3:596-602.
[17] Shi L, Northwood DO. Review dislocation network models for recovery creep deformation. J Mater Sci 1993;28:5963-74.
[18] Basoalto HC, Ghosh RN, Dyson BF, McLean M. Creep modelling of superalloys numerical optimisation of parameters. Micro High Temp Mat 1999:293-303.
[19] Dyson BF, Mclean M. Creep Deformation of Engineering Alloys - Developments from Physical Modeling. Isij Int 1990;30:802-11.
[20] Barboza MJR, Neto CM, Silva CRM. Creep mechanisms and physical modeling for Ti-W-4V. Mat Sci Eng a-Struct 2004;369:201-9.
[21] Ghosh RN, Mclean M. High-Temperature Deformation in Engineering Alloys - Modeling for Strain or Load Control. Acta Metallurgica Et Materialia 1992;40:3075-83.
[22] Dyson BF, Gibbons TB. Tertiary Creep in Nickel-Base Superalloys - Analysis of Experimental-Data and Theoretical Synthesis. Acta Metall Mater 1987;35:2355-69.
[23] Pan LM, Shollock BA, McLean M. Modelling of high-temperature mechanical behaviour of a single crystal superalloy. P Roy Soc Lond a Mat 1997;453:1689-715.
[24] Douglas J, Dennis R, Spindler MW. Development of an advanced creep model for Type 316 stainless steel. Eighth International Conference on Creep and Fatigue at Elevated Temperatures, San Antonio, Texas 2007.
[25] Kubo K, Ohba T, Kimura K, Abe F, Yagi K, Irie H. Effect of microstructural evolution on complex creep deformation behaviour of SUS 316 steel at 823K and 923K. CAMP-ISIJ 1996;9:1435-.
[26] Hull D, Bacon DJ. Introduction to dislocations. 4th ed. Oxford: Butterworth Heinemann; 2001.

[27] Argon AS. Strengthening mechanisms in crystal plasticity. Oxford: Oxford University Press; 2008.
[28] Ramesh KT. Nanomaterials - mechanics and mechanisms. Springer 2009.
[29] Franciosi P, Berveiller M, Zaoui A. Latent Hardening in Copper and Aluminum Single-Crystals. Acta Metall Mater 1980;28:273-83.
[30] Kubin L, Devincre B, Hoc T. Modeling dislocation storage rates and mean free paths in face-centered cubic crystals. Acta Mater 2008;56:6040-9.
[31] Cannelli G, Cantelli R, Cordero F. Statistical-Model for the Trapping of Interstitials by Substitutional (Interstitial) Atoms in Solids. Phys Rev B 1985;32:3573-9.
[32] Dong Y, Nogaret T, Curtin WA. Scaling of Dislocation Strengthening by Multiple Obstacle Types. Metall Mater Trans A 2010;41A:1954-60.
[33] Hirth JP, Lothe J. Theory of dislocations. 2nd ed ed. New York ; Chichester: Wiley; 1982.
[34] Marshall P. Austenitic stainless steels : microstructure and mechanical properties. London: Elsevier Applied Science; 1984.
[35] Feng Z. Microstructural evolution in austenitic stainless steels for extended life power station application. PhD Thesis for Loughborough University 2011.
[36] National Institute of Materials Science N. Micrographs and Microstructural Characteristics of Crept Specimens of 18Cr-12Ni-Mo Stainless steel for Boiler and Heat exchanger seamless tubes (SUS 316H TB). 2003.
[37] Morris DG, Harries DR. Creep and rupture in Type 316 stainless steel at temperatures between 525 and 900oC Part III: Precipitation behaviour Metal Science 1978:542-9.
[38] Ashby MF, Jones DRH. Engineering materials 2 : an introduction to microstructures, processing and design. 3rd ed. Oxford: Butterworth-Heinemann ; Elsevier; 2006.
[39] Challeng KD, Moteff J. Quantitative Characterization of Substructure of Aisi-316 Stainless-Steel Resulting from Creep. Metall Trans 1973;4:749-55.
[40] Morris DG, Harries DR. Creep and rupture in Type 316 stainless steel at temperatures between 525 and 900C-Part 1: creep rate. Metal Science 1978:525-31.
[41] Ashby M. The Hardening of Metals by Non-Deforming Particles. Z Metallkd 1964;55:5-17.
[42] Kelly A, Nicholson RB. Precipitation Hardening. Progress in Materials Science 1963;10:151-391.
[43] Orowan E. Discussion on internal stresses. In Symposium on Internal Stresses in Metals and Alloys, London, The Institute of Metals 1948:451-3.
[44] Foreman AJE, Makin MJ. Dislocation Movement through Random Arrays of Obstacles. Philosophical Magazine 1966;14:911-24.
[45] Callister WD. Materials science and engineering : an introduction. 6th ed. New York ; [Chichester]: Wiley; 2003.
[46] Ashby MF. The theory of the critical shear stress and work hardening of dispersion-hardened crystals. Defense Technical Information Center, UK 1966.
[47] Mclean M. On the Threshold Stress for Dislocation Creep in Particle Strengthened Alloys. Acta Metall Mater 1985;33:545-56.
[48] Aplin PF, Angelo DD. Dislocation-creep mechanisms in type 316 steel. . In Creep and Fracture of Engineering Materials and Structures, eds B Wilshire, RW Evans Institute of Metals, London 1990:537-45.
[49] Mcqueen HJ, Jonas JJ. Recovery and recrystallization during high temperature deformation (metal hot working). Plastic Deformation of Materials 1975:393-493.
[50] Kocks UF. Laws for Work-Hardening and Low-Temperature Creep. J Eng Mater-T Asme 1976;98:76-85.
[51] Mecking H, Kocks UF. Kinetics of Flow and Strain-Hardening. Acta Metall Mater 1981;29:1865-75.
[52] Lagneborg R. A modified recovery-creep model and its evaluation. Metal Science 1972;6:127-33.
[53] Friedel J. Dislocations. Reprinted with corrections ed. Oxford, Reading, Mass: Pergamon; [Distributed in USA by] Addison-Wesley Pub. Co; 1964.
[54] Hillert M. On the theory of normal and abnormal grain growth. Acta Metall Mater 1965;13:227-38.

[55] Shi LQ, Northwood DO. Creep of an Aisi-310 Type Stainless-Steel and Its Numerical-Simulation Using the Ostrom-Lagneborg Creep Model. Acta Metallurgica Et Materialia 1993;41:3393-400.
[56] Lin P, Lee SS, Ardell AJ. Scaling Characteristics of Dislocation Link Length Distributions Generated during the Creep of Crystals. Acta Metall Mater 1989;37:739-48.
[57] Ajaja O. A Dislocation Network Model of Recovery-Controlled Creep. J Mater Sci 1986;21:3351-6.
[58] Shewmon PG. Transformations in metals. New York ; London: McGraw-Hill; 1969.
[59] Sun WA. Particle coarsening: I. Kinetics for reversible dissolution/deposition controlled process. Acta Mater 2005;53:3329-34.
[60] Christian JW. The theory of transformations in metals and alloys : an advanced textbook in physical metallurgy. 2nd ed. Oxford: Pergamon; 1975.
[61] Morral JE, Purdy GR. Thermodynamics of Particle Coarsening. J Alloy Compd 1995;220:132-5.
[62] Robson JD, Bhadeshia HKDH. Modelling precipitation sequences in power plant steels .1. Kinetic theory. Mater Sci Tech Ser 1997;13:631-9.
[63] Yin YF, Faulkner RG. Simulations of precipitation in ferritic steels. Mater Sci Tech Ser 2003;19:91-8.
[64] Cheng LM, Hawbolt EB, Meadowcroft TR. Modeling of dissolution, growth, and coarsening of aluminum nitride in low-carbon steels. Metall Mater Trans A 2000;31:1907-16.
[65] Hirsch PB, Humphreys FJ. Plastic deformation of two-phase alloys containing small nondeformable particles. Physics of Strength and Plasticity 1969:189-216.
[66] Schwarz RB, Labusch R. Dynamic Simulation of Solution Hardening. J Appl Phys 1978;49:5174-87.
[67] Kocks UF. A statistical theory of flow stress and work-hardening. Philosophical Magazine 1966;13:541-66.
[68] Ashby MF. On the Orowan stress. Physics of Strength and Plasticity 1969:19.
[69] Humphrey FJ, Hirsch PB. Deformation of Single Crystals of Copper and Copper-Zinc Alloys Containing Alumina Particles .2. Microstructure and Dislocation-Particle Interactions. Proc R Soc Lon Ser-A 1970;318:73-&.
[70] Calhoun RB, Mortensen A. Equilibrium shape of prismatic dislocation loops under uniform stress. Acta Mater 1999;47:2357-65.
[71] Brown LM, Stobbs WM. Work-Hardening of Copper-Silica .2. Role of Plastic Relaxation. Philosophical Magazine 1971;23:1201-&.
[72] Evans HE, Knowles G. Threshold Stress for Creep in Dispersion-Strengthened Alloys. Metal Science 1980;14:262-6.
[73] Arzt E, Wilkinson DS. Threshold Stresses for Dislocation Climb over Hard Particles - the Effect of an Attractive Interaction. Acta Metall Mater 1986;34:1893-8.
[74] Shewfelt RSW, Brown LM. High-Temperature Strength of Dispersion-Hardened Single-Crystals .2. Theory. Philosophical Magazine 1977;35:945-62.
[75] Arzt E, Ashby MF. Threshold Stresses in Materials Containing Dispersed Particles. Scripta Metall Mater 1982;16:1285-90.
[76] Lagnebor R. Bypassing of Dislocations Past Particles by a Climb Mechanism. Scripta Metall Mater 1973;7:605-13.
[77] Schmidt CG, Miller AK. The Effect of Solutes on the Strength and Strain-Hardening Behavior of Alloys .16. Acta Metall Mater 1982;30:615-25.
[78] Cocks ACF. Final report on constitutive modeling and stress relaxation of 316 stainless steel.
[79] Solberg JK. The Influence of Carbon and Nitrogen on the High-Temperature Creep-Properties of Aisi Type-316 Austenitic Stainless-Steel. Mater Sci Eng 1982;55:39-44.
[80] Chen B, Flewitt PEJ, Smith DJ, Cocks ACF. A review of the changes of internal state related to high temperature creep of polycrystalline metals and alloys. Int Mater Rev 2015;60:1-29.
[81] Miller DA, Langdon TG. Creep Fracture Maps for 316-Stainless Steel. Metall Trans A 1979;10:1635-41.
[82] Hutchinson JW. Bounds and Self-Consistent Estimates for Creep of Polycrystalline Materials. Proc R Soc Lon Ser-A 1976;348:101-27.

[83] Follansbee PS, Kocks UF. A Constitutive Description of the Deformation of Copper Based on the Use of the Mechanical Threshold Stress as an Internal State Variable. Acta Metall Mater 1988;36:81-93.
[84] Lund RW, Nix WD. High-Temperature Creep of Ni-20cr-2tho-2 Single-Crystals. Acta Metall Mater 1976;24:469-81.
[85] Lagneborg R. Dislocation mechanisms in creep. Int Metall Rev 1972;17:130-46.
[86] Wasilkowska A, Bartsch M, Messerschmidt U, Herzog R, Czyrska-Filemonowicz A. Creep mechanisms of ferritic oxide dispersion strengthened alloys. J Mater Process Tech 2003;133:218-24.
[87] Taylor GI. The Mechanism of Plastic Deformation of Crystals. Part I. Theoretical. Proc Roy Soc 1934;145.
[88] Gibeling JC, Nix WD. The Description of Elevated-Temperature Deformation in Terms of Threshold Stresses and Back Stresses - a Review. Mater Sci Eng 1980;45:123-35.
[89] Mclean M. Friction Stress and Recovery during High-Temperature Creep - Interpretation of Creep Transients Following a Stress Reduction. P Roy Soc Lond a Mat 1980;371:279-94.
[90] Parker JD, Wilshire B. Friction-stress measurements during high-temperature creep of polycrystalline copper. Metal Sci 1978;12:453-8.
[91] Crosslan LG, Jones RB, Lewthwai GW. Use of Helically Coiled Springs in Creep Experiments with Special Reference to Case of Bingham Flow. J Phys D Appl Phys 1973;6:1040-6.
[92] Rao A, Chong KB, Bouchard PJ, Fitzpatrick ME. Internal stress generation in austentic stainless steels during creep deformation. 'ASME Pressure Vessels and Piping Division Conference', Baltimore, 2011.
[93] Mishra RS, Nandy TK, Greenwood GW. The Threshold Stress for Creep Controlled by Dislocation Particle Interaction. Philos Mag A 1994;69:1097-109.
[94] Burt H, Dennison JP, Wilshire B. Friction stress measurements during creep of Nimonic 105. Metal Sci 1979;13:295-300.
[95] Withers PJ, Bhadeshia HKDH. Overview - Residual stress part 1 - Measurement techniques. Mater Sci Tech Ser 2001;17:355-65.
[96] Withers PJ, Bhadeshia HKDH. Overview - Residual stress part 2 - Nature and origins. Mater Sci Tech Ser 2001;17:366-75.
[97] Clausen B, Lorentzen T, Leffers T. Self-consistent modelling of the plastic deformation of FCC polycrystals and its implications for diffraction measurements of internal stresses. Acta Mater 1998;46:3087-98.
[98] Daymond MR, Bouchard PJ. Elastoplastic deformation of 316 stainless steel under tensile loading at elevated temperatures. Metall Mater Trans A 2006;37A:1863-73.
[99] Lowe TC, Miller AK. Modeling Internal-Stresses in the Nonelastic Deformation of Metals. J Eng Mater-T Asme 1986;108:365-73.
[100] Lowe TC, Miller AK. Improved Constitutive-Equations for Modeling Strain Softening .1. Conceptual Development. J Eng Mater-T Asme 1984;106:337-42.
[101] Pedersen OB, Brown LM, Stobbs WM. The Bauschinger Effect in Copper. Acta Metall Mater 1981;29:1843-50.
[102] Gong YP, Hyde CJ, Sun W, Hyde TH. Determination of material properties in the Chaboche unified viscoplasticity model. P I Mech Eng L-J Mat 2010;224:19-29.
[103] Miller AK. An inelastic constitutive model for monotonic, cyclic, and creep deformation: Part I—Equations development and analytical procedures. J Eng Mater-T Asme 1976;96:97-105.
[104] Henshall GA, Miller AK. Simplifications and Improvements in Unified Constitutive-Equations for Creep and Plasticity .1. Equations Development. Acta Metallurgica Et Materialia 1990;38:2101-15.
[105] Dyson B. An alternative constitutive description of AISI 316 stainless steel for use in weld reheat cracking. Report prepared for Nuclear Electric plc Barnwood Gloucester 1997.
[106] Basoalto H, Dyson B. Predicting stress relaxation & LCF using a microstructure-based constitutive model. British Energy plc Contract Reference No 40072908 (SW19/02) 2003.
[107] Kocks UF, Mecking H. Physics and phenomenology of strain hardening: the FCC case. . Progress in Materials Science 2003;48:171-273.
[108] Gibbs GB. General Dislocation Model for High-Temperature Creep. Philosophical Magazine 1971;23:771-&.

[109] Armstrong PJ, Frederick CO. A mathematical representation of the multiaxial Bauschinger effect. Report RD/B/N731, Central Electricity Generating Board, Berkeley, UK 1966.
[110] Mclean D. Resistance to Hot Deformation. T Metall Soc Aime 1968;242:1193-&.
[111] Evans HE, Knowles G. Model of creep in pure materials. Acta Metall 1977;25:963-75.
[112] Ardell AJ, Lee SS. A Dislocation Network Theory of Harper-Dorn Creep .1. Steady-State Creep of Monocrystalline Al. Acta Metall Mater 1986;34:2411-23.
[113] Shi L, Northwood DO. On Dislocation Link Length Statistics for Constant Strain-Rate Deformation. Phys Status Solidi A 1993;140:87-95.
[114] Wang BS, Sun FY, Meng QE, Xu WC. An approach to theoretical function of dislocation link length distribution in metal. Acta Metallurgica Sinica (A) 1992;5:314-7.
[115] Ardell AJ, Przystupa MA. Dislocation Link-Length Statistics and Elevated-Temperature Deformation of Crystals. Mech Mater 1984;3:319-32.
[116] Madec R, Devincre B, Kubin LP. From dislocation junctions to forest hardening. Phys Rev Lett 2002;89.
[117] Hu JN, Chen B, Smith DJ, Flewitt PEJ, Cocks ACF. Self-consistent modelling and the evaluation of lattice deformation in a polycrystalline austenitic stainless steel. Materials Today: Proceedings In press 2015.
[118] Shi L, Northwood DO. On Dislocation Link Length Statistics for Plastic-Deformation of Crystals. Phys Status Solidi A 1993;137:75-85.
[119] Brown LM, Stobbs WM. The work-hardening of copper-silica I. A model based on internal stress, with no plastic relaxation. Philosophical Magazine 1971;23:1185-99.
[120] Kroupa F. Interaction between Prismatic Dislocation Loops and Straight Dislocations .1. Philosophical Magazine 1962;7:783-&.
[121] Kocks UF. Kinetics of Solution Hardening. Metall Trans A 1985;16:2109-29.
[122] Picu RC, Li RG, Xu ZJ. Strain rate sensitivity of thermally activated dislocation motion across fields of obstacles of different kind. Mat Sci Eng a-Struct 2009;502:164-71.
[123] Deschamps A, Brechet Y. Influence of predeformation and ageing of an Al-Zn-Mg alloy - II. Modeling of precipitation kinetics and yield stress. Acta Mater 1998;47:293-305.
[124] Taylor GI. Plastic strain in metals. J Inst Metals 1938;62:307-25.
[125] Eshelby JD. The determination of the elastic field of an ellipsoidal inclusion and related problems. Proc R Soc Lond A 1957;241:376-96.
[126] Withers PJ, Stobbs WM, Pedersen OB. The Application of the Eshelby Method of Internal-Stress Determination to Short Fiber Metal Matrix Composites. Acta Metall Mater 1989;37:3061-84.
[127] Hill R. Essential Structure of Constitutive Laws for Metal Composites and Polycrystals. J Mech Phys Solids 1967;15:79-&.
[128] Hill R. Continuum Micro-Mechanics of Elastoplastic Polycrystals. J Mech Phys Solids 1965;13:89-&.
[129] Hill R. Generalized Constitutive Relations for Incremental Deformation of Metal Crystals by Multislip. J Mech Phys Solids 1966;14:95-&.
[130] Kroner E. On the Plastic Deformation of Polycrystals. Acta Metall Mater 1961;9:155-61.
[131] Budiansky B, Wu TT. Theoretical prediction of plastic strains of polycrystals. Proc 4th Congr Appl Mech 1962:1175-85.
[132] Hutchinson JW. Elastic-Plastic Behaviour of Polycrystalline Metals and Composites. Proc R Soc Lon Ser-A 1970;319:247-72.
[133] Neil CJ, Wollmershauser JA, Clausen B, Tome CN, Agnew SR. Modeling lattice strain evolution at finite strains and experimental verification for copper and stainless steel using in situ neutron diffraction. Int J Plasticity 2010;26:1772-91.
[134] Asaro RJ, Needleman A. Overview .42. Texture Development and Strain-Hardening in Rate Dependent Polycrystals. Acta Metall Mater 1985;33:923-53.
[135] Aghababaei R, Joshi SP, Reddy JN. Nonlocal continuum crystal plasticity with internal residual stresses. J Mech Phys Solids 2011;59:713-31.
[136] Bronkhorst CA, Kalidindi SR, Anand L. Polycrystalline Plasticity and the Evolution of Crystallographic Texture in Fcc Metals. Philos T Roy Soc A 1992;341:443-77.

[137] Li DF, Davies CM, Zhang SY, Dickinson C, O'Dowd NP. The effect of prior deformation on subsequent microplasticity and damage evolution in an austenitic stainless steel at elevated temperature. Acta Mater 2013;61:3575-84.
[138] Clausen B, Lorentzen T, Bourke MAM, Daymond MR. Lattice strain evolution during uniaxial tensile loading of stainless steel. Mat Sci Eng a-Struct 1999;259:17-24.
[139] Mura T. Micromechanics of defects in solids. The Hague ; London: Martinus Nijhoff; 1982.
[140] Rice JR. Structure of Stress-Strain Relations for Time-Dependent Plastic Deformation in Metals. J Appl Mech 1970;37:728-+.
[141] Li DF, O'Dowd NP. On the evolution of lattice deformation in austenitic stainless steels-The role of work hardening at finite strains. J Mech Phys Solids 2011;59:2421-41.
[142] Li DF, O'Dowd NP, Davies CM, Zhang SY. Measurement and prediction of the microscale deformation of an austenitic stainless steel under uniaxial loading. Eur J Mech A Solids 2011;30:748-60.
[143] Chen B, Flewitt PEJ, Smith DJ, Jones CP. An improved method to identify grain boundary creep cavitation in 316H austenitic stainless steel. Ultramicroscopy 2011;111:309-13.
[144] Faulkner RG. Microstructural examination of ex-Heysham header creep specimens. Internal report to EDF Energy 2002.
[145] Chen B, Hu JN, Flewitt PEJ, Smith DJ, Cocks ACF, Zhang SY. Quantifying internal stress and internal resistance associated with thermal ageing and creep in a polycrystalline material. Acta Mater 2014;67:207-19.
[146] Chen B, Hu JN, Wang YQ, Zhang SY, Petegem SV, Cocks ACF, et al. Role of the misfit stress between grains in the Bauschinger effect for a polycrystalline material. Acta Mater 2015;85:229-42.
[147] Santisteban JR, Daymond MR, James JA, Edwards L. ENGIN-X: a third-generation neutron strain scanner. J Appl Cryst 2006;39:812-25.
[148] Kamaya M. A procedure for estimating Young's modulus of textured polycrystalline materials. Int J Solids Struct 2009;46:2642-9.
[149] Hu JN, Cocks ACF. A multi-scale self-consistent model describing the lattice deformation in austenitic stainless steels. Int J Solids Struct 2015;Under review.
[150] Kapoor R, Nemat-Nasser S. High-rate deformation of single crystal tantalum: Temperature dependence and latent hardening. Scripta Mater 1998;40:159-64.
[151] Kocks UF, Argon AS, Ashby MF. Thermodynamics and Kinetics of Slip. Progress in Materials Science 1975;19:1-281.
[152] Busso EP, McClintock FA. A dislocation mechanics-based crystallographic model of a B2-type intermetallic alloy. Int J Plasticity 1996;12:1-28.
[153] Shetty MN. Dislocations and Mechanical Behaviour of Materials. 2013;Asoke K. Ghosh:351-4.
[154] Weiner JH, Hikata A, Elbaum C. Vibration of a Pinned Dislocation Segment in an Atomistic Model. Phys Rev B 1976;13:531-43.
[155] Schmidt CG, Miller AK. A Unified Phenomenological Model for Non-Elastic Deformation of Type-316 Stainless-Steel .1. Development of the Model and Calculation of the Material Constants. Res Mech 1981;3:109-29.
[156] Henshall A. Solute-enhanced back stresses and their role in a simplified phenomenological constitutive model for the nonelastic deformation of metals and alloys. Dissertation for Stanford Univeristy 1987.
[157] Schmidt CG, Miller AK. A Unified Phenomenological Model for Non-Elastic Deformation of Type-316 Stainless-Steel .2. Fitting and Predictive Capabilities. Res Mech 1981;3:175-93.
[158] Cottrell AH, Jaswon MA. Distribution of Solute Atoms Round a Slow Dislocation. Proc R Soc Lon Ser-A 1949;199:104-14.
[159] Asbury FE. Factors Influencing Long-Term Creep of Type-316 Steel at 600-Degrees-C. Mater Sci Tech Ser 1986;2:1123-30.
[160] Cocks ACF, Ponter ARS. Constitutive-Equations for the Plastic-Deformation of Solids .2. A Composite Model. Eur J Mech a-Solid 1991;10:351-69.
[161] Cocks ACF, Ponter ARS. Constitutive-Equations for the Plastic-Deformation of Solids .1. Isotropic Material. Eur J Mech a-Solid 1991;10:243-64.
[162] Perez M, Dumont M, Acevedo-Reyes D. Implementation of classical nucleation and growth theories for precipitation. Acta Mater 2008;56:2119-32.

[163] Fanfoni M, Tomellini M. The Johnson-Mehl-Avrami-Kolmogorov model: A brief review. Nuovo Cimento D 1998;20:1171-82.
[164] Perrard F, Deschamps A, Maugis P. Modelling the precipitation of NbC on dislocations in alpha-Fe. Acta Mater 2007;55:1255-66.
[165] Embury JD, Deschamps A, Brechet Y. The interaction of plasticity and diffusion controlled precipitation reactions. Scripta Mater 2003;49:927-32.
[166] Weinberg MC, Birnie DP, Shneidman VA. Crystallization kinetics and the JMAK equation. J Non-Cryst Solids 1997;219:89-99.
[167] Zener C. Theory of Growth of Spherical Precipitates from Solid Solution. J Appl Phys 1949;20:950-3.
[168] Sheng G, Wang T, Du Q, Wang KG, Liu ZK, Chen LQ. Coarsening Kinetics of a Two Phase Mixture with Highly Disparate Diffusion Mobility. Commun Comput Phys 2010;8:249-64.
[169] Baldan A. Review Progress in Ostwald ripening theories and their applications to nickel-base superalloys - Part I: Ostwald ripening theories. J Mater Sci 2002;37:2171-202.
[170] Sauthoff G. Influence of stresses on precipitation. J Phys Iv 1996;6:87-97.
[171] Burton B. The Influence of Solute Drag on Dislocation Creep. Philos Mag A 1982;46:607-16.
[172] Kubo K, Ohba T, Kimura K, Abe F, Yagi K. Effect of changes in microstructure on complex creep deformation behaviour of SUS 316. CAMP-ISIJ 1994;7:1791-.
[173] Chen B, Smith DJ, Flewitt PEJ, Spindler MW. Constitutive equations that describe creep stress relaxation for 316H stainless steel at 550 degrees C. Mater High Temp 2011;28:155-64.
[174] Lo KH, Shek CH, Lai JKL. Recent developments in stainless steels. Mat Sci Eng R 2009;65:39-104.
[175] Weiss B, Stickler R. Phase Instabilities during High-Temperature Exposure of 316 Austenitic Stainless-Steel. Metall Trans 1972;3:851-&.
[176] Tabor D. The hardness of metals. Oxford: At the Clarendon Press; 1951.
[177] Fujita N, Bhadeshia HKDH. Modelling simultaneous alloy carbide sequence in power plant steels. Isij Int 2002;42:760-9.
[178] Robson JD, Bhadeshia HKDH. Modelling precipitation sequences in power plant steels .2. Application of kinetic theory. Mater Sci Tech Ser 1997;13:640-4.
[179] Chen Q, Jeppsson J, Agren J. Analytical treatment of diffusion during precipitate growth in multicomponent systems. Acta Mater 2008;56:1890-6.
[180] Sourmail T. Precipitation in creep resistant austenitic stainless steels. Mater Sci Tech Ser 2001;17:1-14.
[181] Nitta H, Yamamoto T, Kanno R, Takasawa K, Iida T, Yamazaki Y, et al. Diffusion of molybdenum in alpha-iron. Acta Mater 2002;50:4117-25.
[182] Anderson TD, Perricone MJ, DuPont JN, Marder AR. The influence of molybdenum on stainless steel weld microstructures. Weld J 2007;86:281s-92s.
[183] Boeuf A, Crico S, Caciuffo R, Rustichelli F, Pomot I, Uny G. Effects of M23c6 Precipitation on the Lattice-Parameter of Aisi-304 Stainless-Steel. Mater Lett 1985;3:115-8.
[184] Gladman T. The physical metallurgy of microalloyed steels. London: Institute of Materials; 1997.
[185] Smith AF. The diffusion of chromium in type 316 stainless steel. Metal Sci 1975;9:375-8.
[186] Rieth M, Falkenstein A, Graf P, Heger S, Jantsch U, Klimiankou M, et al. Creep of the austenitic steel AISI 316 L(N)-Experiments and models. 2004.
[187] Viatkina EM, Brekelmans WAM, Geers MGD. Modelling of the internal stress in dislocation cell structures. Eur J Mech a-Solid 2007;26:982-98.
[188] Mughrabi H. Dislocation wall and cell structures and long-range internal stresses in deformed metal crystals. Acta Metall Mater 1983;31:1367-79.
[189] Rosler J, Arzt E. A New Model-Based Creep Equation for Dispersion Strengthened Materials. Acta Metallurgica Et Materialia 1990;38:671-83.

Appendix A. Derivation of the two-dimensional distribution of pinning points on a single slip plane

Consider a single slip plane that contains N_d randomly distributed pinning points per unit area. The total number of pinning points on a slip plane of area A (much greater than the square of the separation of the pinning points) is N_dA. Now consider any pinning point. The probability that it lies outside of a prescribed area, x, of the slip plane is

$$\frac{A-x}{A}=1-\frac{x}{A} \tag{A.1}$$

Now consider a second pinning point. The probability that it lies outside of the area is also given by Eq. (A.1). The probability that both pinning points are outside of the area x is $(1-x/A)^2$. Therefore, if we consider all the N_dA points on the plane, the probability for all of them to be outside the area x is $(1-x/A)^{N_dA}$. Expanding this result as a Taylor series and letting $A\to\infty$ gives

$$\begin{aligned}\left(1-\frac{x}{A}\right)^A &= 1-\frac{x}{A}\cdot A+\frac{x^2}{2!A^2}\cdot A(A-1)-\frac{x^3}{3!A^3}\cdot A(A-1)(A-2)+\ldots \\ &\approx 1-x+\frac{x^2}{2!}-\frac{x^3}{3!}+\ldots \\ &= \exp(-x)\end{aligned} \tag{A.2}$$

Therefore, the probability of N_dA pinning points lying outside of the area x is expressed as

$$\left(1-\frac{x}{A}\right)^{N_dA}=\exp\left(-\frac{x}{{L_d}^2}\right) \tag{A.3}$$

where $L_d=N_d^{-1/2}$ is the mean spacing between all the pinning points on the slip plane. Finally, the probability of finding a point inside the area x is given by

$$1-\left(1-\frac{x}{A}\right)^{N_d A}=1-\exp\left(-\frac{x}{L_d{}^2}\right) \tag{A.4}$$

Further, regarding the definition of dislocation links, each link has two pinning points while each pinning point connects two links, thus the number of links is equal to the associated pinning points. Assume that a link connects each pinning point to its nearest neighbour. The number fraction of links with the length in the range λ to $\lambda+d\lambda$ is the probability that a pinning point lies within the circular ring of area $2\pi\lambda d\lambda$ and no points exist in the inner area $\pi\lambda^2$ (Figure A.1).

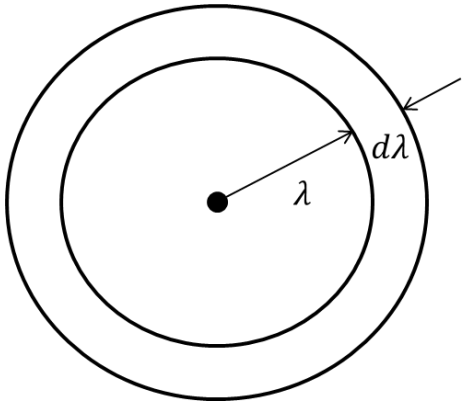

Fig. A.1 Probability description of a link with length in the range λ to $\lambda+d\lambda$

According to the derivation above, since $d\lambda$ is vanishingly small, such number fraction can be written as

$$\begin{aligned}&\exp\left(-\pi\lambda^2 N_d\right)\cdot\left\{1-\exp\left(-2\pi\lambda d\lambda N_d\right)\right\}=\exp\left(-\frac{\pi\lambda^2}{L_d{}^2}\right)\cdot\left\{1-\exp\left(-\frac{2\pi\lambda d\lambda}{L_d{}^2}\right)\right\}\\&\approx\frac{2\pi\lambda d\lambda}{L_d{}^2}\exp\left(-\frac{\pi\lambda^2}{L_d{}^2}\right)\end{aligned} \tag{A.5}$$

Repeating this calculation for all the pinning points results in a distribution function $\phi(\lambda)$, where

$$\phi(\lambda) = N_d \cdot \frac{2\pi\lambda}{L_d{}^2} \exp\left(-\frac{\pi\lambda^2}{L_d{}^2}\right) = \frac{2\pi\lambda}{L_d{}^4} \exp\left(-\frac{\pi\lambda^2}{L_d{}^2}\right) \tag{A.6}$$

and $\phi(\lambda)d\lambda$ is the number of links per unit area with lengths in the range λ to $\lambda + d\lambda$. It proves convenient to interpret this distribution as a distribution of actual (sessile) and virtual links, or as a distribution of the distances of any link to its nearest neighbour.

The total number of pinning points or dislocation links (all the sessile and virtual links shown in Figure 3.1 are potential links) is defined as ($x = \pi\lambda^2 / L_d{}^2$)

$$\int_0^\infty \phi(\lambda) d\lambda = \int_0^\infty N_d \exp\left(-\frac{\pi\lambda^2}{L_d{}^2}\right) \cdot \frac{2\pi\lambda}{L_d{}^2} d\lambda = \int_0^\infty N_d \exp(-x) \cdot dx = N_d \tag{A.7}$$

The total length of potential links is defined as

$$\begin{aligned} &\int_0^\infty \lambda\phi(\lambda) d\lambda = \int_0^\infty N_d \exp\left(-\frac{\pi\lambda^2}{L_d{}^2}\right) \cdot \frac{2\pi\lambda^2}{L_d{}^2} d\lambda = \int_0^\infty \frac{N_d L_d}{\sqrt{\pi}} \exp\left(-x^2\right) \cdot 2x^2 dx \\ &= \frac{N_d L_d}{\sqrt{\pi}} \left\{ \left[-x \exp\left(-x^2\right) \right]_0^\infty + \int_0^\infty \exp\left(-x^2\right) dx \right\} \\ &= \frac{N_d L_d}{\sqrt{\pi}} \left[\sqrt{\pi} erf\,(x) \right]_0^\infty = N_d L_d \end{aligned} \tag{A.8}$$

i.e. the distribution satisfies the requirement that the total length of links is equal to the number of links times the mean link length L_d.

Appendix B. Estimation of the reference shear strain rate regarding climb-controlled bypassing processes

For dislocation climb-controlled bypassing of precipitates, the rate-controlling process is the dislocation climb motion. Thus here we first attempt to approximate the dislocation climb velocity over particles associated with different climb bypassing modes. Taking the local climb process as an example, similar to the derivation in section 6.3, here we consider the variational functional

$$\Pi = \Psi + \dot{\Phi} \tag{B.1}$$

where Ψ is the rate potential related to dislocation climb motion and $\dot{\Phi}$ is the rate of change of the total Gibbs free energy. The best appximation for the dislocation climb velocity is that which minimises the functional Π (i.e. $\delta\Pi = 0$).

Consider a symmetric problem with two particles, as shown in Figure B.1. Assume that energy is only dissipated as a result of climb locally around the particles. Also assume that dislocation climbs up at a constant rate v_c, and atoms predominantly diffuse through the dislocation core.

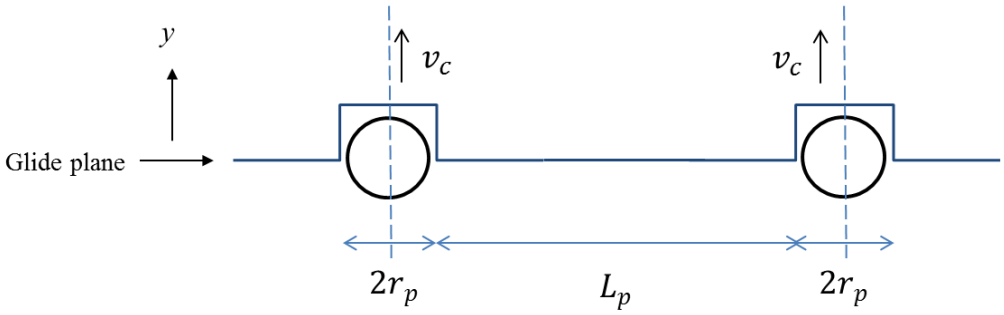

Fig. B.1 Schematic of LOCAL climb (at a constant rate v_c) process bypassing particles (with mean radius r_p) separated by the mean spacing L_p.

Given a small length *dx* on the climbing segment, the magnitude of the rate of volume of atoms flowing into or out of the elemental length is

$$\left|\frac{dV}{dt}\right| = \left|\frac{dJ}{dx}\right| dx \cdot a_c = \left|v_c\right| \cdot dx \cdot b \tag{B.2}$$

where a_c is the area of dislocation core and *J* is the volumetric flux or the volume of atoms flowing through unit area per unit time. Given the distance (the mean inter-particle spacing L_p) between the two particles, the average flux on the dislocation segment can be calculated similar to Eq. (6.19) (consider the boundary condition where *J*=0 at the centre of the climbing segment, *x*=0)

$$\left|\bar{J}\right| = \frac{2}{L_p}\int_0^{L_p/2} \left|J\right| dx = \frac{\left|v_c\right| bL_p}{4a_c} \tag{B.3}$$

The volumetric flux *J* can also be expressed as $J = Mf$, where $M = D_c\Omega/kT$ is the climb mobility (D_c : dislocation core diffusivity; $\Omega \approx b^3$: atomic volume; *k*: Boltzmann constant and *T*: temperature) and *f* is the thermodynamic driving force for diffusion. Note that only the segments around the particles climb (Figure B.1), thus consider a symmetric problem in Figure B.1 between the two dashed lines, the total volume *V* of the climbing segments can be written as

$$V = 2r_p a_c \tag{B.4}$$

Therefore, the rate potential Ψ for local climb process is determined by

$$\Psi = \int_V \frac{1}{2} f \cdot JdV = \int_V \frac{1}{2M} J^2 dV = \frac{1}{2M} \bar{J}^2 \cdot 2r_p a_c \tag{B.5}$$

For the rate of change of Gibbs free energy during local climb process, the first contribution is from the rate of increase in dislocation line energy, which is $(1/2)Gb^2 \cdot 2v_c$. Secondly, as the segments climb around particles, a concomitant glide motion occurs since the segments

always attach to the particles but are not separated from them before climbing over and bypassing. Thus there is some relaxation of the Gibbs free energy from the work done by the force on dislocations, which can be expressed as $\left(|\tau|-\tau_{LC}\right)bL_p v_g$, where $|\tau|$ is the applied shear stress, τ_{LC} is the threshold stress for local climb and v_g is the glide velocity. If we simply assume this glide velocity is proportional to and is much larger than the climb velocity v_c ($v_g = Yv_c >> v_c$, Y is the proportionality), the rate of change of total Gibbs free energy $\dot{\Phi}$ is expressed as

$$\dot{\Phi} = \frac{Gb^2}{2}\cdot 2v_c - \left(|\tau|-\tau_{LC}\right)bL_p v_g \approx -\left(|\tau|-\tau_{LC}\right)bL_p Y v_c \tag{B.6}$$

Finally, substituting Eqs. (B.3) - (B.6) into Eq. (B.1), the functional Π is (taking $a_c \approx 2b^2$)

$$\Pi = \Psi + \dot{\Phi} = \frac{{v_c}^2 {L_p}^2 r_p}{32M} - \left(|\tau|-\tau_{LC}\right)bL_p Y v_c \tag{B.7}$$

Using the principle $\delta\Pi = 0$, i.e.

$$\frac{\partial \Pi}{\partial v_c} = 0 \tag{B.8}$$

The climb rate v_c is obtained as

$$v_c = Y\left(|\tau|-\tau_{LC}\right)\cdot\frac{16Mb}{r_p L_p} = Y\left(|\tau|-\tau_{LC}\right)\cdot\frac{16D_c b^4}{r_p L_p kT} \tag{B.9}$$

Further, note the frequency of dislocation segments climbing over particles can be simply approximated as v_c / r_p (consider that a dislocation always intersects the centre plane of particles before it starts to climb). In addition, according to Rosler and Arzt [189], if we consider all the mobile dislocations climbing over particles at the same rates and assume that the time it takes to move a dislocation between particles is negligible, the generated shear strain after the climb bypassing can be estimated as $\rho_m bL_p$, (ρ_m is the mobile dislocation

density). Therefore, we can now write the expression for the plastic shear strain rate for local climb $\left(\dot{\gamma}_p\right)_{LC}$.

$$\left(\dot{\gamma}_p\right)_{LC} = \frac{v_c}{r_p} \cdot \rho_m b L_p = Y\left(|\tau| - \tau_{LC}\right) \cdot \frac{16 D_c \rho_m b^5}{r_p{}^2 kT} \tag{B.10}$$

Now similar approach can be adopted on the general climb process, with the schematic of which shown in Figure B.2.

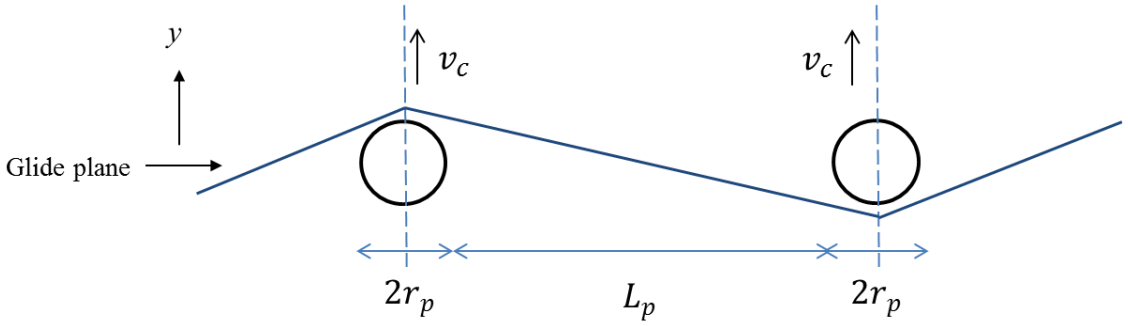

Fig. B.2 Schematic of GENERAL climb (at a constant rate v_c) process bypassing particles (with mean radius r_p) separated by the mean spacing L_p.

Corresponding changes made to the above derivations include a different threshold stress τ_{GC}, an average climb rate $v_c/2$ for the overall climbing segment and the total volume of the climbing segment $L_p a_c$. The final expression of the plastic shear strain rate for general climb $\left(\dot{\gamma}_p\right)_{GC}$ is then determined as

$$\left(\dot{\gamma}_p\right)_{GC} = \frac{v_c}{2r_p} \cdot \rho_m b L_p = Y\left(|\tau| - \tau_{GC}\right) \frac{32 D_c \rho_m b^5}{r_p L_p kT} \tag{B.11}$$

Eqs. (B.10) and (B.11) demonstrate a linear relationship between the plastic shear strain rate and the applied shear stress. Note that for 316 stainless steels employed in this study, the mean inter-particle spacing L_p is always larger than the mean particle size r_p, thus the general climb process is always much slower than local climb process in this material.